

EISSN 1305-3612

DIR

Diagnostic and Interventional Radiology



dirjournal.org

VOLUME 30
ISSUE 6
November 2024

Editor in Chief

Mehmet Ruhi Onur, MD

Department of Radiology, Hacettepe University Faculty of Medicine, Ankara, Türkiye

ORCID ID: 0000-0003-1732-7862

Section Editors and Scientific Editorial Board

Abdominal Imaging

İlkay S. İdilman, MD 

Department of Radiology, Hacettepe University Faculty of Medicine, Ankara, Türkiye

ORCID ID: 0000-0002-1913-2404

Sonay Aydın, MD 

Department of Radiology, Erzincan Binali Yıldırım University Faculty of Medicine, Erzincan, Türkiye

ORCID ID: 0000-0002-3812-6333

Artificial Intelligence and Informatics

Burak Koçak, MD 

Department of Radiology, University of Health Sciences, Başakşehir Çam and Sakura City Hospital, İstanbul, Türkiye

ORCID ID: 0000-0002-7307-396X

Tuğba Akıncı D'Antonoli, MD 

Institute of Radiology and Nuclear Medicine, Cantonal Hospital Baselland, Liestal, Switzerland

ORCID ID: 0000-0002-7237-711X

Breast Imaging

Füsun Taşkın, MD 

Department of Radiology, Acıbadem University Faculty of Medicine, İstanbul, Türkiye

ORCID ID: 0000-0001-7985-3660

Chest and Cardiovascular Imaging

Furkan Ufuk, MD 

Department of Radiology, The University of Chicago, Chicago, USA

ORCID ID: 0000-0002-8614-5387

Hybrid Imaging and Nuclear Medicine

Evrin Bengi Türkbey, MD 

Radiology and Imaging Sciences, Clinical Center, National Institutes of Health Bethesda, Maryland, United States

ORCID ID: 0000-0002-5216-3528

Interventional Radiology

Barbaros Çil, MD, FCIIRSE 

Department of Radiology, Koç University School of Medicine, İstanbul, Türkiye

ORCID ID: 0000-0003-1079-0088

Bahri Üstünsöz, MD 

Department of Radiology, LSUHSC (Louisiana State University Health Science Center) School of Medicine, New Orleans, United States

ORCID ID: 0000-0003-4308-6708

James Milburn, MD 

Department of Radiology, Ochsner Medical System, New Orleans, Louisiana, USA

ORCID ID: 0000-0003-3403-2628

Musculoskeletal Imaging

Zeynep Maraş Özdemir, MD 

Department of Radiology, İnönü University Faculty of Medicine, Malatya, Türkiye

ORCID ID: 0000-0003-1085-8978

Neuroradiology

Gülgün Yılmaz Ovalı, MD 

Department of Radiology, Celal Bayar University Faculty of Medicine, Manisa, Türkiye

ORCID ID: 0000-0001-8433-5622

Erkan Gökçe, MD 

Department of Radiology, Tokat Gaziosmanpaşa University Faculty of Medicine, Tokat, Türkiye

ORCID ID: 0000-0003-3947-2972

Pediatric Radiology

Meltem Ceyhan Bilgici, MD 

Department of Radiology, 19 Mayıs University Faculty of Medicine, Samsun, Türkiye

ORCID ID: 0000-0002-0133-0234

Evrin Özmen, MD 

Department of Radiology, Koç University Hospital, İstanbul, Türkiye

ORCID ID: 0000-0003-3100-4197

Publication Coordinator

Şükrü Mehmet Ertürk, MD 

Department of Radiology, İstanbul University, İstanbul Faculty of Medicine, İstanbul, Türkiye

ORCID ID: 0000-0003-4086-675X

Biostatistical Consultant

İlker Ercan, PhD 

Department of Biostatistics, Uludağ University School of Medicine, Bursa, Türkiye

ORCID ID: 0000-0002-2382-290X

Publication Services

Galenos Publishing, İstanbul, Türkiye

Past Editors

Editors in Chief

Mustafa Seçil, MD (2016-2023)

Nevzat Karabulut, MD (2011-2016)

Üstün Aydingöz, MD (2010-2011)

Okan Akhan, MD (2001-2010)

Ferhun Balkancı, MD (1999-2001)

Aytekin Besim, MD (1994-1999)*

* Dr. Aytekin Besim actually served as the General Coordinator. His work in this capacity, however, was in effect that of an Editor in Chief.

Editors

Ayşenur Cila, MD (2001-2002)

Suat Kemal Aytaç, MD (1997-2001)

Erhan Ilgıt, MD (1994-2001)

Okan Akhan, MD (1994-2001)

Ferhun Balkancı, MD (1994-2000)

Serdar Akyar, MD (1994-1997)

Section Editors

Section Editorship was established in 2002 at the tenure of Dr Okan Akhan, Editor in Chief.

Abdominal Imaging

Bengi Gürses, MD (2020-2023)

Mehmet Ruhi Onur, MD (2016-2023)

Barış Türkbey, MD (2014-2020)

Mustafa N. Özmen, MD (2012-2018)

Murat Acar, MD (2015-2016)

Mustafa Seçil, MD (2011-2016)

Ahmet Tuncay Turgut, MD (2011)

Deniz Akata, MD (2007-2011)

Ayşe Erden, MD (2002-2011)

Okan Akhan, MD (2002-2010)

Hakan Özdemir, MD (2002-2010)

Artificial Intelligence and Informatics

Barış Türkbey, MD (2020-2023)

Breast Imaging

Mustafa Erkin Arıbal, MD (2016-2023)

Sibel Kul (2015-2018)

Ayşenur Oktay, MD (2009-2014)

Ayşegül Özdemir, MD (2004-2009)

Cardiovascular Imaging

Uğur Bozlar, MD (2016-2023)

Muşturay Karçaaltıncaba, MD (2007-2010)

Mecit Kantarcı (2010-2016)

Chest Imaging

Nevzat Karabulut, MD (2010-2014)

Çetin Atasoy, MD (2007-2010)

Macit Arıyürek, MD (2002-2007)

Figen Demirkazık, MD, (2014-2018)

General Radiology

Ersin Öztürk, MD (2014-2017)

Utku Şenol, MD (2010-2013)

Oğuz Dicle, MD (2007-2010)

Interventional Radiology

Cüneyt Aytekin, MD (2016-2023)

Bora Peynircioğlu, MD (2012-2015)

Levent Oğuzkurt, MD (2011-2014)

Fatih Boyvat, MD (2007-2010)

İsmail Oran, MD (2015-2019)

Musculoskeletal Imaging

Hatice Tuba Sanal, MD (2016-2023)

Fatih Kantarcı, MD (2014-2016)

Ayşenur Oktay, MD (2011-2013)

Üstün Aydınöz, MD (2002-2011)

Berna Dirim Mete (2016-2017)

Neuroradiology and Head & Neck Imaging

Kubilay Aydın, MD (2016-2023)

Nafı Aygün, MD (2016-2023)

Kader Karlı Oğuz, MD (2011-2015)

Süleyman Men, MD (2007-2013)

Muhteşem Ağıldere, MD (2002-2011)

Nuclear Medicine

A. Cahid Civelek, MD (2016-2023)

Oktay Sarı, MD (2015)

Akın Yıldız, MD (2011-2014)

Pediatric Radiology

Korgün Koral, MD (2016-2023)

Murat Kocaoğlu, MD (2016-2023)

Ensar Yekeler, MD (2014-2016)

Suat Fitöz, MD (2007-2013)

Diagnostic and Interventional Radiology (Diagn Interv Radiol) is a bimonthly periodical of the Turkish Society of Radiology and the content of the journal is available at <https://www.dirjournal.org/>. It is peer-reviewed and adheres to the highest ethical and editorial standards. The editors of the journal endorse the Editorial Policy Statements Approved by the Council of Science Editors Board of Directors (<https://cse.memberclicks.net/>). The journal is in compliance with the Recommendations for the Conduct, Reporting, Editing and Publication of Scholarly Work in Medical Journals published by the International Committee of Medical Journal Editors (updated May 2022, www.icmje.org).

First ten volumes of Diagnostic and Interventional Radiology have been published in Turkish under the name of Tanısal ve Girişimsel Radyoloji (Index Medicus® abbreviation: Tani Girişim Radyol), the current title's exact Turkish translation.

Diagnostic and Interventional Radiology is an open access publication, and the journal's publication model is based on Budapest Open Access Initiative (BOAI) declaration. All published content is available online, free of charge at <https://www.dirjournal.org/>. Authors retain the copyright of their published work in Diagnostic and Interventional Radiology. The journal's content is licensed under a Creative Commons Attribution-NonCommercial (CC BY-NC) 4.0 International License which permits third parties to share and adapt the content for non-commercial purposes by giving the appropriate credit to the original work.

Please refer to the journal's webpage (<https://dirjournal.org/>) for "Aims and Scope", "Instructions to Authors" and "Instructions to Reviewers".

The editorial and publication processes of the journal are shaped in accordance with the guidelines of the ICMJE, WAME, CSE, COPE, EASE, and NISO.

Diagnostic and Interventional Radiology is indexed in **SCI-Expanded, Pubmed/Medline, Pubmed Central, TUBITAK ULAKBİM TR Index, DOAJ, HINARI, EMBASE, CINAHL, Scopus, Gale and CNKI.**

The journal is published online.

Owner: Can Çevikol on behalf of Turkish Society of Radiology

Responsible Manager: Mehmet Ruhi Onur

Contact Information

Diagnostic and Interventional Radiology Turkish Society of Radiology

Hoşdere Cad., Güzelkent Sok., Çankaya Evleri, F/2, 06540

Ankara, Türkiye

E-mail: info@dirjournal.org

Phone: +90 (312) 442 36 53 **Fax:** +90 (312) 442 36 54

Publisher Contact

Address: Molla Gürani Mah. Kaçamak Sk.

No: 21/1 34093 İstanbul, Türkiye

Phone: +90 (530) 177 30 97

E-mail: info@galenos.com.tr/yayin@galenos.com.tr

Web: www.galenos.com.tr **Publisher Certificate Number:** 14521

Online Publication Date: November 2024

EISSN 1305-3612

International scientific journal published bimonthly.



Contents

ABDOMINAL IMAGING

335 Original Article. Computed tomography for the diagnosis of gastroesophageal varices and risk assessment in patients with cirrhosis: a systematic review and meta-analysis. *Jinkui Li, Yuanhui Zhu, Jinrong Ni, Lili Wang, Junqiang Lei*

351 Original Article. Assessing hepatic steatosis by magnetic resonance in potential living liver donors. *Diğdem Kuru Öz, Zeynep Ellik, Ayşegül Gürsoy Çoruh, Mehmet Adıgüzel, Mesut Gümüşsoy, Saba Kiremitci, Elvan Onur Kırımker, Hale Gökcan, Atilla Halil Elhan, Deniz Balcı, Berna Savaş, Ayşe Erden, Ramazan İdilman*

ARTIFICIAL INTELLIGENCE AND INFORMATICS

357 Invited Review. Choosing the right artificial intelligence solutions for your radiology department: key factors to consider. *Deniz Alis, Toygar Tanyel, Emine Meltem, Mustafa Ege Seker, Delal Seker, Hakkı Muammer Karakaş, Ercan Karaarslan, İlkyay Öksüz*

366 Commentary. Exploring radiomics research quality scoring tools: a comparative analysis of METRICS and RQS. *Burak Koçak, Tugba Akinci D'Antonoli, Renato Cuocolo*

HEAD AND NECK IMAGING

370 Original Article. Diagnostic performance of multishot echo-planar imaging (RESOLVE) and non-echo-planar imaging (HASTE) diffusion-weighted imaging in cholesteatoma with an emphasis on signal intensity ratio measurement. *Ahmet Bozer, Zehra Hilal Adıbelli, Yeşim Yener, Abdullah Dalgıç*

INTERVENTIONAL RADIOLOGY

378 Letter To The Editor. Challenges associated with percutaneous nephrostomy in infants. *Iraklis-Georgios Kagias, Panagiotis Nikolinos, Chloe Mortensen, Joseph M. Norris*

380 Original Article. Pre-procedure ¹⁸F-FDG PET/CT imaging improves the performance of CT-guided transthoracic biopsy. *Al-Fang Jin, Zhe-Huang Luo, Wan-Ling Qi, Qian Liu*

385 Original Article. Correlation between computed tomography-based body composition parameters and hepatic venous pressure gradient in patients with cirrhosis: a systematic review and meta-analysis. *Siwei Yang, Zhiyuan Zhang, Qiyang Chen, Yuefeng Hu, Tianhao Su, Xuedong Sun, Long Jin*

402 Original Article. Experimental study of a canine model for a newly designed adjustable prefenestration aortic stent graft. *Lei Zhang, Chang Shu, Yuchen Qiu, Zeliang Fu, Pengcheng Guo, Xin Li*

MUSKOLOSKELETAL IMAGING

409 Invited Review. Pivotal role of the synovioentheseal complex in the imaging of arthritis and rheumatic diseases. *Adalet Elçin Yıldız, Üstün Aydingöz*

PEDIATRIC RADIOLOGY

419 Original Article. Imaging findings of primary lung tumors in children. *H. Nursun Özcan, Fırat Atak, Berna Oğuz, Tezer Kutluk, Mithat Haliloğlu*



Computed tomography for the diagnosis of gastroesophageal varices and risk assessment in patients with cirrhosis: a systematic review and meta-analysis

Jinkui Li¹
 Yuanhui Zhu²
 Jinrong Ni³
 Lili Wang¹
 Junqiang Lei¹

¹The First Hospital of Lanzhou University; Intelligent Imaging Medical Engineering Research Center of Gansu Province, Department of Radiology; Accurate Image Collaborative Innovation International Science and Technology Cooperation Base of Gansu Province, Lanzhou, China

²Gansu Provincial Hospital, Department of Radiology, Lanzhou, China

³The First Hospital of Lanzhou University, Department of Cardiovascular Surgery, Lanzhou, China

Corresponding author: Junqiang Lei

E-mail: leijq2011@126.com

Received 20 February 2024; revision requested 02 April 2024; accepted 16 April 2024.



Epub: 20.05.2024

Publication date: 06.11.2024

DOI: 10.4274/dir.2024.242723

PURPOSE

This meta-analysis aimed to evaluate the diagnostic accuracy of computed tomography (CT) for detecting gastroesophageal varices (GEVs) and identify high-risk GEVs in patients with cirrhosis.

METHODS

A comprehensive search of databases identified 28 studies reporting on CT-based diagnosis for GEVs confirmed via endoscopy. Meta-analyses were conducted to calculate pooled sensitivity (SEN) and pooled specificity (SPE), positive likelihood ratio (PLR) and negative likelihood ratio (NLR), diagnostic odds ratio (DOR), and the area under the curve (AUC).

RESULTS

Based on the number of patients (or varices), the pooled SEN, SPE, PLR, NLR, DOR, and AUC of CT-based diagnosis were estimated at 0.91 (0.92), 0.81 (0.45), 4.82 (1.67), 0.11 (0.17), 42.47 (10.26), and 0.93 (0.94), respectively, for any GEV and at 0.89 (0.89), 0.90 (0.79), 8.86 (4.28), 0.12 (0.14), 75.71 (30.19), and 0.95 (0.85), respectively, for high-risk GEVs. Subgroup analyses indicated that CT had a higher diagnostic accuracy for esophageal varices compared with gastric varices (AUC: 0.93 vs. 0.89, $P < 0.05$), and the 64-slice CT yielded superior SEN compared with 16-slice and <16-slice CT (AUC: 0.97 vs. 0.92 and 0.82, respectively, $P < 0.05$). Prospective studies demonstrated higher diagnostic accuracy than retrospective studies (AUC: 0.95 vs. 0.90, $P < 0.05$). Regarding variceal size, a cut-off of 3 mm and 5 mm discriminated between low- and high-risk individuals, respectively, with high diagnostic accuracy (AUC: 0.992 vs. 0.997, $P > 0.05$).

CONCLUSION

CT demonstrates promising diagnostic accuracy for identifying gastroesophageal varices and distinguishing high-risk GEVs in patients with cirrhosis. Further research to validate optimal variceal size cut-offs is warranted to enhance clinical utility.

CLINICAL SIGNIFICANCE

Such a high diagnostic accuracy of CT scans for predicting varices is clinically meaningful for patients with cirrhosis accompanied by portal hypertension. If high-risk varices are identified at CT scans, early intervention would be helpful to reduce the risk of variceal bleeding.

KEYWORDS

Computed tomography, gastroesophageal varices, gastric varices, esophageal varices, cirrhosis, meta-analysis

Bleeding of gastroesophageal varices (GEVs) is a serious complication of portal hypertension (PH) in cirrhosis.¹ Gastric varices (GVs) and esophageal varices (EVs) can occur concurrently or separately. EVs are more important for the collateral circulation of PH than GVVs and occur in 20%–40% and approximately 70% of compensated and decompensated patients with cirrhosis, respectively.² Esophagogastroduodenoscopy (EGD) is current-

ly the standard approach for assessment of GEVs when diagnosing cirrhosis.³ Presence of advanced liver disease (Child Pugh's score B or C), large varices (>5 mm), or varices with the red color (RC) sign specify patients with a high hemorrhage risk.^{4,5} The progression from small to large varices is detected in approximately 10% of patients with cirrhosis per year.⁶ In this context, it is of great significance to detect GEVs and predict variceal bleeding in time. EGD screening is recommended for patients with cirrhosis with small varices and patients without any varices every 1–2 and 2–3 years, respectively.^{7,8} However, as a screening method, EGD is limited due to its invasive nature and poor acceptance by patients.⁹ Additionally, it is obvious that a significant part of patients undergoing EGD screening, particularly those with compensated cirrhosis, have no varices or only small EVs. Furthermore, EGD fails to evaluate the entire spectrum of extraparietal GEVs and may miss some GVs.^{10,11}

These drawbacks have driven the ongoing studies to identify alternative, non-invasive techniques for repeat variceal detection.

The Baveno VI guidelines recommend that patients with alcoholic or viral cirrhosis, liver stiffness <20 kPa and a platelet count >150 G/L should avoid EGD screening, which is a highly sensitive approach with limited specificity for the detection of GEVs.¹² Computed tomography (CT) or magnetic resonance imaging of portosystemic collateral vessels has been shown to have a sensitivity of 95% and specificity of 36% in predicting high-risk EVs in patients who do not meet the Baveno VI criteria.¹³ Unlike EGD, contrast-enhanced CT can clearly show the portal vein system and collateral circulation,¹⁴ including in patients with periesophageal and perigastric fundal varices. Furthermore, CT is useful in assessing the risk of GEV bleeding.¹⁵

Main points

- Computed tomography (CT) demonstrates promising diagnostic accuracy for identifying gastroesophageal varices (GEVs) and distinguishing high-risk GEVs in patients with cirrhosis.
- CT with a >16-slice scanner showed a significantly better performance than the <16-slice CT.
- Varices of <3 mm and >5 mm may discriminate against low-risk and high-risk patients, respectively.
- Approximately 84.29% of patients prefer CT instead of endoscopy in screening for varices.

Herein, the study authors conduct a systematic review and meta-analysis to evaluate the diagnostic efficacy of CT for GEVs and analyze its predictive value for high-risk varices in patients with cirrhosis.

Methods

The present study is reported according to the Preferred Reporting Items for Systematic Reviews and Meta-analyses (PRISMA) statement and the published recommendations. The detailed protocol is accessible in PROSPERO (CRD42020220384). Ethics information and informed consent forms were not required, as systematic reviews typically involve synthesizing and summarizing existing literature rather than directly engaging in human or animal experiments.

Literature search

To retrieve eligible studies on CT-based diagnosis of EV and/or GV, a systematic literature search in the PubMed, Embase, Cochrane Library, and Web of Science databases was performed from inception to November 30, 2023. The search was conducted based on the following search terms: "gastroesophageal varices," "gastric varices," "esophageal varices," "varices," "CT," and "computed tomography." The search strategy was determined after multiple pre-searches and combined free words with Medical Subject Headings terms for each database. No language or article-type restriction was applied. The references of the included studies and other systematic reviews and meta-analyses were also reviewed to obtain a comprehensive list of relevant studies.

Eligibility criteria

The inclusion criteria were as follows: (1) the patients were diagnosed with cirrhosis; (2) the diagnostic examination was contrast-enhanced CT; (3) EGD was performed to confirm the presence and/or grade of esophageal and/or GVs; (4) the data provided was sufficient to conduct a 2 × 2 table to assess the diagnostic sensitivity and specificity of CT for the varices; and (5) >20 patients were evaluated for reliable assessment.

The exclusion criteria were as follows: (1) patients without cirrhosis; (2) patients who were not evaluated via endoscopy or CT; (3) duplicates; (4) review articles; (5) case reports; and (6) conference papers, letters, and abstracts.

Study selection, data extraction, and quality assessment

The titles and abstracts of the search results were screened for eligibility by two independent readers (Y. Zhu and L. Wang with 3 years and 12 years of experience in abdominal imaging, respectively) according to the pre-enacted inclusion and exclusion criteria, and full texts meeting the inclusion criteria were retrieved. The following data were extracted according to the predefined data form: the first author's name, the study design (prospective or retrospective), publication year, country, sample size, age, gender, etiology of cirrhosis, Child–Pugh class, time interval between the CT and EGD, number of patients who underwent EGD, location of varices (EVs and/or GVs), prevalence of any-sized and/or high-risk varices, definitions of high-risk varices on CT and EGD, cut-off values (the maximal short-axis diameter of the largest varix), and CT imaging parameters (slice). The true-positive (TP), false-positive (FP), true-negative (TN), and false-negative (FN) values were also extracted directly or calculated. It should be recognized that all the data per study were extracted if the study involved several CT techniques or observers, and serial numbers to this study were given. Finally, two readers independently performed QUADAS-2 criteria¹⁶ assessments. Results were cross-checked at every step, and a consensus was reached in the case of discrepancy.

Statistical analysis

Analyses were performed using the STATA 15.0 (StataCorp, College Station, TX) and Revman 5.4 (The Cochrane Collaboration, 2020) software. However, in the case of <4 articles, MetaDiSc 1.4 was used for analysis, and I^2 statistics were used to analyze heterogeneity of the included studies.¹⁷ Significant heterogeneity was indicated by $I^2 > 50\%$ or $P < 0.10$.

If there is no heterogeneity or if the heterogeneity is low, a fixed effects model should be chosen. A random effects model allows for high heterogeneity, and a sensitivity analysis or subgroup analysis should then be carried out. The pooled sensitivity (SEN), pooled specificity (SPE), positive predictive values and negative predictive values, positive likelihood ratio (PLR) and negative likelihood ratio (NLR), and diagnostic odds ratio (DOR) with a 95% confidence interval (CI) were calculated based on the number of TPs, FPs, FNs, and TNs, respectively. Following

this, the summary receiver operating characteristic and its corresponding area under the curve (AUC) were calculated. If there was significant heterogeneity, subgroup analysis was carried out to identify the sources of heterogeneity. In addition, in the case of >9 studies, the authors assessed for any publication bias by applying Deeks et al.¹⁸ plot test. Statistical significance was indicated by $P < 0.05$.

Results

Literature search and study selection

This systematic review included 28 publications, involving 2,879 participants.^{10,19-45} The PRISMA flow chart of the literature screening is shown in Figure 1.

Study design and properties

The extractive data of the included studies are summarized in Table 1. The 28 selected articles were published between 2007 and 2023. In 27 of these papers, data were presented based on the number of patients,^{10,19-44} and the data in the remaining article (a retrospective report evaluating EVs in 104 participants) were presented based on the number of varices.⁴⁵ Among the patient-based studies, which assessed for varices of any size, 11 (40.7%) were retrospective,^{20,22-24,27,29,30,32,33,37,42} 12 (44.4%) were prospective,^{10,19,26,28,31,34,35,38-41,44} and 4 (14.9%) were undefined;^{21,25,36,43} 24 (88.9%) assessed for EVs^{10,19-35,38-41,43,44}, and 6 (22.2%)^{10,32,35,36,37,42} assessed for both EVs and GVs, including 3 for GVs only.^{10,32,35} The prevalence of EVs and GVs were 33.6%–98% and 10.5%–28.3%, respectively. Two studies included only patients with hepatocellular carcinoma.^{33,34} The remaining studies enrolled patients with various etiological factors, such as viral hepatitis, alcohol abuse, and cryptogenic cirrhosis.

Among the eligible studies, 18 assessed for high-risk varices.^{20-24,27,29-35,36,39,41,43,45} The detailed characteristics of these studies are shown in Supplementary Table 1. A total of 16 articles (88.9%) assessed for high-risk EVs,^{20-24,27,29-35,36,39,41,43,45} 1 assessed for high-risk GVs,³² and 1 assessed for high-risk GEVs.³⁵ The prevalence of high-risk EVs and GVs was 15.4%–75% and 16.5%, respectively. The varix size cut-off of high-risk varices on CT was 2 mm,^{21,22,33,34,45} 3 mm,^{30,41} 3.9 mm,²⁴ 4 mm,^{20,23} and 5 mm,^{31,32,35,36} respectively. Finally, 3 studies did not specify the cut-off on CT.^{27,29,39}

Additionally, 3 studies^{31,40,42} reported that the varix size on CT was significantly correlated with the presence and severity of the RC

sign. A cut-off of 4 or 5 mm was used to predict the RC sign.

A total of 5 studies^{10,38-41} concerned preferences of the patients for CT versus EGD. Most (84.3%) patients preferred undergoing a CT scan instead of EGD for varix screening.

Quality assessment

The results of the quality evaluation of the eligible articles are shown in Supplementary Figure 1. Most studies were identified as low-risk in terms of risk of bias and applicability

concerns, and all of the studies met >4 terms of the 7 total domains. The most common domain of unclear risk was the reference standard regarding the blinding of EGD interpretation to the CT imaging.

Diagnostic accuracy of computed tomography for gastroesophageal varices

The results of the meta-analyses are summarized in Table 2. Significant heterogeneity was observed in all the analyses ($P < 0.05$ and $I^2 > 50\%$).

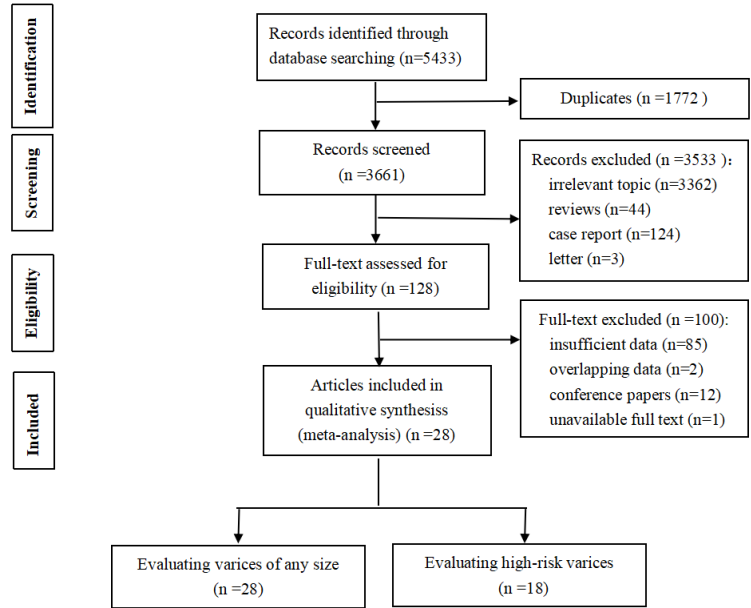


Figure 1. The study screening process.

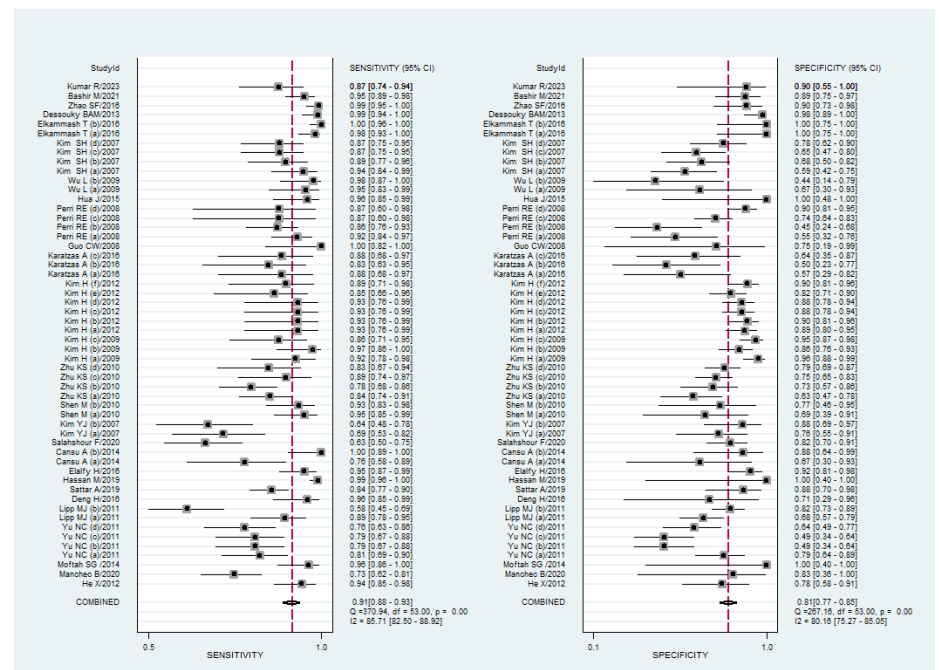


Figure 2. Coupled Forest plots of sensitivity and specificity for diagnosing gastroesophageal varices with CT. CT, computed tomography.

Table 1. Characteristics of computed tomography for diagnosing gastroesophageal varices

Study/journal/year	Study design	Country	Sample	M/ F	Mean age (y)	Etiology	Child-Pugh score
He et al. ¹⁹ , Chin J Radiol (China), 2012	P	China	92	73/19	51 (34–80)	Viral 78, alcohol 12, pancreatic 1, cholestatic 1	A 33, B 44, C 15
Manchec et al. ²⁰ , AJR Am J Roentgenol, 2020	R	US	97	64/33	54.4	HBV 2, HCV 35, alcohol 46, NASH 18	A 36, B 50, C 11
Moftah et al. ²¹ , Egypt J Radiol Nucl Med, 2014	/	Egypt	54	40/14	56.8 (38–75)	/	/
Yu et al. ²² , AJR Am J Roentgenol, 2011	R	US	109	60/49	55.9 (19–82)	HBV 7, HCV 51, alcohol 19, cryptogenic or others 32	/
Lipp et al. ²³ , Dig Dis Sci, 2011	R	US	195	/	55.2	/	/
Deng et al. ²⁴ , J Evid Based Med, 2017	R	China	52	33/19	55.4	HBV 13, HCV 2, HBV and HCV 1, alcohol 16, alcohol and HBV 5, others 15	A 25, B 21, C 6
Sattar et al. ²⁵ , Med Forum, 2019	/	Pakistan	172	96/76	45.01 (35–60)	/	/
Hassan et al. ²⁶ , Cureus, 2019	P	Pakistan	196	106/90	55.8 (11–82)	HBV 13, HCV 79, others 104	/
Elalfy et al. ²⁷ , World J Hepatol, 2016	R	Egypt	124	26/98	56.5	HCV 124	A 78, B 46, C 0
Cansu et al. ²⁸ , Eur J Radiol, 2014	P	Turkey	42	29/13	56.2	HBV 19, HCV 10, HBV and HCV 1, alcohol 2, others 10	A 16, B 13, C 13
Salahshour et al. ²⁹ , Abdom Radiol (NY), 2020	R	Iran	50	27/23	56.8	HBV 20, HCV 15, HBV and HCV 2, alcohol 2, others 11	A 26, B 18, C 6
Salahshour et al. ²⁹ , Abdom Radiol (NY), 2020	R	Iran	124	76/48	50.38 (21–73)	HBV 30, HCV 7, alcohol 5, AIH 12, cryptogenic or others 70	/
Kim et al. ³⁰ , AJR Am J Roentgenol, 2007	R	US	67	39/28	56.2 (33–77)	HBV 15, HCV 24, HBV and HCV 6, alcohol 15, cryptogenic or others 7	A 16, B 25, C 26
Shen et al. ³¹ , Zhonghua Yi Xue Za Zhi, 2010	P	China	69	56/13	53 (23–76)	HBV 60, HCV 4, alcohol and HBV 3, alcohol 2	A 44, B 22, C 3
Zhu et al. ³² , J Clin Gastroenterol, 2010	R	China	127	96/31	45.2 (30–75)	HBV 95, HCV 6, alcohol 13, cryptogenic or others 13	A 48, B 47, C 32
Kim et al. ³³ , Dig Dis Sci, 2009	R	South Korea	110	81/29	61 (27–80)	HBV 67, HCV 32, HBV and HCV 2, alcohol 7, unknown 2	A 70, B 29, C 11
Kim et al. ³⁴ , World J Gastroenterol, 2012	P	South Korea	100	79/21	58.4 (35–82)	HBV 76, HCV 14, alcohol 5, unknown 5	A 89, B 10, C 1
Karatzas et al. ³⁵ , Ann Gastroenterol, 2016	P	Greece	38	30/8	63 (48–81)	Viral 13, alcohol 18, others 7	A 21, B 11, C 6
Perri et al. ¹⁰ , Hepatology, 2008	P	US	101	64/37	57.5	Viral 22, alcohol 19, cholestatic 18, NASH 15, others 27	A 45, B 40, C 16
Guo et al. ³⁶ , Chin J Med Imaging Technol, 2008	/	China	27	14/13	48.6 (28–71)	HBV 23, HCV 2, alcohol 2	A 10, B 12, C 5

Table 1. Continued

CT scanner	CT technique	Patients underwent EGD	Time interval	Patient acceptance	Varice location	Prevalence of varices (%)	TP	FP	FN	TN				
64-slice	MSCT portography	92	Within 4 w	/	GEVs	70.65%	61	6	4	21				
/	/	97	Within 3 m	/	EVs	94.80%	66	1	25	5				
4 or 8-slice	MDCT	54	/	/	EVs	92.59%	48	0	2	4				
16 or 64-slice	MDCT with standard 5 mm and thin-section MPR	109	Within 10 w	/	EVs	56.88%	50	10	12	37				
							49	24	13	23				
							49	24	13	23				
							47	17	15	30				
4 or 16 or 64-slice	MDCT	137	Within 3 m	/	EVs	44.52%	54	24	7	52				
							165	41	17	30	77			
/	/	52	Within 4 w	/	EVs	86.54%	43	2	2	5				
16-slice	MDCT	172	/	/	EVs	84.88%	123	3	23	23				
64-slice	MDCT	196	Within 20 d	/	EVs	97.95%	190	0	2	4				
16-slice	MDCT	124	/	/	EVs	59.68%	70	4	4	46				
16-slice	MDCT with effervescent powder	42	Within 4 w	/	EVs	78.57%	25	3	8	6				
16-slice	MDCT without effervescent powder	50	Within 4 w	/	EVs	66%	33	2	0	15				
16 or 64-slice	MDCT	124	Within 6 m	/	EVs	50.81%	40	11	23	50				
single or 4 slice	Single-detector helical CT or MDCT	67	Within 4 w	/	EVs	62.69%	29	6	13	19				
							27	3	15	22				
320-slice	MDCT	69	Within 1 w	/	EVs	81.16%	53	4	3	9				
							52	3	4	10				
4-slice	MDCT	127	Within 4 w	/	EVs	67.72%	72	15	14	26				
							32	23	4	68				
											30	19	6	72
16-slice	MDCT	110	Within 4 w	/	EVs	33.64%	34	3	3	70				
							36	10	1	63				
							32	4	5	69				
64-slice	MDCT with and without MPR	100	Within 4 h	/	EVs	50.00%	25	8	2	65				
							25	7	2	66				
							25	9	2	64				
							25	9	2	64				
							23	13	4	60				
							24	7	3	66				
16-slice	MDCT	38	Within 1 m	/	EVs	60.53%	21	6	3	8				
							20	7	4	7				
							21	5	3	9				
							20	7	3	8				
							19	8	4	7				
							20	6	3	9				
16-slice	MDCT	38	Within 1 m	/	EVs	60.53%	3	4	1	30				
							3	4	1	30				
											3	4	1	30
4 slice or higher	MDCT	101	Within 5 d	88% CT, 6% EGD, 6% no preference	EVs	78.22%	73	10	6	12				
							68	12	11	10				
							13	22	2	64				
							13	9	2	77				
14.85%														
64-slice	MSCT portography	23	/	/	GEVs	82.61%	19	1	0	3				

Table 1. Continued

Study/journal/year	Study design	Country	Sample	M/ F	Mean age (y)	Etiology	Child– Pugh score
Hua et al. ³⁷ , J Dig Dis, 2015	R	China	90	57/33	54.4 (31–75)	HBV 49, HCV 3, alcohol 8, AIH 5, others 25	A 36, B 34, C 20
Wu et al. ³⁸ , Chin J Gastroenterol, 2009	P	China	50	30/20	57.7 (31–78)	HBV 38, HBV, and HCV 1, AIH 1, others 10	A 13, B 31, C 6
Kim et al. ³⁹ , Radiology, 2007	P	China	90	65/25	54.8 (21–77)	HBV 66, HCV 19, Alcohol 2, cryptogenic 3	A 73, B 17, C 0
Elkammash et al. ⁴⁰ , Egypt J Radiol Nucl Med, 2016	P	Egypt	112	77/45	51.4 (38–72)	HBV 52, HCV 49, bilharziasis 11	/
Dessouky and Abdel Aal ⁴¹ , Arab J Gastroenterol, 2013	P	Egypt	137	73/64	58.7 (45–77)	HBV 27, HCV 93, HBV and HCV 14, steatohepatitis 3	A 75, B 42, C 20
Zhao et al. ⁴² , Chin J Gastroenterol, 2016	R	China	143	96/47	52.39 (23–78)	HBV 101, HCV 5, alcohol 16, cryptogenic or others 21	A 54, B 48, C 41
Bashir et al. ⁴³ , P J M H S, 2021	/	Rawalpindi	145	/	35–80	/	/
Kumar et al. ⁴⁴ , Pol J Radiol, 2023	P	India	621	/	62	/	/
Kim et al. ⁴⁵ , J Gastroenterol Hepatol, 2009*	R	South Korea	104	77/27	59 (27–80)	HBV 75, HCV 13, alcohol 7, cryptogenic 9	A 43, B 32, C 29

*Data presented based on number of varices. R, retrospective; P, prospective; HBV, hepatitis B virus; HCV, hepatitis C virus; AIH, autoimmune hepatitis; PSC, primary sclerosing cholangitis; NASH, non-alcoholic steatohepatitis; MDCT, multi-detector computed tomography; MPR, multiplanar reconstruction; MSCT, multi-slice spiral computed tomography; EVs, esophageal varices; GVs, gastric varices; GEVs, gastroesophageal varices; TP, true-positive; FP, false-positive; TN, true-negative; FN, false-negative.

Based on the number of patients: In 27 studies,^{10,19–44} which contained 54 sets of data regarding GEVs of any size, the pooled SEN and SPE were 0.91 and 0.81, respectively (Figure 2), with an AUC of 0.93 (Supplementary Figure 2). There were 35 sets of data from 17 studies^{20–24,27,29–35,36,39,41,43} that assessed for high-risk GEVs. The pooled SEN and SPE were 0.90 and 0.90, respectively (Figure 3), with an AUC of 0.96 (Supplementary Figure 3). The pooled SPE and PLR for high-risk varices were significantly higher than those for varices of any size ($P = 0.001$ and 0.020 , respectively).

Based on the number of varices: There was only 1 study⁴⁵ with 3 sets of data. The pooled SEN, SPE and AUC for varices of any size (and high-risk EVs) were 0.92 (0.89), 0.45 (0.85), and 0.94 (0.95), respectively.

Patient-based subgroup analysis of gastro-esophageal varices of any size

To identify the sources of heterogeneity, the authors performed subgroup analysis according to the location of varices, study design, and CT scanners used.

Location of the varices

EVs: There were 47 sets of data from 24 studies^{10,20–35,38–41,43,44} that assessed for EVs of any size, and 32 sets of data from 15 studies^{20–24,27,29–31,33,34,36,37,41,43} that assessed for high-risk EVs (Table 2). The pooled SPE and PLR for high-risk EVs were significantly higher than those for EVs of any size ($P = 0.010$ and 0.034 , respectively). However, no statistically significant difference in SEN, NLR, DOR or AUC was found between high-risk EVs and EVs of any size (all $P > 0.05$). According to

the corresponding I^2 (82.5%–100%), there was substantial heterogeneity in the EV subgroup among the studies. Then, a subgroup analysis was carried out for EVs (Supplementary Table 2).

GVs: There were 7 data sets from 3 studies^{10,32,35} concerning the presence of GVs of any size (Table 2). There was no statistically significant heterogeneity in the GV subgroup among these studies. Since only 1 study³² reported on high-risk GVs, a pooled analysis could not be performed.

Study design

Prospective vs. retrospective: There were 29 and 21 sets of data from 12 prospective^{10,19,26,28,31,34,35,38–41,44} and 11 retrospective^{20,22–24,27,29,30,32,33,37,42} studies, respectively (Table 3). Between the prospective studies

Table 1. Continued

CT scanner	CT technique	Patients underwent EGD	Time interval	Patient acceptance	Varice location	Prevalence of varices (%)	TP	FP	FN	TN
/	MSCT	50	/	/	GEVs	90%	43	0	2	5
16-slice	MSCT	50	Within 4 w	74% CT, 1% EGD, 24% no preference	EVs	82%	39	3	2	6
16-slice	CT esophagograms	90	Within 4 h	66.67% CT, 14.44% EGD, 18.89% no preference	EVs	58.89%	40	5	1	4
16-slice	CT esophagograms	90	Within 4 h	66.67% CT, 14.44% EGD, 18.89% no preference	EVs	58.89%	50	15	3	22
16-slice	CT esophagograms	90	Within 4 h	66.67% CT, 14.44% EGD, 18.89% no preference	EVs	58.89%	47	12	6	25
16-slice	CT esophagograms	90	Within 4 h	66.67% CT, 14.44% EGD, 18.89% no preference	EVs	58.89%	46	13	7	24
16-slice	CT esophagograms	90	Within 4 h	66.67% CT, 14.44% EGD, 18.89% no preference	EVs	58.89%	46	8	7	29
64-slice	MDCT	112	Within 2 w	83% CT, 7.1% EGD, 9.9% no preference	EVs	88.39%	97	0	2	13
64-slice	MDCT	112	Within 2 w	83% CT, 7.1% EGD, 9.9% no preference	EVs	88.39%	99	0	0	13
16-slice	MDCT	137	Within 24 h	98% CT, 2% EGD	EVs	65.69%	89	1	1	46
64-slice	MDCT	143	Within 1 w	/	GEVs	80.42%	112	3	1	27
/	MDCT	145	/	/	EVs	74.5%	102	4	6	33
128-slice	MDCT	62	Within 2 d	/	EVs	37.30%	45	1	7	9
128-slice	MDCT	62	Within 2 d	/	EVs	37.30%	180	9	8	11
16 or 64-slice	MDCT	104	Within 4 w	/	EVs	90.38%	169	9	19	11
16 or 64-slice	MDCT	104	Within 4 w	/	EVs	90.38%	172	15	16	5

*Data presented based on number of varices. R, retrospective; P, prospective; HBV, hepatitis B virus; HCV, hepatitis C virus; AIH, autoimmune hepatitis; PSC, primary sclerosing cholangitis; NASH, non-alcoholic steatohepatitis; MDCT, multi-detector computed tomography; MPR, multiplanar reconstruction; MSCT, multi-slice spiral computed tomography; EVs, esophageal varices; GV, gastric varices; GEVs, gastroesophageal varices; TP, true-positive; FP, false-positive; TN, true-negative; FN, false-negative.

Table 2. Overall diagnostic accuracy of studies researching gastroesophageal varices

Study characteristic	No. of article/set/patient	SEN (95% CI)	SPE (95% CI)	PLR (95% CI)	NLR (95% CI)	DOR (95% CI)	AUC (95% CI)
Patient-based							
Any sized GEVs	27/54/5217	0.91 (0.88–0.93)	0.81 (0.77–0.85)	4.82 (3.84–6.03)	0.11 (0.08–0.15)	42.47 (26.61–67.77)	0.93 (0.90–0.95)
High-risk GEVs	17/35/3526	0.90 (0.85–0.93)	0.90 (0.86–0.93)	8.85 (6.25–12.70)	0.12 (0.08–0.17)	75.10 (41.44–136.11)	0.96 (0.93–0.97)
P value	/	0.682	0.001	0.020	0.728	0.215	0.069
Any sized EVs	24/47/4596	0.91 (0.87–0.93)	0.81 (0.76–0.85)	4.75 (3.67–6.15)	0.12 (0.08–0.16)	41.00 (24.17–69.55)	0.93 (0.90–0.95)
High-risk EVs	15/32/3234	0.90 (0.85–0.93)	0.89 (0.85–0.93)	8.36 (5.82–12.01)	0.11 (0.08–0.17)	73.75 (39.62–137.30)	0.95 (0.93–0.97)
P value	/	0.682	0.010	0.034	0.739	0.233	0.224
Any sized GVs	3/7/570	0.85 (0.76–0.91)	0.83 (0.77–0.87)	4.88 (3.59–6.62)	0.19 (0.12–0.30)	26.03 (14.02–48.33)	0.89 (0.86–0.92)
High-risk GVs*	1/2/252	0.83 (0.69–0.93)	0.97 (0.93–0.99)	25.06 (11.95–52.54)	0.17 (0.09–0.34)	149.43 (48.87–456.86)	/
P value	/	0.789	<0.001	<0.001	0.787	0.007	/
Varix-based							
Any sized (EVs)*	1/3/104	0.92 (0.90–0.94)	0.45 (0.32–0.58)	1.67 (1.07–2.61)	0.17 (0.08–0.36)	10.26 (3.38–31.17)	0.9373 (0.1522)
High-risk (EVs)*	1/3/104	0.89 (0.85–0.92)	0.79 (0.74–0.84)	4.28 (3.31–5.53)	0.14 (0.09–0.22)	30.19 (17.42–52.33)	0.8483 (0.0532)
P value	/	0.145	<0.001	<0.001	0.664	0.088	0.581

*Data calculated using Meta-Disc 1.4. GEVs, gastroesophageal varices; EVs, esophageal varices; GVs, gastric varices; SEN, sensitivity; SPE, specificity; PPV, positive predictive value; NPV, negative predictive value; DOR, diagnostic odds ratio; AUC, area under the curve; 95% CIs, corresponding 95% confidence interval.

and the retrospective studies, statistically significant differences were found in the pooled SEN, NLR, and AUC (0.93 vs. 0.85; 0.08 vs. 0.18; and 0.95 vs. 0.90, respectively; $P = 0.007$, 0.015, and 0.002, respectively), but no statistically significant difference in SPE or PLR was found ($P = 0.883$ and 0.598, respectively).

Computed tomography scanner

<16-slice vs. 16-slice vs. 64-slice: There were 7, 17, and 12 sets of data from 3,^{21,30,32} 8,^{25,27,28,33,35,38,39,41} and 6^{19,26,34,36,40,42} studies that assessed for varices by using the <16-slice, 16-slice, and 64-slice CT scans, respectively (Table 3). Among the three subgroups, the 64-slice CT yielded the highest SEN, whereas the 16-slice CT and 64-slice CT yielded a sim-

ilarly high SPE and AUC, which were higher than those of the <16-slice CT (all $P < 0.05$).

Patient-based subgroup analysis of the high-risk esophageal varices

The results of the subgroup analyses for high-risk EVs are summarized in Table 4. A study that used a cut-off of 3.9 mm²⁴ was classified into the 4 mm subgroup. The SEN from a cut-off of 2 mm was close to that from a cut-off of 3 mm (0.92 vs. 0.97, $P = 0.107$) and higher than that from a cut-off of 4 or 5 mm ($P < 0.001$). Likewise, the SPE from a cut-off of 3 mm was close to that from a cut-off of 5 mm (0.91 vs. 0.93, $P = 0.491$) and higher than that from a cut-off of 2 mm ($P = 0.001$ and <0.001 , respectively). Cut-offs of 3 and 5 mm shared the approximate AUC (0.992 vs. 0.997, $P = 0.657$), which was higher than for cut-offs of 2 and 4 mm ($P = 0.004$ and 0.006, respectively).

Publication bias

Deek's funnel plot (Supplementary Figure 4) revealed no evidence of significant publication bias ($P = 0.410$).

Discussion

In this study, the authors confirmed the feasibility of CT in diagnosing GEVs, including high-risk varices, in patients with cirrhosis. The data were analyzed according to each patient and lesion, the relationship between the GEV size and RC sign was assessed, and the patient's acceptance of CT and EGD was

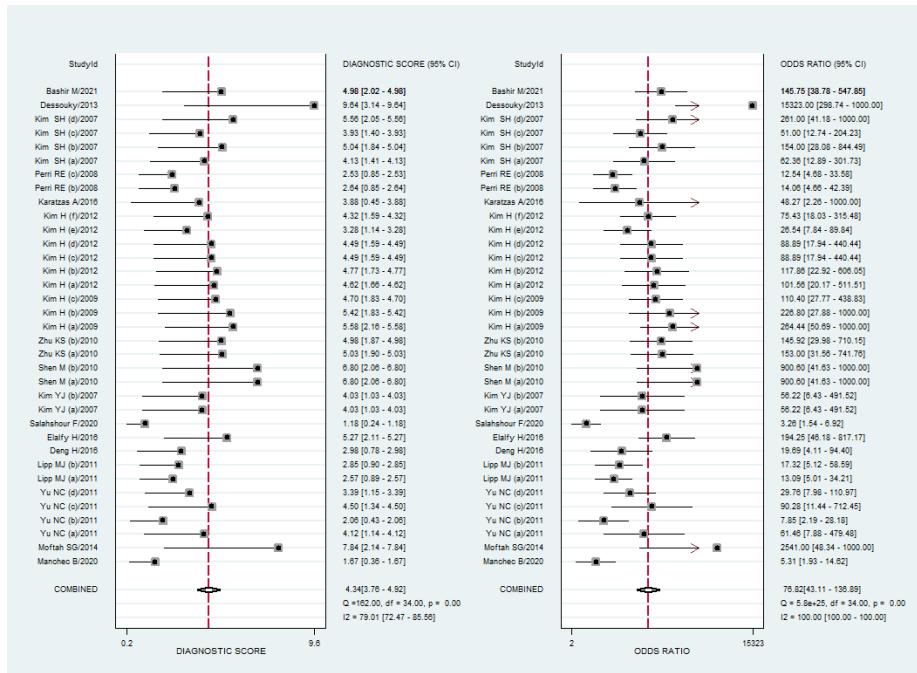


Figure 3. Coupled Forest plots of sensitivity and specificity for predicting high-risk varices with CT. CT, computed tomography.

Table 3. Subgroup results of meta-analyses regarding any sized gastroesophageal varices based on number of patients

Study subgroups	No. of article/ set/patient	SEN (95% CI)	SPE (95% CI)	PLR (95% CI)	NLR (95% CI)	DOR (95% CI)	AUC (95% CI)
Location of varices							
Any sized EVs	24/47/4596	0.91 (0.87–0.93)	0.81 (0.75–0.85)	4.75 (3.67–6.15)	0.12 (0.08–0.16)	41.00 (24.17–69.55)	0.93 (0.90–0.95)
Any sized GVVs	3/7/570	0.85 (0.76–0.91)	0.83 (0.77–0.87)	4.88 (3.59–6.62)	0.19 (0.12–0.30)	26.03 (14.02–48.33)	0.89 (0.86–0.92)
<i>P</i> value	/	0.164	0.585	0.896	0.117	0.302	0.046
Study design							
Retrospective	11/21/2300	0.85 (0.79–0.90)	0.80 (0.73–0.86)	4.32 (3.08–6.06)	0.18 (0.12–0.27)	23.56 (12.00–46.23)	0.90 (0.87–0.92)
Prospective	12/29/2519	0.93 (0.91–0.95)	0.81 (0.74–0.87)	4.93 (3.51–6.93)	0.08 (0.06–0.12)	60.52 (31.18–117.44)	0.95 (0.93–0.97)
<i>P</i> value	/	0.007	0.883	0.598	0.015	0.118	0.002
Computed tomography scanner							
<16 detector	3/7/696	0.82 (0.73–0.88)	0.76 (0.71–0.81)	3.39 (2.77–4.17)	0.24 (0.16–0.36)	14.10 (8.41–23.64)	0.81 (0.77–0.84)
16 detector	8/17/129	0.92 (0.88–0.94)	0.80 (0.70–0.88)	4.64 (2.97–7.25)	0.10 (0.07–0.16)	44.64 (20.44–97.50)	0.94 (0.92–0.96)
64 detector	6/12/1278	0.97 (0.93–0.98)	0.89 (0.85–0.93)	9.09 (6.45–12.82)	0.04 (0.02–0.08)	239.76 (99.27–579.06)	0.95 (0.93–0.97)
<i>P</i> _{<16 vs.16}	/	0.023	0.446	0.21	0.003	0.016	<0.001
<i>P</i> _{<16 vs.64}	/	0.001	<0.001	<0.001	<0.001	<0.001	<0.001
<i>P</i> _{16 vs.64}	/	0.014	0.089	0.019	0.026	0.005	0.488

GEVs, gastroesophageal varices; SEN, sensitivity; SPE, specificity; PPV, positive predictive value; NPV, negative predictive value; DOR, diagnostic odds ratio; AUC, area under the curve; 95% CIs, corresponding 95% confidence interval.

Table 4. Subgroup results of meta-analyses regarding high-risk esophageal varices based on number of patients

Study subgroups	No. of article/ set/patient	SEN (95% CI)	SPE (95% CI)	PLR (95% CI)	NLR (95% CI)	DOR (95% CI)	AUC (95% CI)
Study design							
Retrospective	9/17/1732	0.89 (0.81–0.93)	0.87 (0.78–0.92)	6.67 (3.96–4.76)	0.13 (0.08–0.22)	50.68 (22.08–116.31)	0.94 (0.92–0.96)
Prospective	4/13/1299	0.90 (0.82–0.95)	0.90 (0.87–0.93)	4.95 (3.48–7.05)	0.11 (0.06–0.20)	82.17 (35.20–191.81)	0.95 (0.93–0.97)
<i>P</i> value	/	0.828	0.455	0.109	0.677	0.425	0.488
Cut-off of high-risk in computed tomography							
≥2 mm	4/14/1420	0.92 (0.89–0.94)	0.83 (0.81–0.86)	6.63 (4.26–10.31)	0.11 (0.08–0.16)	70.24 (39.22–125.81)	0.9599 (0.0089)*
≥3 mm	2/3/271	0.97 (0.89–1.00)	0.91 (0.87–0.95)	11.11 (2.17–56.78)	0.07 (0.02–0.23)	227.33 (13.44–3846.11)	0.9919 (0.0066)*
≥4 mm	3/4/451	0.72 (0.64–0.78)	0.87 (0.82–0.91)	3.93 (1.57–9.82)	0.39 (0.22–0.68)	11.13 (6.21–19.96)	0.8270 (0.0301)*
≥5 mm	2/4/340	0.78 (0.71–0.84)	0.93 (0.88–0.96)	9.98 (3.23–30.83)	0.20 (0.08–0.48)	59.06 (9.67–360.73)	0.9974 (0.0105)*
<i>P</i> _{≥2 mm vs. ≥3 mm}	/	0.107	0.001	0.550	0.485	0.425	0.004
<i>P</i> _{≥2 mm vs. ≥4 mm}	/	<0.001	0.125	0.314	<0.001	<0.001	<0.001
<i>P</i> _{≥2 mm vs. ≥5 mm}	/	<0.001	<0.001	0.508	0.223	0.858	0.006
<i>P</i> _{≥3 mm vs. ≥4 mm}	/	<0.001	0.196	0.277	0.012	0.041	<0.001
<i>P</i> _{≥3 mm vs. ≥5 mm}	/	<0.001	0.491	0.916	0.174	0.431	0.657
<i>P</i> _{≥4 mm vs. ≥5 mm}	/	0.227	0.054	0.209	0.216	0.085	<0.001

*Data calculated using Meta-Disc 1.4. EVs, esophageal varices; SEN, sensitivity; SPE, specificity; PPV, positive predictive value; NPV, negative predictive value; DOR, diagnostic odds ratio; AUC, area under the curve; 95% CIs, corresponding 95% confidence interval.

evaluated. The diagnosis of high-risk GEVs showed higher specificity than that of any-sized GEVs, without compromising the sensitivity. The sensitivity of CT is currently not sufficient to replace EGD as the first screening approach for GEVs in these patients. Additionally, given the high accuracy and better patient acceptance, CT may be used in cases where patients refuse to or are unable to undergo EGD. Furthermore, several subgroup analyses of GEVs were also conducted according to the location of varices, study design, and CT scanner.

The authors observed a better diagnostic performance of CT in detecting GEVs than that observed by a previous meta-analysis.⁴⁶ Based on the location of varices, the AUC of CT for EVs was found to be significantly higher than that for GV, which was inconsistent with the previous study.⁴⁶ This discrepancy might be due to the different sample sizes or inclusion/exclusion criteria of the studies. Additionally, more recent studies, which used CT with >16 slices to detect varices and mostly evaluated EVs, were included. The present subgroup-analysis results also confirmed that the >16-slice CT showed a significantly better performance for diagnosing varices of any size than the <16-slice CT, and the 64-slice CT yielded the highest sensitivity. With recent advancements in multi-detector CT, CT with >16 detectors provide isotropic or near isotropic data sets that enable multi-planner details, and consequently, GEVs can be easily evaluated. In addition,

prospective studies demonstrated higher diagnostic accuracy compared with retrospective studies, which is likely attributable to their stringent inclusion criteria, standardized data collection protocols, fostering of homogeneity in study populations, and enhanced control over confounding variables.

In the subgroup analyses, CT yielded a higher specificity in identifying high-risk EVs than EVs of any size, which was similar to the previous report.⁴⁷ At present, there is no consensus regarding the diagnostic criteria for high-risk EVs on CT, and no systematic review or meta-analysis has used multiple thresholds to risk-stratify patients. Therefore, the authors of the present study attempted to perform subgroup analyses based on the cut-off values for high-risk EVs on CT. They identified an interesting result: a threshold of 3 mm provided the highest sensitivity and a high specificity, with a PLR of 11.11 and an NLR of 0.07 as substantial evidence to rule in or rule out a large varix, respectively. These results suggested that EGD is not necessary in individuals with small (<3 mm) or undetectable EVs via CT scan since they are unlikely to experience variceal bleeding, which is in line with a previous case-control study.⁴⁸ In contrast, a cut-off of 5 mm provided similar specificity and AUC, but lower sensitivity for large varices than that of a cut-off of 3 mm. Preventive medication with beta-blockers might be considered against possible bleeding in this setting. Only patients who have contraindications to beta-blockers and need

endoscopic variceal ligation would require EGD. Consequently, EGD may be efficiently allocated to those who need it the most. However, given the small number of included studies in the subgroup, it would be best evaluated using prospective cohort studies to demonstrate the diagnostic and prognostic value of these different variceal sizes.

Bleeding events caused by GVs tend to be more severe than EV bleeds.⁴⁹ It is clinically meaningful to accurately identify patients at a high risk of GV bleeding. The authors identified that CT has a relatively high sensitivity and specificity in detecting GVs of any size, and a relatively high sensitivity and extremely high specificity in detecting large GVs. The size of GVs has been reported to be the most important risk factor for GV bleeding.⁵⁰ However, only 1 included study³² was concerned with high-risk GVs with a diameter >5 mm. GVs are always located in deep submucosa or subserosa and the overlying mucosa is normal, meaning the endoscopic diagnosis of GVs is limited. Studies have found that CT is more sensitive than EGD in identifying GVs, detecting GVs missed by EGD.^{10,11,42,51} The clinical implications of these results need to be verified using additional prospective cohorts in the future.

Although variceal size is a valuable predictor of bleeding, other important risk factors, such as the RC sign, cannot be observed in CT images.⁵² Studies have revealed that the presence and severity of the RC sign are significantly correlated with CT variceal grade

or size.^{15,31,40,41,53} Such a significant correlation may serve as a basis for a CT-based screening method. A diameter of 4 mm^{15,41} or 5 mm³¹ was used as the cut-off value to predict the RC sign, with a sensitivity of 97%–100%.

Although the present findings are significant, several limitations should be acknowledged. First, there was a variable time interval (from 4 hours to 6 months) between the EGD and CT assessments. Therefore, the interval progression or regression of GEVs cannot be entirely ruled out. Second, the definitions or cut-off values of high-risk varices were different among the analyzed studies. Thus, we could not determine a standard diagnostic cut-off size for CT assessment of GEVs. Third, contrast-enhanced CT has a risk of radiation and allergy. Nevertheless, CT is routinely used to evaluate the complications of cirrhosis and hepatocellular carcinoma, as well as concurrently assess for GEVs without adding extra cost and radiation exposure. Such a dual-screening strategy would further improve the cost-effectiveness of CT.

In conclusion, contrast-enhanced CT, especially with >16 slices, has a high diagnostic accuracy for GEVs and high-risk varices in patients with cirrhosis. Although EGD remains the gold standard for the diagnosis and risk stratification of GEVs, CT is a relatively more tolerable modality and may be an effective alternative in patients unwilling or contraindicated to undergo EGD.

Conflict of interest disclosure

The authors declared no conflicts of interest.

Funding

This work was supported by the science and technology development guiding plan project of Lanzhou (grant numbers: 2019-ZD-46).

References

1. Marshall JP, Smith PD, Hoyumpa AM Jr. Gastric varices. Problem in diagnosis. *Am J Dig Dis*. 1977;22(11):947-955. [\[CrossRef\]](#)
2. Garcia-Tsao G, Bosch J. Management of varices and variceal hemorrhage in cirrhosis. *N Engl J Med*. 2010;362(9):823-832. Erratum in: *N Engl J Med*. 2011;364(5):490. [\[CrossRef\]](#)
3. Spiegel BM, Targownik L, Dulai GS, Karsan HA, Gralnek IM. Endoscopic screening for esophageal varices in cirrhosis: Is it ever cost effective? *Hepatology*. 2003;37(2):366-377. [\[CrossRef\]](#)
4. Garcia-Tsao G, Abraldes JG, Berzigotti A, Bosch J. Portal hypertensive bleeding in cirrhosis: risk stratification, diagnosis, and management: 2016 practice guidance by the American Association for the study of liver diseases. *Hepatology*. 2017;65(1):310-335. [\[CrossRef\]](#)
5. ASGE Standards of Practice Committee; Early DS, Lightdale JR, et al. Guidelines for sedation and anesthesia in GI endoscopy. *Gastrointest Endosc*. 2018;87(2):327-337. [\[CrossRef\]](#)
6. Zoli M, Merkel C, Magalotti D, et al. Natural history of cirrhotic patients with small esophageal varices: a prospective study. *Am J Gastroenterol*. 2000;95(2):503-508. [\[CrossRef\]](#)
7. Tripathi D, Stanley AJ, Hayes PC, et al. U.K. guidelines on the management of variceal haemorrhage in cirrhotic patients. *Gut*. 2015;64(11):1680-1704. [\[CrossRef\]](#)
8. de Franchis R; Baveno VI Faculty. Expanding consensus in portal hypertension: Report of the Baveno VI Consensus Workshop: Stratifying risk and individualizing care for portal hypertension. *J Hepatol*. 2015;63(3):743-752. [\[CrossRef\]](#)
9. Sharma VK, Nguyen CC, Crowell MD, Lieberman DA, de Garmo P, Fleischer DE. A national study of cardiopulmonary unplanned events after GI endoscopy. *Gastrointest Endosc*. 2007;66(1):27-34. [\[CrossRef\]](#)
10. Perri RE, Chiorean MV, Fidler JL, et al. A prospective evaluation of computerized tomographic (CT) scanning as a screening modality for esophageal varices. *Hepatology*. 2008;47(5):1587-1594. [\[CrossRef\]](#)
11. El-Assaly H, Metwally LIA, Azzam H, Seif Elnasr Ml. A comparative study of multi-detector CT portography versus endoscopy in evaluation of gastro-esophageal varices in portal hypertension patients. *Egypt J Radiol Nucl Med*. 2020;51(1):2-10. [\[CrossRef\]](#)
12. Rosman M, Aneke-Nash C, Whitsett M, et al. The utility of radiographic evidence of portosystemic collateral vessels to improve the Baveno VI consensus recommendations in the non-invasive prediction of esophageal varices. *Gastroenterology*. 2019;156:1334. [\[CrossRef\]](#)
13. Sousa M, Fernandes S, Proença L, et al. The Baveno VI criteria for predicting esophageal varices: validation in real life practice. *Rev Esp Enferm Dig*. 2017;109(10):704-707. [\[CrossRef\]](#)
14. Januszewicz MM, Hałaburda-Rola M, Pruszyńska-Włodarczyk I, Czachór-Zielińska A, Rowiński O. Computed tomography evaluation of patent paraumbilical vein and its aneurysm in relation to other portosystemic collateral channels in patients with liver cirrhosis and portal hypertension. *Pol J Radiol*. 2019;84:112-117. [\[CrossRef\]](#)
15. Mifune H, Akaki S, Ida K, Sei T, Kanazawa S, Okada H. Evaluation of esophageal varices by multidetector-row CT: correlation with endoscopic 'red color sign'. *Acta Med Okayama*. 2007;61(5):247-254. [\[CrossRef\]](#)
16. Whiting PF, Rutjes AW, Westwood ME, et al. QUADAS-2: a revised tool for the quality assessment of diagnostic accuracy studies. *Ann Intern Med*. 2011;155(8):529-536. [\[CrossRef\]](#)
17. Higgins JP, Thompson SG, Deeks JJ, Altman DG. Measuring inconsistency in meta-analyses. *BMJ*. 2003;327(7414):557-560. [\[CrossRef\]](#)
18. Deeks JJ, Macaskill P, Irwig L. The performance of tests of publication bias and other sample size effects in systematic reviews of diagnostic test accuracy was assessed. *J Clin Epidemiol*. 2005;58(9):882-893. [\[CrossRef\]](#)
19. He X, Huang Z, Long L, et al. Comparison of multi-slice spiral CT portography and endoscopy in the diagnosis of esophageal and gastric varices in liver cirrhosis. *Chin J Radiol (China)*. 2012;46(12):1092-1095. [\[CrossRef\]](#)
20. Manchec B, Pham E, Noor M, et al. Contrast-Enhanced CT may identify high-risk esophageal varices in patients with cirrhosis. *AJR Am J Roentgenol*. 2020;215(3):617-623. [\[CrossRef\]](#)
21. Mofteh SG, Kamal S, Hanna ATK. CT esophagography: non invasive screening and grading of esophageal varices in cirrhosis. *Egypt J Radiol Nucl Med*. 2014;45(2):263-270. [\[CrossRef\]](#)
22. Yu NC, Margolis D, Hsu M, Raman SS, Lu DS. Detection and grading of esophageal varices on liver CT: comparison of standard and thin-section multiplanar reconstructions in diagnostic accuracy. *AJR Am J Roentgenol*. 2011;197(3):643-649. [\[CrossRef\]](#)
23. Lipp MJ, Broder A, Hudesman D, et al. Detection of esophageal varices using CT and MRI. *Dig Dis Sci*. 2011;56(9):2696-2700. [\[CrossRef\]](#)
24. Deng H, Qi X, Zhang Y, Peng Y, Li J, Guo X. Diagnostic accuracy of contrast-enhanced computed tomography for esophageal varices in liver cirrhosis: a retrospective observational study. *J Evid Based Med*. 2017;10(1):46-52. [\[CrossRef\]](#)
25. Sattar A, Anjum S, Rana S, Hamid N. Diagnostic accuracy of multidetector computed tomography (MDCT) in evaluation of varices in cirrhotic patients. *Med Forum*. 2019;30(9):7-9. [\[CrossRef\]](#)
26. Hassan M, Husen Y, Abbasi SU, Hussain Z. Diagnostic accuracy of multidetector computed tomography in detection of esophageal varices. *Cureus*. 2019;11(1):e3933. [\[CrossRef\]](#)
27. Elalfy H, Elsherbiny W, Abdel Rahman A, et al. Diagnostic non-invasive model of large risky esophageal varices in cirrhotic hepatitis C virus patients. *World J Hepatol*. 2016;8(24):1028-1037. [\[CrossRef\]](#)
28. Cansu A, Ahmetoglu A, Kul S, et al. Diagnostic performance of using effervescent powder for detection and grading of esophageal varices by multi-detector computed tomography. *Eur J Radiol*. 2014;83(3):497-502. [\[CrossRef\]](#)

29. Salahshour F, Mehrabinejad MM, Rashidi Shahpasandi MH, et al. Esophageal variceal hemorrhage: the role of MDCT characteristics in predicting the presence of varices and bleeding risk. *Abdom Radiol (NY)*. 2020;45(8):2305-2314. [\[CrossRef\]](#)
30. Kim YJ, Raman SS, Yu NC, To'o KJ, Jutabha R, Lu DS. Esophageal varices in cirrhotic patients: evaluation with liver CT. *AJR Am J Roentgenol*. 2007;188(1):139-144. [\[CrossRef\]](#)
31. Shen M, Zhu KS, Meng XC, Zhang JS, Liu LY, Shan H. [Evaluation of esophageal varices and predicting the risk of esophageal varices bleeding with multi-detector CT in patients with portal hypertension]. *Zhonghua Yi Xue Za Zhi*. 2010;90(41):2911-2915. [\[CrossRef\]](#)
32. Zhu K, Meng X, Pang P, et al. Gastric varices in patients with portal hypertension: evaluation with multidetector row CT. *J Clin Gastroenterol*. 2010;44(5):108-115. [\[CrossRef\]](#)
33. Kim H, Choi D, Gwak GY, et al. High-risk esophageal varices in patients treated with locoregional therapies for hepatocellular carcinoma: evaluation with regular follow-up liver CT. *Dig Dis Sci*. 2009;54(10):2247-2252. [\[CrossRef\]](#)
34. Kim H, Choi D, Lee JH, et al. High-risk esophageal varices in patients treated with locoregional therapy for hepatocellular carcinoma: assessment with liver computed tomography. *World J Gastroenterol*. 2012;18(35):4905-4911. [\[CrossRef\]](#)
35. Karatzas A, Triantos C, Kalafateli M, et al. Multidetector computed tomography versus platelet/spleen diameter ratio as methods for the detection of gastroesophageal varices. *Ann Gastroenterol*. 2016;29(1):71-78. [\[CrossRef\]](#)
36. Guo CW, Quan XY, Fang CH, et al. Portography diagnostic value of collateral circulation of portal hypertension on 64-slice spiral CT. *Chin J Med Imaging Technol*. 2008;24(6):932-935. [\[CrossRef\]](#)
37. Hua J, Liu GQ, Bao H, et al. The role of liver stiffness measurement in the evaluation of liver function and esophageal varices in cirrhotic patients. *J Dig Dis*. 2015;16(2):98-103. [\[CrossRef\]](#)
38. Wu L, Fan Z, Gu H, Feng Q. Value of multislice spiral ct in detecting and grading of esophageal varices in cirrhotic patients. *Chin J Gastroenterol*. 2009;14(1):12-15. [\[CrossRef\]](#)
39. Kim SH, Kim YJ, Lee JM, et al. Esophageal varices in patients with cirrhosis: multidetector CT esophagography--comparison with endoscopy. *Radiology*. 2007;242(3):759-768. [\[CrossRef\]](#)
40. Elkammash T, Elfiky I, Zaiton F, Khorshed SE. Diagnostic performance of multidetector computed tomography in the evaluation of esophageal varices. *Egypt J Radiol Nucl Med*. 2016;47(1):43-51. [\[CrossRef\]](#)
41. Dessouky BA, Abdel Aal el SM. Multidetector CT oesophagography: an alternative screening method for endoscopic diagnosis of oesophageal varices and bleeding risk. *Arab J Gastroenterol*. 2013;14(3):99-108. [\[CrossRef\]](#)
42. Zhao S, Feng K, Qu Q, et al. Application of ct portography in esophagogastric varices in cirrhotic patients. *Chin J Gastroenterol*. 2016;21(10):615-619. [\[CrossRef\]](#)
43. Bashir M, Mughal HH, Mehmood F, Aftab MI, Ali M, Muhammad MD. Diagnostic accuracy of multi-detector computed tomography esophagography in grading of esophageal varices in cirrhotic patients. *P J M H S*. 2021;15(8):2175-2177. [\[CrossRef\]](#)
44. Kumar R, Nandolia KK, Sharma P, et al. Computed tomography virtual oesophagography for the grading of oesophageal varices in cirrhotic liver disease patients with upper gastrointestinal endoscopic examination as the gold standard: a diagnostic validation study. *Pol J Radiol*. 2023;88:187-193. [\[CrossRef\]](#)
45. Kim H, Choi D, Gwak GY, et al. Evaluation of esophageal varices on liver computed tomography: receiver operating characteristic analyses of the performance of radiologists and endoscopists. *J Gastroenterol Hepatol*. 2009;24(9):1534-1540. [\[CrossRef\]](#)
46. Deng H, Qi X, Guo X. Computed tomography for the diagnosis of varices in liver cirrhosis: a systematic review and meta-analysis of observational studies. *Postgrad Med*. 2017;129(3):318-328. [\[CrossRef\]](#)
47. Li Y, Li L, Weng HL, Liebe R, Ding HG. Computed tomography vs liver stiffness measurement and magnetic resonance imaging in evaluating esophageal varices in cirrhotic patients: A systematic review and meta-analysis. *World J Gastroenterol*. 2020;26(18):2247-2267. [\[CrossRef\]](#)
48. Somsouk M, To'o K, Ali M, et al. Esophageal varices on computed tomography and subsequent variceal hemorrhage. *Abdom Imaging*. 2014;39(2):251-256. [\[CrossRef\]](#)
49. Ryan BM, Stockbrugger RW, Ryan JM. A pathophysiologic, gastroenterologic, and radiologic approach to the management of gastric varices. *Gastroenterology*. 2004;126(4):1175-1189. [\[CrossRef\]](#)
50. Kim T, Shijo H, Kokawa H, et al. Risk factors for hemorrhage from gastric fundal varices. *Hepatology*. 1997;25:307-312. [\[CrossRef\]](#)
51. Suvak B, Kekilli M, Beyazit Y, Okten S, Tanoglu A, Sasmaz N. Is computerised tomography better than fiberoptic gastroscopy for early detection of gastric varices. Is computerised tomography better than fiberoptic gastroscopy for early detection of gastric varices? *Prz Gastroenterol*. 2017;12(1):34-37. [\[CrossRef\]](#)
52. Yoshida H, Mamada Y, Taniai N, et al. Risk factors for bleeding esophagogastric varices. *J Nippon Med Sch*. 2013;80(4):252-259. [\[CrossRef\]](#)
53. Murachima N, Ikeda K, Kobayashi M, et al. Incidence of the appearance of the red color sign on esophageal varices and its predictive factors: long-term observations of 359 patients with cirrhosis. *J Gastroenterol*. 2001;36(6):368-374. [\[CrossRef\]](#)

Supplementary Table 1. Characteristics of CT to predict high-risk varices

Study/journal/year	Study design	CT canner	Patients underwent EGD	Varices location	Prevalence of high-risk varices (%)	Cut-off of high-risk varices on EGD	Cut-off of high-risk varices on CT	TP	FP	FN	TN
Manchec et al. ²⁰ , AJR Am J Roentgenol, 2020	R	/	97	EVs	60.82%	Grade 3 or higher	≥4 mm	51	18	8	15
Moftah et al. ²¹ , Egypt J Radiol Nucl Med, 2014	/	4 or 8-slice	54	EVs	29.63%	Grade 3 or 4, mucosal red signs, recommendation of endoscopic or medical prophylactic therapy	≥2 mm	16	0	0	38
Yu et al. ²² , AJR Am J Roentgenol, 2011	R	16 or 64-slice	109	EVs	23.85%	Grade 3 or 4, variceal mucosal red signs or platelet plug	≥2 mm	25	24	1	59
Lipp et al. ²³ , Dig Dis Sci, 2011	R	4 or 16 or 64-slice	137	EVs	15.38%	≥5 mm, or ≥3/4 of the normal esophageal lumen being obstructed	≥4 mm	18	11	12	96
Deng et al. ²⁴ , J Evid Based Med, 2016	R	/	52	EVs	75%	Slight tortuous varices with RC signs; or snake-like varices with or without RC signs; or beady, nodular, or tumor-shaped varices with or without RC signs	≥3.9 mm	35	4	4	9
Elalfy et al. ²⁷ , World J Hepatol, 2016	R	16-slice	124	EVs	37.10%	medium/large varices	/	42	4	4	74
Salahshour et al. ²⁹ , Abdom Radiol (NY), 2020	R	16 or 64-slice	124	EVs	40.32%	grade 2, 3, or grade 1 with red signs or Child-Pugh class C	/	29	22	21	52
Kim et al. ³⁰ , AJR Am J Roentgenol, 2007	R	single or 4 slice	67	EVs	17.91%	Protrude into the esophageal lumen and touch each other	≥3 mm	11	9	1	46
Shen et al. ³¹ , Zhonghua Yi Xue Za Zhi, 2010	P	320 slice	69	EVs	59.42%	Grade 2 and 3	≥5 mm	39	0	2	28
Zhu et al. ³² , J Clin Gastroenterol, 2010	R	4 slice	127	GVs	16.54%	≥5mm	≥5 mm	39	0	2	28
								18	4	3	102
								17	3	4	103

Supplementary Table 1. Continued

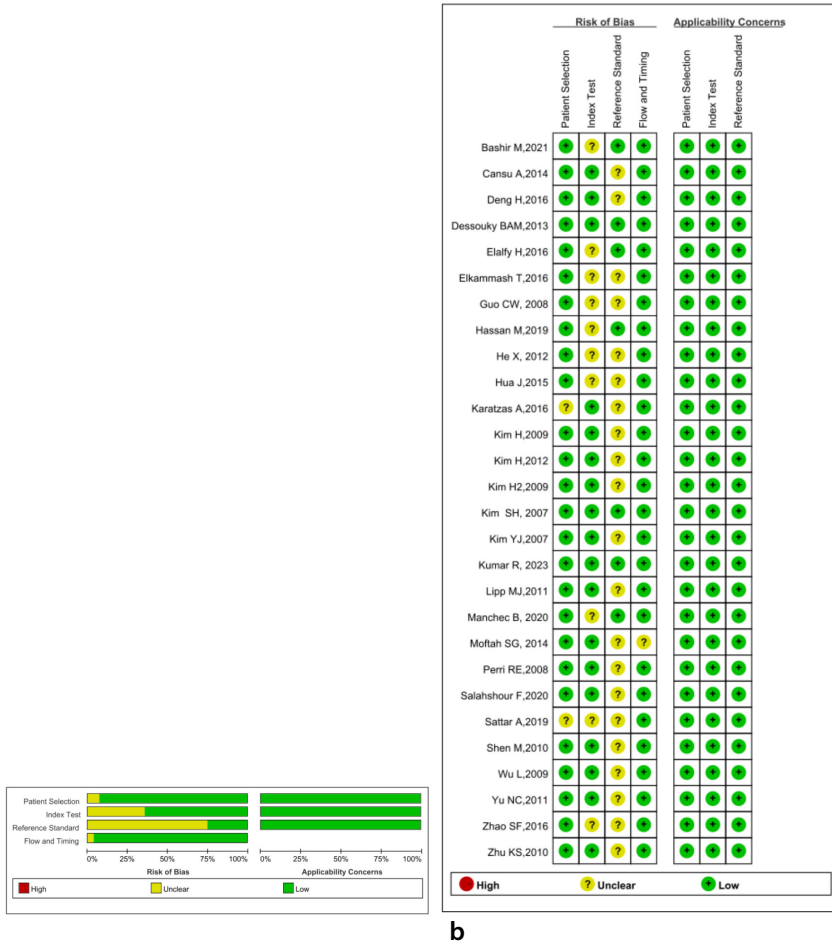
Study/journal/year	Study design	CT scanner	Patients underwent EGD	Varices location	Prevalence of high-risk varices (%)	Cut-off of high-risk varices on EGD	Cut-off of high-risk varices on CT	TP	FP	FN	TN
Kim et al. ³³ , Dig Dis Sci, 2009	R	16-slice	110	EVs	33.63%	Grade 2 and 3	≥2 mm	34	3	3	70
Kim et al. ³⁴ , World J Gastroenterol, 2012	P	64-slice	100	EVs	27.00%	Grade 2 and 3	≥2 mm	36	10	1	63
								32	4	5	69
								25	8	2	65
								25	7	2	66
								25	9	2	64
								25	9	2	64
								23	13	4	60
								24	7	3	66
Karatzas et al. ³⁵ , Ann Gastroenterol, 2016	P	16-slice	38	EVs + GVs	10.52%	≥5 mm	≥5 mm	4	5	0	29
Perri et al. ¹⁰ , Hepatology, 2008	P	4 slice or higher	101	EVs	40.59%	≥5 mm	≥5 mm	23	5	18	55
								27	8	14	52
Kim et al. ³⁹ , Radiology, 2007	P	16-slice	90	EVs	33.33%	Grade 2 and 3	/	28	11	2	49
								28	5	2	55
								27	9	3	51
								27	2	3	58
Dessouky and Abdel Aal ⁴¹ , Arab J Gastroenterol, 2013	P	16-slice	137	EVs	27.74%	≥ Grade 2	≥3 mm	38	0	0	99
Bashir et al. ⁴³ , P J M H S, 2021	/	/	145	EVs	74.5%	/	/	102	4	6	33
Kim et al. ⁴⁵ , J Gastroenterol Hepatol, 2009 *	R	16 or 64-slice	104	EVs	64.42%	Grade 2 and 3	≥2 mm	123	15	9	61
								113	17	19	59
								115	15	17	61

*Data presented base on number of varices. R, retrospective; P, prospective; EGD, Esophagogastroduodenoscopy; EVs, esophageal varices; GVs, gastric varices; TP, true positive; FP, false-positive; FN, true-negative; TN, false-negative; Grade 2: Varices show beaded appearance; Grade 3: Varices run in oblique course and are tortuous with tumorlike appearance.

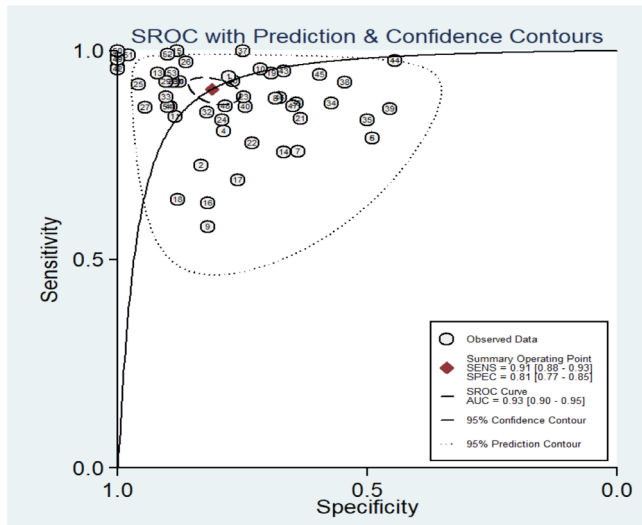
Supplementary Table 2. Subgroup results of meta-analyses regarding any sized EVs based on number of patients

Study subgroups	No.of article/set/patient	SEN (95% CI)	SPE (95% CI)	PLR (95% CI)	NLR (95% CI)	DOR (95% CI)	AUC (95% CI)
Study design							
Retrospective	9/17/1853	0.82 (0.75–0.87)	0.79 (0.71–0.87)	3.95 (2.72–5.73)	0.23 (0.16–0.33)	17.29 (8.96–33.33)	0.88 (0.84–0.90)
Prospective	11/26/2225	0.94 (0.91–0.96)	0.81 (0.73–0.87)	4.91 (3.34–7.23)	0.08 (0.05–0.12)	61.81 (29.22–130.76)	0.95 (0.93–0.97)
P value	/	<0.001	0.715	0.444	<0.001	0.095	<0.001
CT scanner							
<16 detector	3/7/696	0.82 (0.73–0.88)	0.76 (0.71–0.81)	3.39 (2.77–4.17)	0.24 (0.16–0.36)	14.10 (8.41–23.64)	0.81 (0.77–0.84)
16 detector	8/17/1429	0.92 (0.88–0.94)	0.80 (0.70–0.88)	4.64 (3.00–7.25)	0.10 (0.07–0.16)	44.64 (20.44–97.50)	0.94 (0.92–0.96)
64 detector	3/9/1020	0.96 (0.91–0.98)	0.91 (0.85–0.94)	10.19 (6.31–16.44)	0.05 (0.02–0.10)	228.85 (75.50–693.65)	0.96 (0.94–0.98)
P < _{16 vs. 16}	/	0.023	0.446	0.206	0.003	0.016	<0.001
P < _{16 vs. 64}	/	0.002	<0.001	<0.001	<0.001	<0.001	<0.001
P _{16 vs. 64}	/	0.093	0.043	0.018	0.133	0.018	0.166

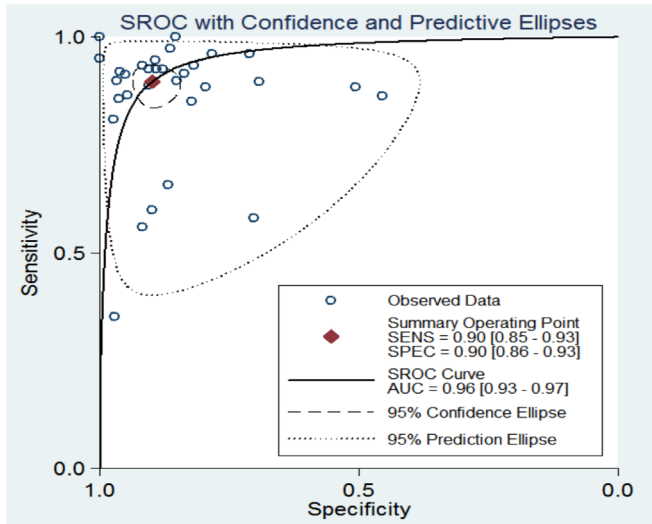
EVs, esophageal varices; SEN, sensitivity; SPE, specificity; PPV, positive predictive value; NPV, negative predictive value; DOR, diagnosis odds ratio; AUC, area under the curve; 95% CIs, corresponding 95% confidence interval.



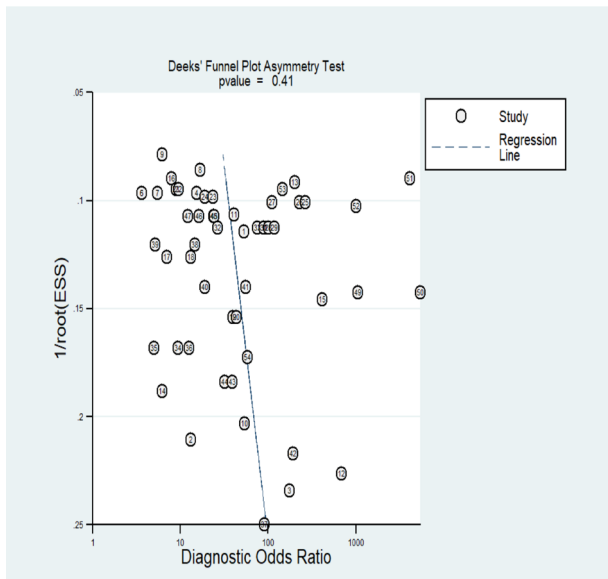
Supplementary Figure 1. Risk bias and applicability concerns of QUDADS 2 assessment in summary (a) and graph (b).



Supplementary Figure 2. Summary receiver operating characteristics (SROC) curves of computed tomography (CT) for diagnosing gastroesophageal varices with CT.



Supplementary Figure 3. Summary receiver operating characteristics (SROC) curves of computed tomography (CT) for predicting high-risk varices with CT.



Supplementary Figure 4. Deeks' funnel plot for evaluation of publication bias of studies.



Assessing hepatic steatosis by magnetic resonance in potential living liver donors

- Diğdem Kuru Öz¹
 Zeynep Ellik²
 Ayşegül Gürsoy Çoruh¹
 Mehmet Adıgüzel¹
 Mesut Gümüşsoy²
 Saba Kiremitci³
 Elvan Onur Kırımker⁴
 Hale Gökcan²
 Atilla Halil Elhan⁵
 Deniz Balcı⁶
 Berna Savaş³
 Ayşe Erden¹
 Ramazan İdilman^{2,7*}

¹Ankara University Faculty of Medicine, Department of Radiology, Ankara, Türkiye

²Ankara University Faculty of Medicine, Department of Gastroenterology, Ankara, Türkiye

³Ankara University Faculty of Medicine, Department of Pathology, Ankara, Türkiye

⁴Ankara University Faculty of Medicine, Department of General Surgery, Ankara, Türkiye

⁵Ankara University Faculty of Medicine, Department of Biostatistics, Ankara, Türkiye

⁶Bahçeşehir University Faculty of Medicine, Department of General Surgery, İstanbul, Türkiye

⁷Ankara University Hepatology Institute, Ankara, Türkiye

*Ramazan İdilman is a member of the Science Academy (BA).

Corresponding author: Diğdem Kuru Öz

E-mail: digdem_k@hotmail.com

Received 05 February 2024; revision requested 18 March 2024; accepted 17 April 2024.



Epub: 13.05.2024

Publication date: 06.11.2024

DOI: 10.4274/dir.2024.242697

PURPOSE

To determine the accuracy of magnetic resonance imaging-proton density fat fraction (MRI-PDFF) measurements for detecting liver fat content in potential living liver donors and to compare these results using liver biopsy findings.

METHODS

A total of 139 living liver donors (men/women: 83/56) who underwent MRI between January 2017 and September 2021 were included in this analysis retrospectively. The PDFFs were measured using both MR spectroscopy (MRS) and chemical shift-based MRI (CS-MRI) for each donor in a blinded manner.

RESULTS

Significant positive correlations were found between liver biopsy and MRS-PDFF and CS-MRI PDFF in terms of hepatic steatosis detection [$r = 0.701$, 95% confidence interval (CI): 0.604–0.798, $r = 0.654$, 95% CI: 0.544–0.765, $P < 0.001$, respectively]. A weak level correlation was observed between liver biopsy, MRI methods, and vibration-controlled transient elastography attenuation parameters in 42 available donors. Based on receiver operating characteristic (ROC) analysis, MRS-PDFF and CS-MRI PDFF significantly distinguished >5% of histopathologically detected hepatic steatosis with an area under the ROC curve (AUC) of 0.837 ± 0.036 ($P < 0.001$, 95% CI: 0.766–0.907) and 0.810 ± 0.036 ($P < 0.001$, 95% CI: 0.739–0.881), respectively. The negative predictive values (NPVs) of MRS-PDFF and CS-MRI PDFF were 88.3% and 81.3%, respectively. In terms of distinguishing between clinically significant hepatic steatosis ($\geq 10\%$ on histopathology), the AUC of MRS-PDFF and CS-MRI were 0.871 ± 0.034 ($P < 0.001$, 95% CI: 0.804–0.937) and 0.855 ± 0.036 ($P < 0.001$, 95% CI: 0.784–0.925), respectively. The NPVs of MRS-PDFF and CS-MRI were 99% and 92%, respectively.

CONCLUSION

The methods of MRS-PDFF and CS-MRI PDFF provide a non-invasive and accurate approach for assessing hepatic steatosis in potential living liver donor candidates. These MRI PDFF techniques present a promising clinical advantage in the preoperative evaluation of living liver donors by eliminating the requirement for invasive procedures like liver biopsy.

KEYWORDS

Magnetic resonance spectroscopy, proton density fat fraction, chemical shift-based magnetic resonance imaging, liver transplantation, living liver donor, metabolic-associated steatotic liver disease

Metabolic dysfunction-associated steatotic liver disease (MASLD) is a public health problem that affects more than 25% of adults worldwide, causing hepatic and extrahepatic morbidity and mortality.¹⁻³ This disease encompasses a broad spectrum of hepatic conditions, ranging from metabolic dysfunction-associated steatosis, characterized by macrovesicular hepatic steatosis that may be accompanied by mild inflammation, to metabolic dysfunction-associated steatohepatitis, which is additionally characterized by the presence of inflammation and hepatocyte injury, with or without fibrosis, cirrhosis, or hepatocellular carcinoma.^{1,2} MASLD is the most prevalent chronic liver disease, especially in

Western countries, and the proportion of MASLD-related cirrhosis cases among patients on liver transplantation (LT) waiting lists has increased over the years.^{2,3} In Türkiye, the prevalence of MASLD is estimated to be more than 30% in the general population.⁴

Living donor LT (LDLT) is an important mortality-reducing treatment approach for patients with acute and chronic liver failure.^{5,6} The use of LDLT has been gradually increasing due to a lack of available cadaveric liver grafts. Several factors are associated with successful graft organ survival following LT.^{5,7} Donor liver steatosis is critical for successful graft function, graft, and recipient survival in the early post-transplant period, and donor safety.^{6,8} Although <5% hepatic steatosis is universally acceptable for liver organ donation, the inclusion thresholds of the hepatic steatosis fraction may vary among liver transplant centers. Some centers use a threshold of <10%,^{9,10} while others consider <20% or <30% as acceptable for donation.^{11,12} Liver biopsy remains the gold standard diagnostic method for accurately assessing hepatic steatosis. However, due to the invasive nature of biopsy, the potential for sampling errors, and intra- and inter-observer variability, there is a tendency to perform liver biopsies on select donors rather than on all potential donors.^{13,14}

Magnetic resonance (MR)-based fat quantification [proton density fat fraction (PDFF)] is an accurate, non-invasive method for determining and quantifying hepatic steatosis.^{11,15-19} PDFF is the ratio of the MR signal from fat protons to the total MR signal from fat and water protons.²⁰ PDFF is mainly measured using two MRI methods: magnetic resonance spectroscopy (MRS) and chemical shift (CS)-based MRI. MRS data can be acquired efficiently using a high-speed T2-corrected multi-echo sequence during a single-hold breath, minimizing motion arti-

facts. This streamlined approach facilitates the rapid acquisition of metabolic information from a specific voxel region, as described previously.²¹ Conversely, the multi-echo CS-MRI technique, which employs six echoes and is known by various commercial vendor-specific names (e.g., Multi-echo Dixon for Siemens, IDEAL IQ for GE, and mDixon Quant for Philips), can generate a comprehensive PDFF map of the entire liver. As mentioned in one of the initial studies using this technique, there is a close correlation between liver biopsy results and CS-MRI PDFF in patients with non-alcoholic fatty liver disease.²² The most significant advantages of this technique include the ability to obtain a PDFF map for the entire liver and perform measurements in different liver regions. In contrast, MRS is limited to sampling a voxel area of a few cm³. MRI is also used in donor hepatic vascular and biliary system anatomy examination.

Increasingly prevalent in the general population, MASLD poses a significant problem in LDLT, leading to morbidity and mortality in both the recipient and the donor. MRS and CS-MRI are proven techniques for assessing and quantifying liver fat presence. However, data regarding the diagnostic accuracy and utility of MRI-based fat quantification in transplant settings is limited. Accordingly, this study aims to determine the accuracy of MRS-PDFF and CS-MRI PDFF measurements for detecting and quantifying the liver fat content in potential living liver donors and to compare these results with liver biopsy findings.

an MRI examination between January 2017 and September 2021. Six donors with suboptimal examinations due to artifacts were excluded from the investigation to ensure the reliability of the data analysis (Figure 1 represents patient accrual). The median time interval between MR and liver biopsy was 12 days (range: 1–30 days). Data were collected from outpatient visit charts. Percutaneous liver biopsy was performed in living liver donors who had abnormal liver injury and/or cholestatic liver tests, obesity, or hepatic steatosis detected by ultrasonography. This study was approved by the Ankara University Human Research Ethics Committee (date: October 2021, decision no: I5-365-21). Written informed consent was waived due to the study's retrospective design.

Serum alanine aminotransferase (ALT), aspartate aminotransferase (AST), gamma-glutamyl transpeptidase (GGT), alkaline phosphatase, bilirubin, fasting glucose, lipid profiles, and complete blood cell counts were measured in our central laboratory.

Magnetic resonance imaging technique

The MRI scans were performed using a 1.5 Tesla MRI device (Aera, Siemens Healthcare, Erlangen, Germany) with an 18-channel body matrix coil and a 32-channel spine matrix coil, utilizing eight channels. In liver donor candidates, in addition to the standard non-contrast abdomen MRI protocol, the LiverLab program provided by the vendor was used to determine and quantify the presence of iron and fat accumulation in the liver. The LiverLab program integrated into liver MRI comprised three sequences: T1 volumetric interpolated breath-hold examination (VIBE) e-Dixon, VIBE q-dixon, and HISTO. The VIBE q-dixon is a single-breath-hold sequence comprising six echoes, which en-

Main points

- The magnetic resonance spectroscopy-proton density fat fraction (MRS-PDFF) and chemical shift-based-MR imaging (CS-MRI) PDFF methods are effective, non-invasive techniques for assessing hepatic steatosis in living liver donor candidates.
- MRI methods, with their high negative predictive value, can eliminate the need for liver biopsy by detecting clinically significant hepatic steatosis.
- The MRS-PDFF and CS-MRI PDFF methods exhibit a high level of correlation in evaluating hepatic steatosis, suggesting that they can be used interchangeably.

Methods

Participants

This retrospective study comprised 145 potential living liver donors who underwent

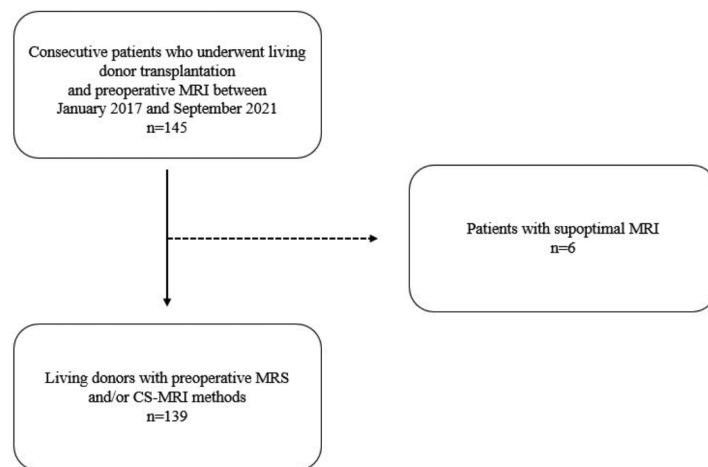


Figure 1. Flowchart summarizing patient accrual. MRI, magnetic resonance imaging; MRS, magnetic resonance spectroscopy; CS, chemical shift.

ables the acquisition of volumetric PDFF and R2* maps, forming the basis of CS-MRI. The HISTO sequence, forming the basis of MRS, was obtained using a 15-second breath-hold T2-corrected multi-echo stimulated echo acquisition mode sequence, utilizing a single voxel of 3 × 3 × 3 cm dimensions. The MRS data were acquired from a single voxel positioned by an experienced MR technician in a homogenous area away from vascular and biliary structures and liver edges in the right lobe during the scan.

Image analysis

The values of MRS PDFF were obtained from the report generated by the HISTO sequence provided by the manufacturer (calculated using Siemens software). Then, CS-MRI PDFF was performed on a dedicated workstation (Syngo., Siemens Healthcare), using the volumetric FF map transferred to it. The measurements of PDFF were conducted by two abdominal radiologists, with 10 (D.K.Ö.) and 2 (M.A.) years of experience. Measurements were obtained by placing three 200–300 mm² regions of interest (ROI) in at least 3 sections of the FF map at the level of the mid-right hepatic lobe (Figure 2). The radiologists conducting the measurements were unaware of the clinical data. Inconsistent measurement results were reevaluated until a consensus was reached. In cases of similar results, measurements performed by experienced radiologists were evaluated statistically. The ROIs were positioned within the homogeneous parenchymal area, avoiding vascular and biliary structures and the liver edges. The average PDFF values for each participant were calculated.

Transient elastography

Hepatic steatosis was also measured using a FibroScan probe (Echosens, Paris,

France) with an M or XL probe to cater to patients with different body types. All measurements were performed by one of the authors (Z.E.). Patients were examined after fasting overnight. The FibroScan probe was placed in the appropriate intercostal space window on the anterior axillary line. At least 10 valid measurements were obtained within 5–10 minutes. The median ratio of 10 successive measurements to the interquartile range was <30%. Simultaneously, vibration-controlled transient elastography (VCTE) was used to measure the controlled attenuation parameter (CAP) (dB/m) and liver stiffness (kPa). Morbidly obese patients [body mass index (BMI) >40 kg/m²] and severely underweight patients (BMI <16 kg/m²), patients with ascites, and patients with moderate and severe cholestasis were excluded.

Histological assessments

Two pathologists (S.K., B.S.) blinded to the clinical and biochemical data re-evaluated all liver biopsy specimens. The histological features of the samples were interpreted using the criteria of Brunt et al.²³ Hepatocellular steatosis was graded on a scale of 0–3 based on the percentage of hepatocytes: 0 = <5%, 1 = 5%–33%, 2 = 33%–66%, and 3 = >66%.

Definitions

The primary endpoint was the assessment of hepatic steatosis using MRI methods, MRS-PDFF, and CS-MRI PDFF. The secondary endpoint was to compare the MRI results with the liver biopsy findings.

Statistical analysis

Descriptive statistics were summarized as percentages for categorical variables, mean and standard deviations for normally

distributed continuous variables, and median, minimum, and maximum for ordinal and non-normally distributed continuous variables. Spearman's correlation coefficient analysis was performed to determine the degree of association between PDFF and histopathology. Bootstrapping was used to estimate confidence intervals (CIs) for Spearman's correlation coefficient. Intra-group comparison of categorical variables was performed using the McNemar test. Receiver operating characteristic (ROC) curves were used to describe and compare the performance of the diagnostics value of the MRI methods. Youden's index was used to determine the optimal cut-off value. The PDFF measurement results were compared with the liver biopsy results. The significance level was established as $\alpha = 0.05$, and the R programming language 4.3.1 was used for statistical analysis.

Results

A total of 139 potential living liver donors (men/women: 83/56) were included in this study. The median age of the donors was 31.0 years (range: 17–59 years). The median BMI was 24.9 kg/m² (range: 17.6–33.2 kg/m²), 40% of the patients were overweight (25–29.9 kg/m²), and 18% were obese (≥ 30 kg/m²). Of the donors, 35% had diabetes mellitus, and 28% had hypertension. The median serum ALT level was 18 U/L (range: 6–56 U/L), the median AST level was 20 U/L (range: 10–4 U/L), and the median GGT level was 20 U/L (range: 7–95 U/L). The donors' clinical data and laboratory values are presented in Table 1.

Hepatic steatosis was detected in 54 donors in the liver biopsy assessment. A total of 50 (36%) donors had grade 1 steatosis, 3 (2%) had grade 2 steatosis, and 1 (1%) had grade 3 steatosis, whereas 85 (61%) had no steatosis. Using the threshold values obtained from ROC analysis with MRS and CS-MRI methods, 9 out of 54 donors confirmed to have hepatic steatosis histopathologically showed no steatosis with MRS, while 12 showed no steatosis with CS-MRI. While there were 7 cases with no detected steatosis by both MRI methods, the PDFF value of 1 case using MRS and 2 cases using CS-MRI could not be obtained due to artifacts. In 5 out of 7 cases, histopathologically, there was minimal steatosis at the lower limit (5%), whereas in the remaining cases, there was mild steatosis (8%–10%).

The mean MRS-PDFF and CS-MRI PDFF were 5.8% \pm 3.9% and 4.1% \pm 3.9%, respec-

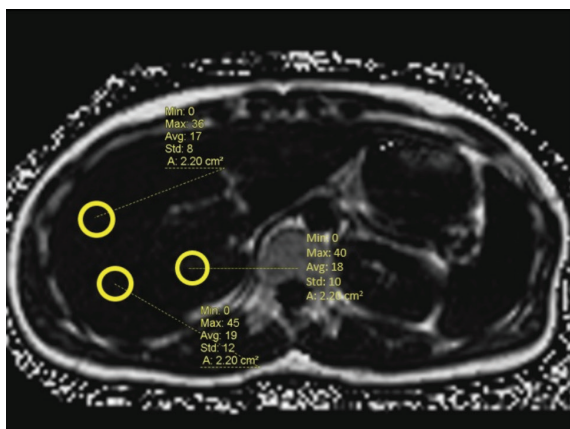


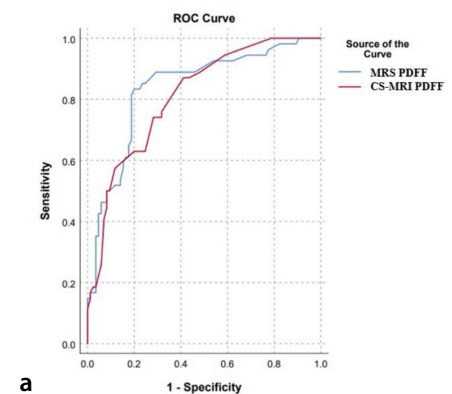
Figure 2. The CS-MRI PDFF measurements were obtained by averaging the values of circular ROIs placed at the level of the mid-right hepatic lobe of the liver in at least three different areas, each measuring 200–300 mm², on the FF map. CS-MRI, chemical shift-magnetic resonance imaging; PDFF, proton density fat fraction; ROI, regions of interest; FF, fat fraction.

tively. Significant positive correlations were found between liver biopsy and MRS-PDFF and CS-MRI-PDFF in terms of hepatic steatosis detection ($r = 0.701$, 95% CI: 0.604–0.798 and $r = 0.654$, 95% CI: 0.544–0.765, $P < 0.001$, respectively). Additionally, VCTE was performed on 42 available donors. The mean CAP was 248.4 ± 60.0 dB/m. A weak-moderate correlation was observed between liver biopsy, MRS-PDFF, CS-MRI PDFF, and VCTE CAP in terms of hepatic steatosis detection ($r = 0.616$, $P < 0.001$, 95% CI: 0.402–0.831, and $r = 0.513$, $P < 0.001$, 95% CI: 0.254–0.772, and

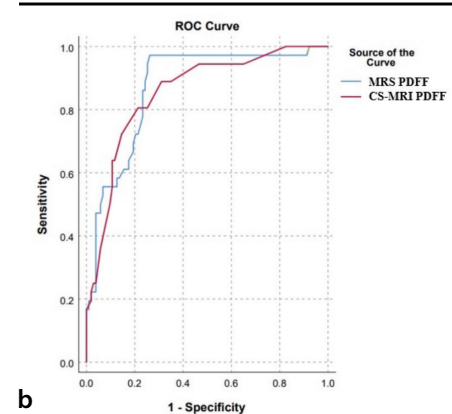
$r = 0.351$, $P = 0.017$, 95% CI: 0.062–0.640, respectively) (Table 2).

An ROC analysis was performed to distinguish between clinically significant and non-significant hepatic steatosis. Significantly, MRS-PDFF and CS-MRI PDFF distinguished $>5\%$ of histopathologically detected patients of hepatic steatosis with an area under the ROC curve (AUC) of 0.837 ± 0.036 (95% CI: 0.766–0.907) and 0.810 ± 0.036 (95% CI: 0.739–0.881), $P = 0.345$ (Table 3, Figure 3a). The optimal thresholds for MRS-PDFF and CS-MRI were 4.65% and 3.45%,

respectively. The sensitivities of MRS-PDFF and CS-MRI were 83.3% (95% CI: 71.3%–91.0%) and 74.1% (95% CI: 61.1%–83.9%, $P = 0.063$), respectively, whereas the specificities of MRS-PDFF and CS-MRI were 80.0% (95% CI: 70.3%–87.1%) and 71.8% (95% CI: 61.4%–80.2%, $P = 0.118$), respectively. The negative predictive values (NPVs) of MRS-PDFF and CS-MRI PDFF were 88.3% (95% CI, 79.3%–93.7%) and 81.3% (95% CI: 71.1%–88.5%), respectively. In terms of distinguishing clinically significant hepatic steatosis ($\geq 10\%$ on histopathology), the AUCs of MRS-PDFF and CS-MRI were 0.871 ± 0.034 , (95% CI: 0.804–0.937, $P < 0.001$) and 0.855 ± 0.036 , (95% CI: 0.784–0.925, $P < 0.001$), respectively (Table 3, Figure 3b). The cut-off values were 4.65% and 3.95%, respectively. The sensitivity of MRS-PDFF was significantly better than that of CS-MRI PDFF for distinguishing significant hepatic steatosis ($\geq 10\%$ on histopathology) [97.2% (95% CI: 85.8%–99.5%) vs. 80.6% (95% CI: 0.65.0%–90.2%), $P = 0.031$]. The specificities of these MRI methods were 73.8% (95% CI: 64.5%–81.3%) and 78.6% (95% CI: 69.8%–85.5%, $P = 0.302$), respectively.



a



b

Figure 3. ROC curve for MRS-PDFF and CS-MRI PDFF for the detection of hepatic fat content, (a) $>5\%$ on histopathology, and (b) $\geq 10\%$ on histopathology. ROC, receiver operating characteristic; MRS, magnetic resonance spectroscopy; PDFF, proton density fat fraction; CS-MRI, chemical shift-magnetic resonance imaging; VCTE-CAP, vibration-controlled transient elastography-controlled attenuation parameter.

Table 1. Clinical data and laboratory values of donors			
Demographics	n, %	Mean \pm SD	Median (min–max)
Age (years)			31 (17–59)
Men	83 (59.7)		
Women	56 (40.3)		
BMI	133 (95.7)	24.8 \pm 3.11	
Overweight and obesity	80 (58)		
Laboratory tests			
Serum ALT levels	139 (100)		18 (6–56)
Serum AST levels	139 (100)		20 (10–44)
Serum ALP levels	139 (100)		78 (28–208)
Serum GGT levels	139 (100)		20 (7–95)
Total bilirubin levels	139 (100)		0.59 (0.20–3.10)
Albumin levels	139 (100)	45.5 \pm 3.11	
Thrombocyte count	139 (100)		268 (141–548)
INR	139 (100)		1.02 (0.82–1.30)
LDL levels	137 (98.6)	114.6 \pm 34.7	
HDL levels	137 (98.6)		45 (29–80)
Total cholesterol level	136 (97.8)	184.5 \pm 40.5	
Non-HDL levels	136 (97.8)	137.1 \pm 39.7	
Triglyceride levels	137 (98.6)		99 (18–606)
VLDL levels	137 (98.6)		20 (3–121.2)
VCTE-CAP	42 (30.2)	248.4 \pm 60.0	

SD, standard deviation; min, minimum; max, maximum; BMI, body mass index; ALT, alanine transaminase; AST, aspartate transaminase; ALP, alkaline phosphatase; GGT, gamma-glutamyl transferase; INR, international normalized ratio; LDL, low-density lipoprotein cholesterol; HDL, high-density lipoprotein cholesterol; VLDL, very low-density lipoprotein cholesterol; VCTE-CAP, vibration controlled transient elastography-controlled attenuation parameter.

Table 2. The correlation analysis between histopathology and MRI PDFF methods and VCTE CAP						
	Histopathology Fat content		MRS PDFF		CS-MRI PDFF	
	r	P	r	P	r	P
MRS PDFF	0.704 (n = 136)	<0.001*				
CS-MRI PDFF	0.690 (n = 125)	<0.001*	0.823	<0.001*		
VCTE CAP	0.616 (n = 42)	<0.001*	0.566	<0.001*	0.379	0.014*

*Statistically significant. MRS, magnetic resonance spectroscopy; PDFF, proton density fat fraction; CS-MRI, chemical shift-magnetic resonance imaging; VCTE-CAP, vibration-controlled transient elastography-controlled attenuation parameter.

The NPVs of MRS-PDF and CS-MRI were 98.7% (95% CI: 93.0%–99.8%) and 92% (95% CI: 84.5%–96.1%), respectively.

Discussion

This large-sample study compared the accuracy of MRI techniques in assessing hepatic fat content in potential living liver donors. It was found that MRS-PDF and CS-MRI PDFF accurately assessed hepatic fat content and were strongly positively correlated with evaluating hepatic steatosis by liver biopsy. However, VCTE showed a weak-moderate correlation with liver biopsy assessment and MRI methods.

Steatotic liver graft has been associated with an increased risk of graft dysfunction or graft failure, especially in the early post-transplant period, mainly due to ischemia-reperfusion injury.⁸ There are still unanswered questions regarding what constitutes acceptable risk concerning the level of fat content in living liver donors. The prevalence of MASLD is increasing globally, and LDLT is a vital therapeutic option for managing end-stage liver disease. Therefore, it is crucial to understand how to effectively assess donor liver fat content. Several previous studies have investigated the role of MRI in liver fat content assessment in both transplant and non-transplant settings.^{15,24-26} A meta-analysis reported that MRI-PDF demonstrated 89% specificity and 84% sensitivity in detecting donor candidates with >5% hepatic steatosis, as determined by liver biopsy.²⁷ In addition, in a study of 32 potential liver donors, MRS distinguished donors with significant hepatic steatosis designated as >10% on histopathological examination. The investigators concluded

that CS-MRI and MRS would eliminate the need for liver biopsy.²⁸ In this study, MRS-PDF and CS-MRI PDFF could distinguish between liver donors with/without clinically significant hepatic steatosis (>5%) on histopathological examination, with high NPVs. The accuracy and the NPVs of the MRI methods were increased when distinguishing donors with >10% hepatic steatosis on histopathology.

This study found cut-off values for MRS-PDF and CS-MRI PDFF of 4.65% and 3.45%, respectively, for distinguishing >5% of hepatic steatosis, as detected by liver biopsy. These values improved the identification of histopathological liver fat content with a high NPV. These findings suggest that living donor candidates with <4.65% PDFF on MRI could potentially qualify as living liver donors. Previous studies reported no significant differences between the two MRI methods for identifying hepatic fat content.²¹ According to Idilman et al.²⁹, in scanners where one of the two software tools is not available, the hepatic steatosis percentage can be accurately determined using the alternative method currently in place. However, having both methods in the standard MRI protocol for liver donors offers several advantages. The results of both methods can be used to corroborate each other. For instance, in cases of heterogeneous fat deposition or misplacement of the voxel, MRS may yield incorrect results. Furthermore, in the case of fat-water swapping artifacts, the PDFF cannot be obtained through CS-MRI. In such cases, PDFF can be determined using MRS. The increase in the correlation with histopathology when both MRI methods are used to complement each other, despite miss-

ing PDFF data, is the strongest evidence of the advantages of using both MRI methods with donors.

The VCTE CAP values exhibited a relatively weak correlation with the histopathological findings. Previous studies have reported a VCTE moderate correlation between VCTE CAP and MRI-PDF.^{30,31} This study confirms previous studies demonstrating a weak-moderate correlation between CAP and liver biopsy, as well as MRI methods assessing hepatic steatosis.

While this study demonstrated a correlation between histopathology and MRI methods in identifying hepatic fat content, it possesses several notable limitations. First, it relied on retrospective observational data from a tertiary referral center. Moreover, there is a potential for bias related to the participants' data and confounding factors. Additionally, although all candidates underwent extensive investigation before donation and were deemed healthy, the donor's hepatic iron content was not measured, potentially impacting fat quantification with MRI. Despite being costly techniques for routine practice, they should be acknowledged as cost-effective methods in evaluating patients before complex surgical procedures such as LT, which carry high morbidity and mortality rates in tertiary referral healthcare centers.

In conclusion, MRS-PDF and CS-MRI PDFF accurately assess the presence and grade of hepatic fat content in potential living liver donor candidates. MRI is a non-invasive and valuable tool for use in the liver donor selection process for LDLT.

Table 3. The diagnostic accuracy of MRI methods in detecting >5% and >10% hepatic steatosis on histopathology

n=139	> 5% steatosis			>10 steatosis		
	MRS	CS-MRI	P	MRS	CS-MRI	P
Cutt-off FF (%)	4.65	3.45		4.65	3.95	
AUC	0.837 ± 0.036	0.810 ± 0.036		0.871 ± 0.034	0.855 ± 0.036	
95% CI	(0.766–0.907)	(0.739–0.881)	0.345	(0.804–0.937)	(0.784–0.925)	0.508
P value	<0.001	<0.001		<0.001	<0.001	
Sensitivity	0.833	0.741		0.972	0.806	
95% CI	(0.712–0.910)	(0.611–0.839)	0.063	(0.858–0.995)	(0.650–0.902)	0.031
Specificity	0.800	0.718		0.738	0.786	
95% CI	(0.703–0.871)	(0.615–0.803)	0.118	(0.645–0.813)	(0.698–0.855)	0.302
PPV	0.726	0.625		0.565	0.569	
95% CI	(0.604–0.821)	(0.503–0.734)		(0.441–0.681)	(0.433–0.695)	
NPV	0.883	0.814		0.987	0.920	
95% CI	(0.792–0.937)	(0.711–0.886)		(0.930–0.998)	(0.845–0.961)	
Accuracy	0.813	0.727		0.799	0.791	

MRI, magnetic resonance imaging; FF, fat fraction; AUC, area under the curve; CI, confidence interval; PPV, positive predictive value; MRS, magnetic resonance spectroscopy; CS, chemical shift; NPV, negative predictive value.

Conflict of interest disclosure

The authors declared no conflicts of interest.

References

1. Rinella ME, Lazarus JV, Ratziu V, et al. A multisociety Delphi consensus statement on new fatty liver disease nomenclature. *Ann Hepatol*. 2023;101133. [CrossRef]
2. Younossi ZM, Koenig AB, Abdelatif D, Fazel Y, Henry L, Wymer M. Global epidemiology of nonalcoholic fatty liver disease—meta-analytic assessment of prevalence, incidence, and outcomes. *Hepatology*. 2016;6473-6484. [CrossRef]
3. Wong RJ, Aguilar M, Cheung R, et al. Nonalcoholic steatohepatitis is the second leading etiology of liver disease among adults awaiting liver transplantation in the United States. *Gastroenterology*. 2015;148:547-555. [CrossRef]
4. Yilmaz Y, Yilmaz N, Ates F, et al. The prevalence of metabolic-associated fatty liver disease in the Turkish population: a multicenter study. *Hepatol Forum*. 2021;21:37-42. [CrossRef]
5. Yilmaz S, Kayaalp C, Ara C, et al. Single-center analysis of the first 304 living-donor liver transplantations in 3 years. *Hepatogastroenterology*. 2013;60:1105-1109. [CrossRef]
6. Chen CL, Fan ST, Lee SG, Makuuchi M, Tanaka K. Living-donor liver transplantation: 12 years of experience in Asia. *Transplantation*. 2003;75(3 Suppl):6-11. [CrossRef]
7. Cheng YF, Chen CL, Lai CY, et al. Assessment of donor fatty livers for liver transplantation. *Transplantation*. 2001;71:1221-1225. [CrossRef]
8. Perez-Daga JA, Santoyo J, Suárez MA, et al. Influence of degree of hepatic steatosis on graft function and postoperative complications of liver transplantation. *Transplant Proc*. 2006;38:2468-2470. [CrossRef]
9. Sharma A, Ashworth A, Behnke M, Cotterell A, Posner M, Fisher RA. Donor selection for adult-to-adult living donor liver transplantation: well begun is half done. *Transplantation*. 2013;95:501-506. [CrossRef]
10. Trotter JF, Campsen J, Bak T, et al. Outcomes of donor evaluations for adult-to-adult right hepatic lobe living donor liver transplantation. *Am J Transplant*. 2006;6:1882-1889. [CrossRef]
11. Gallegos-Orozco JF, Silva AC, Batheja MJ, et al. Magnetic resonance elastography can discriminate normal vs. abnormal liver biopsy in candidates for live liver donation. *Abdom Imaging*. 2015;40:795-802. [CrossRef]
12. Kim SH, Lee JM, Han JK, et al. Hepatic macrosteatosis: predicting appropriateness of liver donation by using MR imaging—correlation with histopathologic findings. *Radiology*. 2006;240:116-129. [CrossRef]
13. Ratziu V, Charlotte F, Heurtier A, et al. Sampling variability of liver biopsy in nonalcoholic fatty liver disease. *Gastroenterology*. 2005;128:1898-1906. [CrossRef]
14. Myers RP, Fong A, Shaheen AA. Utilization rates, complications and costs of percutaneous liver biopsy: a population-based study including 4275 biopsies. *Liver Int*. 2008;28:705-712. [CrossRef]
15. Hwang I, Lee JM, Lee KB, et al. Hepatic steatosis in living liver donor candidates: preoperative assessment by using breath-hold triple-echo MR imaging and 1H MR spectroscopy. *Radiology*. 2014;271:730-738. [CrossRef]
16. Loomba R, Adams LA. Advances in non-invasive assessment of hepatic fibrosis. *Gut*. 2020;69:1343-4352. [CrossRef]
17. Hsu C, Caussy C, Imajo K, et al. Magnetic resonance vs transient elastography analysis of patients with nonalcoholic fatty liver disease: a systematic review and pooled analysis of individual participants. *Clin Gastroenterol Hepatol*. 2019;17:630-637. [CrossRef]
18. Cui J, Heba E, Hernandez C, et al. Magnetic resonance elastography is superior to acoustic radiation force impulse for the diagnosis of fibrosis in patients with biopsy-proven nonalcoholic fatty liver disease: A prospective study. *Hepatology*. 2016;63:453-461. [CrossRef]
19. Park CC, Nguyen P, Hernandez C, et al. Magnetic resonance elastography vs transient elastography in detection of fibrosis and noninvasive measurement of steatosis in patients with biopsy-proven nonalcoholic fatty liver disease. *Gastroenterology*. 2017;152(3):598-607.e2. [CrossRef]
20. Yokoo T, Serai SD, Pirasteh A, et al. Linearity, bias, and precision of hepatic proton density fat fraction measurements by using MR imaging: a meta-analysis. *Radiology*. 2018;286:486-498. [CrossRef]
21. Rastogi R, Gupta S, Garg B, Vohra S, Wadhawan M, Rastogi H. Comparative accuracy of CT, dual-echo MRI and MR spectroscopy for preoperative liver fat quantification in living related liver donors. *Indian J Radiol Imaging*. 2016;26:5-14. [CrossRef]
22. Idilman IS, Aniktar H, Idilman R, et al. Hepatic steatosis: quantification by proton density fat fraction with MR imaging versus liver biopsy. *Radiology*. 2013;267:767-775. [CrossRef]
23. Brunt EM, Kleiner DE, Carpenter DH, et al. NAFLD: reporting histologic findings in clinical practice. *Hepatology*. 2021;73:2028-2038. [CrossRef]
24. Tang A, Tan J, Sun M, et al. Nonalcoholic fatty liver disease: MR imaging of liver proton density fat fraction to assess hepatic steatosis. *Radiology*. 2013;267:422-431. [CrossRef]
25. Chiang HJ, Chang WP, Chiang HW, et al. Magnetic resonance spectroscopy in living-donor liver transplantation. *Transplant Proc*. 2016;48:1003-1006. [CrossRef]
26. Chaudhary A, Sood G, Kumar N, et al. Validation of accuracy of non-invasive imaging methods (magnetic resonance imaging (MRI) fat fraction calculation and computed tomography (CT) liver attenuation index) for hepatic graft fat quantification in living liver transplant donors. *Ann Transplant*. 2021;26:e933801. [CrossRef]
27. Zheng D, Guo Z, Schroder PM, et al. Accuracy of MR imaging and MR spectroscopy for detection and quantification of hepatic steatosis in living liver donors: a meta-analysis. *Radiology*. 2017;282:92-102. [CrossRef]
28. Satkunasingham J, Nik HH, Fischer S, et al. Can negligible hepatic steatosis determined by magnetic resonance imaging-proton density fat fraction obviate the need for liver biopsy in potential liver donors? *Liver Transpl*. 2018;24:470-477. [CrossRef]
29. Idilman IS, Keskin O, Celik A, et al. A comparison of liver fat content as determined by magnetic resonance imaging-proton density fat fraction and MRS versus liver histology in non-alcoholic fatty liver disease. *Acta Radiol*. 2016;57:271-278. [CrossRef]
30. Zhuang RH, Weinstock AK, Ganesh S, et al. Characterization of hepatic steatosis using controlled attenuation parameter and MRI-derived proton density fat fraction in living donor liver transplantation. *Clin Transplant*. 2022;36:e14786. [CrossRef]
31. Ferraioli G, Maiocchi L, Savietto G, et al. Performance of the attenuation imaging technology in the detection of liver steatosis. *J Ultrasound Med*. 2021;40:1325-1332. [CrossRef]



Choosing the right artificial intelligence solutions for your radiology department: key factors to consider

- Deniz Alis¹
 Toygar Tanyel²
 Emine Meltem³
 Mustafa Ege Seker¹
 Delal Seker⁴
 Hakkı Muammer Karakaş⁵
 Ercan Karaarslan¹
 İlkay Öksüz⁶

¹Acıbadem Mehmet Ali Aydınlar University Faculty of Medicine, Department of Radiology, İstanbul, Türkiye

²Istanbul Technical University, Biomedical Engineering Graduate Program, İstanbul, Türkiye

³University of Health Sciences Türkiye, İstanbul Training and Research Hospital, Clinic of Diagnostic and Interventional Radiology, İstanbul, Türkiye

⁴Dicle University Faculty of Engineering, Department of Electrical-Electronics Engineering, Diyarbakır, Türkiye

⁵University of Health Sciences, Clinic of Radiology, İstanbul, Türkiye

⁶Istanbul Technical University Faculty of Engineering, Department of Computer Engineering, İstanbul, Türkiye

Corresponding author: Deniz Alis

E-mail: drdenizalis@gmail.com

Received 31 December 2023; revision requested 09 March 2024; last revision received 06 April 2024; accepted 15 April 2024.



Epub: 29.04.2024

Publication date: 06.11.2024

DOI: 10.4274/dir.2024.232658

ABSTRACT

The rapid evolution of artificial intelligence (AI), particularly in deep learning, has significantly impacted radiology, introducing an array of AI solutions for interpretative tasks. This paper provides radiology departments with a practical guide for selecting and integrating AI solutions, focusing on interpretative tasks that require the active involvement of radiologists. Our approach is not to list available applications or review scientific evidence, as this information is readily available in previous studies; instead, we concentrate on the essential factors radiology departments must consider when choosing AI solutions. These factors include clinical relevance, performance and validation, implementation and integration, clinical usability, costs and return on investment, and regulations, security, and privacy. We illustrate each factor with hypothetical scenarios to provide a clearer understanding and practical relevance. Through our experience and literature review, we provide insights and a practical roadmap for radiologists to navigate the complex landscape of AI in radiology. We aim to assist in making informed decisions that enhance diagnostic precision, improve patient outcomes, and streamline workflows, thus contributing to the advancement of radiological practices and patient care.

KEYWORDS

Radiology, artificial intelligence, clinical decision-making, computer-assisted healthcare economics and organizations, data security in healthcare, regulatory compliance in medicine

Over the last few years, the field of artificial intelligence (AI), particularly deep learning (DL), has advanced exponentially. This powerful technology has made its way into numerous sectors, with healthcare being a prime example.¹ DL involves creating robust models capable of performing tasks that traditionally require human intelligence, and it relies heavily on data. Radiology, in particular, has garnered significant interest within the DL context due to its digital nature and the abundance of structured data, such as medical images and radiology reports.²

In the initial phases of DL's emergence in the healthcare sector, its application was largely confined to academic and research settings.³ These environments provided the perfect proving ground for DL algorithms, allowing researchers to refine their models against vast repositories of medical images and data. However, as the technology matured and demonstrated its efficacy, there was a noticeable shift from academic research to real-world clinical applications.⁴⁻⁷

This transition was marked by a significant uptick in the development and deployment of DL-based tools and systems in clinical settings. As of 2023, the market has seen a proliferation of DL-based applications, with approximately 692 United States Food and Drug Administration (FDA)-approved and 220 "Conformité Européenne" (CE)-marked products available from a diverse range of vendors.^{8,9} This surge reflects not only the growing confidence in DL technologies but also an increasing demand for advanced AI tools in medical diagnostics. Each year, the commercial market is enriched with new and innovative DL products designed

for medical image interpretation, signaling a dynamic and rapidly evolving landscape in radiological practices. Figure 1 illustrates the commercially available CE and FDA-marked DL applications per subspecialty, while Figure 2 depicts the number of commercially available FDA-approved applications each year since 2010.⁸

In radiology, DL is broadly utilized for two types of tasks: interpretative and non-interpretative. Interpretative tasks include quantification, segmentation, and diagnosis, which traditionally required manual labor from radiologists or were not available at all.¹⁰⁻¹² Non-interpretative tasks, on the other hand, encompass image creation using DL reconstruction, patient scheduling, and other administrative processes.^{13,14} This distinction is crucial in understanding the comprehensive impact of DL in this field.

Although non-interpretative tasks are critical for the efficiency of radiology departments, they predominantly address administrative aspects that typically concern a specific subset of radiologists, such as department heads. These tasks are often managed through built-in features provided by image manufacturers, hospital information systems, or picture archive and communication systems, which may minimize the need for active radiologist involvement in decision-making.

In contrast, interpretative tasks, which form the core of radiological practice, are significantly impacted by DL technologies. These tasks necessitate the expertise and active participation of radiologists, placing

them at the forefront of decision-making processes and directly benefiting from DL advancements.

Scope of the paper

Considering the substantial role and direct involvement of radiologists in interpretative tasks, this paper focuses on the selection and implementation of AI solutions for these specific functions. The emphasis on interpretative tasks aligns with the overarching goal of the paper: to guide radiology departments in choosing AI solutions that not only enhance diagnostic precision but also improve patient outcomes and streamline workflows.

This review-opinion paper does not aim to provide an exhaustive list of commercially available applications or to meticulously review the scientific evidence behind them, as these topics have already been explored in earlier studies.¹⁵⁻¹⁸ Instead, the focus is on outlining the key factors to consider when choosing the right AI solutions for your radiology department. While several earlier review-opinion pieces have addressed key factors relevant to purchasing an AI solution for radiology departments,¹⁸⁻²⁰ the rapid pace of developments in this field highlights the need for up-to-date and practical guidance.

Furthermore, the authors of this paper, drawing on over 5 years of clinical, industrial, and academic experience, offer unique insights on each topic, thereby contributing to and enriching the existing literature. Throughout this paper, we aim to illustrate each factor with hypothetical scenarios to enhance understanding and relatability for our readers, thereby making the content more accessible and practically applicable.

The genesis of these hypothetical scenarios lies in our extensive firsthand experience, which spans clinical usage, participation in radiology hackathons, contributions to academic research, and involvement in the development and assessment of AI technologies—both commercially available and in experimental stages. While these scenarios are presented in a hypothetical format, they are deeply informed by real-world situations and challenges we have encountered in our professional journey. This methodological choice is driven by our commitment to sharing valuable, generalized insights without referencing specific brands, entities, or institutions, thereby avoiding potential bias and preserving the focus on the universal applicability of the guidelines we propose.

These scenarios are crafted to provide a clearer understanding of the fundamental aspects of each factor, enabling readers to make more informed decisions when considering the purchase of an AI solution. Ultimately, this paper aspires to serve as a practical guide for radiologists and department administrators, aiding them in making well-informed decisions about integrating AI solutions into their practice and thus contributing significantly to the advancement of radiological services and patient care.

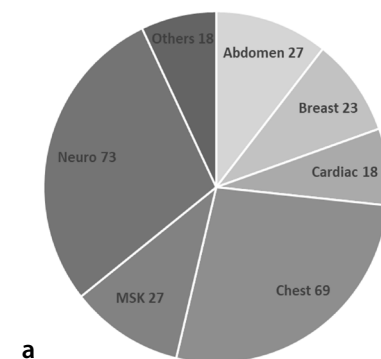
Key factors to consider

Among the numerous commercially available AI products, the first step for radiologists is to sift through the “hype” surrounding the use of AI and assess its “clinical relevance.” This involves identifying their current or near-term needs and goals and determining which AI products may meet those needs. We have determined that assessing clinical

Main points

- The paper provides guidance on choosing artificial intelligence (AI) solutions that align with clinical goals and enhance diagnostic accuracy in radiology.
- It emphasizes the importance of thorough performance evaluation and external validation of AI models for reliable clinical application.
- The paper highlights the necessity for AI solutions to integrate smoothly into existing workflows with user-friendly interfaces.
- The paper discusses the financial aspects of AI solutions, focusing on cost-effectiveness and the potential for a positive return on investment.
- The paper stresses the importance of adhering to regulatory standards and ensuring data security and privacy in AI integration in radiology.

CE-Marked AI Software for Radiology per Subspecialty



FDA-Approved AI Software for Radiology per Subspecialty

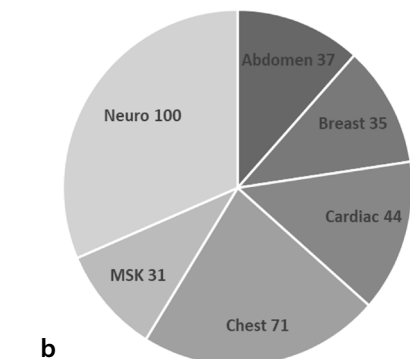


Figure 1. The number of (a) CE-marked and (b) FDA-approved commercially available radiology AI software per subspecialty. The most common AI software is for neuro followed by chest imaging for both CE-marked and FDA-approved products. CE, Conformité Européenne; FDA, Food and Drug Administration; AI, artificial intelligence.

relevance is the most crucial initial step for radiologists. This is because, without ensuring the suitability of a proposed solution for the department's needs, attention to other outlined aspects may divert focus and complicate the decision-making process. Indeed, in its 2019 white paper, the European Society of Radiology underscored the significance of the clinical relevance of AI products to specific radiology departments, introducing the term "use case." This paper defines a use case as a specific clinical application of AI in radiology, suggesting that use cases represent precise scenarios within the radiology service chain where automation could deliver significant value and help establish standards.²¹

Following this initial evaluation of a product's use case and its relevance to a radiology department's needs (i.e., clinical relevance) and drawing from our experience and previous work, radiologists should consider the following key factors: performance and validation,²² implementation and integration,⁴ clinical usability,^{23,24} costs and return on investment (ROI),⁴ regulations,^{25,26} security and privacy.²⁷⁻²⁹

Figure 3 presents a roadmap for choosing the right AI solutions for radiology departments, addressing these key factors. Additionally, Table 1 provides a checklist presenting items for each factor when purchasing an AI solution for a radiology department.

Clinical relevance

In the context of the burgeoning AI technology market, it is crucial for radiology departments to critically review and evaluate the myriad of commercial AI products available. An AI solution can provide a wide spectrum of clinical value, as documented in earlier work.^{30,31} However, most current AI solutions in medical imaging are designed to focus on one or, at most, two aspects of radiological tasks, limiting their scope to specific diagnostic or operational challenges. This specialization underscores the narrow focus of AI, which, while beneficial in certain contexts, may not fully address the complexity of radiological diagnostics or operational efficiency. These products, while offering a broad spectrum of potential clinical value, are predominantly examples of "narrow AI." Narrow AI, also known as weak AI, refers to AI systems that are designed and trained for a particular task. These systems, unlike their "broad AI" or "artificial general intelligence (AGI)" counterparts, do not possess the ability to perform any intellectual task that a human can. An example of AGI, which remains a theoretical concept at this stage, would be an AI such as ChatGPT, which can engage in a wide range of tasks, including conversing, reasoning, and learning across different domains without being explicitly programmed for them.³²

Given this backdrop, the clinical relevance of an AI solution for one department may not necessarily align with the needs of another, emphasizing the importance of departments defining their unique requirements and expectations from AI technologies. This is best illustrated through a hypothetical scenario: imagine an AI solution designed for prostate magnetic resonance imaging (MRI) interpretation, aiming to automate the Prostate Imaging Reporting and Data System process.³³

This hypothetical product does not offer automated volumetric analyses of the gland or prostate density scores using prostate-specific antigen, nor does it assess the probability of lesions harboring clinically significant prostate cancer. Its performance surpasses that of radiology residents and less-experienced readers but does not reach the level of expertise of prostate imaging specialists. Primarily, this product is aimed at institutions with high volumes of prostate MRI examinations and those employing less-experienced radiologists or residents for interpretations.

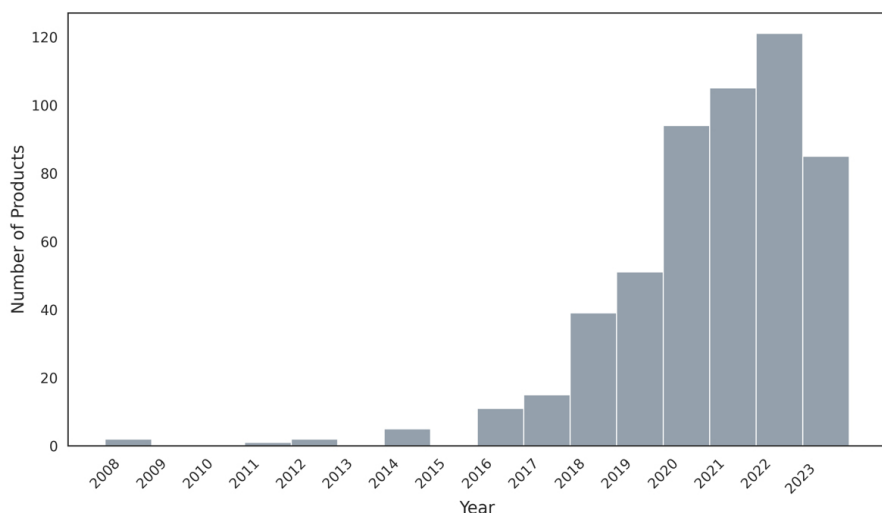


Figure 2. The number of FDA-approved commercially available radiology AI software each year. There has been an increasing trend in the number of commercially available applications, with a steep increase observed after 2015. However, there appears to be a stabilization after 2022 and even a slight decrease in 2023 compared with 2022. FDA, Food and Drug Administration; AI, artificial intelligence.

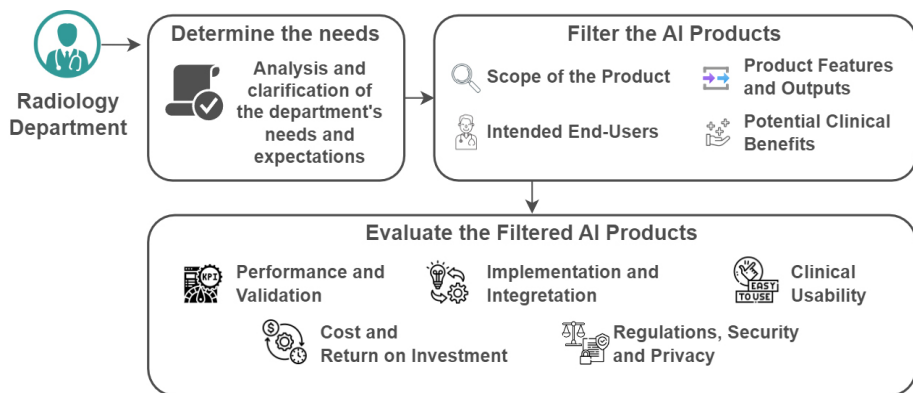


Figure 3. The roadmap for choosing the right AI solutions for radiology departments, addressing key factors. First, radiologists must critically evaluate the clinical relevance of AI products for their department's specific needs, covering the scope of the product, its features and outputs, intended end-users, and potential clinical benefits. Then, they should thoroughly evaluate performance and validation, implementation and integration, clinical usability, cost and return on investment, and regulations, security, and privacy. AI, artificial intelligence.

In an academic center specializing in prostate imaging, where radiology residents frequently pre-read prostate MRI examinations, such a product may yield high user satisfaction and a strong ROI. Conversely, its benefits may be minimal in a center that seldom performs prostate MRI examinations or in a tertiary center where only expert radiologists interpret these examinations.

If this hypothetical product were to include additional features such as volumetric assessment and structured reporting, it could significantly reduce reporting time and improve interdisciplinary communication.^{34,35} Thus, the product could also become invaluable in the tertiary center only staffed by expert prostate radiologists. Additionally, it could enhance the performance of less-ex-

perienced radiologists in the center who infrequently perform prostate MRI examinations, potentially enabling these centers to expand their patient base into prostate imaging.³⁶

While this example is hypothetical, it mirrors the complexity and diversity of real-world scenarios in radiology departments. It serves as a prompt for radiologists and

Table 1. Checklist for choosing the right AI solutions for your radiology department

Clinical relevance	<p>Scope of the product: Assess if the product's focus area aligns with the department's priorities.</p> <p>Intended end-users: Identify the primary users of the product-will it be more beneficial for less-experienced or experienced readers?</p> <p>Product features and outputs: Examine the system's outputs critically.</p> <p>Potential clinical benefits: Evaluate how many patients or procedures could benefit daily from the product's use.</p>
Performance and validation	<p>Evidence of external validation: Seek validation from external independent bodies, studies, or reference centers.</p> <p>Comprehensive performance metrics: Review all relevant performance metrics and compare them with field standards or benchmarks.</p> <p>Real-world performance data: Inquire about the model's performance in diverse real-world clinical settings.</p> <p>Pilot testing: Consider conducting a pilot test using the AI solution within the department to observe its real-time performance and impact.</p>
Implementation and integration	<p>Vendor compatibility: Examine how well the AI tool integrates with MRI, CT, PACS, and products from different vendors.</p> <p>IT resource availability: Assess if the department has adequate IT personnel for setup and integration or if additional resources are required.</p> <p>Implementation support: Determine if the vendor provides direct implementation support or if it is outsourced to a third party.</p> <p>Hardware requirements: Check if the AI tool demands high-performance GPUs or other specific hardware.</p> <p>Workflow Integration: Evaluate how the AI tool will fit into the existing workflow and its potential impact on diagnostic processes.</p>
Clinical usability	<p>Integration with PACS system: Check the seamless integration of the AI tool with the existing PACS system.</p> <p>User interface: Evaluate the intuitiveness and ease of navigation of the AI tool's user interface, and the extent of training required for effective usage.</p> <p>Efficiency of use: Consider the number of steps or mouse clicks needed to operate the AI tool, particularly for high-volume examination scenarios.</p> <p>Automated processing and result presentation: Determine if the AI tool automates processing and offers a user-friendly result presentation, such as through DICOM secondary capture or PDF reports.</p> <p>Alignment with workflow and case types: Ensure that the AI tool's design and functionality align with the department's workflow and the types of cases commonly handled.</p> <p>Outputs: Evaluate the simplicity and accessibility of the AI outputs, including the placement of elements such as binary labels ("normal image," "abnormal image") and the option to hide or display additional features, such as bounding boxes or heat maps.</p>
Costs and ROI	<p>Financial investment evaluation: Assess the overall financial investment required for implementing the AI solution, including initial costs and any recurring expenses.</p> <p>Insurance reimbursement: Determine the availability and extent of insurance reimbursements for the AI solution.</p> <p>Purchasing models comparison: Compare different purchasing models offered, such as annual licenses versus per-use fees, to identify which is most cost-effective for your department's needs.</p> <p>ROI analysis: Analyze the potential value and efficiency improvements provided by the AI solution to justify its costs, focusing on both quality and efficiency improvements.</p> <p>Potential benefits estimation: Estimate potential financial benefits, such as reduced workload or diagnostic errors, and consider scientific evidence to support these benefits.</p>
Regulations, security and privacy	<p>Compliance with international standards: Verify that the AI system complies with international regulatory standards, such as the FDA in the United States and the European Union's CE marking.</p> <p>Adherence to data protection laws: Confirm that the AI solution adheres to health data protection standards relevant to the region, such as HIPAA in the United States or GDPR in Europe, and any national standards, such as Türkiye's KVKK.</p> <p>Data security measures: Evaluate the AI system's data security measures, including encryption protocols and access controls, to ensure patient data are protected, particularly if cloud-based solutions are used.</p> <p>Local data storage capabilities: For regions with specific data residency requirements, check whether the AI solution can store data locally, in compliance with national laws.</p> <p>Vendor data usage policies: Review the AI vendor's policies regarding the use of hospital data, particularly clauses related to data usage for product improvement or other purposes, to ensure alignment with the hospital's data privacy policies.</p> <p>Trial integration and IT assessment: Conduct a trial integration of the AI solution with the assistance of IT professionals to identify potential compliance or technical issues before full implementation.</p>

AI, artificial intelligence; MRI, magnetic resonance imaging; CT, computed tomography; PACS, picture archiving and communication system; IT, information technology; GPU, graphics processing unit; DICOM: Digital Imaging and Communications in Medicine; PDF, portable document format; ROI, return on investment; FDA, Food and Drug Administration; CE, "Conformité Européenne" (European Conformity); HIPAA, Health Insurance Portability and Accountability Act; GDPR, General Data Protection Regulation; KVKK, "Kişisel Verileri Koruma Kanunu" (Personal Data Protection Act).

administrators to consider a wide array of factors in their decision-making process, ensuring that the AI solutions they adopt truly enhance their practice and patient care.

This scenario underscores several critical considerations for radiology departments when selecting an AI solution: scope of the product, intended end-users, product features and outputs, and potential clinical benefits. Further details are presented in Table 1.

Performance and validation

The evaluation of diagnostic performance in AI models is led by established guidelines, such as the Consolidated Standards of Reporting Trials-Artificial Intelligence and the Checklist for Artificial Intelligence in Medical Imaging.^{37,38} These standards advocate best practices in assessing AI models, necessitating detailed information about the AI model. This includes model architecture, training strategy, hyperparameters, unique additions to the base model, overfitting avoidance techniques, and explainability mechanisms. In addition, comprehensive data details, such as size, demographics, scanner types, potential biases, preprocessing methods, and augmentation techniques, are crucial.

In research contexts, where models are trained, validated, and tested, this exhaustive information is typically available for review and audit. This transparency facilitates the assessment of AI models against performance and transparency standards.

However, in clinical settings, AI solutions are often provided by commercial firms or startups, which may be hesitant to disclose in-depth information about their technology or data due to proprietary concerns and commercial sensitivities.³⁹

To illustrate these challenges, let us consider a hypothetical scenario: imagine an AI solution designed for detecting large vessel occlusion (LVO) in computed tomography (CT) angiography. This product, boasting a diagnostic accuracy of 88% on an external dataset from two hospitals and 24,355 patients, is marketed for its rapid assessment capability, alerting physicians within 5 minutes of image receipt.

At first glance, this seems promising; however, critical information is often missing. For example:

- The diagnostic accuracy alone offers an incomplete performance picture; additional metrics, such as sensitivity, specificity, and negative and positive predictive values

scores, are necessary for a comprehensive understanding.

- The prevalence of LVO in the study population and the patient demographics should be clarified.

- Details on the model's ability to detect distal or posterior system LVOs and whether these cases were included in the performance metrics are crucial.

- Information on whether the study was retrospective or if the model was tested in real-time clinical settings is vital.

- Independent research using the software, potential conflicts of interest among authors, and the nature of the research are important considerations.

Radiologists may also seek real-life performance evidence from peers who have used similar products or may request the company to demonstrate the product's efficacy with their own cases.

This scenario underscores several critical considerations regarding the performance and validation for radiology departments when selecting an AI solution: evidence of external validation, comprehensive performance metrics, real-world performance data, and pilot testing. These are summarized in Table 1.

Although the "performance and validation" is crucial, as discussed above, we also acknowledge the difficulty of rigorously evaluating the diagnostic performance of AI models, particularly in high-demand radiological environments. The practical challenges of conducting such evaluations in busy practices cannot be overlooked, given that not every radiology department has the necessary infrastructure or resources for comprehensive, independent assessments of AI solutions.

This recognition extends to well-established and trusted firms in our sector, including picture archiving and communication systems (PACS) and hardware providers, who have already begun offering validated products from third-party vendors (e.g., startups that are relatively new compared with the sector's stalwarts).^{40,41} Such initiatives by trusted firms and collaborations between radiology departments and these entities are crucial. They enable radiology departments to leverage the expertise and resources of established providers, streamlining the process and ensuring that the evaluation of AI solutions meets rigorous and reliable standards.

This collaborative approach not only reduces the workload on individual departments but also facilitates a more efficient and effective integration of AI technologies into radiological practices.

Implementation and integration

A critical, yet often overlooked, aspect of AI products is the ease of integration into the existing workflow of a radiology department. It is essential that this integration causes minimal-ideally no-disruption. Determining who will perform the implementation is equally important. Additionally, choosing between cloud-based or on-premises solutions, and considering the necessary computational power, are key elements. These latter factors are often more apparent to potential buyers of radiology AI solutions.

A recent survey by the Dutch Society of Radiology highlights implementation challenges as a major obstacle to broader AI adoption in radiology clinics.⁴ The implementation process, though seemingly straightforward, is in fact complex and multifaceted, requiring collaboration between radiologists, IT specialists, software engineers, and hospital administrators to ensure accurate and safe integration.⁴²

Hospitals vary in their infrastructure, expertise, and PACS capabilities. Many experts emphasize the need to build a suitable infrastructure for the seamless integration of machine learning-based applications in radiology clinics.^{43,44} This infrastructure development requires substantial effort and time and extends beyond the sole responsibility of radiologists. However, radiologists should be aware of their current capabilities and seek products that align well with their existing infrastructure.

From our perspective, the burden of ensuring smooth integration should not rest solely on radiologists. AI solution developers for radiology must provide flexible, easily integrable products suitable for a range of infrastructures, from basic to advanced. They should actively participate in the integration process, alleviating the strain on IT resources and facilitating the adoption of their products.⁴⁵

Here, we construct a hypothetical scenario to illustrate the complexity of implementation and the factors radiologists should consider when purchasing an AI product. Consider a small team of radiologists from a mid-sized department who are evaluating an

AI solution for chest X-ray analysis, driven by an inability to keep pace with high imaging demand. Having successfully identified their clinical needs and evaluated the diagnostic performance of the solution, they now face several implementation challenges.

First, system compatibility issues arise, as the AI tool is not fully compatible with their existing PACS system, necessitating system modifications or additional modules from the AI vendor. This adds complexity to the implementation process. Additionally, dedicated IT personnel are needed for the set-up and integration, but the department's IT resources are already overstretched and are raising concerns about managing this extra workload. After buying the product, the radiologists realize that the vendor of the software provided implementation via a third party in their country, which does not have the necessary expertise or knowledge regarding the product.

As the implementation process progresses, the radiology department encounters additional challenges related to hardware requirements. The AI tool, being advanced in its capabilities, requires a robust computational setup, including high-performance graphics processing units, to efficiently process the imaging data. The department's existing hardware infrastructure is not equipped to handle such demanding computational tasks, leading to the necessity of significant hardware upgrades.

This example shows the importance and complexity of implementation and what may go wrong and cause frustrations during the implementation. Unfortunately, such a hypothetical scenario is not uncommon and underscores the need for a thorough evaluation of various factors beyond clinical utility and performance when implementing an AI solution in a radiology department.⁴⁶

Detailed explanations of critical considerations concerning the implementation and integration of AI solutions for radiology departments are provided in Table 1, categorized under the subheadings of vendor compatibility, availability of IT resources, support for implementation, hardware requirements, and workflow integration.

Apart from the key factors discussed above, we acknowledge that the challenges of implementing AI in radiology, notably the communication gap between AI developers and PACS administrators, alongside the necessity for interface customization, are well recognized. In addressing these, the emer-

gence of commercial platforms, including AI application marketplaces, offers a promising solution.⁴⁷⁻⁵⁰ These platforms enhance the integration process, providing standardized frameworks and addressing customization needs, thereby supporting productivity improvements in radiological practices. Their role in facilitating effective communication and streamlined implementation is crucial for the seamless adoption of AI technologies in radiology.

Clinical usability

The widespread adoption and success of AI in radiology depend on several factors, notably how radiologists interact with AI systems. While no universally established best practices exist for designing effective AI tools in radiology, lessons can be learned from successful technology products in other industries. A common feature of such products is their simplicity, offering benefits in the most straightforward manner possible.

Simplicity and user-centric design are essential. AI tools that are easy to use and feature intuitive interfaces are more likely to be adopted by radiologists, facilitating their integration into daily practice. Our experience and literature review indicate that simplicity in design and operation is crucial for the effectiveness and acceptance of AI tools in clinical settings.^{23,24}

Consider a hypothetical scenario highlighting the importance of simplicity: radiologists at a tertiary center specializing in musculoskeletal imaging purchase an AI solution for automated fracture evaluation in plain radiographs. This high-performing product integrates well with the department's infrastructure and PACS. Radiologists interact with the tool through a hyperlink in their patient browser, which opens a graphical user interface for running the AI engine and viewing results.

While this software may be suitable for low-throughput examinations such as prostate or cardiac imaging, its use becomes problematic for high-volume radiographic examinations, particularly for time-pressed radiologists. The repetitive interaction, taking a few minutes per case, adds up significantly over the day. A more efficient solution would be an AI tool that processes steps automatically and presents results directly in PACS, reducing the need for additional interactions.

It is noteworthy that many products in the market are even more difficult to use,

as they require radiologists to switch from their PACS to open the AI program or even change computers. Purchasing a product not integrated into PACS and having a complex, intrusive interface can be more burdensome and time-consuming than manually examining the image.

We suggest that a successful AI solution must be fully integrated with PACS, featuring a user-friendly interface that can be used with minimal mouse clicks, or even without any clicks in a fully automated fashion for high-volume examinations. Such a solution should immediately distinguish pathological cases from normal ones with binary classification, ideally identify priority cases with acute findings, and highlight them on the radiologist's worklist for triage. Such a product would effectively serve as a second eye for the radiologist, exemplifying the vital role of simplicity in the design and functionality of AI tools in radiology.

In this context, radiologists should evaluate the simplicity of a radiology solution as follows: integration with a PACS system, user interface, efficiency of use, automated processing and result presentation, alignment with workflow and case types, and outputs (Table 1).

Costs and return on investment

According to the Dutch Society of Radiology, the primary obstacle to AI adoption in radiology clinics is cost.⁴ Implementing AI solutions in radiology departments involves significant financial investments. In most healthcare systems, AI solutions are not generally covered by government or private insurance policies, with a few exceptions in the United States, as indicated by the expanding coverage of certain AI products under Medicare or Medicaid.⁵¹ This supports the findings of the Dutch Society of Radiology survey, which highlights the crucial role of cost in AI solution adoption.

AI solutions are presently available with various purchasing models, including life-long licensing, annual licenses, and per-use fees. Radiologists must carefully consider which model best suits their department's needs. Many AI startups favor subscription-based models over outright capital investments in contrast to traditional medical hardware or software manufacturers.²⁰

Determining the most suitable purchasing model is a critical task that requires careful evaluation. For example, consider a

radiology department that performs 10,000 mammography examinations each year and is considering adopting software to perform breast cancer evaluation for mammography screening. Suppose this software is available with an annual licensing fee of \$20,000, inclusive of hardware and service costs. Although this may be a familiar purchasing approach for many radiologists, it is not necessarily the most cost-effective option.

Now consider an alternative purchasing model where the software is available with an initial installation fee of \$2,000, plus a per-examination fee of \$1. In this scenario, the department may realize significant cost savings. With 10,000 examinations a year, the total cost would be \$12,000 (\$2,000 installation plus \$10,000 for examinations), substantially lower than the flat annual license fee. This example underscores the importance of thoroughly examining and comparing different purchasing models to identify the most economically viable option for the department.

When evaluating the costs of AI solutions in radiology, it is equally important to consider the ROI. This analysis assesses whether the AI solution will provide sufficient value and efficiency improvements to justify its expenses. While ROI analysis is more straightforward for algorithms that speed up MRI examinations or reduce CT radiation doses, it becomes complex for AI solutions aimed at medical image interpretation.⁵² This complexity arises from the challenge of quantifying intangible benefits.

For hospital or radiology administrators, financial viability often hinges on ROI, which can be a major obstacle, particularly in the absence of insurance reimbursements for radiology AI software.⁵³ The evaluation of ROI encompasses two aspects: quality and efficiency improvement. Quality improvement, such as enhanced diagnostic accuracy or error reduction, can be difficult to translate into financial ROI due to its complexity and reliance on assumptions. Efficiency improvements, however, can be more directly measured by time savings in study read times using AI software. Saved person-hours provide a tangible way to demonstrate the software's value, making it particularly appealing in competitive markets where efficiency in repetitive tasks is prized.⁵⁴

Although calculating the exact ROI can be challenging or even impossible for radiology departments or hospital managers, it remains a critical exercise. This challenge is comparable with the difficulty in demon-

strating the financial benefits of national breast cancer screening programs, which require extensive time and data across numerous cases.⁵⁵ Consequently, it may not be feasible for a radiology department to precisely determine the ROI of an AI solution for breast cancer detection in mammography.

Despite this, radiologists should still evaluate potential financial benefits and roughly estimate the ROI, while also considering other key factors, such as clinical relevance, performance, implementation, and simplicity. If a department has the necessary budget or means to cover the product's costs, and there is an expectation of benefits, such as reduced workload or diagnostic errors, potentially supported by scientific evidence, it may still be justifiable to invest in an AI solution without exact ROI calculations.

In this context, radiologists should evaluate the costs and ROI of radiology solutions as follows: financial investment evaluation, insurance reimbursement, purchasing models comparison, ROI analysis, and potential benefits estimation (Table 1).

In addition to the considerations discussed above, it is important to acknowledge the geographical variability in practices related to the cost and reimbursement for AI solutions in radiology. For example, in the United States, Medicare offers reimbursement for certain medical imaging AI solutions, such as those related to stroke imaging, as well as candidate applications, such as pulmonary embolism and subdural hematoma.⁵¹ However, even these policies are subject to change, being valid for defined periods with uncertain futures regarding their continuation. Therefore, it is essential to stress that reimbursement policies for AI solutions are rapidly evolving. While it may be possible to describe the current state of affairs, these conditions are likely to change over time, making it challenging to provide a static overview that remains accurate.

Regulations, security, and privacy

Security and privacy are paramount in healthcare and radiology departments, particularly when considering the sensitive nature of health and imaging data. The rapid integration of AI solutions into radiology necessitates robust security and privacy measures. AI solutions, whether on-premises or cloud-based, involve integration with various data sources, such as health information systems (HIS), research information systems (RIS), and PACS, encompassing both imaging and other data processing tasks. The sensi-

tive nature of medical data, including patient images, diagnostic information, and personally identifiable information, requires stringent data protection mechanisms. Radiology departments, being central hubs of medical data, AI solutions, and caregivers, must adhere to strict security standards and regulations. In 2021, Expert Insights from Health Devices identified AI in radiology as a major healthcare risk.⁵⁶

Medical device regulations vary globally but typically align with major standards, such as the FDA in the United States²⁵ or the European Union's CE marking.²⁶ Health data protection standards, such as the Health Insurance Portability and Accountability Act (HIPAA) in the United States or the General Data Protection Regulation (GDPR) in Europe,^{27,28} are also critical. Additionally, national standards, such as Türkiye's "Kişisel Veri Koruma Kanunu" (Personal Data Protection Act) have similarities with GDPR and HIPAA but also include unique requirements, such as mandating that healthcare providers keep health data within the country's borders, irrespective of anonymization.²⁹ Furthermore, the FDA and CE markings encompass responsibilities regarding patient data integrity and cybersecurity.^{57,58}

However, it is important to note that addressing regulations, security, and privacy in the context of AI acquisition is a complex task. It involves not only radiologists but also hospital managers, IT specialists, device providers, and legal experts specializing in medical devices. Consider a scenario in which a leading radiology department in Europe plans to implement an AI system for enhanced brain MRI analysis. The department is known for its innovative approach and diverse patient base and must navigate complex regulatory and security challenges. The AI system, developed by a global technology company, claims compliance with stringent regulations, including the FDA standards in the United States, the European Union's CE marking, and the HIPAA and GDPR frameworks.

The integration of the device involves connecting with existing HIS, RIS, and PACS systems. It is declared compliant with international standards and incorporates data security measures, encryption protocols, and access controls. The radiologists conduct evaluations with the manufacturer, focusing on the "CIA triad": confidentiality, integrity, and availability,⁵⁹ which includes robust authentication protocols, regular security audits, and keeping up with cybersecurity best

practices.⁶⁰ A decision is made to initiate a demonstration integration of the product.

However, initial document checks by the information technology (IT) department reveal that the device complies with HIPAA but not GDPR requirements and runs on the cloud, not accommodating the local data storage rule of their country. Discussions with the manufacturer reveal that they are close to finalizing GDPR registration, as evidenced by their documents. When the hospital IT team and the manufacturer assess the possibility of running the device on cloud servers within the country's borders, they find no dedicated hardware available for running this advanced algorithm locally. Moreover, the legal team, upon reviewing the contract proposed by the manufacturer, discovers a clause allowing the company to use the hospital's data to improve their product, which is firmly opposed by the hospital administrators.

Despite initial intentions, the process brings many challenges and ends in disappointment, highlighting the complexities and importance of considering regulations, security, and privacy. This scenario underscores the need for involvement from legal experts and IT personnel in the early stages and the meticulous assessment of these key areas.

Table 1 offers additional elaboration with subsections including compliance with international standards, adherence to data protection laws, data security measures, local data storage capabilities, vendor data usage policies, and trial integration and IT assessment.

These items provide a comprehensive checklist to guide radiologists and hospital administrators in ensuring that the integration of AI solutions into radiology practices complies with necessary regulations and maintains the highest standards of security and privacy.

Final thoughts and conclusions

In this review-opinion article, we first provided an overview of the current AI solutions for radiology and discussed key factors to consider when choosing appropriate AI solutions for radiology departments. We mainly focused on AI solutions aiming at carrying out interpretative tasks, which routinely necessitate the expertise and active participation of radiologists.

Although we did not and could not cover every aspect of choosing the right solution

for a radiology department, and key factors and their content may rapidly change due to the fast pace of developments of AI technologies, throughout the paper, we attempted to simplify the concepts with hypothetical examples, drawing on our 5 years of clinical, industrial, and academic experience and the existing literature. Furthermore, we provided a checklist consisting of a set of questions and/or items for each criterion, which radiologists may quickly check before starting discussions with AI providers. This will help them make well-informed decisions about integrating AI solutions into their practice, thus contributing significantly to the advancement of radiological services and patient care.

In addition to the considerations outlined above, we recommend the establishment of a departmental review (or assessment) board specifically for the procurement of AI solutions. This board should ideally comprise a multidisciplinary team, including institutional IT officials, legal counsel, end-users, and administrative officials. The creation of such a board facilitates a structured and comprehensive evaluation process, ensuring that the selected AI solutions align with the strategic goals of the department, adhere to legal and ethical standards, and meet the practical needs of end-users. The establishment of these boards, as observed in our experiences and those of our international colleagues, may represent a proactive step towards embracing the complexities and opportunities presented by AI in radiology.

Conflict of interest disclosure

Deniz Alis is the CEO and co-founder of Hevi AI Health Tech. The authors declared no conflicts of interest.

Funding

This paper has been produced benefiting from the 1001 Science and Technology Grant Program National Program of TUBITAK (project no: 122E022). However, the entire responsibility of the publication/paper belongs to the owner of the paper. The financial support received from TUBITAK does not mean that the content of the publication is approved in a scientific sense by TUBITAK.

References

1. Miller DD, Brown EW. Artificial intelligence in medical practice: the question to the answer? *Am J Med.* 2018;131(2):129-133. [\[CrossRef\]](#)
2. Chartrand G, Cheng PM, Vorontsov E, et al. Deep learning: a primer for radiologists. *Radiographics.* 2017;37(7):2113-2131. [\[CrossRef\]](#)

3. Rodríguez-Ruiz A, Krupinski E, Mordang JJ, et al. Detection of breast cancer with mammography: effect of an artificial intelligence support system. *Radiology.* 2019;290(2):305-314. [\[CrossRef\]](#)
4. van Leeuwen KG, de Rooij M, Schalekamp S, van Ginneken B, Rutten MJCM. Clinical use of artificial intelligence products for radiology in the Netherlands between 2020 and 2022. *Eur Radiol.* 2024;34(1):348-354. [\[CrossRef\]](#)
5. Allen B, Agarwal S, Coombs L, Wald C, Dreyer K. 2020 ACR data science institute artificial intelligence survey. *J Am Coll Radiol.* 2021;18(8):1153-1159. [\[CrossRef\]](#)
6. Coppola F, Faggioni L, Regge D, et al. Artificial intelligence: radiologists' expectations and opinions gleaned from a nationwide online survey. *Radiol Med.* 2021;126(1):63-71. [\[CrossRef\]](#)
7. Agrawal A, Khatri GD, Khurana B, Sodickson AD, Liang Y, Dreizin D. A survey of ASER members on artificial intelligence in emergency radiology: trends, perceptions, and expectations. *Emerg Radiol.* 2023;30(3):267-277. [\[CrossRef\]](#)
8. AI for Radiology. Accessed November 19, 2023. [\[CrossRef\]](#)
9. Health C for D and R. Artificial intelligence and machine learning (AI/ML)-enabled medical devices. FDA. Published online October 20, 2023. Accessed November 19, 2023. [\[CrossRef\]](#)
10. Heuvelmans MA, van Ooijen PMA, Ather S, et al. Lung cancer prediction by deep learning to identify benign lung nodules. *Lung Cancer.* 2021;154:1-4. [\[CrossRef\]](#)
11. Karagoz A, Alis D, Seker ME, et al. Anatomically guided self-adapting deep neural network for clinically significant prostate cancer detection on bi-parametric MRI: a multi-center study. *Insights into Imaging.* 2023;14(1):110. [\[CrossRef\]](#)
12. Park HJ, Park B, Lee SS. Radiomics and deep learning: hepatic applications. *Korean J Radiol.* 2020;21(4):387-401. [\[CrossRef\]](#)
13. Sandino CM, Cole EK, Alkan C, et al. Upstream machine learning in radiology. *Radiol Clin North Am.* 2021;59(6):967-985. [\[CrossRef\]](#)
14. Bizzo BC, Almeida RR, Michalski MH, Alkasab TK. Artificial Intelligence and clinical decision support for radiologists and referring providers. *J Am Coll Radiol.* 2019;16(9 Pt B):1351-1356. [\[CrossRef\]](#)
15. van Leeuwen KG, de Rooij M, Schalekamp S, van Ginneken B, Rutten MJCM. How does artificial intelligence in radiology improve efficiency and health outcomes? *Pediatr Radiol.* 2022;52(11):2087-2093. [\[CrossRef\]](#)
16. Tariq A, Purkayastha S, Padmanaban GP, et al. Current clinical applications of artificial intelligence in radiology and their best supporting evidence. *J Am Coll Radiol.* 2020;17(11):1371-1381. [\[CrossRef\]](#)

17. Tanguay W, Acar P, Fine B, et al. Assessment of radiology artificial intelligence software: a validation and evaluation framework. *Can Assoc Radiol J.* 2023;74(2):326-333. [\[CrossRef\]](#)
18. Tadavarthi Y, Vey B, Krupinski E, et al. The state of radiology AI: considerations for purchase decisions and current market offerings. *Radiol Artif Intell.* 2020;2(6):e200004. [\[CrossRef\]](#)
19. Filice RW, Mongan J, Kohli MD. Evaluating artificial intelligence systems to guide purchasing decisions. *J Am Coll Radiol.* 2020;17(11):1405-1409. [\[CrossRef\]](#)
20. Omoumi P, Ducarouge A, Tournier A, et al. To buy or not to buy-evaluating commercial AI solutions in radiology (the ECLAIR guidelines). *Eur Radiol.* 2021;31(6):3786-3796. [\[CrossRef\]](#)
21. European Society of Radiology (ESR). What the radiologist should know about artificial intelligence - an ESR white paper. *Insights Imaging.* 2019;10(1):44. [\[CrossRef\]](#)
22. Wamba-Taguimdje SL, Fosso Wamba S, Kala Kamdjoug JR, Tchatchouang Wanko CE. Influence of artificial intelligence (AI) on firm performance: the business value of AI-based transformation projects. *Business Process Management Journal.* 2020;26(7):1893-1924. [\[CrossRef\]](#)
23. Lam Shin Cheung J, Ali A, Abdalla M, Fine B. U"AI" testing: user interface and usability testing of a chest X-ray AI tool in a simulated real-world workflow. *Can Assoc Radiol J.* 2023;74(2):314-325. [\[CrossRef\]](#)
24. Combi C, Amico B, Bellazzi R, et al. A manifesto on explainability for artificial intelligence in medicine. *Artif Intell Med.* 2022;133:102423. [\[CrossRef\]](#)
25. Commissioner O of the U.S. Food and Drug Administration. FDA. Published December 4, 2023. Accessed December 9, 2023. [\[CrossRef\]](#)
26. CE marking. Accessed December 9, 2023. [\[CrossRef\]](#)
27. Health | European Data Protection Supervisor. Accessed December 9, 2023. [\[CrossRef\]](#)
28. Health Insurance Portability and Accountability Act of 1996 (HIPAA) | CDC. Published June 28, 2022. Accessed December 9, 2023. [\[CrossRef\]](#)
29. Kişisel Verileri Koruma Kurumu | KVKK | Kişisel Verileri Koruma Kurumu Başkanlığı. Accessed December 9, 2023. [\[CrossRef\]](#)
30. Martín Noguerol T, Paulano-Godino F, Martín-Valdivia MT, Menias CO, Luna A. Strengths, weaknesses, opportunities, and threats analysis of artificial intelligence and machine learning applications in radiology. *J Am Coll Radiol.* 2019;16(9 Pt B):1239-1247. [\[CrossRef\]](#)
31. Hwang EJ, Park CM. Clinical implementation of deep learning in thoracic radiology: potential applications and challenges. *Korean J Radiol.* 2020;21(5):511-525. [\[CrossRef\]](#)
32. Zhang T, Tan T, Samperna R, et al. Radiomics and artificial intelligence in breast imaging: a survey. *Artif Intell Rev.* 2023;56(Suppl 1):857-892. [\[CrossRef\]](#)
33. Turkbey B, Rosenkrantz AB, Haider MA, et al. Prostate imaging reporting and data system version 2.1: 2019 update of prostate imaging reporting and data system version 2. *Eur Urol.* 2019;76(3):340-351. [\[CrossRef\]](#)
34. Soerensen SJC, Fan RE, Seetharaman A, et al. Deep learning improves speed and accuracy of prostate gland segmentations on magnetic resonance imaging for targeted biopsy. *J Urol.* 2021;206(3):604-612. [\[CrossRef\]](#)
35. Wetterauer C, Winkel DJ, Federer-Gsponer JR, et al. Structured reporting of prostate magnetic resonance imaging has the potential to improve interdisciplinary communication. *PLoS One.* 2019;14(2):e0212444. [\[CrossRef\]](#)
36. Labus S, Altmann MM, Huisman H, et al. A concurrent, deep learning-based computer-aided detection system for prostate multiparametric MRI: a performance study involving experienced and less-experienced radiologists. *Eur Radiol.* 2023;33(1):64-76. [\[CrossRef\]](#)
37. Liu X, Cruz Rivera S, Moher D, Calvert MJ, Denniston AK; SPIRIT-AI and CONSORT-AI Working Group. Reporting guidelines for clinical trial reports for interventions involving artificial intelligence: the CONSORT-AI extension. *Lancet Digit Health.* 2020;2(10):537-e548. [\[CrossRef\]](#)
38. Mongan J, Moy L, Kahn CE Jr. Checklist for artificial intelligence in medical imaging (CLAIM): a guide for authors and reviewers. *Radiol Artif Intell.* 2020;2(2):e200029. [\[CrossRef\]](#)
39. Clark P, Kim J, Aphinyanaphongs Y. Marketing and US Food and Drug Administration Clearance of Artificial Intelligence and Machine Learning Enabled Software in and as Medical Devices: a systematic review. *JAMA Network Open.* 2023;6(7):e2321792. [\[CrossRef\]](#)
40. Lunit Expands Collaboration with GE Healthcare to Advance AI Adoption across Healthcare Industry. Accessed March 12, 2024. [\[CrossRef\]](#)
41. Lunit AI Solutions to Power Samsung's X-ray Devices for Advanced Chest Screening. Accessed March 12, 2024. [\[CrossRef\]](#)
42. Vandewinckele L, Claessens M, Dinkla A, et al. Overview of artificial intelligence-based applications in radiotherapy: Recommendations for implementation and quality assurance. *Radiother Oncol.* 2020;153:55-66. [\[CrossRef\]](#)
43. Bassett M. The reality of deep learning/artificial intelligence in radiology: they will redefine the specialty. Accessed November 25, 2023. [\[CrossRef\]](#)
44. Dikici E, Bigelow M, Prevedello LM, White RD, Erdal BS. Integrating AI into radiology workflow: levels of research, production, and feedback maturity. *J Med Imaging (Bellingham).* 2020;7(1):016502. [\[CrossRef\]](#)
45. Gleeson F, Revel MP, Biederer J, et al. Implementation of artificial intelligence in thoracic imaging-a what, how, and why guide from the European Society of Thoracic Imaging (ESTI). *Eur Radiol.* 2023;33(7):5077-5086. [\[CrossRef\]](#)
46. Strohm L, Hehakaya C, Ranschaert ER, Boon WPC, Moors EHM. Implementation of artificial intelligence (AI) applications in radiology: hindering and facilitating factors. *Eur Radiol.* 2020;30(10):5525-5532. [\[CrossRef\]](#)
47. Sectra Amplifier Marketplace - Easily navigate the ecosystem of AI applications. Sectra Amplifier Marketplace. Accessed March 12, 2024. [\[CrossRef\]](#)
48. Edison Artificial Intelligence & Analytics. Accessed March 12, 2024. [\[CrossRef\]](#)
49. Blackford Analysis - Your strategic AI platform partner. Accessed March 12, 2024. [\[CrossRef\]](#)
50. deepcOS - The Radiology AI Operating System. Accessed March 12, 2024. [\[CrossRef\]](#)
51. Parikh RB, Helmchen LA. Paying for artificial intelligence in medicine. *NPJ Digit Med.* 2022;5(1):63. [\[CrossRef\]](#)
52. Lee MH, Schemmel AJ, Pooler BD, et al. Radiology workflow dynamics: how workflow patterns impact radiologist perceptions of workplace satisfaction. *Acad Radiol.* 2017;24(4):483-487. [\[CrossRef\]](#)
53. Reimbursement for AI in Radiology: Current Practices and Future Considerations. Accessed November 25, 2023. [\[CrossRef\]](#)
54. Liew C. The future of radiology augmented with artificial intelligence: a strategy for success. *Eur J Radiol.* 2018;102:152-156. [\[CrossRef\]](#)
55. Rim SH, Allaire BT, Ekwueme DU, et al. Cost-effectiveness of breast cancer screening in the National Breast and Cervical Cancer Early Detection Program. *Cancer Causes Control.* 2019;30(8):819-826. [\[CrossRef\]](#)
56. Top 10 Health Technology Hazards for 2023 Executive Brief. ECRI. Accessed December 9, 2023. [\[CrossRef\]](#)
57. Harrington SG, Johnson MK. The FDA and artificial intelligence in radiology: defining new boundaries. *J Am Coll Radiol.* 2019;16(5):743-744. [\[CrossRef\]](#)
58. Harvey HB, Gowda V. How the FDA Regulates AI. *Acad Radiol.* 2020;27(1):58-61. [\[CrossRef\]](#)
59. Jennett P, Watanabe M, Igras E, Premkumar K, Hall W. Telemedicine and security. Confidentiality, integrity, and availability: a Canadian perspective. *Stud Health Technol Inform.* 1996;29:286-298. [\[CrossRef\]](#)
60. Shah C, Nachand D, Wald C, Chen PH. Keeping patient data secure in the age of radiology artificial intelligence: cybersecurity considerations and future directions. *J Am Coll Radiol.* 2023;20(9):828-835. [\[CrossRef\]](#)



Exploring radiomics research quality scoring tools: a comparative analysis of METRICS and RQS

Burak Koçak¹
 Tugba Akinci D'Antonoli²
 Renato Cuocolo³

¹University of Health Sciences, Başakşehir Çam and Sakura City Hospital, Clinic of Radiology, Istanbul, Türkiye

²Cantonal Hospital Baselland, Institute of Radiology and Nuclear Medicine, Liestal, Switzerland

³University of Salerno, Department of Medicine, Surgery and Dentistry, Baronissi, Italy

Radiomics facilitates the extraction of vast quantities of quantitative data from medical images, which can substantially aid in several diagnostic and prognostic tasks.¹ Although numerous studies have demonstrated promising results with this approach, its integration into clinical practice remains limited, necessitating additional validation for clinical application.² A major barrier to this integration is the lack of standardization of key stages in the complex multi-step radiomic pipeline,³ which could be assessed and enhanced through structured guidelines and quality assessment tools.⁴⁻⁷

In 2017, Lambin et al.⁸ introduced the radiomics quality score (RQS) as a methodological assessment tool to enhance the quality of radiomics studies. The RQS comprises 16 items that evaluate the entire lifecycle of radiomics research, with a total raw score ranging from -8 to +36. Although the rationale for the scores assigned to each item remains unclear, the radiomics research community has widely adopted this tool since its introduction, leading to numerous systematic reviews.⁹ The success of the RQS within the research community also signifies a strong desire for standardization in radiomics, despite its limitations.

Recently, new consensus guidelines specific to radiomics research, namely, the Check-List for EvaluAtion of Radiomics Research (CLEAR) and the METHodological RadiomiCs Score (METRICS), have been introduced and endorsed by leading imaging societies.^{6,7} CLEAR aims to promote transparent reporting practices, whereas METRICS provides a standardized tool for assessing the methodological quality of radiomics research. METRICS includes 30 items spread over five conditions, designed to accommodate almost all potential methodological scenarios in radiomics research, from traditional handcrafted methods to advanced deep-learning computer vision models.⁶ The development process for METRICS involved a modified Delphi method and a broad international panel to mitigate bias and focus on specific aspects of radiomics research related to medical imaging. The European Society of Medical Imaging Informatics has endorsed the METRICS tool, and its website offers an online calculator for the final quality score, which also considers item conditionality (available online at <https://metricscore.github.io/metrics/METRICS.html>).⁶

Published in 2024,⁶ METRICS is just beginning its journey, and its differences from RQS have not yet been fully explored, which could offer valuable insights for the radiomics community. Therefore, we aimed to compare METRICS and RQS through hypothetical examples, focusing on the unique or missing items of each quality scoring tool. For this comparison, the methodological quality of an ideal hypothetical study was defined as achieving a score of 100% using one tool before being assessed using the other tool, and vice versa. For simplicity, all conditions of METRICS were deemed fulfilled (i.e., scored as “yes”) in both comparisons. To establish a baseline, we assumed that a perfect study meets only the minimum requirements of a quality scoring tool (either RQS or METRICS) to attain the highest possible score. This assumption allowed us to evaluate the probable lowest boundary of the highest potential score achievable by the alternative tool. Following the conventions in the literature and recommendations by its developers, the RQS percentage score was calculated by dividing the total points by 36 and multiplying by 100. We also examined the scaling method used for RQS in the literature compared with that of METRICS.

Corresponding author: Burak Koçak

E-mail: drburakkocak@gmail.com

Received 05 April 2024; accepted 25 April 2024.



Epub: 03.05.2024

Publication date: 06.11.2024

DOI: 10.4274/dir.2024.242793

You may cite this article as: Koçak B, Akinci D'Antonoli T, Cuocolo R. Exploring radiomics research quality scoring tools: a comparative analysis of METRICS and RQS. *Diagn Interv Radiol.* 2024;30(6):366-369.

The upper panels of Figure 1 clearly depict a comparison of final quality scores using alternative tools in these hypothetical scenarios. A hypothetical perfect study based on RQS could only achieve a 30% score, which means it lacks up to 70% of the total METRICS percentage score. Conversely, a hypothetical perfect study based on METRICS could reach a 42% score, thus missing 58% of the potential RQS percentage score. Notably, the hypothetical perfect study based on METRICS achieved a higher score in the RQS (42% or 15 total points) compared with the study based on RQS (METRICS: 30%). In the scenario where the perfect study adheres to RQS standards (i.e., RQS: 100%), the requirements for 20 of the 30 items (67%) were not fully met in the METRICS tool. Conversely, in the scenario where METRICS is the standard (i.e., METRICS: 100%), 12 of the 16 (75%) RQS items were not satisfied. Of these, 9 had no direct counterpart in the other tool, whereas the remaining 3 were only partially covered. The lower panels of Figure 1 provide further details about the item-wise comparison in these hypothetical scenarios. Additionally, the items missed in the alternative tools are comprehensively listed in Table 1.

In a perfect study based on RQS, the METRICS evaluation revealed numerous missing items that span almost all sections of the tool, with some sections completely lacking coverage: “study design,” “segmentation,” “image processing and feature extraction,” and “preparation for modeling.” The “study design” section of METRICS places substantial emphasis on transparent reporting practices and encourages adherence to specific guidelines tailored to radiomics, such as CLEAR.⁷ These METRICS items also highlight crucial aspects of any experimental setup, including the accurate reporting of patient eligibility criteria and reference standards. The “segmentation” section emphasizes the important but often overlooked nuances of data labeling methodology. These include the formal evaluation of fully automatic segmentation (when employed) and the clinical applicability of the segmentation methodology. Specifically, if masks are required for the test set to simulate real-world inference, they should mirror what would reasonably be expected in this context (i.e., produced by a single reader or automated software). “Image processing and feature extraction” considers standardization initiatives such as the Image Biomarker Standardization Initiative, as well as the transparency and appropriateness of settings used in data preprocessing and feature extraction.⁵ The items in “preparation

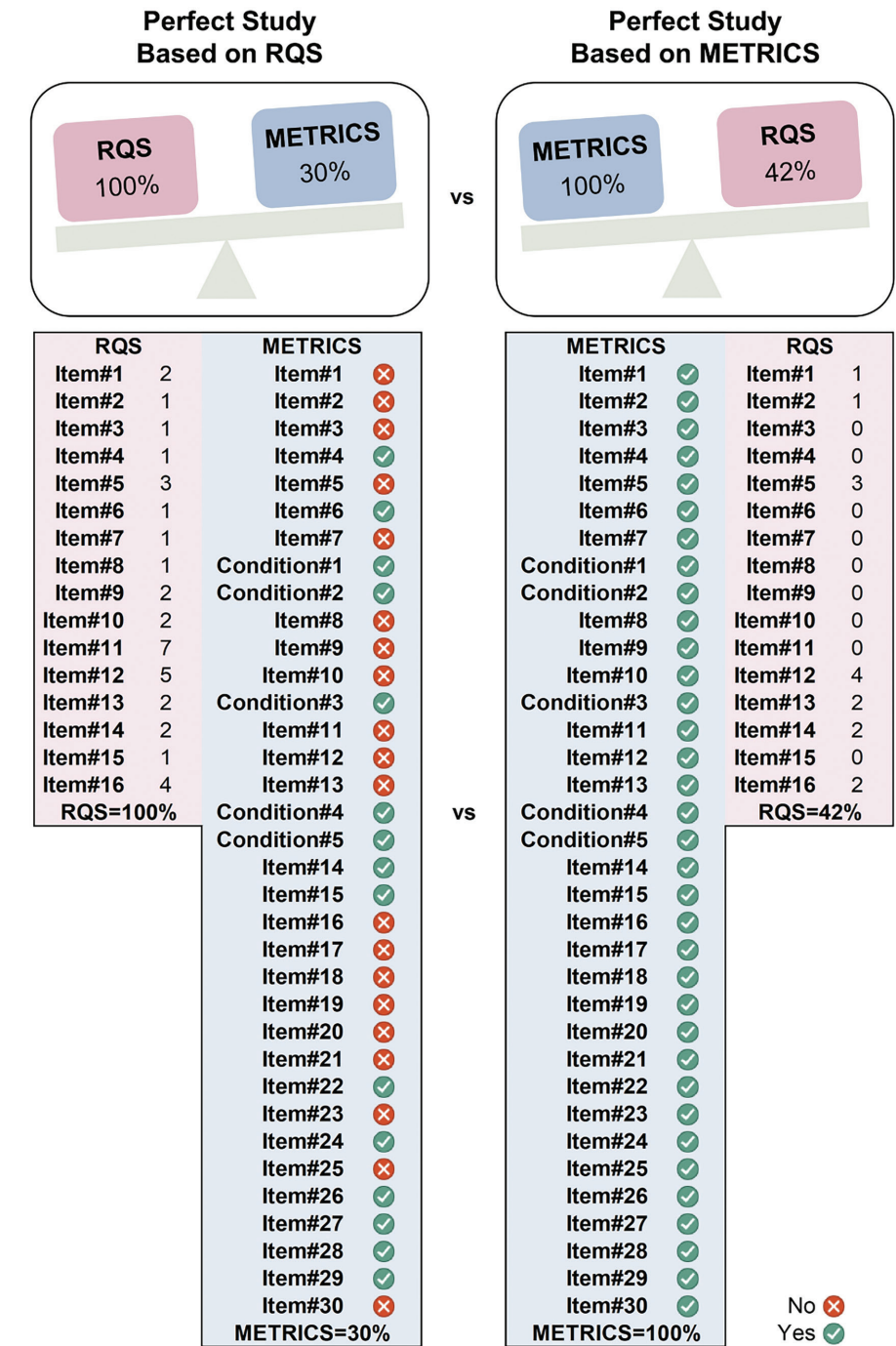


Figure 1. Score-wise (upper panels) and item-wise (lower panels) comparisons of METHodological RadiomiCS Score (METRICS) and radiomics quality score (RQS) evaluations in methodologically exemplary hypothetical radiomic studies using RQS and METRICS, respectively. Note: The RQS was calculated by dividing the total score by 36 and then multiplying by 100.

for modeling” address key sources of bias, such as proper data partitioning to prevent information leakage during model development and the handling of confounders. Importantly, missed items extend beyond these sections. For instance, METRICS emphasizes the importance of model availability in the “open science” section, which is critical for validating proposed approaches with new data, ideally from a diverse source.

In the same vein, METRICS has not addressed several RQS items. While theoretically possible, certain RQS items such as “phantom study,” “multiple time points,” “biological correlates,” and “prospective study” may be deemed too abstract or lack practical relevance to necessitate their systematic inclusion in every radiomics study.¹⁰ Interestingly, the “prospective study” was initially considered and voted on during the development

Table 1. Missed METRICS and RQS items in the case of methodologically perfect scores in RQS and METRICS, respectively^{6,8}

Category	Item no.	Item definition
Missed METRICS items in a perfect study according to RQS ¹	Item#1	Adherence to radiomics and/or machine learning-specific checklists or guidelines
	Item#2	Eligibility criteria that describe a representative study population
	Item#3	High-quality reference standard with a clear definition
	Item#5	Clinical translatability of the imaging data source for radiomics analysis
	Item#7	The interval between imaging used and reference standard
	Item#8	Transparent description of segmentation methodology
	Item#9	Formal evaluation of fully automated segmentation
	Item#10	Test set segmentation masks produced by a single reader or automated tool
	Item#11	Appropriate use of image preprocessing techniques with transparent description
	Item#12	Use of standardized feature extraction software
	Item#13	Transparent reporting of feature extraction parameters, otherwise providing a default configuration statement
	Item#16	Appropriateness of dimensionality compared with data size
	Item#17	Robustness assessment of end-to-end deep learning pipelines
	Item#18	Proper data partitioning process
	Item#19	Handling of confounding factors
	Missed RQS items in a perfect study according to METRICS ¹	Item#1
Item#3		Phantom study
Item#4		Multiple time points
Item#6		Multi-variable analysis with non-radiomic features
Item#7		Biological correlates
Item#8		Cut-off analyses
Item#9		Discrimination statistics
Item#10		Calibration statistics
Item#11		Prospective study
Item#12		Validation (5 th and 6 th sub-items)
Item#15	Cost-effectiveness analysis	
Item#16	Open science and data (any two of 1 st , 2 nd , or 4 th sub-items)	

¹A perfect study is defined as one that meets only the minimum requirements of a quality scoring tool (e.g., RQS or METRICS) to achieve the maximum score available. METRICS, METHodological Radiomics Score; RQS, radiomics quality score.

of METRICS but failed to reach the consensus threshold for inclusion in the final scoring tool. Likewise, other items were proposed by participants during the METRICS development phase but were excluded from the final tool following open and anonymous discussions throughout the Delphi process, indicating a general consensus on their limited utility. For additional METRICS and RQS items not discussed here, please refer to Table 1.

Although METRICS presents the final score as a percentage value with linear scaling, the RQS does not advocate for this method when converting total RQS points to

a percentage. A re-analysis of the papers in the seminal study by Spadarella et al.⁹, which included 44 systematic reviews using RQS, revealed that 32 used non-linear scaling (i.e., total points/36*100), and none used linear scaling (i.e., [total points + 8]/44*100). Despite questions about the appropriateness of the non-linear conversion method, this practice follows the developer's suggestion (i.e., 36 = 100%).⁸ This method of calculation does not account for negative values in scaling, where both scores of -8 and 0 correspond to 0%, potentially overestimating the score of studies with negative RQS totals. This could

lead to the impression that the absence of "feature reduction or adjustment for multiple testing" and "validation" renders the remaining methodological points unsubstantial until an overall positive score is achieved, possibly underestimating the quality of studies on the percentage scale. The upper panel of Figure 2 illustrates a simple comparison of RQS percentage calculations by the widely used non-linear method versus the linear method. The lower panel of Figure 2 shows the impact of using the non-linear method compared with the linear method. This simulation demonstrates that the non-linear

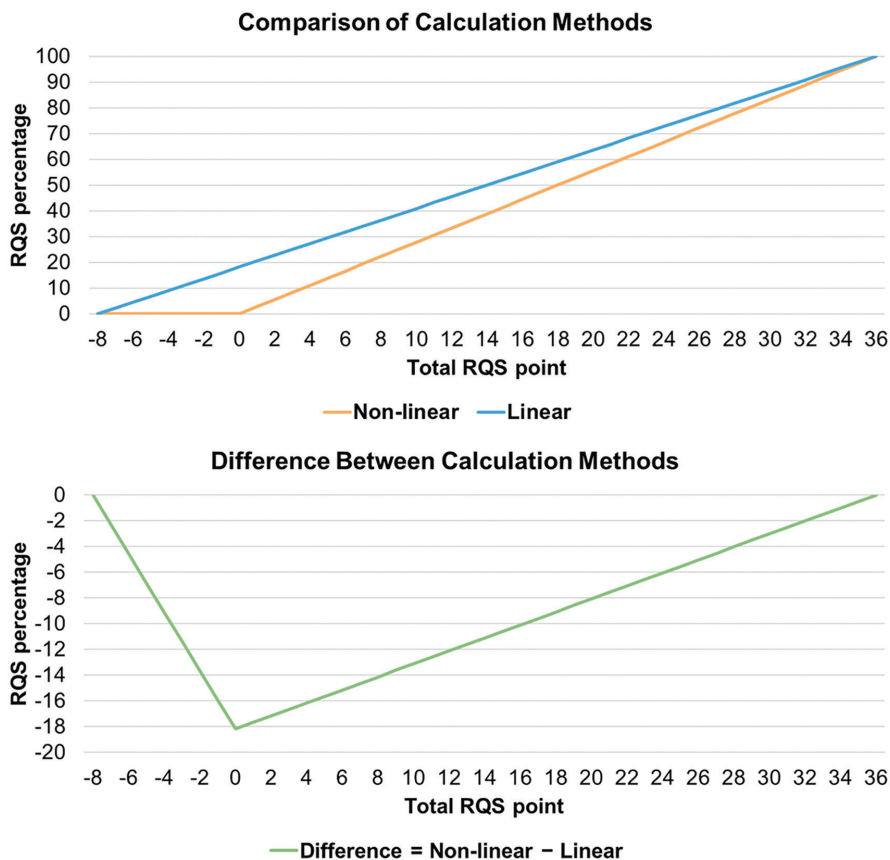


Figure 2. Upper panel: comparison of non-linear (widely used) and linear scaling methods for calculating radiomics quality score (RQS) percentages. Lower panel: differences and consequences resulting from the use of these methods.

method tends to underestimate the final RQS percentage, with a mean, standard deviation, and maximum of -8.9% , 5.4% , and 18% , respectively.

In this brief article, we aimed to draw the scientific community's attention to the differences between two quality scoring tools for radiomics research, specifically the recently published METRICS and the well-established RQS. Given the absence of an independent reference standard, which would provide invaluable additional insights, we relied on hypothetical perfect studies to evaluate these tools' relative value and content. Although this approach was hypothetical, it underscored the distinct focus of each tool on different aspects of the radiomic pipeline, given the substantial disparity in relative scores and missed items. Therefore, a direct com-

parison of the scores from these tools is not feasible, and researchers should consider the unique features of each tool. Based on the insights from this analysis and the emerging limitations regarding the reproducibility and accuracy of the RQS percentage score,^{9,10} METRICS may be the preferable choice if only one tool is to be used.

Conflict of interest disclosure

Burak Koçak, MD, Tugba Akinci D'Antonoli are Section Editors in Diagnostic and Interventional Radiology. They had no involvement in the peer-review of this article and had no access to information regarding its peer-review. Burak Koçak, Tugba Akinci D'Antonoli, and Renato Cuocolo took part in the development of METRICS.

References

- van Timmeren JE, Cester D, Tanadini-Lang S, Alkadhi H, Baessler B. Radiomics in medical imaging—"how-to" guide and critical reflection. *Insights Imaging*. 2020;11(1):91. [\[CrossRef\]](#)
- Zhong J, Lu J, Zhang G, et al. An overview of meta-analyses on radiomics: more evidence is needed to support clinical translation. *Insights Imaging*. 2023;14:111. [\[CrossRef\]](#)
- Cobo M, Menéndez Fernández-Miranda P, Bastarrika G, Lloret Iglesias L. Enhancing radiomics and Deep Learning systems through the standardization of medical imaging workflows. *Sci Data*. 2023;10(1):732. [\[CrossRef\]](#)
- Whybra P, Zwanenburg A, Andrearczyk V, et al. The image biomarker standardization initiative: standardized convolutional filters for reproducible radiomics and enhanced clinical insights. *Radiology*. 2024;310(2):e231319. [\[CrossRef\]](#)
- The Image Biomarker Standardization Initiative: Standardized Quantitative Radiomics for High-Throughput Image-based Phenotyping. *Radiology*. 2020;295(2):328-338. [\[CrossRef\]](#)
- Kocak B, Akinci D'Antonoli T, Mercaldo N, et al. METHodological Radiomics Score (METRICS): a quality scoring tool for radiomics research endorsed by EuSoMII I. *Insights Imaging*. 2024;15(1):8. [\[CrossRef\]](#)
- Kocak B, Baessler B, Bakas S, et al. CheckList for Evaluation of Radiomics research (CLEAR): a step-by-step reporting guideline for authors and reviewers endorsed by ESR and EuSoMII. *Insights Imaging*. 2023;14(1):75. [\[CrossRef\]](#)
- Lambin P, Leijenaar RTH, Deist TM, et al. Radiomics: the bridge between medical imaging and personalized medicine. *Nat Rev Clin Oncol*. 2017;14(12):749-762. [\[CrossRef\]](#)
- Spadarella G, Stanzione A, Akinci D'Antonoli T, et al. Systematic review of the radiomics quality score applications: an EuSoMII Radiomics Auditing Group Initiative. *Eur Radiol*. 2023;33(3):1884-1894. [\[CrossRef\]](#)
- Akinci D'Antonoli T, Cavallo AU, Vernuccio F, et al. Reproducibility of radiomics quality score: an intra- and inter-rater reliability study. *Eur Radiol*. 2024;34(4):2791-2804. [\[CrossRef\]](#)



Diagnostic performance of multishot echo-planar imaging (RESOLVE) and non-echo-planar imaging (HASTE) diffusion-weighted imaging in cholesteatoma with an emphasis on signal intensity ratio measurement

Ahmet Bozer¹
 Zehra Hilal Adibelli¹
 Yeşim Yener¹
 Abdullah Dalgıç²

¹İzmir City Hospital, Clinic of Radiology, İzmir, Türkiye

²İzmir City Hospital, Clinic of Otolaryngology Head and Neck Surgery, İzmir, Türkiye

PURPOSE

To evaluate the diagnostic efficacy of multishot echo-planar imaging (EPI) [RESOLVE (RS)] and non-EPI (HASTE) diffusion-weighted imaging (DWI) in detecting cholesteatoma (CHO), and to explore the role of signal intensity (SI) ratio measurements in addressing diagnostic challenges.

METHODS

We analyzed RS-EPI and non-EPI DWI images from 154 patients who had undergone microscopic middle ear surgery, with pathological confirmation of their diagnoses. Two radiologists, referred to as Reader A and Reader B, independently reviewed the images without prior knowledge of the outcomes. Their evaluation focused on lesion location, T1-weighted (T1W) signal characteristics, and contrast enhancement in temporal bone magnetic resonance imaging. Key parameters included lesion hyperintensity, size, SI, SI ratio, and susceptibility artifact scores across both imaging modalities.

RESULTS

Of the patients, 62.3% (96/154) were diagnosed with CHO, whereas 37.7% (58/154) were found to have non-CHO conditions. In RS-EPI DWI, Reader A achieved 89.6% sensitivity, 79.3% specificity, 87.8% positive predictive value (PPV), and 82.1% negative predictive value (NPV). Non-EPI DWI presented similar results with sensitivities of 89.6%, specificities of 86.2%, PPVs of 91.5%, and NPVs of 83.3%. Reader B's results for RS-EPI DWI were 82.3% sensitivity, 84.5% specificity, 89.8% PPV, and 74.2% NPV, whereas, for non-EPI DWI, they were 86.5% sensitivity, 89.7% specificity, 93.3% PPV, and 80% NPV. The interobserver agreement was excellent (RS-EPI, κ : 0.84; non-EPI, κ : 0.91). The SI ratio measurements were consistently higher in non-EPI DWI (Reader A: 2.51, Reader B: 2.46) for the CHO group compared with RS-EPI. The SI ratio cut-off (>1.98) effectively differentiated hyperintense lesions between CHO and non-CHO groups, demonstrating 82.9% sensitivity and 100% specificity, with an area under the curve of 0.901 (95% confidence interval: 0.815–0.956; $P < 0.001$). Susceptibility artifact scores averaged 1.18 ± 0.7 (Reader A) and 1.04 ± 0.41 (Reader B) in RS-EPI, with non-EPI DWI recording a mean score of 0.

CONCLUSION

Both RS-EPI and non-EPI DWI exhibited high diagnostic accuracy for CHO. While RS-EPI DWI cannot replace non-EPI DWI, their combined use improves sensitivity. SI ratio measurement in non-EPI DWI was particularly beneficial in complex diagnostic scenarios.

CLINICAL SIGNIFICANCE

This study refines CHO diagnostic protocols by showcasing the diagnostic capabilities of both RS-EPI and non-EPI DWI and highlighting the utility of SI measurements as a diagnostic tool. These findings may reduce false positives and aid in more accurate treatment planning, offering substantial insights for clinicians in managing CHO.

KEYWORDS

Cholesteatoma, diffusion-weighted imaging, non-EPI, RESOLVE, signal intensity ratio

Corresponding author: Ahmet Bozer

E-mail: drahmetbozer@gmail.com

Received 19 March 2024; revision requested 11 April 2024; last revision received 24 April 2024; accepted 08 May 2024.



Epub: 27.05.2024

Publication date: 06.11.2024

DOI: 10.4274/dir.2024.242767

You may cite this article as: Bozer A, Adibelli ZH, Yener Y, Dalgıç A. Diagnostic performance of multishot echo-planar imaging (RESOLVE) and non-echo-planar imaging (HASTE) diffusion-weighted imaging in cholesteatoma with an emphasis on signal intensity ratio measurement. *Diagn Interv Radiol.* 2024;30(6):370-377.

Cholesteatoma (CHO), characterized by its invasive growth in the middle ear, poses substantial health risks, including hearing loss, vestibular disturbances, facial paralysis, and potential intracranial complications.¹ Accordingly, accurate diagnosis and effective treatment are essential. Magnetic resonance imaging (MRI) with diffusion-weighted imaging (DWI) serves as a critical tool for the initial assessment and diagnosis of CHO, as well as for monitoring local recurrence or residual CHO.² Due to its practicality and diagnostic efficacy, DWI has increasingly been adopted as a substitute for post-contrast sequences in MRI assessments.

The DWI techniques are primarily divided into two categories: echo-planar imaging (EPI)-based and non-EPI-based methods. Despite its rapid acquisition capability, single-shot (SS) EPI-DWI is susceptible to artifacts such as susceptibility, chemical shift, and geometric distortion.³ These artifacts can obscure areas showing restricted diffusion, substantially compromising the detection of CHO. Additionally, the inherent limitations of EPI-DWI in terms of spatial resolution and section thickness pose challenges in detecting CHOs smaller than 5 mm.⁴

Recent technological advancements have led to the development of an improved multishot (MS) EPI technique that offers high-resolution DWI while reducing geometric distortions. However, this method necessitates longer imaging times. The RESOLVE DWI, utilizing a readout-segmented echo-planar [RESOLVE EPI (RS-EPI)] approach, introduces a cutting-edge method for capturing high-quality DWI images. This technique enhances image sharpness, increases spatial resolution, and reduces slice thickness,⁵ thereby improving the detection of even

small CHOs. By segmenting the k-space trajectory into multiple parts in the phase encoding direction, RESOLVE DWI reduces echo time (TE) and is substantially less affected by distortions, susceptibility, and T2* blurring artifacts, enhancing overall image quality.

Non-EPI DWI turbo spin-echo (TSE) is a spin-echo-based technique that can be applied in either SS or MS formats. It is renowned for its higher signal-to-noise ratio (SNR) and minimal image distortions, surpassing SS EPI-DWI in these respects. TSE provides enhanced spatial resolution in the middle ear, facilitating rapid multiplanar imaging and thinner slice capabilities compared with EPI sequences.⁶ Moreover, TSE-DWI can be integrated with half-fourier acquisition SS TSE (HASTE), which offers excellent motion insensitivity and notably reduced susceptibility artifacts. Additional non-EPI DWI techniques, such as PROPELLER DWI and BLADE DWI, further minimize susceptibility artifacts and improve overall imaging quality.

The current body of literature features numerous studies that have compared standard EPI DWI with non-EPI DWI sequences in diagnosing CHO, consistently highlighting the superiority of non-EPI sequences.⁷ Nevertheless, there have been limited studies comparing MS EPI sequences, such as RESOLVE, with non-EPI sequences. This study aims to assess the diagnostic performance of the MS EPI sequence, which offers shorter imaging times, as a viable alternative to non-EPI sequences. Furthermore, this research seeks to explore the role of signal intensity (SI) measurement in DWI, particularly when addressing diagnostic challenges, to potentially enhance the accuracy and reliability of CHO diagnosis.

Methods

Patient selection and criteria

Following approval from the Clinical Research Ethics Committee of University of Health Sciences Türkiye, İzmir Bozyaka Training and Research Hospital (approval no: 2023/123, dated 23.08.2023), we conducted a retrospective single-center study. This study encompassed patients who underwent tympanoplasty and mastoidectomy for chronic otitis media (COM) between 2017 and 2023. Inclusion criteria included individuals with pre-operative temporal MRI scans featuring both RS-EPI and non-EPI (HASTE) sequences, as well as confirmed pathological diagnoses. The exclusion criteria were cases with incomplete or excessively artifact-laden

MRI sequences and patients whose pathological results were inconclusive for diagnosis. Lesions located solely in the external acoustic canal (EAC) were also excluded. Ultimately, 154 patients met the criteria and were enrolled in the study.

Imaging technique

MRI was conducted using a 1.5T scanner (Siemens Healthineers, Magnetom Aera, Germany). Informed consent was obtained from all participants prior to imaging. The imaging protocol comprised axial T2-weighted (T2W) SPACE and T2W TSE sequences with fat saturation alongside axial and coronal T1-weighted (T1W) TSE sequences. Additionally, the protocol included coronal RESOLVE for DWI and apparent diffusion coefficient sequences, as well as coronal HASTE DWI. Post-contrast imaging was performed using axial and coronal T1W TSE sequences with gadobutrol (Gadovist™, Bayer AG, Berlin, Germany, 0.1 mmol/kg).

The RESOLVE DWI parameters were as follows: TR/TE: 3,780/60 ms; flip angle: 180°; 15 slices; slice thickness: 2.5 mm; *b* values (*s/mm*²) = 0–1,000; field of view (FOV): 218; and matrix: 160 × 104, with an imaging duration of 2 minutes and 55 seconds. The HASTE DWI parameters included TR/TE: 2,000/103 ms; flip angle: 150°; 11 slices; slice thickness: 3 mm; *b* value (*s/mm*²): 1,000; FOV: 220; matrix = 192 × 144; and an imaging time of 3 minutes and 42 seconds.

Imaging analysis

Two radiologists, with 32 years (Reader A) and 7 years (Reader B) of neuroradiological experience, respectively, independently assessed the MRI scans of the patients at workstations (Siemens Healthineers) without prior knowledge of the pathological outcomes. The study focused on patients who underwent surgical treatment and had a confirmed diagnosis, assessing both ears in each case.

The evaluation process commenced with an examination of standard temporal MR sequences. Lesion locations were categorized into several groups: middle ear; mastoid antrum; a combination of both; or middle ear and EAC.

The analysis proceeded with the selection of a single diffusion sequence for each patient, chosen randomly without a predetermined order. Approximately 1 month after completing the initial evaluations for all patients, the second diffusion sequence was reviewed. Lesions demonstrating hyperintensity in diffusion sequences relative to the

Main points

- RESOLVE echo-planar imaging (RS-EPI) and non-EPI (HASTE) diffusion-weighted imaging (DWI) both demonstrate high diagnostic accuracy for cholesteatoma (CHO) individually. However, when used in conjunction, these techniques enhance diagnostic sensitivity.
- Signal intensity ratio measurements, particularly in non-EPI DWI, serve as a valuable quantitative tool for differentiating CHO from other conditions, thereby increasing diagnostic certainty.
- Susceptibility artifacts are minimal in RS-EPI DWI and completely absent in non-EPI DWI, underscoring the latter's potential for higher imaging quality and greater diagnostic value.

brain parenchyma were classified as diffusion-positive; those that did not were classified as diffusion-negative.^{2,8}

For the radiological assessment, both the RS-EPI and non-EPI sequences were reviewed for each ear to determine the presence or absence of CHO. A positive finding in at least one of the sequences led to a radiological conclusion of CHO presence; absence in both indicated no CHO (Figures 1, 2).

The maximum diameter of hyperintensity was measured in the coronal plane for both diffusion sequences. Additionally, using a region of interest (ROI) approach, the SI of the area showing the highest hyperintensity and the SI of the temporal cortex on the same side were measured. The size of the ROI varied depending on the lesion size, and signal measurements were not performed in cases without diagnostic hyperintensity.

Susceptibility artifact scores were assigned as follows: 0 for no artifact; 1 for artifacts at the skull base; 2 for artifacts below

the skull base; and 3 for artifacts interfering with diagnosis (Figures 1, 3). These scores were noted for both the RS-EPI and non-EPI DWI sequences and were included in the statistical analysis, considering the side (right or left) that underwent surgery.

Lesion T1W signal characteristics were categorized as either iso-hypointense or hyperintense relative to cerebral white matter. Post-contrast T1W enhancement of lesions was classified into four categories: no enhancement; peripheral enhancement; homogeneous enhancement; or heterogeneous enhancement.

Surgical and pathological confirmation

All patients included in the study underwent microscopic middle ear surgery, with histopathological results subsequently analyzed. For those diagnosed with CHO, the presence of the condition was confirmed both intraoperatively -indicated by the detection of keratinized squamous epitheli-

um and debris within the middle ear- and through histopathological examination. Conversely, the non-CHO group comprised patients for whom no CHO was detected during surgery, a finding supported by histopathology, which confirmed the diagnosis of COM.

Statistical analysis

The data analysis was conducted using SPSS version 26 (IBM Corp., Armonk, NY, USA). Continuous variables were summarized using the mean, standard deviation (SD), and median interquartile range. Categorical variables were presented as frequencies and percentages. The distribution of continuous variables was assessed through graphical methods, normality tests, and consideration of sample size to determine normalcy.

Comparisons between independent groups were made using both the Student's t-test and the Mann-Whitney U test, depending on the distribution of the data. The Wilcoxon signed ranks test was employed for related samples. The distribution of categorical variables across independent groups was analyzed using the chi-square test. Changes in related samples were assessed using the McNemar test and the McNemar-Bowker test.

The agreement between the observations of the two radiologists and the pathological results was quantified using kappa (κ) values. Diagnostic test values, such as sensitivity, specificity, positive predictive value, and negative predictive value, were calculated based on the radiologists' assessments and compared with the pathology results. For all statistical tests, the significance level for type I error was set at α : 0.05, and the tests were conducted as 2-tailed.

Results

In this study, we evaluated 154 patients, comprising 94 men and 60 women, with a mean age of 44.79 years (\pm SD of 16.78 years). Of these, 96 patients (62.3%) were allocated to the CHO group, whereas 58 patients (37.7%) were classified in the non-CHO group.

Reader A identified CHO in 86 out of 96 patients (89.5%) in the CHO group using both RS-EPI and non-EPI DWI sequences. Reader B detected CHO in 79 out of 96 patients (82.3%) with RS-EPI DWI and in 83 out of 96 patients (86.5%) with non-EPI DWI within the same group. In the non-CHO group, Reader A correctly identified 46 out of 58 patients (79.3%) as not having CHO using

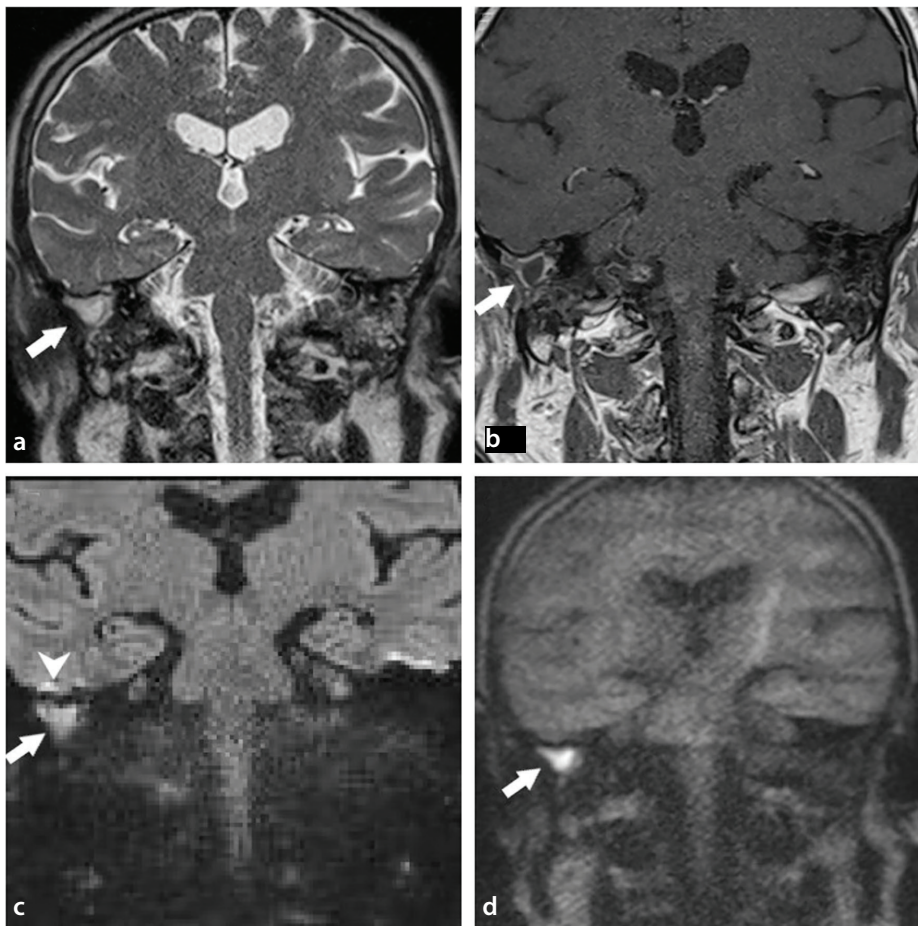


Figure 1. Cholesteatoma case confirmed intraoperatively and histopathologically. A hyperintense lesion (arrow) appears in the middle ear on the coronal T2-weighted image (a), with peripheral contrast enhancement (arrow) visible in the post-contrast T1-weighted coronal image (b). The lesion is also hyperintense (arrow) in readout-segmented (RS)-echo-planar imaging (EPI) (c) and non-EPI (d) diffusion-weighted images, which is typical for cholesteatoma. Additionally, a susceptibility artifact score of 1 (arrowhead indicating artifact at the skull base) is evident in RS-EPI (c).

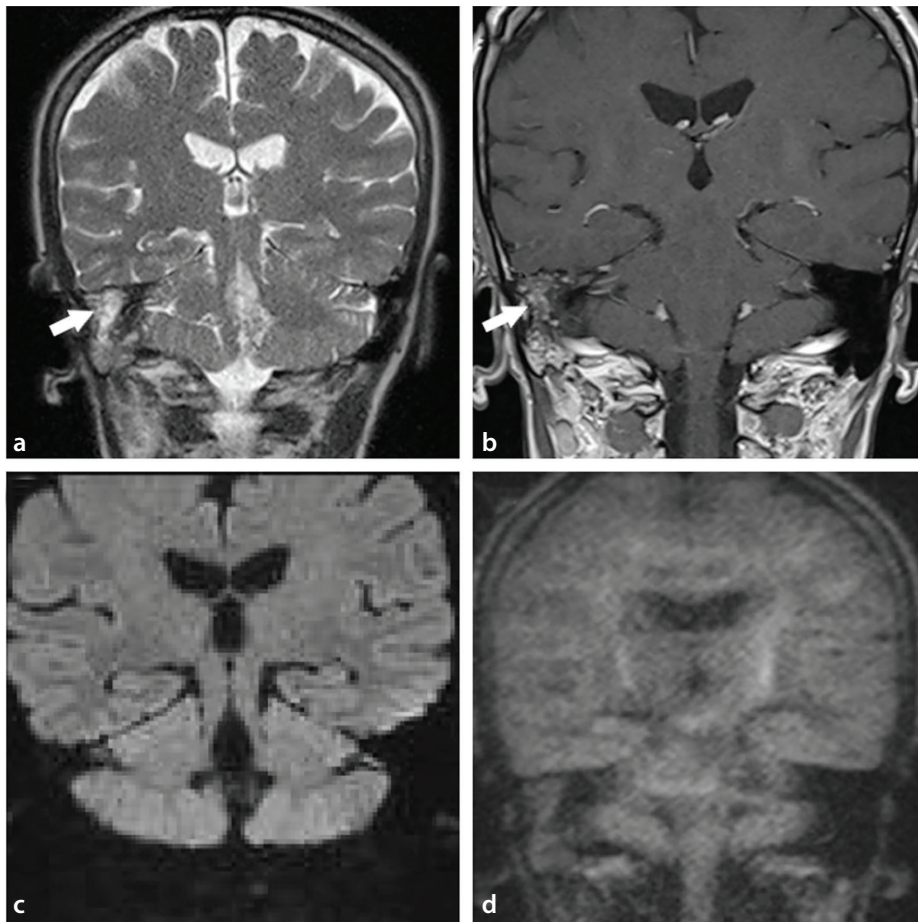


Figure 2. Intraoperatively and histopathologically confirmed case of chronic otitis media (non-cholesteatoma). In the coronal T2-weighted image (a), a hyperintense lesion (arrow) appears in the middle ear. The post-contrast T1-weighted coronal image (b) shows homogeneous contrast enhancement (arrow). The lesion, displaying no diffusion restriction in readout-segmented-echo-planar imaging (EPI) (c) and non-EPI diffusion-weighted images (d), is consistent with chronic otitis media.

RS-EPI DWI and 50 out of 58 patients (86.2%) using non-EPI DWI. Reader B's specificities in the non-CHO group were 84.5% with RS-EPI DWI (49 out of 58) and 89.7% with non-EPI DWI (52 out of 58).

Table 1 outlines the diagnostic accuracy of CHO detection by Readers A and B across both imaging sequences. Reader A had 10 false negative results in both RS-EPI and non-EPI sequences (10.4% of the CHO group), whereas Reader B recorded false negative results for 17 patients (17.7%) in RS-EPI and for 13 patients (13.5%) in non-EPI.

For false positives in the RS-EPI sequence, Reader A incorrectly diagnosed 12 out of 58 (20.7%) patients with non-CHO and 8 out of 58 (13.8%) in the non-EPI DWI sequence. Reader B identified false positives in 9 out of 58 patients (15.5%) in the RS-EPI DWI sequence and in 6 out of 58 (10.3%) in the non-EPI DWI sequence.

The RS-EPI DWI interobserver agreement coefficient was κ : 0.84 [95% confidence interval (CI): 0.75–0.92], indicating substantial

consistency between the readers. Similarly, the non-EPI DWI coefficient was κ : 0.91 (95% CI: 0.84–0.97), signifying a high level of agreement in their interpretations (Table 1).

Reader A measured a minimum CHO size of 2 mm using the RS-EPI DWI sequence and 2.5 mm with the non-EPI DWI sequence. Conversely, Reader B recorded minimum sizes of 2.2 mm for RS-EPI and 1.7 mm for non-EPI DWI sequences. The median values of the longest diameters measured by the readers are detailed in Table 2.

In the group of patients with CHO, Reader A observed the most common contrast enhancement pattern to be peripheral enhancement, occurring at a rate of 66/96 (68.8%); in the non-CHO group, the prevalent pattern was homogeneous enhancement at a rate of 33/58 (56.9%). Reader B reported peripheral enhancement in 73/96 (76.0%) and homogeneous enhancement in 29/58 (50.0%) of cases, respectively. Other contrast enhancement patterns were less frequently observed in both groups (Table 3).

In the analysis of RS-EPI DWI images from 154 patients, the mean \pm SD susceptibility artifact score was 1.18 ± 0.70 for Reader A and 1.04 ± 0.41 for Reader B. The mean susceptibility artifact score in non-EPI DWI images was recorded as 0.

Reader A and Reader B measured the SI ratio higher in lesions of the CHO group compared with lesions in the non-CHO group for both RS-EPI and non-EPI DWI sequences. SI measurements were conducted on lesions exhibiting diagnostic hyperintensity. In the non-CHO group, SI measurements consisted of lesions that the readers mistakenly classified as CHO, but histopathological results later confirmed as non-CHO (false positives). Furthermore, both readers noted that the SI ratio in non-EPI DWI images was higher than in RS-EPI DWI images, with measurements of 2.51 for Reader A and 2.46 for Reader B in the CHO group.

The cut-off value for detecting lesions in the CHO and non-CHO groups was determined by averaging the SI measurements of the two readers. In the RS-EPI sequence, the cut-off was >1.15 , providing 88.2% specificity, 50% sensitivity, an area under the curve (AUC) of 0.660 (95% CI: 0.547–0.761), and a *P* value of 0.216. For the non-EPI sequence, the cut-off was >1.98 , yielding 82.9% sensitivity, 100% specificity, an AUC of 0.901 (95% CI: 0.815–0.956), and a *P* value of <0.001 (Figure 4, Table 4).

The AUC superiority analysis between the RS-EPI and non-EPI sequences showed a difference of 0.241, favoring the non-EPI sequence (*P* = 0.042) (Table 4).

Discussion

In this study, high sensitivity and specificity were achieved with RS-EPI and non-EPI DWI sequences in detecting CHO, with both readers demonstrating consistent results (Table 1). There was a high level of agreement between the readers across both diffusion sequences.

Simultaneous evaluation of RS-EPI DWI and non-EPI DWI images led to enhanced sensitivity in detecting CHO for both readers. Reader A achieved a sensitivity of 91.7%, whereas Reader B reported a sensitivity of 88.5%. The specificity when evaluating RS-EPI alongside non-EPI DWI was comparable to that observed with RS-EPI DWI alone, although it was lower than that observed with non-EPI DWI for both readers (Table 1).

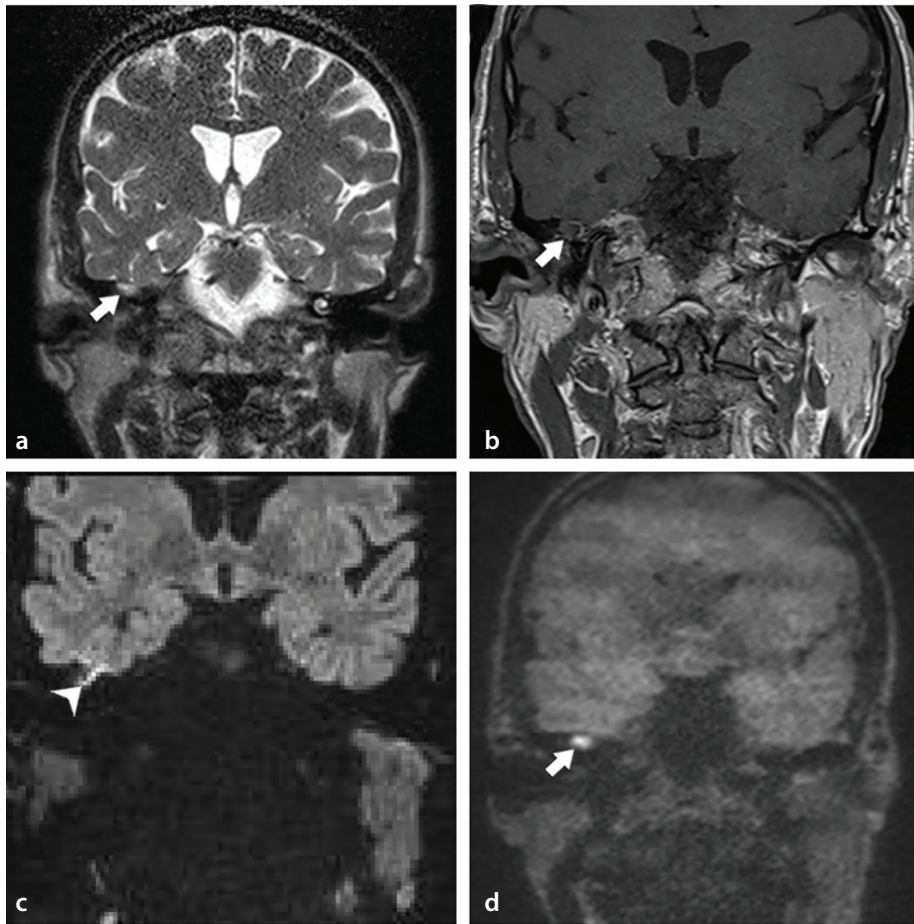


Figure 3. A false positive case in non-echo-planar imaging (EPI) diffusion-weighted imaging (DWI) confirmed histopathologically and intraoperatively as non-cholesteatoma. The lesion in the middle ear is hyperintense (arrow) on the T2-weighted coronal image (a) and exhibits peripheral contrast enhancement (arrow) on the post-contrast T1-weighted coronal image (b). In readout-segmented-EPI DWI (c), a susceptibility artifact score of 3 (artifact interfering with diagnosis) (arrowhead) is present. Despite appearing hyperintense (arrow) on the non-EPI diffusion-weighted image (d), the lesion has been surgically and histopathologically confirmed to be non-cholesteatoma (false positive).

Wiesmueller et al.⁹ study, which involved a smaller sample size ($n = 25$) and used the same device and similar DWI sequence parameters, yielded different results. For TSE DWI, their readers achieved sensitivities of 92% and 88%, respectively, and a specificity of 80% for both. In the case of RESOLVE DWI, the sensitivities were 76% and 68% for readers 1 and 2, respectively, with both readers showing a specificity of 60%. Their study reported an overall agreement of 97% ($\kappa: 0.9$) for TSE DWI and 87% ($\kappa: 0.7$) for RESOLVE DWI.

In our research, the slice thickness for RESOLVE DWI was 2.5 mm, whereas HASTE DWI had a slice thickness of 3 mm. In contrast, Wiesmueller et al.⁹ used a 3-mm slice thickness for both sequences. This difference in slice thickness, in addition to reader-dependent factors, may explain the lower sensitivity and specificity in their RESOLVE DWI compared with ours.

Benson et al.¹⁰ study involving 23 participants demonstrated high accuracy in HASTE images, correctly identifying CHO in all patients (100%). In contrast, with RS-EPI sequences, the results were 69.6% positive identifications, 21.7% equivocal, and 8.7% falsely negative. They also observed a substantial degree of interobserver agreement with κ values of 1.0 for HASTE and 0.9 for RS-EPI sequences, highlighting the consistency across readers.

In the present study, the matrix size of the RS-EPI DWI (160×104) was smaller than that of the non-EPI DWI (192×144). Additionally,

Table 1. Diagnostic performance and interobserver agreement of RS-EPI DWI and non-EPI DWI sequences in diagnosing cholesteatoma

	RS-EPI DWI		Non-EPI DWI		RS-EPI DWI with non-EPI DWI	
	Reader A	Reader B	Reader A	Reader B	Reader A	Reader B
True positive	86/96 (89.6%)	79/96 (82.3%)	86/96 (89.6%)	83/96 (86.5%)	88/96 (91.7%)	85/96 (87.5%)
True negative	46/58 (79.3%)	49/58 (84.5%)	50/58 (86.2%)	52/58 (89.7%)	46/58 (79.3%)	49/58 (84.5%)
False positive	12/58 (20.7%)	9/58 (15.5%)	8/58 (13.8%)	6/58 (10.3%)	12/58 (20.7%)	9/58 (15.5%)
False negative	10/96 (10.4%)	17/96 (17.7%)	10/96 (10.4%)	13/96 (13.5%)	8/96 (8.3%)	11/96 (12.5%)
Sensitivity (%)	89.6 (81.7–94.9)	82.3 (73.2–89.3)	89.6 (81.7–94.9)	86.5 (78–92.6)	91.7 (84.2–96.3)	88.5 (80.4–94.1)
Specificity (%)	79.3 (66.7–88.8)	84.5 (72.6–92.7)	86.2 (74.6–93.7)	89.7 (78.8–96.1)	79.3 (66.7–88.8)	84.5 (72.6–92.7)
LR (+)	4.3 (2.6–7.2)	5.30 (2.9–9.7)	6.5 (3.4–12.4)	8.36 (3.9–17.9)	4.4 (2.7–7.4)	5.7 (3.1–10.5)
LR (-)	0.1 (0.1–0.2)	0.21 (0.1–0.3)	0.1 (0.1–0.2)	0.15 (0.1–0.3)	0.1 (0.1–0.2)	0.1 (0.1–0.2)
Disease pre. (%)	62.3 (54.2–70)	62.3 (54.2–70)	62.3 (54.2–70)	62.34 (54.2–70)	62.3 (54.2–70)	62.3 (54.2–70)
PPV (%)	87.8 (81.2–92.3)	89.8 (82.7–94.2)	91.5 (84.9–95.4)	93.3 (86.6–96.7)	88 (81.5–92.4)	90.4 (83.8–94.5)
NPV (%)	82.1 (71.6–89.4)	74.2 (64.9–81.8)	83.3 (73.4–90.1)	80 (70.5–87)	85.2 (74.5–91.9)	80.7 (71.7–88.7)
Accuracy (%)	85.7 (79.2–90.8)	83.1 (76.3–88.7)	88.3 (82.2–92.9)	87.7 (81.4–92.4)	87 (80.7–91.9)	87 (80.7–91.9)
Interobserver agreement (κ) (95% CI)	0.84 (0.75–0.93)		0.91 (0.84–0.97)		0.89 (0.81–0.96)	

LR (+), positive likelihood ratio; LR (-), negative likelihood ratio; PPV, positive predictive value; NPV, negative predictive value; κ : Cohen's kappa coefficient; CI, confidence interval; RS-EPI, readout-segmented echo-planar imaging; DWI, diffusion-weighted imaging; non-EPI: non-echo-planar imaging.

Table 2. Quantitative analysis of lesion characteristics in histopathologically confirmed cholesteatoma and non-cholesteatoma groups by Readers A and B

	Reader A					Reader B				
	CHO (Histo)		Non-CHO (Histo)		<i>P</i> *	CHO (Histo)		Non-CHO (Histo)		<i>P</i> *
	N	Median (IQR)	N	Median (IQR)		N	Median (IQR)	N	Median (IQR)	
RS-EPI DWI size longest diameter (mm)	86	9.40 (6.30–13.90)	12	9.80 (5.15–11.95)	0.637	79	7.70 (5.00–13.40)	9	6.00 (5.10–9.20)	0.320
RS-EPI DWI SI mean	86	482 (342–571)	12	280 (232–369)	0.003	79	411 (307–503)	9	272 (225–373)	0.026
RS-EPI DWI temporal cortex SI	86	271 (238–298)	12	251 (234–274)	0.293	79	258 (228–281)	9	225 (196–248)	0.097
RS-EPI DWI SI ratio	86	1.66 (1.33–2.33)	12	1.11 (0.91–1.39)	0.003	79	1.56 (1.31–1.88)	9	1.21 (1.09–1.83)	0.116
Non-EPI size longest diameter (mm)	86	10.35 (7.00–14.20)	8	7.15 (5.40–9.45)	0.063	83	8.20 (5.60–12.00)	6	6.60 (5.50–7.70)	0.266
Non-EPI DWI SI mean	86	201 (155–265)	8	134.50 (92.50–161.50)	0.002	83	189 (144–246)	6	157 (114–179)	0.060
Non-EPI DWI temporal cortex SI	86	81 (74–93)	8	86.5 (77–96)	0.420	83	79 (70–89)	6	89.5 (84–94)	0.185
Non-EPI DWI SI ratio	86	2.51 (1.94–3.06)	8	1.49 (1.19–1.80)	<0.001	83	2.46 (1.92–3.15)	6	1.88 (1.61–2.01)	0.026

*Mann–Whitney test. CHO, cholesteatoma; non-CHO, non-cholesteatoma; RS-EPI, readout-segmented echo-planar imaging; DWI, diffusion-weighted imaging; non-EPI, non-echo-planar imaging; SI, signal intensity; IQR, interquartile range.

Table 3. Comparative lesion characteristics in histopathologically confirmed cholesteatoma and non-cholesteatoma groups by Readers A and B

	Reader A				Reader B			
	Histopathological			<i>P</i> *	Histopathological			<i>P</i> *
	CHO N (%)	Non-CHO N (%)			CHO N (%)	Non-CHO N (%)		
T1-weighted signal	Hypointense or isointense	88 (91.7%)	49 (84.5%)	0.266	90 (93.8%)	47 (81.0%)	0.030	
	Hyperintense	8 (8.3%)	9 (15.5%)		6 (6.3%)	11 (19.0%)		
Contrast enhancement	No contrast enhancement	2 (2.1%)	0 (0.0%)	NA	15 (15.6%)	3 (5.2%)	<0.001	
	Peripheral	66 (68.8%)	12 (20.7%)		73 (76.0%)	15 (25.9%)		
	Homogeneous	14 (14.6%)	33 (56.9%)		7 (7.3%)	29 (50.0%)		
	Heterogeneous	14 (14.6%)	13 (22.4%)		1 (1.0%)	11 (19.0%)		
Location	Middle ear	33 (34.4%)	7 (12.1%)	NA	45 (46.8%)	10 (17.2%)	NA	
	Mastoid antrum	3 (3.1%)	1 (1.7%)		2 (2.1%)	4 (6.9%)		
	Both of two	56 (58.3%)	48 (82.8%)		45 (46.9%)	42 (72.4%)		
	Middle ear and EAC	4 (4.2%)	2 (3.4%)		4 (4.2%)	2 (3.4%)		
RS-EPI susceptibility artifact scores	No artifact	14 (14.6%)	4 (6.9%)	NA	3 (3.1%)	6 (10.3%)	NA	
	Artifact at the skull base	55 (57.3%)	44 (75.9%)		85 (88.5%)	46 (79.3%)		
	Artifact below the skull base	19 (19.8%)	10 (17.2%)		7 (7.3%)	6 (10.3%)		
	Artifact interfering with diagnosis	8 (8.3%)	0 (0.0%)		1 (1.0%)	0 (0.0%)		
Non-EPI susceptibility artifact scores	No artifact	96 (100%)	58 (100%)	NA	96 (100%)	58 (100%)	NA	

*Chi-square tests. CHO, cholesteatoma; non-CHO, non-cholesteatoma; RS-EPI, readout-segmented echo-planar imaging; non-EPI, non-echo-planar imaging; EAC, external acoustic canal.

the slice thickness for our RS-EPI DWI sequence (2.5 mm) was less than that for the non-EPI DWI (3 mm). Generally, increasing the matrix size improves resolution but may reduce the SNR. Conversely, a thicker slice increases SNR but may compromise resolution.¹¹ Although the RS-EPI DWI sequence had a smaller matrix size and slice thickness compared with the non-EPI DWI, the resolution was still lower. De-

spite this, the smaller slice thickness can facilitate better image evaluation.

Fischer et al.'s¹² study, involving 50 patients, found that the sensitivity of RESOLVE DWI in detecting CHO was similar to our results but exhibited higher specificity. They reported an accuracy of 92%, with a sensitivity of 88% and a specificity of 96%.

In light of these findings, non-EPI DWI remains the most effective diffusion sequence for detecting CHO. However, with its shorter imaging times, RS-EPI DWI also proves to be a viable option, boasting high sensitivity and specificity. Reducing the slice thickness, if feasible, may further enhance diagnostic accuracy.

Table 4. Determining signal intensity ratio cut-offs for hyperintense lesions in RS-EPI DWI and non-EPI DWI in cholesteatoma diagnosis

	Signal intensity ratio (reader mean)		
	RS-EPI DWI	Non-EPI DWI	Difference between areas
AUC (95% CI)	0.660 (0.547 to 0.761)	0.901 (0.815 to 0.956)	0.241(0.009–0.474)
<i>p</i>	0.216a	<0.001 ^a	0.042
<i>J</i> _{Youden index}	0.382	0.829 ^a	-
Cut-off value for cholesteatoma	>1.15	>1.98	
True positive	67/76 (88.2%)	63/76 82.9%	
True negative	3/6 (50%)	6/6 (100%)	
False positive	3/6 (50%)	0/6 (0.0%)	
False negative	9/76 (11.8%)	13/76 (17.1%)	
Sensitivity (%)	88.2 (78.7–94.4)	82.9 (72.5–90.6)	
Specificity (%)	50 (11.8–88.2)	100 (54.1–100)	
LR (+)	1.8 (0.8– 3.9)	-	
LR (-)	0.2 (0.1–0.7)	0.2 (0.1– 0.3)	
Disease pre. (%)	92.7 (84.8–97.3)	92.68 (84.8–97.3)	
PPV (%)	95.7 (90.9–98.0)	100	
NPV (%)	25 (10.8–47.7)	31.6 (22–43.1)	
Accuracy (%)	85.4 (75.8–92.2)	84.2 (74.4–91.3)	

^a*p* (area: 0.5). LR (+), positive likelihood ratio; LR (-), negative likelihood ratio; PPV, positive predictive value; NPV, negative predictive value; AUC: area under curve; RS-EPI, readout-segmented echo-planar; DWI, diffusion-weighted imaging; non-EPI, non-echo-planar imaging.

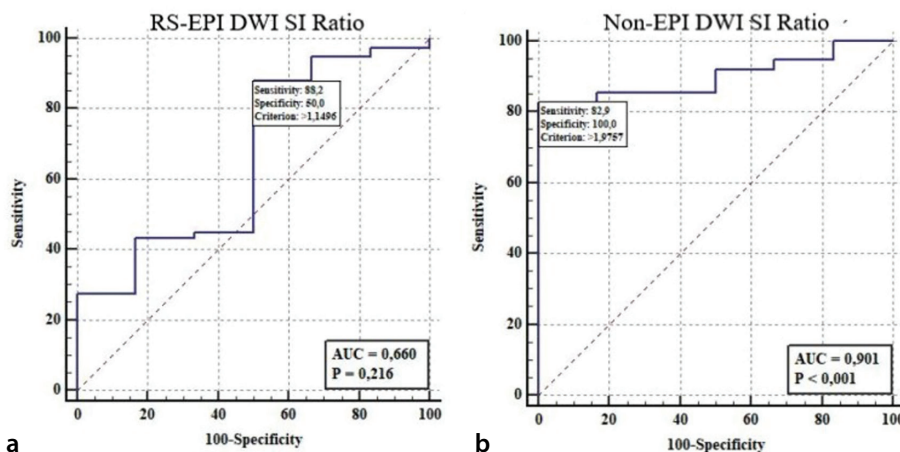


Figure 4. Receiver operating characteristic analysis of signal intensity ratio cut-off in cholesteatoma diagnosis using readout-segmented-echo-planar imaging (EPI) diffusion-weighted imaging (DWI) (a) and non-EPI DWI (b).

In the present study, 6 patients exhibited false positives in both RS-EPI and non-EPI DWI images. The histopathological results revealed “granulation tissue with foreign body giant cells” in 1 patient; “polypoid granulation tissue with chronic pyogenic infection” in another; “inflammatory pseudopolyp and granulation tissue” in 2 patients; and “chronic inflammatory granulation tissue” in 2 other patients. Additionally, other cases of false positives in either RS-EPI or non-EPI DWI im-

ages were diagnosed with “chronic inflammatory granulation tissue.”

The literature identifies several entities as potential sources of false positives, including cholesterol granuloma,¹³ earwax,¹⁴ abscesses,¹⁵ ceruminous adenomas,¹⁶ and bone grafts.¹⁷

The literature reveals varying rates of false positives in CHO detection using DWI MRI. A study by Muhonen et al.¹⁸ showed that out

of 27 patients who underwent second-look surgery after detecting increased SI on non-EPI DWI, two cases (7.4%) were identified as false positives. Another study by Semiz-Oysu et al.¹⁹, which involved 112 ears, reported five cases (4.5%) as false positives.

Reducing the false positive rate could minimize unnecessary surgical interventions and reduce the frequency of second-look surgeries. In the present study, we conducted SI measurements on two DWI sequences to differentiate between false positives and true positive cases, establishing a cut-off value in non-EPI DWI. The literature on this subject is sparse. Özgen et al.²⁰ established an SI ratio cut-off of 0.9 in TSE-DWI images, achieving 100% sensitivity and specificity in distinguishing between CHO and non-CHO in 57 patients. In contrast, our investigation focused solely on lesions identified with hyperintensity on DWI, and we established a cut-off value to discern the more challenging cases of true positives and false positives. Consequently, a substantially higher cut-off value was identified in our study.

Specifically, in the present study, when the SI ratio in the non-EPI DWI sequence exceeded the established cut-off value of 1.98, the consideration of CHO was supported by high sensitivity and specificity. The reported values are as follows: sensitivity 82.9% and specificity 100%. The RS-EPI DWI sequence demonstrated a cut-off value with lower sensitivity and specificity, reporting a sensitivity of 88.2% and a specificity of 50% (Table 4). To the best of our knowledge, no existing study has measured SI in both diffusion sequences and established cut-off values. Further research in this area is warranted, and our findings could pave the way for future investigations.

Dudau et al.²¹ reported an average artifact score of 0.73 for RS-EPI (range: 0–3), assessing all 426 scored entries. They also found an average artifact score of 0 for non-EPI DWI, aligning with our results. The increased susceptibility artifact in RS-EPI DWI, compared with non-EPI DWI, may contribute to a higher incidence of false-negative results in RS-EPI DWI for Reader B. By implementing measures to reduce susceptibility artifacts, we can enhance both the utilization and diagnostic performance of the RS-EPI DWI technique.

It is widely acknowledged that non-EPI techniques exhibit fewer susceptibility artifacts at the skull base compared with EPI techniques.²² However, in the present study, when examining the artifact score distribu-

tion in RS-EPI DWI, Reader A reported “artifact interfering with diagnosis” in 8 images (5.2%), whereas Reader B reported it in only 1 image (0.65%) (Table 3). This suggests that while RS-EPI DWI may present more artifacts compared with non-EPI DWI, these do not substantially affect the diagnosis.

This study has certain limitations. First, it was conducted retrospectively, which may have influenced the outcomes. Additionally, there were differences in slice thickness between RS-EPI DWI and non-EPI DWI. The measurement of SI was performed manually using a ROI. Despite efforts to minimize bias through the involvement of two readers and averaging their measurements for the cut-off assessment, acknowledging the potential limitations due to individual practitioner variability remains important.

To validate and expand upon the findings of this research, conducting prospective studies with a larger sample size is recommended. Increasing the number of studies that thoroughly evaluate SI measurements will contribute to a more nuanced understanding of DWI in the diagnosis of CHO. Future research should prioritize efforts to mitigate susceptibility artifacts in RS-EPI DWI acquisition while maintaining an optimal acquisition time.

In conclusion, our research suggests that both non-EPI and RS-EPI DWI sequences effectively detect CHO with notable sensitivity and specificity when used individually. While RS-EPI DWI does not serve as a substitute for non-EPI DWI, integrating both sequences may enhance overall sensitivity. The assessment of SI in DWI appears to be beneficial for diagnosing CHO. Moreover, establishing an SI ratio cut-off value seems to reliably differentiate between CHO and non-CHO with high precision. Finally, RS-EPI DWI demonstrated minimal susceptibility artifacts, which did not substantially affect the diagnostic accuracy.

Conflict of interest disclosure

The authors declared no conflicts of interest.

References

- Schürmann M, Goon P, Sudhoff H. Review of potential medical treatments for middle ear cholesteatoma. *Cell Commun Signal.* 2022;20(1):148. [\[CrossRef\]](#)
- Henninger B, Kremser C. Diffusion weighted imaging for the detection and evaluation of cholesteatoma. *World J Radiol.* 2017;9(5):217-222. [\[CrossRef\]](#)
- Bammer R. Basic principles of diffusion-weighted imaging. *Eur J Radiol.* 2003;45(3):169-184. [\[CrossRef\]](#)
- Vercruyse JP, De Foer B, Pouillon M, Somers T, Casselman J, Offeciers E. The value of diffusion-weighted MR imaging in the diagnosis of primary acquired and residual cholesteatoma: a surgical verified study of 100 patients. *Eur Radiol.* 2006;16(7):1461-1467. [\[CrossRef\]](#)
- Fischer N, Plaikner M, Schartinger VH, et al. MRI of middle ear cholesteatoma: the importance of observer reliance from diffusion sequences. *J Neuroimaging.* 2022;32(1):120-126. [\[CrossRef\]](#)
- Schwartz KM, Lane JI, Bolster BD Jr, Neff BA. The utility of diffusion-weighted imaging for cholesteatoma evaluation. *AJNR Am J Neuroradiol.* 2011;32(3):430-436. [\[CrossRef\]](#)
- Muzaffar J, Metcalfe C, Colley S, Coulson C. Diffusion-weighted magnetic resonance imaging for residual and recurrent cholesteatoma: a systematic review and meta-analysis. *Clin Otolaryngol.* 2017;42(3):536-543. [\[CrossRef\]](#)
- Moustin D, Veillon F, Karch-Georges A, et al. Importance of signal intensity on T1-weighted spin-echo sequence for the diagnosis of chronic cholesteatomatous otitis. *Eur Arch Otorhinolaryngol.* 2020;277(6):1601-1608. [\[CrossRef\]](#)
- Wiesmueller M, Wuest W, May MS, et al. Comparison of readout-segmented echo-planar imaging and single-shot TSE DWI for cholesteatoma diagnostics. *AJNR Am J Neuroradiol.* 2021;42(7):1305-1312. [\[CrossRef\]](#)
- Benson JC, Carlson ML, Lane JI. Non-EPI versus multishot EPI DWI in cholesteatoma detection: Correlation with operative findings. *Am J Neuroradiol.* 2021;42(3):573-577. [\[CrossRef\]](#)
- McRobbie DW, Moore EA, Graves MJ, Prince MR. MRI from picture to proton. *MRI from Pict to Prot.* Published online January 1, 2006:1-397. [\[CrossRef\]](#)
- Fischer N, Schartinger VH, Dejaco D, et al. Readout-segmented echo-planar DWI for the detection of cholesteatomas: correlation with surgical validation. *AJNR Am J Neuroradiol.* 2019;40(6):1055. [\[CrossRef\]](#)
- Fukuda A, Morita S, Harada T, et al. Value of T1-weighted magnetic resonance imaging in cholesteatoma detection. *Otol Neurotol.* 2017;38(10):1440-1444. [\[CrossRef\]](#)
- Zaman SU, Rangankar VP, Krishnarjun M, et al. Readout-segmented echo-planar (RESOLVE) diffusion-weighted imaging on 3T MRI in detection of cholesteatoma-our experience. *Indian J Radiol Imaging.* 2023;34(1):16-24. [\[CrossRef\]](#)
- Profant M, Sláviková K, Kabátová Z, Slezák P, Waculiková I. Predictive validity of MRI in detecting and following cholesteatoma. *Eur Arch Oto-Rhino-Laryngology.* 2012;269(3):757-765. [\[CrossRef\]](#)
- Esmaili AA, Hasan Z, Withers SJ, Kuthubutheen J. A retrospective cohort study on false positive diffusion weighted MRI in the detection of cholesteatoma. *Aust J Otolaryngol.* 2021;4:18. [\[CrossRef\]](#)
- Osman NM, Rahman AA, Ali MT. The accuracy and sensitivity of diffusion-weighted magnetic resonance imaging with apparent diffusion coefficients in diagnosis of recurrent cholesteatoma. *Eur J Radiol Open.* 2017;4:27. [\[CrossRef\]](#)
- Muhonen EG, Mahboubi H, Moshtaghi O, et al. False-Positive cholesteatomas on non-echo-planar diffusion-weighted magnetic resonance imaging. *Otol Neurotol.* 2020;41(5):588-592. [\[CrossRef\]](#)
- Semiz-Oysu A, Oysu C, Kulali F, Bukte Y. PROPELLER diffusion weighted imaging for diagnosis of cholesteatoma in comparison with surgical and histopathological results: emphasis on false positivity and false negativity. *Eur Arch Otorhinolaryngol.* 2023;280(11):4845-4850. [\[CrossRef\]](#)
- Özgen B, Bulut E, Dolgun A, Bajin MD, Sennaroğlu L. Accuracy of turbo spin-echo diffusion-weighted imaging signal intensity measurements for the diagnosis of cholesteatoma. *Diagn Interv Radiol.* 2017;23(4):300-306. [\[CrossRef\]](#)
- Dudau C, Draper A, Gkagkanasiou M, Charles-Edwards G, Pai I, Connor S. Cholesteatoma: multishot echo-planar vs non echo-planar diffusion-weighted MRI for the prediction of middle ear and mastoid cholesteatoma. *BJR|Open.* 2019;1(1):20180015. [\[CrossRef\]](#)
- De Foer B, Vercruyse JP, Bernaerts A, et al. Detection of postoperative residual cholesteatoma with non-echo-planar diffusion-weighted magnetic resonance imaging. *Otol Neurotol.* 2008;29(4):513-517. [\[CrossRef\]](#)



Challenges associated with percutaneous nephrostomy in infants

Iraklis-Georgios Kagias^{1*}
 Panagiotis Nikolinakos^{2*}
 Chloe Mortensen³
 Joseph M. Norris^{2,4}

¹University Hospitals Sussex NHS Foundation Trust,
Department of Neurosurgery, Brighton, United
Kingdom

²West Middlesex University Hospital, Chelsea
& Westminster Hospital NHS Foundation Trust,
Department of Urology, London, United Kingdom

³University Hospitals Sussex NHS Foundation Trust,
Department of Interventional Radiology, Brighton,
United Kingdom

⁴University College London, UCL Division of Surgery
& Interventional Science, London, United Kingdom

KEYWORDS

Image-guided, interventional radiology, pe-
diatric urology, percutaneous nephrostomy,
radiology

*These authors are joint first authors.

Corresponding author: Iraklis-Georgios Kagias

E-mail: iraklis.kagias96@gmail.com

Received 18 September 2023; accepted 14 October 2023.



Epub: 06.11.2023

Publication date: 06.11.2024

DOI: 10.4274/dir.2023.232507

Dear Editor,

We read with great interest and commend Taydaş et al.¹ for their detailed description of their experience with percutaneous nephrostomies (PCN) in neonates and infants (<1 year of age). The authors have contributed to the literature by examining the feasibility, safety, and efficacy of imaging-guided PCN in infants over a period of 20 years. Taydaş et al.¹ reported a 100% technical success and low major complication rates. In this single-center trial, 75 infants underwent PCN for various underlying pathologies, such as ureteropelvic junction obstruction, ureterovesical junction obstruction and others. We would like to raise questions regarding the specifics of this trial to potentially enhance the interpretation and further applicability of its results.

First, both fluoroscopic and sonographic guidance were implemented for the nephrostomy insertions. Reports on the radiation dose information are of great interest for any interventional radiology procedure, such as a PCN, especially given the very young age of this cohort and the ramifications it can have later in life. We believe that this would have enriched the current study, as the authors already recognise.² As with all trials of procedural techniques, patient safety is paramount and should take precedence.

Second, Taydaş et al.¹ found a low occurrence of major complications and no perioperative/postoperative sepsis, hemorrhage, or vascular/bowel injury. The number of patients in this single-center trial is low (n = 75), and reporting the outcomes of a larger cohort might be beneficial to drawing more concrete conclusions associated with a higher statistical power. Cyphers et al.³ reported a 2.3% incidence of urosepsis and a 18.6% incidence of urinary tract infections in 46 cases; hence, they concluded that infection constitutes a challenge of PCN placement in infants and neonates.

Third, some key details needed to fully evaluate this study are missing, including the specific timeframe of the conducted follow-up. Taydaş et al.¹ assessed serum creatinine levels and the presence of hydronephrosis at 3-month intervals. However, the total duration of the follow-up has been omitted. In addition, as far as the underlying pathology necessitating PCN is concerned, the authors reported the outcomes, along with the clinical and laboratory findings, of a quite heterogenous cohort. Hence, given the variability in underlying pathologies (e.g., ureteropelvic junction obstruction, ureterovesical junction obstruction, and vesicoureteral reflux), examining and reporting the long-term outcomes might be more beneficial to drawing conclusions regarding the safety and efficacy of PCN in infants.

Fourth, the experience of the operators has not been included in the paper. This constitutes a key detail that would allow for a complete appraisal of their technical success and a low prevalence of complications. Lee et al.⁴ demonstrated that the operator's level of experience can influence the occurrence of complications.

We would like to congratulate Taydaş et al.¹ for contributing to the literature, expounding their methodology and evaluating PCN in infants. However, we believe their findings should be interpreted cautiously considering the issues highlighted here.¹ We welcome Taydaş et al.'s¹ next work and eagerly await the results of further research on this very interesting topic.

Conflict of interest disclosure

The authors declared no conflicts of interest.

Funding

Joseph M. Norris has received funding from the MRC (UK) and RCSEng for his PhD.

References

1. Taydaş O, Ünal E, Akıncı D, et al. Percutaneous nephrostomy in infants: a 20-year single-center experience. *Diagn Interv Radiol*. 2023. [\[CrossRef\]](#)
2. Kutanzi KR, Lumen A, Koturbash I, Miousse IR. Pediatric exposures to ionizing radiation: carcinogenic considerations. *Int J Environ Res Public Health*. 2016;13(11):1057. [\[CrossRef\]](#)
3. Cyphers E, Gaballah M, Acord M, et al. Percutaneous nephrostomy in neonates and young infants. *J Vasc Interv Radiol*. 2023;34(10):1815-1821. [\[CrossRef\]](#)
4. Lee WJ, Mond DJ, Patel M, Pillari GP. Emergency percutaneous nephrostomy: technical success based on level of operator experience. *J Vasc Interv Radiol*. 1994;5(2):327-330. [\[CrossRef\]](#)



Pre-procedure ¹⁸F-FDG PET/CT imaging improves the performance of CT-guided transthoracic biopsy

Ai-Fang Jin^{1*}
 Zhe-Huang Luo^{1*}
 Wan-Ling Qi¹
 Qian Liu²

¹The First Affiliated Hospital of Nanchang Medical College, Jiangxi Provincial People's Hospital, PET/CT Center, Department of Nuclear Medicine, Nanchang, China

²The First Affiliated Hospital of Nanchang Medical College, Jiangxi Provincial People's Hospital, Department of Pathology, Nanchang, China

PURPOSE

To compare computed tomography (CT)-guided transthoracic lung biopsies (CTLB) with and without pre-procedure ¹⁸F-fluorodeoxyglucose positron emission tomography (¹⁸F-FDG PET)/CT images in the diagnosis of pulmonary nodules/masses.

METHODS

This is a case-control study in a single center. The data of patients with a transthoracic lung biopsy guided by CT and pre-procedure ¹⁸F-FDG PET/CT (group 2, here called the "PETCTLB" group), including demographics, clinical characteristics, and biopsy-related parameters, were collected. The PET/CT scan was performed within 15 days before the biopsy. The data from patients with CTLB were used as controls (group 1). Biopsies for all patients were performed by the same physician between January 2019 and December 2021. The final diagnosis was based on surgical outcomes, or imaging findings, and the results of at least one 6-month follow-up. The demographics and clinical characteristics of patients, lesions and biopsy-related variables, diagnostic yields, and incidence of complications were compared between the two groups. Two-tailed t-tests were used to compare the mean values in the two independent groups, while categorical variables were compared using the Pearson chi-squared test, and *P* values < 0.05 were considered to be significant.

RESULTS

A total of 84 patients were included, and 84 biopsies of 84 lung nodules/masses were analyzed. The demographics and clinical characteristics of group 2 (*n* = 39; 21 men; mean age, 63.2 ± 9.29 years) and group 1 (*n* = 45; 30 men; mean age, 61.2 ± 12.3 years) had no significant difference (*P* = 0.230 and 0.397, respectively). The procedure duration (11.1 ± 3.0 vs. 12.9 ± 3.3 minutes, *P* = 0.008), the number of samples (2.6 ± 0.5 vs. 3.1 ± 0.4, *P* < 0.001), diagnostic accuracy (97.4% vs. 82.2%, *P* = 0.033), and bleeding complication (25.6% vs. 42.2%, *P* = 0.034) of group 2 and group 1 were statistically different.

CONCLUSION

A biopsy guided by CT plus pre-procedure ¹⁸F-FDG PET/CT (PETCTLB) is a safe procedure that can provide a precise diagnosis in the majority of lung nodules/masses. It has better diagnostic performance than CTLB.

KEYWORDS

¹⁸F-FDG PET/CT, CT-guided transthoracic biopsy, lung, nodule, mass

*Joint first authors

Corresponding author: Zhe-Huang Luo

E-mail: lzh6392@sina.com

Received 08 July 2023; revision requested 09 September 2023; last revision received 30 November 2023; accepted 11 December 2023.



Epub: 31.01.2024

Publication date: 06.11.2024

DOI: 10.4274/dir.2023.232364

Lung cancer is currently the leading cancer in incidence and cancer-related mortality worldwide,¹ and tumor screening is an important approach to its early diagnosis and management.² Lung nodules/masses are frequent findings on radiography and/or computed tomography (CT) scans. With the gradual promotion and popularization of low-dose CT as a device for lung cancer screening, a large number of suspicious lung nodules/masses are being discovered. The biggest challenge in the management of suspected lung nodules/masses is the need to distinguish malignant and benign occurrences, as malignant lesions are treated using a completely different strategy when compared with benign lesions.

You may cite this article as: Jin AF, Luo ZH, Qi WL, Liu Q. Pre-procedure ¹⁸F-FDG PET/CT imaging improves the performance of CT-guided transthoracic biopsy. *Diagn Interv Radiol.* 2024;30(6):380-384.

Common methods for clinical diagnosis of malignant lung nodules/mass include the detection of serum biomarkers (DSB), exfoliative sputum cytological analysis (ESC), chest imaging, fiberoptic bronchoscopy examination (FBE), and transthoracic lung biopsy.³ Tumor cells can be found only in a small number of patients with lung cancer using ESC;⁴ the application of FBE (including endobronchial ultrasound-guided transbronchial needle aspiration) is restricted by its limited scope;⁵ DSB and imaging fail to obtain histological and cytological evidence in the diagnosis. A computed tomography-guided transthoracic lung biopsy (CTLB) is a minimally invasive procedure and widely implemented for the histologic analysis of suspected lung lesions, but may be inconclusive. Strategies that improve CTLB performance are required. Both CTLB and ¹⁸F-fluorodeoxyglucose positron emission tomography (¹⁸F-FDG PET)/CT are conducted routinely in patients with suspected pulmonary nodules/masses for diagnosis and staging. ¹⁸F-FDG PET/CT metabolic information about lung lesions, and several studies have explored its use in lung biopsies.^{6,7} In the present study, we aim to evaluate the performance of CTLB without and with pre-procedure ¹⁸F-FDG-PET/CT images [i.e., a transthoracic lung biopsy by CT plus pre-procedure ¹⁸F-FDG PET/CT (PETCTLB)].

Methods

This is a retrospective case-control study in a single center concerning the period between January 2019 and December 2021. The Research Ethics Committee of the Institutional Ethics Committee of Jiangxi Provincial People's Hospital (the First Affiliated Hospital of Nanchang Medical College) has confirmed that no ethical approval is required. Individ-

ual consent for this retrospective study was exempted.

Inclusion and exclusion criteria

All patients were considered for a biopsy due to pulmonary nodules. All enrolled patients had signed written informed consent forms for the biopsy and had undergone a routine blood test, coagulation function test, renal and hepatic function test, and electrocardiogram before the biopsy. The inclusion criteria of the PETCTLB patients were as follows: PET/CT imaging was performed within 15 days before the biopsy; no suspicious distant metastases were found on the PET/CT images; the lesion had high metabolic activity (the FDG uptake in the lesion was higher than that in the liver); all biopsies were performed by the same physician and guided by the same PET/CT scanner. The exclusion criteria were as follows: patients with preoperative pneumothorax or hemothorax; patients with obstructive emphysema before the biopsy; patients with incomplete medical records, including follow-up data. The inclusion criteria of the patients undergoing CTLB were as follows: as the control group, the CTLB was performed on the same days on which PETCTLB was performed; the CTLB was performed by the same practitioner who performed the PETCTLB. The exclusion criteria were the same as the PETCTLB exclusion criteria. The patients with CTLB and PETCTLB each formed a consecutive series.

The histological specimens were reviewed, and the pathological diagnoses of the histologic grades and types were confirmed by a pathologist.

The patients who had undergone CTLB were assigned to group 1 (the control group), and the patients who had undergone PETCT-

LB were assigned to group 2 (the study group).

Computed tomography-guided transthoracic lung biopsy

A CTLB is a commonly performed and minimally invasive diagnostic procedure for pulmonary nodules and masses.

Group 1: all relevant laboratory examinations and imaging (not including ¹⁸F-FDG PET/CT) were performed before the biopsy to exclude patients with contraindications to transthoracic biopsy; the CT technician trained the patients to breath-hold to ensure that they could cooperate with the biopsy; the principles of the biopsy pathway selection were the minimum vertical distance, no big blood vessel on the pathway, and easy for the patient to cooperate. The entry site, depth, and inclination angle to direct the needle into the lesion were determined by initial low-dose CT localization scans (tube voltage 120 kV, tube current 80–100 mA, reconstruction thickness 5.0 mm. PET/CT scanner; GE Healthcare, USA, Discovery STE) with a gradient grid metallic marker fixed on the patient's body surface (Figure 1). The biopsy was performed using an 18-gauge × 160 mm co-axial core needle.

Computed tomography-guided transthoracic lung biopsy with pre-procedure ¹⁸F-FDG PET/CT

Group 2: all the patients underwent an ¹⁸F-FDG PET/CT examination. PET/CT imaging: all patients were instructed to fast for at least 6 hours before the ¹⁸F-FDG injection, and their blood glucose levels remained in a normal range. Each patient was injected via a venous line with an activity of mean 282 MBq (5.5 MBq/kg) ¹⁸F-FDG. The patient was rested

Main points

- Compared with a computed tomography (CT)-guided biopsy, a biopsy guided by CT plus pre-procedure ¹⁸F-fluorodeoxyglucose positron emission tomography (¹⁸F-FDG PET)/CT can offer better diagnostic performance.
- ¹⁸F-FDG PET/CT can distinguish between viable tumors and necrosis or fibrosis in residual masses.
- The complementary morphological and metabolic data (using 40% of maximum standardized uptake value as the threshold) can be relevant for defining biopsy targets.
- Marking the target of a percutaneous biopsy in the ¹⁸F-FDG PET/CT images before puncture biopsy can improve the success rate of a CT-guided puncture biopsy.

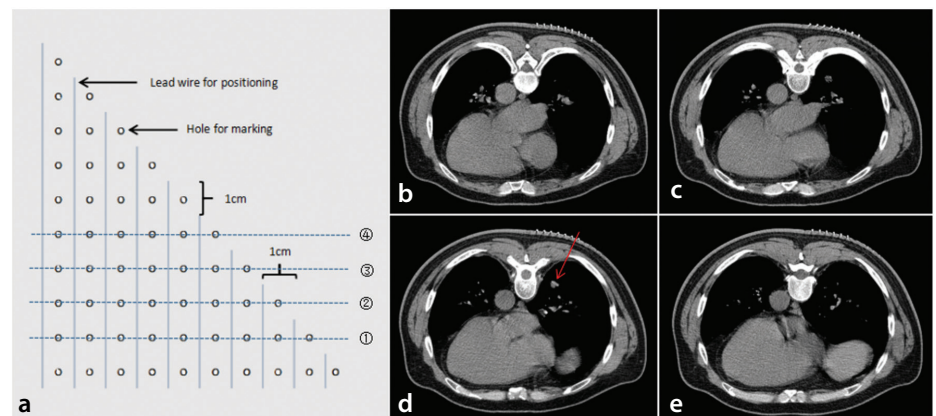


Figure 1. Schematic diagram of body surface gradient grid locating technique. The dashed lines ①–④ on the locator correspond to the slices (b–e), respectively, on the computed tomography (CT) scan. (a) Homemade body surface gradient grid locator; (b–e) CT localization slices; red arrow, indicating the biopsy path.

for a scheduled 45–60-minute uptake period, followed by image acquisition on a PET/CT scanner (Discovery STE; GE Healthcare, USA). No oral or intravenous contrast was administered. A CT scan from the vertex of the skull to the upper thigh, with the patient supine, was performed for PET attenuation correction and anatomical location. The CT parameters were as follows: 120 kV, automatic tube current, and CT reconstruction thickness of 3.75 mm. The PET data were acquired covering the same area in three-dimensional mode, the acquisition time per bed position was 2.5 or 3.0 minutes, with a total of 6–8 bed positions acquired. Two-dimensional PET images were reconstructed with a slice thickness of 3.75 mm using the ordered subset expectation maximization iterative image reconstruction method. Forty percent of the maximum standardized uptake value of the lesion was used as a threshold to delineate the target on axial, coronal, and sagittal fusion images (Figure 2); the optimal entry

sites and pathway were then determined according to the metabolic distribution and the shortest distance from the surface puncture site. The remaining procedures were the same as in group 1.

The depth of the needle was measured from the pleura to the edge of the intrapulmonary lesion along the needle path (Figure 3a).

After the biopsy was completed, a low-dose chest CT scan was performed to observe whether there were complications, such as pneumothorax or lung bleeding (Figure 3b), and corresponding treatment was carried out.

Biopsy results

(1) Definition of “diagnosis”: tumor cells (primary or metastatic), mycobacterium tuberculosis, and fungi were found; (2) definition of “possible diagnosis”: the pathological diagnosis of the specimen was non-specific inflammation or granuloma; (3) definition of

“biopsy failure”: no pathological tissues were observed, or only normal lung, diaphragm, and liver tissues were observed.

The final diagnosis was based on surgical outcomes or imaging findings and the results of a 6-month follow-up.

Follow-up

All patients were routinely followed up. The patients in this study were followed up for 6–28 months (mean: 12.8 ± 9.3 months). The follow-up methods included telephone or web chat ($n = 47$), outpatient examination ($n = 19$), and assessment of inpatient medical records ($n = 4$). Patients who did not have surgery ($n = 35$) were followed up for at least 6 months, during which at least one CT was performed. The follow-up time was calculated from the biopsy date to the last CT follow-up date of patients; the mean CT follow-up time was 6.2 months (range: 3–11 months). When the suspected lung nodules/masses were confirmed to be stable in size and features, or subsided on CT, it was considered to be truly benign.

Statistical analysis

The measurement data was described as mean \pm standard deviation (SD) and categorical variables were reported as n (%). Statistical analysis was performed using SPSS v19 statistical software. The t-test was used to compare continuous variables in the groups. Pearson’s chi-squared test or Fisher’s exact test was used to compare categorical variables in the groups. The significance level was established as $\alpha = 0.05$.

Results

Demographics and clinical characteristics of the eligible patients

A total of 84 patients were finally included in this study, including 51 men and 33 women, with a mean age of 61.2 ± 12.3 years. Of 84 biopsy lesions, 17 were benign and 67 were malignant. The longest diameter of the lesion measured in the axial CT ranged from 10 mm to 68 mm, with a mean of 33.1 ± 13.9 mm. A CTLB was performed in 45 (53.6%) patients (group 1) and PETCTLB in 39 (46.4%) patients (group 2). All biopsies were completed between January 2019 and December 2021. The demographic and clinical data of the two groups are summarized in Table 1 and show that there was no significant difference between the two groups ($P > 0.05$).

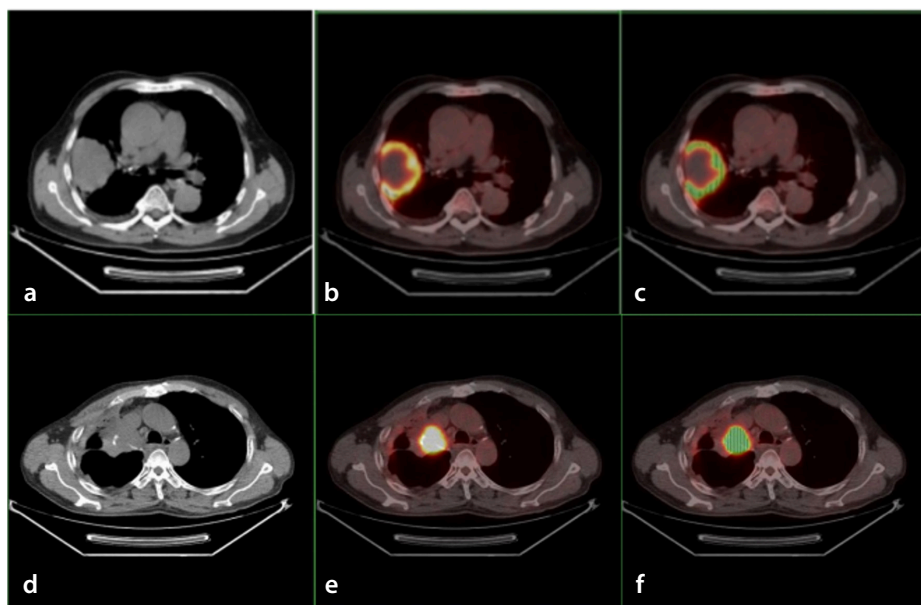


Figure 2. Metabolic distribution of lung lesions on positron emission tomography/computed tomography image. (a-c) An adenocarcinoma of the right upper lung; (d-f) postoperative recurrence of the right upper lung squamous cell carcinoma. Left: axial CT; middle: fused image; right: the biopsy area represented by green on the fused image.

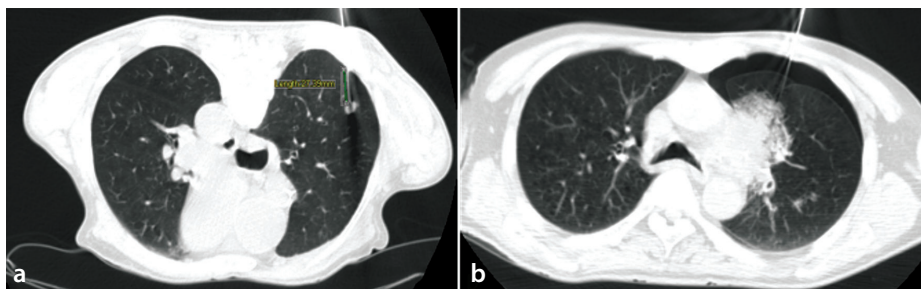


Figure 3. Needle path length and complication. (a) Needle path length through the ventilated lung, measured from the pleura to the edge of the lesion; (b) pneumothorax and pulmonary hemorrhage.

The number of needle adjustments, the number of samples, and the procedure time

The needle placement efficiency for obtaining specimens was evaluated by the number of needle adjustments and the procedure time.

The mean number of needle adjustments for each patient was (3.3 ± 1.0 SD, range: 2–6) for PETCTLB procedures and (3.6 ± 1.1 SD, range: 2–8) for CTLB procedures. A comparison of the two groups showed no significant statistical difference between them ($P > 0.05$). The mean number of samples was (2.6 ± 0.5 SD, range: 2–3) in group 2 and (3.1 ± 0.4 SD, range: 2–5) in group 1, respectively; the difference between the two groups was

significant ($P < 0.05$). The procedure time was calculated from the start of the localization scan to the acquisition of the specimen. The mean procedure time was (11.1 ± 3.0 SD, range: 7–17) minutes in group 2 and (12.9 ± 3.3 SD, range: 7–19) minutes in group 1; a significant statistical difference was observed in the comparison of the procedure time in the two groups ($P < 0.05$, Table 2), with the procedure time in group 2 being less than that in group 1.

Initial pathological results and complications

In group 1, the initial pathological results in 37 (82.2%) patients were consistent with the final diagnosis, biopsies failed in 1 patient, and no malignant cells were observed

in the samples of 6 patients with malignancies. In group 2, the initial pathological results in 38 (97.4%) patients were consistent with the final diagnosis, and only one case of pulmonary tuberculosis was misdiagnosed as non-specific inflammation. The difference between the two groups was statistically significant for them ($P < 0.05$), and the diagnostic coincidence rate was higher in group 2 than in group 1. Developed pneumothorax and/or subcutaneous emphysema were observed in 10 (22.2%) patients of group 1 and in 9 (23.1%) patients of group 2, during or after the procedure; no statistically significant differences were observed between the two groups ($P > 0.05$). However, the incidence of hemorrhage (intrapulmonary hemorrhage and/or hemothorax) during or after the biopsy was observed in 13 (42.2%) patients of group 1 and 4 (25.6%) patients of group 2, and a significant statistical difference was observed between the two groups ($P < 0.05$); bleeding complications occurred less in group 2 than in group 1. One patient in group 1 developed massive hemoptysis (single hemoptysis >100 cc), there were four cases of massive pneumothorax (pneumothorax volume $>30\%$ of volume thoracic cavity) in each group, and no procedure-related deaths were reported in either group.

Discussion

In the present study, we compared the outcomes of PETCTLB and CTLB. We found that (1) the mean procedure time was less (11.1 ± 3.0 vs. 12.9 ± 3.3), (2) the mean number of samples was less (2.6 ± 0.5 vs. 3.1 ± 0.4), (3) the diagnostic accuracy was higher (97.4% vs. 82.2%), and (4) bleeding complications occurred less (25.6% vs. 42.2%) in the PETCTLB group than in the CTLB group, respectively. These results suggest that PETCTLB is a feasible approach that improves the diagnostic performance of a transthoracic lung biopsy, thus providing greater potential benefits for patients than CTLB.

As a reliable and safe procedure for the diagnosis of indefinite pulmonary lesions, CTLB, which allows both histological and biomolecular study, is a standard sampling technique and is widely used.⁸ Although it has a higher accuracy,^{1,9} the inhomogeneity (such as necrotic and cystic area) of lung nodules/masses, atelectasis or consolidation, obstructive pneumonia, and peripheral region of reactive inflammatory tissue inevitably leads to an increase in false negatives. Since histological cuts of biopsies can only obtain a small part of the lesion for analysis, CTLB of lung nodules/masses may be subject

Table 1. Demographic data and clinical characteristics of the two groups

	CTLB (group 1) n = 45	PETCTLB (group 2) n = 39	P value
Age (years)	61.2 \pm 12.3	63.2 \pm 9.3	0.397
Sex, male, n (%)	66.7% (30/45)	53.8% (21/39)	0.230
Lesion sites			
U/M lobes	26	24	0.726
Lower lobe	19	15	
LD of lesion (mm)	32.8 \pm 14.0	33.4 \pm 13.9	0.837
Lesion nature			
Benign	10	7	0.627
Malignant	35	32	

CTLB, computed tomography guided transthoracic lung biopsy; PETCTLB, computed tomography guided transthoracic lung biopsy with pre-procedure ¹⁸F-FDG PET/CT images; UM lobes, upper and middle lobe of the lung; LD, the longest transverse diameter in the axial computed tomography plane; ¹⁸F-FDG PET/CT, ¹⁸F-fluorodeoxyglucose positron emission tomography/computed tomography.

Table 2. Comparison of the procedure and results of biopsies between the two groups

	CTLB (group 1) n = 45	PETCTLB (group 2) n = 39	P value
Number of needle position checks	3.6 \pm 1.1	3.3 \pm 1.0	0.329
Procedure time (minutes)	12.9 \pm 3.3	11.1 \pm 3.0	0.008
Needle path length (mm)			
≤ 20	18	17	0.739
> 20	27	22	
Number of samples	3.1 \pm 0.4	2.6 \pm 0.5	<0.001
Diagnostic accuracy of the biopsy (cases)	82.2% (37/45)	97.4% (38/39)	0.033
Complications, % (cases)			
Subcutaneous emphysema and/or pneumothorax	22.2% (10/45)	23.1% (9/39)	0.926
Intrapulmonary hemorrhage and/or hemothorax	42.2% (13/45)	25.6% (4/39)	0.034
Biopsy failure, % (cases)	4.4% (2/45)	0% (0/39)	0.497

CTLB, computed tomography guided transthoracic lung biopsy; PETCTLB, computed tomography guided transthoracic lung biopsy with pre-procedure ¹⁸F-FDG PET/CT images; needle path length, needle path length through the ventilated lung, measured from the pleura to the edge of the lesion; ¹⁸F-FDG PET/CT, ¹⁸F-fluorodeoxyglucose positron emission tomography/computed tomography.

to sampling errors.¹⁰ There are more advantages to PETCTLB than CTB, since PET/CT can show the distribution of metabolic activity in the lesion, providing a well-defined biopsy target and effectively avoiding areas of necrosis, cystic degeneration, atelectasis, and some inflammation, leading to higher accuracy.

There is currently no consensus or guidelines for the number of samples to be taken, but the number of samples taken is usually 3–4,¹¹ and to obtain reliable samples during CTB, the sampling sites are often scattered in the lesion. However, in the metabolic distribution provided by PET/CT images, the biopsy target is specific, the biopsy sites selected are relatively concentrated, and with the accumulation of technique experience, a smaller number of samples may be required, thus reducing the adjustment range of inclination of the needle and shortening the procedure time. In the present study, comparing the number of samples taken by the two groups, the difference was statistically significant, and the mean number of samples taken in group 2 was less than that in group 1; the procedure time and the bleeding complication incidence were also reduced correspondingly.

Biopsies guided by PET/CT can be broadly divided into real-time PET/CT-guided biopsies and PETCTLB.^{6,11,12} One study¹³ showed that the accuracy of real-time PET/CT-guided lung biopsies was higher than that of CTB, reducing re-biopsies. However, there are currently no guidelines on real-time PET/CT-guided biopsies, and they also carry some radiation risks for the operators and patients. ¹⁸F-FDG PET/CT has been widely used in the evaluation of tumors, and despite patients being inevitably also exposed to a certain amount of radiation, it has been proven to be safe. A study of PET/CT examinations in children showed that a proper scanning regimen can minimize the radiation dose received during the examination.¹⁴ Lin et al.¹¹ compared the results of intraprocedural CT-guided biopsies with prior PET/CT fusion images and CT-guided biopsies alone, showing no significant difference in procedure time, but there was a higher diagnostic yield for malignancy in the fusion images group than that in the routine group. Our study is a more comprehensive comparison of CTB and PETCTLB. Although PETCTLB requires less time and fewer samples, it has higher diagnostic accuracy and fewer bleeding complications.

In group 2, the low incidence of bleeding may be because the sample was taken in the middle of the tumor tissue rather than the edge.

In addition, we also highlight herein the importance of body surface determination during a transthoracic biopsy. In the present study, we used a self-made gradient grid locator. Verified through clinical application and evaluation, it is simple, practical, and effective in ensuring the stability and reliability of body surface positioning.

There are several limitations in our study. First, this is a single-center retrospective study. Second, PET/CT is not a routine item covered by health insurance in China, and a potential selection bias is inevitable for the patients in PETCTLB. Third, in both group 1 and group 2, the range of sizes of the pulmonary lesions was large.

In conclusion, compared with CTB, PETCTLB can reduce the number of samples taken, shorten procedure time, improve diagnostic yield, and reduce bleeding complications; it is a safe procedure that can provide a precise diagnosis in the majority of lung nodules/masses, and it has a better diagnostic performance.

Conflict of interest disclosure

The authors declared no conflicts of interest.

Funding

The Science-Technology Supporting Projects of Jiangxi Sci-Tech Department (20142BBG70095) and the Science and Technology Plan of Jiangxi Provincial Health Commission (202130087) is gratefully acknowledged.

References

1. Zhang S, Yu X, Huang Y, et al. Pneumonic-type invasive mucinous adenocarcinoma and infectious pneumonia: clinical and CT imaging analysis from multiple centers. *BMC Pulm Med.* 2022;22(1):460. [\[CrossRef\]](#)
2. Chen S, Ben S, Xin J, et al. The biogenesis and biological function of PIWI-interacting RNA in cancer. *J Hematol Oncol.* 2021;14(1):93. [\[CrossRef\]](#)
3. Ma L, Du J, Sui Y, Wang S. Clinical significance of plasma free DNA in patients with non-small cell lung cancer. *J Int Med Res.* 2019;47(11):5593-5600. [\[CrossRef\]](#)
4. Liang R, Chen TX, Wang ZQ, et al. A retrospective analysis of the clinicopathological

characteristics of large cell carcinoma of the lung. *Exp Ther Med.* 2015;9(1):197-202.

[\[CrossRef\]](#)

5. Wang W, Yu L, Wang Y, et al. Radial EBUS versus CT-guided needle biopsy for evaluation of solitary pulmonary nodules. *Oncotarget.* 2018;9(19):15122-15131. [\[CrossRef\]](#)
6. Jain TK, Singh H, Kumar R, Bal A, Sood A, Mittal BR. Real time F-18 FDG PET-CT-guided metabolic biopsy targeting differential FDG avidity in a pulmonary blastoma. *Nucl Med Mol Imaging.* 2020;54(5):261-263. [\[CrossRef\]](#)
7. Cerci JJ, Bogoni M, Cerci RJ, et al. PET/CT-guided biopsy of suspected lung lesions requires less rebiopsy than CT-guided biopsy due to inconclusive results. *J Nucl Med.* 2021;62(8):1057-1061. [\[CrossRef\]](#)
8. Najafi A, Al Ahmar M, Bonnet B, et al. The PEARL Approach for CT-guided lung biopsy: assessment of complication rate. *Radiology.* 2022;302(2):473-480. [\[CrossRef\]](#)
9. Huang ZG, Sun HL, Wang CL, et al. CT-guided transthoracic needle biopsy of pulmonary lesions: comparison between the cutting needle and aspiration needle. *Br J Radiol.* 2021;94(1118):20190930. [\[CrossRef\]](#)
10. Brioulet J, David A, Sagan C, Cellerin L, Frampas E, Morla O. Percutaneous CT-guided lung biopsy for the diagnosis of persistent pulmonary consolidation. *Diagn Interv Imaging.* 2020;101(11):727-732. [\[CrossRef\]](#)
11. Lin Y, Xu Y, Lin J, et al. Improving CT-guided transthoracic biopsy diagnostic yield of lung masses using intraprocedural CT and prior PET/CT fusion imaging. *BMC Pulm Med.* 2022;22(1):311. [\[CrossRef\]](#)
12. Guralnik L, Rozenberg R, Frenkel A, Israel O, Keidar Z. Metabolic PET/CT-guided lung lesion biopsies: impact on diagnostic accuracy and rate of sampling error. *J Nucl Med.* 2015;56(4):518-522. [\[CrossRef\]](#)
13. Guo W, Hao B, Chen HJ, et al. PET/CT-guided percutaneous biopsy of FDG-avid metastatic bone lesions in patients with advanced lung cancer: a safe and effective technique. *Eur J Nucl Med Mol Imaging.* 2017;44(1):25-32. [\[CrossRef\]](#)
14. Yu S, Qian Z, Liu H, et al. Optimized low-dose positron emission tomography/computed tomography schemes in pediatric tumor patients: a randomized clinical trial. *Transl Pediatr.* 2022;11(9):1510-1520. [\[CrossRef\]](#)



Correlation between computed tomography-based body composition parameters and hepatic venous pressure gradient in patients with cirrhosis: a systematic review and meta-analysis

Siwei Yang¹
 Zhiyuan Zhang¹
 Qiyang Chen²
 Yuefeng Hu¹
 Tianhao Su¹
 Xuedong Sun¹
 Long Jin¹

¹Capital Medical University, Beijing Friendship Hospital, Department of Interventional Radiology, Beijing, China

²Capital Medical University, Beijing Tongren Hospital, Department of Ultrasound, Beijing, China

This study was registered prospectively on the International Prospective Register of Systematic Reviews (PROSPERO) in 2023 (registration number: CRD42023392942).

Corresponding author: Long Jin

E-mail: jinlong@ccmu.edu.cn

Received 12 October 2023; revision requested 13 November 2023; accepted 14 December 2023.



Epub: 31.01.2024

Publication date: 06.11.2024

DOI: 10.4274/dir.2023.232553

PURPOSE

Computed tomography (CT)-based body composition parameters and the hepatic venous pressure gradient (HVPG) are key characteristics in patients with liver cirrhosis. The present study aims to explore the correlation between CT-based body composition parameters and HVPG, as well as the difference in HVPG between patients with and patients without sarcopenia.

METHODS

A literature search for studies reporting the correlation between HVPG and CT-based body composition parameters published in English up to August 2023 in four databases, Embase, MEDLINE (via PubMed), Web of Science, and Cochrane Library, was conducted. The correlation coefficient between HVPG and CT-based body composition parameters was the primary outcome, and the difference in the HVPG value between the sarcopenia and non-sarcopenia groups was the secondary outcome. A meta-analysis was conducted using a random-effects models. The methodologic quality was assessed using the Quality Assessment of Diagnostic Studies instrument.

RESULTS

A total of 652 articles were identified, of which nine studies ($n = 1,569$) met the eligibility criteria. Among them, seven studies reported the primary outcome via the muscle index, five via the skeletal muscle index (SMI), two via the psoas-muscle-related index (PRI), and three via two adipose tissue indexes. A total of five studies reported the secondary outcome: four via SMI and one via PRI. No evidence of a significant correlation was determined between the various body composition parameters and the HVPG value, either in the muscle index or the adipose tissue index. Higher HVPG values were observed in patients with sarcopenia than in patients without sarcopenia [pooled standardized mean difference (SMD): 0.628 (-0.350, 1.606), $P < 0.001$; $I^2 = 92.8\%$; $P < 0.001$] when an Asian sarcopenia definition was adopted. In contrast, when a Western cut-off value was applied, the HVPG value was higher in patients without sarcopenia than in patients with sarcopenia [pooled SMD: -0.201 (-0.366, -0.037), $P = 0.016$; $I^2 = 0.00\%$; $P = 0.785$].

CONCLUSION

No sufficient evidence regarding a correlation between the CT-based body composition and HVPG value was discovered. The difference in the HVPG value between the sarcopenia and non-sarcopenia groups was likely dependent on the sarcopenic cut-off value.

KEYWORDS

Liver cirrhosis, portal hypertension, sarcopenia, body composition, meta-analysis

Sarcopenia, a disease entity representing a progressive and generalized skeletal muscle disorder, is a prevalent morbidity of liver cirrhosis (LC).¹ Due to the concomitant altered catabolic state, insulin resistance, chronic systemic inflammation and physical inactivity, sarcopenia exists in different LC stages and is closely related with decompensation risk and postoperative complications, as well as mortality independent of commonly used tools, such as Child–Pugh score or the model for end-stage liver disease (MELD) score.^{2–4} Furthermore, the role of adipose quantity or distribution as a precipitating event for poor prognosis in patients with LC has also been proposed.^{5,6} Importantly, as two body phenotypes, the muscle and adipose quantity may interact with each other instead of acting as two independent pathophysiological conditions.⁷

Computed tomography (CT) is considered the gold standard for assessing muscle or adipose quantity, and CT-based muscle quantity is recommended for defining sarcopenia.^{8,9} In patients with LC, CT is routinely performed with the aim of monitoring portal-systemic collaterals and tumor development or recurrence; thus, CT-based body composition parameters are accessible and reproducible. In addition, the hepatic venous pressure gradient (HVPG) is recognized as the gold standard for evaluating portal hypertension (PH).¹⁰ To stratify the risk of decompensation with intent for early intervention, HVPG measurement has also been encouraged in patients with LC in real-life practice.¹¹

Body composition, especially muscle quantity, and HVPG have been characterized as important characteristics in patients with LC. With the progress of LC, clinically signif-

icant PH is concomitant. Muscle depletion and fat accumulation or redistribution also likely occur in this course.^{1,12} Specifically, the metabolism changes of such a population are characterized by insulin resistance, dysregulated muscle protein turnover, and altered lipid redistribution.¹³ Furthermore, some clinical events, such as loss of appetite, fluid retention, and sedentary behavior, contribute to alterations of the body phenotype. A large sample cross-sectional study revealed that muscle mass depletion was independently associated with the liver fibrosis stage.¹⁴ In addition, a preclinical study showed that ammonia-lowering therapy could result in an increase of skeletal muscle mass.¹⁵ Nevertheless, the evidence on the correlation between HVPG and body composition is still weak. The number of existing studies is too limited to provide relevant data. Discrepant results were yielded among these studies. The study by Matsui et al.¹⁶ showed that the HVPG value was inversely correlated with the skeletal muscle index (SMI). In contrast, other published data showed a null association.^{5,17–19} Similarly inconsistent results have also been observed regarding the adipose tissue index and HVPG. Rodrigues et al.⁵ concluded that there was a significant negative correlation between the subcutaneous adipose tissue index (SATI) and the HVPG value, but Cho et al.¹⁸ and Zeng et al.¹⁹ did not.

Whether the HVPG value is correlated with a certain body composition parameter, and to what extent the HVPG value differs between patients with sarcopenia and patients without sarcopenia remains unknown. Knowledge of the impact of PH on muscle or adipose tissue is highly desirable, guiding nutrition support and tailoring individualized therapy. The additional value of HVPG, known as a validated index mirroring PH, would be detected for association with body tissue alternations in patients with LC. Hence, a meta-analysis was conducted to overview the current evidence and address this issue.

Methods

Protocol registration

The present review was performed following the 2020 Preferred Reporting Items for Systematic Reviews and Meta-Analyses (PRISMA) statement.²⁰ The PRISMA checklist is shown in Online Resource 1. This study was registered prospectively in the International Prospective Register of Systematic Reviews in 2023 (registration number: CRD42023392942). The requirement for informed consent and ethical approval from

the Institutional Review Board were waived because the study quantified all existing publicly available data instead of involving specific patients.

Eligibility criteria

Population, interventions, comparisons, outcomes: the population of interest was patients with LC. The interventions of interest included CT scanning and HVPG within an acceptable interval. The outcomes of interest included: (1) the correlation analysis between various body composition parameters and HVPG; and (2) the HVPG value reported in patients with or without sarcopenia. The comparison and study of interest were not applicable or limited.

The abstract of a conference poster containing relevant information was also eligible. The authors contacted the corresponding author for detailed information. References cited in the text of selected articles were also further searched to minimize publication bias.

Search strategy

Peer-reviewed articles written in English and published up to August 2023 were searched in Embase, MEDLINE (via PubMed), Web of Science, and Cochrane Library. The retrieval protocol combined medical subject headings and text, which were mostly derived from entry terms in the PubMed and Embase databases. The search strategy is available in Online Resource 2.

Study selection

The exclusion criteria were as follows: (1) duplicate and irrelevant articles; (2) cell-line studies; (3) review articles; (4) case reports; (5) letters; (6) comments and editorials; (7) subjects from pediatric and non-human sources; and (8) cadavers.

The further exclusion criteria in a full-text assessment were as follows: patients with (1) LC with non-intrahepatic causes; (2) presence of evident intrahepatic vessel communication in measuring HVPG; and (3) a history of transjugular intrahepatic portosystemic shunt.

The HVPG value and body composition parameter on a continuous scale were eligible for analysis.

The correlation analysis should be performed using Pearson's (*r*) or Spearman's rho analysis according to the normality of the raw data. Presently, the impact of tumors

Main points

- The present study is deemed to be the first meta-analysis to quantify evidence of a correlation between the hepatic venous pressure gradient (HVPG) and the body composition parameters.
- The association between portal hypertension (PH) and body composition parameters as two characteristics in patients with cirrhosis was revealed, with the goal of exploring the impact of PH on skeletal muscle loss or adipose tissue change.
- No evidence of significant correlation was determined between various body composition parameters and HVPG.
- The difference in the HVPG value between patients with sarcopenia and patients without sarcopenia is likely dependent on the sarcopenic definition.

not involving an intra- or extra-hepatic great vessel on the HVPG value remains unclear. Measurements of HVPG were performed in selected patients with hepatocellular carcinoma (HCC) and LC in real-life practice; thus, patients with HCC with a Barcelona Clinic Liver Cancer stage of 0, A, or B would not have been excluded in this meta-analysis. In addition, this potential effect could be further eliminated in the subgroup analysis.

Definitions

Transversal-psoas muscle thickness and psoas muscle thickness by height are the same measurement with different names, referring to the transversal diameter of the psoas muscle perpendicular to the largest axial psoas muscle diameter at the L3 plane normalized by height. Therefore, these two indexes were replaced with the psoas-muscle-related index (PRI) for analysis. All muscle and adipose indexes are defined and illustrated in Supplementary Figure 1.

Outcomes

The primary outcome was the correlation coefficient between various body composition parameters and HVPG. The difference in HVPG value between the sarcopenia group and the non-sarcopenia group was the secondary outcome. Due to a lack of a validated cut-off value to define adipopenia, the secondary outcome analysis was not performed in adipose indexes.

Data extraction

Two review authors (S.Y. and Q.C.) blindly and independently extracted the following items from each article: the first co-author, year of publication, country, study design, sample size, body mass index (BMI), sex, cause of liver disease, albumin, decompen-

sation proportion, Child–Pugh score, MELD score, the interval between CT scan and HVPG measurement, sarcopenia definition, sarcopenia cut-off value, sarcopenia proportion, HVPG value in the sarcopenia and non-sarcopenia groups, correlation coefficient between body composition parameters and the HVPG value, and details of the HVPG measurement technique.

All data were respectfully recorded by two review authors using Microsoft Excel. Any inconsistency was resolved by reviewing the original article to achieve a consensus.

Risk of bias and certainty of evidence assessment

Two review authors independently assessed the methodological quality with regard to risk of bias and applicability concern using the Quality Assessment of Diagnostic Studies instrument. The Grading of Recommendations Assessment, Development and Evaluation (GRADE) system and online tool (GRADE Pro GDT, <https://gdt.gradepro.org/>) were used to rate the outcome if possible. The certainty of evidence was classified into four levels based on the five domains (<https://training.cochrane.org/resource/grade-handbook>) high, moderate, low, and very low.

Statistical analysis

The HVPG values in the sarcopenia and non-sarcopenia groups presenting as mean \pm standard deviation were summarized. Values presenting as the median (interquartile range) would have been converted using an established fashion if necessary.²¹

The difference in the HVPG values was compared using the standardized mean difference (SMD) with a 95% confidence inter-

val (CI). The Pearson correlation coefficient was collected and converted to the Fisher-Z value according to the following equation: $Z = 0.5 [\ln(1+r) - \ln(1-r)]$; the corresponding standard error was calculated according to the following equation: $SE_z = \frac{1}{\sqrt{n-3}}$, and summary r was recovered using the following equation: $r = (e^{2Z} - 1) / (e^{2Z} + 1)$.²²

A Fisher transformation was used to convert the Spearman coefficient into an approximately normal distribution and further calculate the 95% CI. Subsequently, the same summary process was conducted as a Pearson analysis. Fisher's Z value was used in the meta-analysis and shown in the plots, and the correlation coefficient derived from the inverse Fisher's transformation was presented as the summary result. The heterogeneity was identified using Cochran's Q test and further quantified using the I^2 statistic among the studies. When the P value was <0.05 or the I^2 value was $>50\%$, the heterogeneity was considered high, and the source of bias was explored. Publication bias was assessed if the number of included studies was >10 .²³ In the prespecified sensitivity analysis, pooled correlation coefficient estimates were further stratified as per presence of HCC and different sarcopenic cut-off values.

A P value of <0.05 was indicative of a significant difference. Considering the heterogeneity and sample size, a random effects model was selected to calculate the pooled effect size. The Stata MP (version 16.0, Stata Corp, College Station, USA) package was used for meta-analysis, and Review Manager (version 5.3) was used to evaluate the methodological quality.

Results

Study characteristics

Of the 652 studies screened initially, nine involving a total of 1,569 patients with LC were included for meta-analysis.^{5,16-19,24-27} A corresponding flow diagram is shown in Figure 1.

One poster including relevant data was excluded because it had not been published officially, and the request for raw data or effect size had not been answered.²⁸ The characteristics of the included studies are shown in Table 1.

Regarding the characteristics of the included patients, the sarcopenia proportion ranged from 34.7% to 71% across the eligible studies. The most common cause of liver disease was alcohol in six studies, followed by

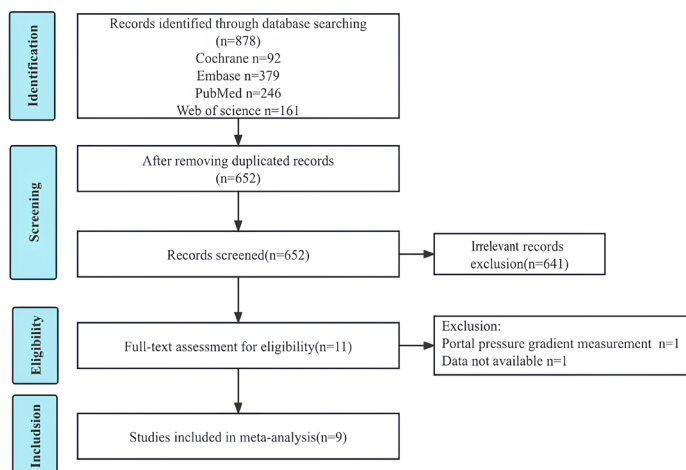


Figure 1. Flow diagram of the study selection process.

Table 1. Characteristics of included studies

Author and year	Country	Participants				Index				Outcomes				
		Sample size	BMI	Male (%)	Decompensation proportion (%)	Child-Pugh score	MELD score	Interval between CT and HVPG	Measured index	Sarcopenia cut-off (men/women)	HVPG in sarcopenia group	HVPG in non-sarcopenia group	Correlation coefficient*	P
Jeong et al. ²⁴ (2018)	Korea	131	23.3 ± 4.1	71.8	87.8	7.6 ± 2.1	10.7 ± 4.4	Within 2 months	SMI	52.4 cm ² /m ² and 38.5 cm ² /m ²	14.7 ± 5.0	15.6 ± 6.2	NA	0.357
Paternostro et al. ²⁵ (2021)	Australia	203	24.6 (22.4–28.0)	68.0	73.4	NA	12 (9–15)	±200 days	TPMT	12 mm/m and 8 mm/m	18 (16–22.5)	20 (16–23)	0.031	0.211/0.66*
Maruyama et al. ¹⁷ (2017)#	Japan	98	24.3 ± 4.8	65.3	NA	NA	9.6 ± 2.7	<1 year	SMI	42 cm ² /m ² and 38 cm ² /m ²	15.2 ± 5.4	14.6 ± 4.8	NA	0.56
Non-sarcopenia group		64	26.1 ± 4.6	70.3		9.8 ± 2.9					NA	NA	–0.096	0.45*
Sarcopenia group		34	20.8 ± 2.6	55.9		9.2 ± 2.2					NA	NA	0.122	0.49*
Kim et al. ²⁶ (2014)	Korea	65	NA	63.1	100.0	NA	9.0 ± 1.7	Within 2 months	PMTH	14 mm/m	NA	NA	–0.127	0.313*
Kang et al. ²⁷ (2018)	Korea	452	23.1 (20.7, 24.8)	83.8	NA	NA	10.4 ± 3.6	Within 3 months	SMI	52.4 cm ² /m ² and ≤38.5 cm ² /m ²	14.0 (10.0, 17.0)	14.0 (11.0, 17.25)	NA	0.313
Matsui et al. ¹⁶ (2022)	Japan	202	23.8 ± 4.4	69.8	NA	7.5 ± 2.0	10.3 ± 6.2	NA	SMI	42 cm ² /m ² and 38 cm ² /m ²	15.0 ± 6.2	8.4 ± 5.1	–0.476	<0.001/<0.001*
Cho et al. ¹⁸ (2021)	Korea	166	23.3 ± 3.9	70.5	62.7	7.6 ± 2.1	10.8 ± 4.4	Within 2 months	SMI	50 cm ² /m ² and ≤39 cm ² /m ²	NA	NA	0.111	>0.05*
									SATI				0.03	>0.05*
									VATI				–0.057	>0.05*
Rodrigues et al. ⁵ (2019)	Switzerland	84	28.0 ± 5.0	60.7	54.8	7.0 ± 2.0	13.0 ± 8.0	Within 12 weeks	SMI	50 cm ² /m ² and 39 cm ² /m ²	NA	NA	–0.006	0.96*
									SATI				–0.282	0.01*
									VATI				–0.07	0.55*
Zeng et al. ¹⁹ (2023)	China	168	23.0 ± 3.6	64.9	NA	6.9 ± 1.7	10.8 ± 3.4	Within 1 month	SMI	44.77 cm ² /m ² and 32.50 cm ² /m ²	NA	NA	–0.083	0.583
									SATI				0.042	0.589
									VATI				0.024	0.762

#This study reported the correlation coefficient separately in sarcopenia and non-sarcopenia groups. Results for continuous data are expressed as means ± standard deviations and for categorical data as n (%). The MELD score in Matsui et al.¹⁶ (2022) was the MELD-Na score. *Indicates the P value of the correlation coefficient between a certain body composition parameter and the HVPG value. CT, computed tomography; BMI, body mass index; MELD, model for end-stage liver disease; HVPG, hepatic vein pressure gradient; SMI, skeletal muscle index; SATI, subcutaneous adipose tissue index; VATI, visceral adipose tissue index; PMTH, transversal-psoas muscle thickness; PMTH, psoas muscle thickness by height; NA, not available.

virus in the remaining three studies. There were 13 participants with HCC in the context of LC included in one study.¹⁷

A total of seven studies reported the primary outcome. Of these, five comprised 718 patients reported via SMI^{5,16-19} (one reported the correlation coefficient separately in the sarcopenia and non-sarcopenia subgroups)¹⁷ and two comprised 268 patients reported in PRI.^{25,26} A total of three studies provided the primary outcome in SATI and the visceral adipose tissue index (VATI).^{5,18,19}

In addition, five studies reported the secondary outcome: four reported via SMI and one reported via PRI.²⁵ Among the four studies reporting via SMI, the cut-off value was 42 cm²/m² for men and 38 cm²/m² for women in two studies^{16,17} and 52.4 cm²/m² in men and 38.5 cm²/m² in women in the other two studies.^{24,27} Considering that SMI was recommended for defining sarcopenia by most societies, the study reporting via PRI was not included for the secondary outcome.

For the publication nation, one study was conducted in Australia,²⁵ one in Switzerland,⁵

and the remaining seven in Asian countries, including China,¹⁹ Japan,^{16,17} and the Republic of Korea.^{18,24,26,27}

All included studies were retrospective studies published in the last 5 years.

Quality assessment and risk of bias

All included studies were considered to be of low or moderate risk of bias, as illustrated in Figure 2. The detailed scales are shown in Online Resource 3. The GRADE summary of findings for the outcome is provided in Supplementary Table S1.

Primary outcome

Muscle index

Only Matsui et al.¹⁶ reported a significantly negative correlation between SMI and HVPG in 202 patients; the remaining studies reported a null correlation.

The pooled correlation coefficient, regardless of muscle index, was -0.08 ($-0.25, 0.09$; $P = 0.368$), with significant heterogeneity observed (overall: $I^2 = 85.3%$; $P < 0.001$); similar results were observed in the SMI and

PRI subgroups [SMI: $r = -0.09$ ($-0.31, 0.14$); $P = 0.442$; $I^2 = 88.4%$; $P < 0.001$; PRI: $r = -0.01$ ($-0.15, 0.12$); $P = 0.852$; $I^2 = 16.1%$; $P = 0.275$] (Figure 3).

Adipose tissue index

No significant correlation was pooled [$r = -0.03$ ($-0.12, 0.05$), $I^2 = 34.5%$, $P = 0.177$] in either of the adipose index subgroups [SATI: $r = -0.06$ ($-0.24, 0.13$), $P = 0.545$; VATI: $r = -0.03$ ($-0.12, 0.07$), $P = 0.586$]. The high heterogeneity was detected in the SATI subgroup ($I^2 = 71.1%$, $P = 0.032$) but not in the VATI subgroup ($I^2 = 0.0%$, $P = 0.695$). The corresponding forest plot is shown in Figure 4.

Secondary outcome

The summary difference of the HVPG value between the sarcopenia and non-sarcopenia groups indicated statistical significance, with unstable results due to different sarcopenia definitions. When using the cut-off value from the Japan Society of Hepatology guidelines for sarcopenia (SMI <42 cm²/m² for men or <38 cm²/m² for women), higher HVPG values were observed in patients with sarcopenia than in patients without sarcopenia [pooled SMD: 0.628 ($-0.350, 1.606$), $P < 0.001$; $I^2 = 92.8%$; $P < 0.001$]. When a commonly used cut-off value in the Western population was applied (50 cm²/m² for men and 39 cm²/m² for women), the HVPG value was higher in patients without sarcopenia than in patients with sarcopenia [pooled SMD: -0.201 ($-0.366, -0.037$), $P = 0.016$; $I^2 = 0.00%$; $P = 0.785$] (Figure 5).

Sensitivity analysis

After exclusion of the study including 13 patients with HCC, the correlation between either PRI or SMI and HVPG was not significant [overall: $r = -0.10$ ($-0.30, 0.11$), $P = 0.341$; $I^2 = 89.1%$, $P < 0.001$; SMI: $r = -0.13$ ($-0.40, 0.17$), $P = 0.401$; $I^2 = 92.6%$; $P < 0.001$]. The corresponding forest plot is shown in Figure 6.

Discussion

In the present review, a meta-analysis was performed to identify and quantify the current evidence regarding the correlation between body composition parameters and HVPG. The pooled results indicated that there was no significant correlation between muscle or adipose quantity and the HVPG value, regardless of muscle index. The results of the secondary outcome were unstable due to different sarcopenia definitions. With consideration of the statistical significance and ethnicity-specific cut-off value of sarco-

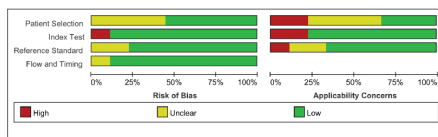


Figure 2. Methodological quality of all included studies. Left: methodological quality graph; right: methodological quality summary.

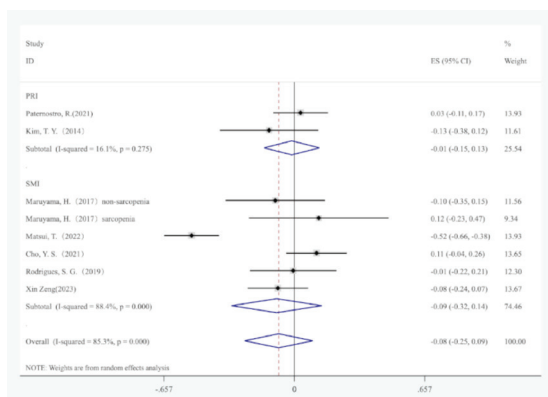


Figure 3. Pooled correlation coefficient for the muscle index in all eligible studies.

penia, the result appears to reveal that patients with lower muscle mass may have a higher HVPG value.

Body composition and HVPG are of paramount importance for patients with LC. Nevertheless, a knowledge gap remains in the correlation between them. To the best of the present authors' knowledge, this meta-analysis is the first to quantitatively combine current data to assess the correlation between body composition parameters and HVPG.

In fact, limited LC-related studies have reported both composition parameters and

HVPG values at the same time, seldom exploring the association between them. Specifically, CT-based quantitative analysis and invasive operation hamper the acquisition of data in clinical practice. Despite the fact that the limited evidence grade leads to a cautious interpretation of the results, the findings of this meta-analysis could help explore the impact of PH on body composition parameters and might be instrumental in refining a comprehensive evaluation algorithm of patients with LC.

In this meta-analysis, several points merit attention. First, the HVPG value was used

to evaluate the PH instead of the portosystemic pressure gradient, largely because the portosystemic pressure gradient was commonly collected in the transjugular intrahepatic portosystemic shunt procedure with a limited clinical application prospect. Second, to reduce the bias derived from different global cut-off values of sarcopenia, only the muscle or adipose tissue quantity as the continuous variable normalized to height or height² was extracted and comparable. In addition, other statistics would have been summarized if they could have been converted to the correlation coefficient using a validated statistical method, including the contingency coefficient and standardized beta value; however, such a study was not found in the study screening. Third, SMI is recognized as the gold standard for measuring muscle quantity in defining sarcopenia, and psoas-muscle-related parameters have been shown to be less strongly correlated with the total body protein or mortality risk compared with SMI.^{29,30} Therefore, of the five studies reporting the secondary outcome, one study reporting via PRI was not included in the meta-analysis. Last, all included studies were published in the past 5 years, thereby enabling a standard care for patients with LC.

Figure 4. Pooled correlation coefficient for the adipose tissue index.

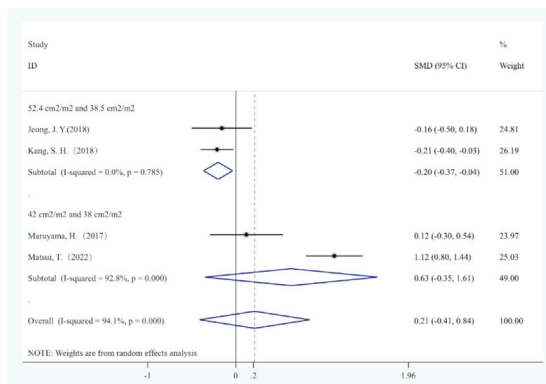
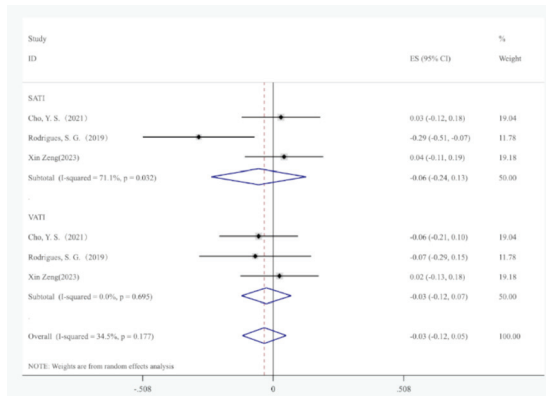


Figure 5. Summary difference of the hepatic venous pressure gradient value between the sarcopenia and non-sarcopenia groups.

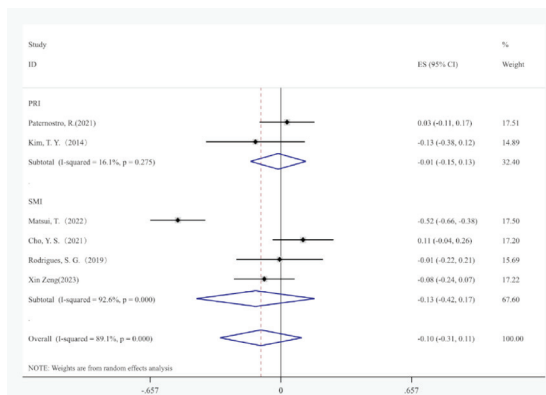


Figure 6. Sensitivity analysis. The pooled correlation coefficient for muscle index after the exclusion of patients with hepatocellular carcinoma.

Negative results of the primary outcome are partly explainable because of a considerable interindividual variation of the liver function reserve among the included patients. In the included studies, decompensated cirrhosis or clinical signs of PH, such as ascites, gastro-esophageal varices, and hepatic encephalopathy, were deemed indications of HVPG measurement. Among all the evaluable patients, the mean values of the MELD score were 9–13, the decompensation proportions were 54.8%–100%, and the baseline HVPG values were 14–19 mmHg. In fact, sarcopenia is relatively frequently found in advanced liver disease or the decompensated stage.^{31,32} Furthermore, some characteristics of patients with LC, including the cause of liver disease, decompensated cirrhosis, or oral beta-blocker administration should have been used in the subgroup analyses with the aim of ruling out confounding factors and further identifying a potential association between the muscle quantity and the HVPG value in a certain subgroup of patients with LC. Likewise, adipose tissue change and re-distribution could be affected by BMI and sex.³³ Therefore, for the primary outcome of the adipose tissue, the non-significant summary result may indicate the likelihood of the correlation between adipose tissue indexes and HVPG depending on the baseline characteristics of the included patients.

In addition, the result of the secondary outcome was not robust. It is speculated that a lower cut-off value (42 cm²/m² for men or <38 cm²/m² for women) could identify more individuals with a low muscle quantity and further re-classify a proportion of patients as having sarcopenia; that is, a lower cut-off value of sarcopenia has more statistic power to differentiate patients with different PH stratifications. It is noted that all included studies on the secondary outcome were from Asian countries (Japan and the Republic of Korea). The Asian sarcopenia definition (42 cm²/m² for men or <38 cm²/m² for women) thus allows for better interpretability and practical applicability.⁹

As the present study is a pilot meta-analysis exploring the unknown relationship between two important characteristics of patients with LC, some limitations exist. First, a considerable interindividual variation of baseline characteristics among included patients, especially liver function status, leads to a cautious interpretation of the results. Second, some included studies only presented the effect size instead of analyzing it in the subgroups. The evidence grade is limited by the number of included studies and the data blank. Most importantly, the number of available studies that fulfilled the present study's inclusion criteria is low, precluding meta-regression to further identify the potential confounding factors. Hence, a prospective study dedicated to recording relevant information is required in the future.

In conclusion, overall, this meta-analysis showed a non-significant correlation between body composition parameters, including muscle and adipose tissue quantity, and the HVPG value. However, its current clinical usefulness is uncertain due to a lack of universal definition and limited research.

Reporting checklist

This review was performed following the 2020 Preferred Reporting Items for Systematic Reviews and Meta-Analyses (PRISMA) statement.

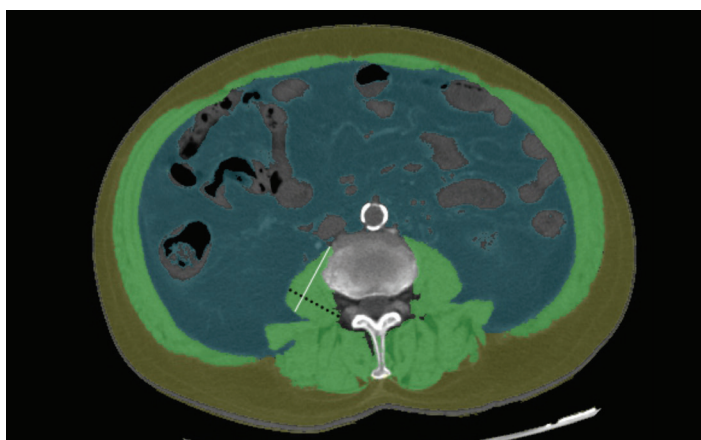
Conflict of interest disclosure

The authors declared no conflicts of interest.

References

- Lai JC, Tandon P, Bernal W, et al. Malnutrition, frailty, and sarcopenia in patients with cirrhosis: 2021 Practice Guidance by the American Association for the Study of Liver Diseases. *Hepatology*. 2021;74(3):1611-1644. [\[CrossRef\]](#)
- Welch N, Dasarathy J, Runkana A, et al. Continued muscle loss increases mortality in cirrhosis: impact of aetiology of liver disease. *Liver Int*. 2020;40(5):1178-1188. [\[CrossRef\]](#)
- Montano-Loza AJ, Meza-Junco J, Prado CM, et al. Muscle wasting is associated with mortality in patients with cirrhosis. *Clin Gastroenterol Hepatol*. 2012;10(2):166-173. [\[CrossRef\]](#)
- Yang S, Zhang Z, Su T, et al. CT-based skeletal muscle loss for predicting poor survival in patients with hepatocellular carcinoma experiencing curative hepatectomy plus adjuvant transarterial chemoembolization: a preliminary retrospective study. *Eur J Med Res*. 2022;27(1):131. [\[CrossRef\]](#)
- Rodrigues SG, Brabant B, Stirnimann G, Maurer MH, Berzigotti A. Adipopenia correlates with higher portal pressure in patients with cirrhosis. *Liver Int*. 2019;39(9):1672-1681. [\[CrossRef\]](#)
- Ebadi M, Tandon P, Moctezuma-Velazquez C, et al. Low subcutaneous adiposity associates with higher mortality in female patients with cirrhosis. *J Hepatol*. 2018;69(3):608-616. [\[CrossRef\]](#)
- Li CW, Yu K, Shyh-Chang N, et al. Pathogenesis of sarcopenia and the relationship with fat mass: descriptive review. *J Cachexia Sarcopenia Muscle*. 2022;13(2):781-794. [\[CrossRef\]](#)
- European Association for the Study of the Liver. Electronic address: easloffice@easloffice.eu; European Association for the Study of the Liver. EASL Clinical Practice Guidelines on nutrition in chronic liver disease. *J Hepatol*. 2019;70(1):172-193. [\[CrossRef\]](#)
- Nishikawa H, Shiraki M, Hiramatsu A, Moriya K, Hino K, Nishiguchi S. Japan Society of Hepatology guidelines for sarcopenia in liver disease (1st edition): recommendation from the working group for creation of sarcopenia assessment criteria. *Hepatol Res*. 2016;46(10):951-963. [\[CrossRef\]](#)
- Bosch J, Abraldes JG, Berzigotti A, Garcia-Pagan JC. The clinical use of HVPG measurements in chronic liver disease. *Nat Rev Gastroenterol Hepatol*. 2009;6(10):573-582. [\[CrossRef\]](#)
- de Franchis R, Bosch J, Garcia-Tsao G, Reiberger T, Ripoll C; Baveno VII Faculty. Baveno VII - renewing consensus in portal hypertension. *J Hepatol*. 2022;76(4):959-974. [\[CrossRef\]](#)
- Eguchi Y, Eguchi T, Mizuta T, et al. Visceral fat accumulation and insulin resistance are important factors in nonalcoholic fatty liver disease. *J Gastroenterol*. 2006;41(5):462-469. [\[CrossRef\]](#)
- Kumar R, Prakash SS, Priyadarshi RN, Anand U. Sarcopenia in chronic liver disease: a metabolic perspective. *J Clin Transl Hepatol*. 2022;10(6):1213-1222. [\[CrossRef\]](#)
- Lee YH, Kim SU, Song K, et al. Sarcopenia is associated with significant liver fibrosis independently of obesity and insulin resistance in nonalcoholic fatty liver disease: nationwide surveys (KNHANES 2008-2011). *Hepatology*. 2016;63(3):776-786. [\[CrossRef\]](#)
- Kumar A, Davuluri G, Silva RNE, et al. Ammonia lowering reverses sarcopenia of cirrhosis by restoring skeletal muscle proteostasis. *Hepatology*. 2017;65(6):2045-2058. [\[CrossRef\]](#)
- Matsui T, Nagai H, Watanabe G, et al. Measurement of skeletal muscle volume is useful for predicting prognosis in patients with liver cirrhosis. *Eur J Gastroenterol Hepatol*. 2022;34(11):1151-1157. [\[CrossRef\]](#)
- Maruyama H, Kobayashi K, Kiyono S, et al. Compensating effect of minor portal hypertension on the muscle mass loss-related poor prognosis in cirrhosis. *Int J Med Sci*. 2017;14(9):804-810. [\[CrossRef\]](#)
- Cho YS, Lee HY, Jeong JY, et al. Computed tomography-determined body composition abnormalities usefully predict long-term mortality in patients with liver cirrhosis. *J Comput Assist Tomogr*. 2021;45(5):684-690. [\[CrossRef\]](#)
- Zeng X, Shi ZW, Yu JJ, et al. Skeletal muscle alterations indicate poor prognosis in cirrhotic patients: a multicenter cohort study in China. *Hepatol Int*. 2023. [\[CrossRef\]](#)
- Page MJ, McKenzie JE, Bossuyt PM, et al. The PRISMA 2020 statement: an updated guideline for reporting systematic reviews. *BMJ*. 2021;372:n71. [\[CrossRef\]](#)
- McGrath S, Zhao X, Steele R, Thombs BD, Benedetti A; DEPRESSion Screening Data (DEPRESSD) collaboration. Estimating the sample mean and standard deviation from commonly reported quantiles in meta-analysis. *Stat Methods Med Res*. 2020;29(9):2520-2537. [\[CrossRef\]](#)
- Fonseca-Rodrigues D, Rodrigues A, Martins T, et al. Correlation between pain severity and levels of anxiety and depression in osteoarthritis patients: a systematic review and meta-analysis. *Rheumatology (Oxford)*. 2021;61(1):53-75. [\[CrossRef\]](#)
- Dalton JE, Bolen SD, Mascha EJ. Publication bias: the elephant in the review. *Anesth Analg*. 2016;123(4):812-813. [\[CrossRef\]](#)
- Jeong JY, Lim S, Sohn JH, Lee JG, Jun DW, Kim Y. Presence of sarcopenia and its rate of change are independently associated with long-term mortality in patients with liver cirrhosis. *J Korean Med Sci*. 2018;33(50):e299. [\[CrossRef\]](#)
- Paternostro R, Bardach C, Hofer BS, et al. Prognostic impact of sarcopenia in cirrhotic patients stratified by different severity of portal hypertension. *Liver Int*. 2021;41(4):799-809. [\[CrossRef\]](#)
- Kim TY, Kim MY, Sohn JH, et al. Sarcopenia as a useful predictor for long-term mortality in cirrhotic patients with ascites. *J Korean Med Sci*. 2014;29(9):1253-1259. [\[CrossRef\]](#)
- Kang SH, Jeong WK, Baik SK, Cha SH, Kim MY. Impact of sarcopenia on prognostic value of cirrhosis: going beyond the hepatic venous pressure gradient and MELD score. *J Cachexia Sarcopenia Muscle*. 2018;9(5):860-870. [\[CrossRef\]](#)

28. Zhao X, Alabdulkarim B, Kablawi D, et al. Low subcutaneous adipose tissue is associated with mortality independently from portal hypertension in patients with cirrhosis. Conference abstract. *Journal of Hepatology*. 2022;77:S614. [CrossRef]
29. Wells CI, McCall JL, Plank LD. Relationship between total body protein and cross-sectional skeletal muscle area in liver cirrhosis is influenced by overhydration. *Liver Transpl*. 2019;25(1):45-55. [CrossRef]
30. Ebadi M, Wang CW, Lai JC, et al. Poor performance of psoas muscle index for identification of patients with higher waitlist mortality risk in cirrhosis. *J Cachexia Sarcopenia Muscle*. 2018;9(6):1053-1062. [CrossRef]
31. Montano-Loza AJ, Meza-Junco J, Baracos VE, et al. Severe muscle depletion predicts postoperative length of stay but is not associated with survival after liver transplantation. *Liver Transpl*. 2014;20(6):640-648. [CrossRef]
32. Tandon P, Ney M, Irwin I, et al. Severe muscle depletion in patients on the liver transplant wait list: its prevalence and independent prognostic value. *Liver Transpl*. 2012;18(10):1209-1216. [CrossRef]
33. Noori N, Kovesdy CP, Dukkipati R, et al. Survival predictability of lean and fat mass in men and women undergoing maintenance hemodialysis. *Am J Clin Nutr*. 2010;92(5):1060-1070. [CrossRef]



Supplementary Figure 1. The skeletal muscle index was the total skeletal muscle area normalized by height², including the psoas major, erector spinae, quadratus lumborum, transverse abdominis, internal and external oblique, and rectus abdominis (green mask). Transversal-psoas muscle thickness and psoas muscle thickness by height were named differently but measured in the same way; they were defined as the transversal diameter of the psoas muscle perpendicular to the largest axial psoas muscle diameter. Therefore, the psoas-muscle-related index replaced two aforementioned indexes for statistics (dotted line). The subcutaneous adipose tissue index and visceral adipose tissue index were estimated as the adipose area normalized by height² between the skin line and outer abdominal wall (yellow mask) and the adipose tissue within the abdominal wall, respectively (blue mask).

Supplementary Table S1. GRADE summary of findings of secondary outcome

Patient or population: Patients with HVPG value and CT-based body composition parameter
Question: HVPG of sarcopenia compared to HVPG of non-sarcopenia for liver cirrhosis patients

Setting: All

Bibliography:

Certainty assessment		No of patients		Effect		Certainty		Importance				
No of studies	Study design	Risk of bias	Inconsistency	Indirectness	Imprecision	Other considerations	HVPG of sarcopenia	HVPG of non-sarcopenia	Relative (95% CI)	Anticipated absolute effects (95% CI)		
SMD (Western cut-off)												
2	Observational studies	Not serious	Not serious	Not serious	Serious ^a	Strong association all plausible residual confounding would reduce the demonstrated effect	254/583 (43.6%)	329/583 (56.4%)	Not estimable	SMD -0.20 (-0.37 lower to -0.04 higher)	⊕⊕⊕○ Moderate	Important
SMD (Eastern cut-off)												
2	Observational studies	Not serious	Very serious ^b	Not serious	Serious ^c	Strong association all plausible residual confounding would reduce the demonstrated effect	177/300 (59.0%)	123/300 (41.0%)	Not estimable	SMD 0.63 (-0.35 lower to 1.61 higher)	⊕○○○ Very low	Important

^a, obvious benefit or damage; ^b, I² value is more than 90% and a good explanation could not be given; ^c, the 95% confidence interval contains 1 and is invalid, GRADE, Grading of Recommendations Assessment, Development and Evaluation; HVPG, hepatic venous pressure gradient; CT, computed tomography; SMD, standardized mean difference; CI, confidence interval.

Online Resource 1.



PRISMA 2020 Checklist

Section and Topic	Item #	Checklist item	Location where item is reported
TITLE			
Title	1	Identify the report as a systematic review.	Line 1-2
ABSTRACT			
Abstract	2	See the PRISMA 2020 for Abstracts checklist.	Line 3-28
INTRODUCTION			
Rationale	3	Describe the rationale for the review in the context of existing knowledge.	Line 61-82
Objectives	4	Provide an explicit statement of the objective(s) or question(s) the review addresses.	Line 83-88
METHODS			
Eligibility criteria	5	Specify the inclusion and exclusion criteria for the review and how studies were grouped for the syntheses.	Line 98-105
Information sources	6	Specify all databases, registers, websites, organisations, reference lists and other sources searched or consulted to identify studies. Specify the date when each source was last searched or consulted.	Line 107-110
Search strategy	7	Present the full search strategies for all databases, registers and websites, including any filters and limits used.	Line 110
Selection process	8	Specify the methods used to decide whether a study met the inclusion criteria of the review, including how many reviewers screened each record and each report retrieved, whether they worked independently, and if applicable, details of automation tools used in the process.	Line 111-123
Data collection process	9	Specify the methods used to collect data from reports, including how many reviewers collected data from each report, whether they worked independently, any processes for obtaining or confirming data from study investigators, and if applicable, details of automation tools used in the process.	Line 143-151
Data items	10a	List and define all outcomes for which data were sought. Specify whether all results that were compatible with each outcome domain in each study were sought (e.g. for all measures, time points, analyses), and if not, the methods used to decide which results to collect.	Line 130-134
	10b	List and define all other variables for which data were sought (e.g. participant and intervention characteristics, funding sources). Describe any assumptions made about any missing or unclear information.	Line 143-149
Study risk of bias assessment	11	Specify the methods used to assess risk of bias in the included studies, including details of the tool(s) used, how many reviewers assessed each study and whether they worked independently, and if applicable, details of automation tools used in the process.	Line 152-158
Effect measures	12	Specify for each outcome the effect measure(s) (e.g. risk ratio, mean difference) used in the synthesis or presentation of results.	Line 130-134
Synthesis methods	13a	Describe the processes used to decide which studies were eligible for each synthesis (e.g. tabulating the study intervention characteristics and comparing against the planned groups for each synthesis (item #5)).	Line 185-186
	13b	Describe any methods required to prepare the data for presentation or synthesis, such as handling of missing summary statistics, or data conversions.	Line 163-176
	13c	Describe any methods used to tabulate or visually display results of individual studies and syntheses.	Line 177-180
	13d	Describe any methods used to synthesize results and provide a rationale for the choice(s). If meta-analysis was performed, describe the model(s), method(s) to identify the presence and extent of statistical heterogeneity, and software package(s) used.	Line 177
	13e	Describe any methods used to explore possible causes of heterogeneity among study results (e.g. subgroup analysis, meta-regression).	Line 172-176
	13f	Describe any sensitivity analyses conducted to assess robustness of the synthesized results.	Line 175
Reporting bias assessment	14	Describe any methods used to assess risk of bias due to missing results in a synthesis (arising from reporting biases).	not applicable
Certainty assessment	15	Describe any methods used to assess certainty (or confidence) in the body of evidence for an outcome.	Line 155-158



PRISMA 2020 Checklist

Section and Topic	Item #	Checklist item	Location where item is reported
RESULTS			
Study selection	16a	Describe the results of the search and selection process, from the number of records identified in the search to the number of studies included in the review, ideally using a flow diagram.	Line 175-179
	16b	Cite studies that might appear to meet the inclusion criteria, but which were excluded, and explain why they were excluded.	Line 177-179
Study characteristics	17	Cite each included study and present its characteristics.	Line 180-200
Risk of bias in studies	18	Present assessments of risk of bias for each included study.	Line 201-203
Results of individual studies	19	For all outcomes, present, for each study: (a) summary statistics for each group (where appropriate) and (b) an effect estimate and its precision (e.g. confidence/credible interval), ideally using structured tables or plots.	Line 204-233
Results of syntheses	20a	For each synthesis, briefly summarise the characteristics and risk of bias among contributing studies.	Line 204-233
	20b	Present results of all statistical syntheses conducted. If meta-analysis was done, present for each the summary estimate and its precision (e.g. confidence/credible interval) and measures of statistical heterogeneity. If comparing groups, describe the direction of the effect.	Line 204-233
	20c	Present results of all investigations of possible causes of heterogeneity among study results.	Line 204-233
	20d	Present results of all sensitivity analyses conducted to assess the robustness of the synthesized results.	Line 204-233
Reporting biases	21	Present assessments of risk of bias due to missing results (arising from reporting biases) for each synthesis assessed.	not applicable
Certainty of evidence	22	Present assessments of certainty (or confidence) in the body of evidence for each outcome assessed.	Line 204-233
DISCUSSION			
Discussion	23a	Provide a general interpretation of the results in the context of other evidence.	Line 236-243
	23b	Discuss any limitations of the evidence included in the review.	Line 297-302
	23c	Discuss any limitations of the review processes used.	Line 297-302
	23d	Discuss implications of the results for practice, policy, and future research.	Line 303-307
OTHER INFORMATION			
Registration and protocol	24a	Provide registration information for the review, including register name and registration number, or state that the review was not registered.	Line 86-87
	24b	Indicate where the review protocol can be accessed, or state that a protocol was not prepared.	Line 86-87
	24c	Describe and explain any amendments to information provided at registration or in the protocol.	not applicable
Support	25	Describe sources of financial or non-financial support for the review, and the role of the funders or sponsors in the review.	not applicable
Competing interests	26	Declare any competing interests of review authors.	not applicable
Availability of data, code and other materials	27	Report which of the following are publicly available and where they can be found: template data collection forms; data extracted from included studies; data used for all analyses; analytic code; any other materials used in the review.	available

From: Page MJ, McKenzie JE, Bossuyt PM, Boutron I, Hoffmann TC, Mulrow CD, et al. The PRISMA 2020 statement: an updated guideline for reporting systematic reviews. *BMJ* 2021;372:n71. doi: 10.1136/bmj.n71

For more information, visit: <http://www.prisma-statement.org/>

Online Resource 2.

Pubmed searching strategy

#1	<p>(((((("Body Composition"[Mesh]) OR ("Intra-Abdominal Fat"[Mesh])) OR ("Subcutaneous Fat"[Mesh])) OR ("Adiposity"[Mesh])) OR ("Sarcopenia"[Mesh])) OR ("Muscle, Skeletal"[Mesh])) AND (((Hepatic venous pressure gradient[Title/Abstract]) OR ("Hypertension, Portal"[Mesh])) OR ("Hepatic Veins"[Mesh])) OR ("Portal Pressure"[Mesh]))</p>	156
#2	<p>((((((((pressure, portal[Title/Abstract]) OR (portal venous pressure[Title/Abstract])) OR (pressure, portal venous[Title/Abstract])) OR (venous pressure, portal[Title/Abstract])) OR ((hepatic vein[Title/Abstract]) OR (vein, hepatic[Title/Abstract])) OR (veins, hepatic[Title/Abstract])) OR (((((((portal hypertension[Title/Abstract]) OR (portal hypertensions[Title/Abstract])) OR (cruveilhier-baumgarten syndrome[Title/Abstract])) OR (cruveilhier baumgarten syndrome[Title/Abstract])) OR (syndrome, cruveilhier-baumgarten[Title/Abstract])) OR (cruveilhier-baumgarten disease[Title/Abstract])) OR (cruveilhier baumgarten disease [Title/Abstract])) OR (disease, cruveilhier-baumgarten[Title/Abstract])) OR (Hepatic venous pressure gradient[Title/Abstract])) AND (((((((((((((((muscles, skeletal[Title/Abstract]) OR (skeletal muscles[Title/Abstract])) OR (muscle, voluntary[Title/Abstract])) OR (muscles, voluntary[Title/Abstract])) OR (voluntary muscle[Title/Abstract])) OR (voluntary muscles[Title/Abstract])) OR (skeletal muscle[Title/Abstract])) OR (soleus muscle[Title/Abstract])) OR (muscle, soleus[Title/Abstract])) OR (plant aris muscle[Title/Abstract])) OR (muscle, plantaris[Title/Abstract])) OR (anterior tibial muscle[Title/Abstract])) OR (muscle, anterior tibial[Title/Abstract])) OR (tibial muscle, anterior[Title/Abstract])) OR (gastrocnemius muscle[Title/Abstract])) OR (muscle, gastrocnemius[Title/Abstract])) OR (((sarcopenias[Title/Abstract]) OR (presarcopenia[Title/Abstract])) OR (skeletal muscle index[Title/Abstract])) OR (SMI[Title/Abstract])) OR (muscle atrophy[Title/Abstract])) OR (((fats, subcutaneous[Title/Abstract]) OR (subcutaneous fats[Title/Abstract])) OR (adipose tissue, subcutaneous[Title/Abstract])) OR (fat, subcutaneous [Title/Abstract])) OR (subcutaneous adipose tissue[Title/Abstract])) OR (((((((((((((((fats, intra-abdominal[Title/Abstract]) OR (intra abdominal fat[Title/Abstract])) OR (intra-abdominal fats[Title/Abstract])) OR (fat, intra-abdominal[Title/Abstract]) OR (fat, intra abdominal[Title/Abstract])) OR (intra-abdominal adipose tissue[Title/Abstract])) OR (adipose tissue, intra-abdominal[Title/Abstract])) OR (intra abdominal adipose tissue[Title/Abstract])) OR (retroperitoneal fat[Title/Abstract])) OR (fat, retroperitoneal[Title/Abstract])) OR (fats, retroperitoneal[Title/Abstract])) OR (retroperitoneal fats[Title/Abstract])) OR (retr operitoneal adipose tissue[Title/Abstract])) OR (adipose tissue, retroperitoneal[Title/Abstract])) OR (visceral fat[Title/Abstract]) OR (fat, visceral[Title/Abstract])) OR (fats, visceral[Title/Abstract])) OR (visceral fats[Title/Abstract])) OR (abdominal v isceral fat[Title/Abstract])) OR (abdominal visceral fats[Title/Abstract])) OR (fat, abdominal visceral[Title/Abstract])) OR (fat s, abdominal visceral[Title/Abstract])) OR (visceral adipose tissue[Title/Abstract])) OR (adipose tissue, visceral[Title/Abstract]) OR (((body compositions[Title/Abstract]) OR (composition, body[Title/Abstract])) OR (compositions, body[Title/Abstract]))</p>	90
<p>#1: MeSH word search</p> <p>#2: Text word search</p>		

Embase searching strategy

#1	'hepatic venous pressure gradient'/exp	1,042
#2	'portal vein blood pressure'/exp	6,542
#3	'portal hypertension'/exp	41,132
#4	'hepatic vein pressure gradient':ti,ab,kw OR 'porta pressure':ti,ab,kw OR 'porta vein pressure':ti,ab,kw OR 'portal blood pressure':ti,ab,kw OR 'portal pressure':ti,ab,kw OR 'portal vein pressure':ti,ab,kw OR 'portal venous pressure':ti,ab,kw OR 'pressure, portal vein':ti,ab,kw OR 'hypertension, portal':ti,ab,kw OR 'hypertension, portal vein':ti,ab,kw OR 'porta hypertension':ti,ab,kw OR 'portal congestion':ti,ab,kw OR 'portal vein hypertension':ti,ab,kw OR 'vena portae hypertension':ti,ab,kw	6,933
#5	'skeletal muscle'/exp	432,889
#6	'sarcopenia'/exp	20,474
#7	'subcutaneous fat'/exp	25,911
#8	'body composition'/exp	128,357
#9	'intra-abdominal fat'/exp	25,745
#10	'cross striated muscle':ab,ti OR 'cross striped muscle':ab,ti OR 'muscle, skeletal':ab,ti OR 'skeletal musculature':ab,ti OR 'skeleton muscle':ab,ti OR 'trunk muscle':ab,ti OR presarcopenia:ab,ti OR 'fat, subcutaneous':ab,ti OR 'panniculus adiposus':ab,ti OR 'subcutaneous adipose tissue':ab,ti OR 'subcutaneous fat tissue':ab,ti OR 'abdominal visceral adipose tissue':ab,ti OR 'abdominal visceral fat':ab,ti OR 'intra-abdominal adipose tissue':ab,ti OR 'intraabdominal adipose tissue':ab,ti OR 'intraabdominal fat':ab,ti OR 'organ adipose tissue':ab,ti OR 'organ fat':ab,ti OR 'visceral abdominal adipose tissue':ab,ti OR 'visceral abdominal fat':ab,ti OR 'visceral adipose tissue':ab,ti OR 'visceral fat':ab,ti OR 'composition, body':ab,ti	36,031
#11	#1 OR #2 OR #3 OR #4	45,318
#12	#5 OR #6 OR #7 OR #8 OR #9 OR #10	596,687
#13	#11 AND #12	379

Web of Science searching strategy

#1	TS="Hepatic venous pressure gradient" OR "hepatic vein pressure gradient" OR "portal vein blood pressure" OR "porta pressure" OR "porta vein pressure" OR "portal blood pressure" OR "portal pressure" OR "portal vein pressure" OR "portal venous pressure" OR "pressure, portal vein" OR "portal hypertension" OR "hypertension, portal" OR "hypertension, portal vein" OR "porta hypertension" OR "portal congestion" OR "portal vein hypertension" OR "vena portae hypertension"	23,028
#2	TS="skeletal muscle" OR "cross striated muscle" OR "cross striped muscle" OR "muscle, skeletal" OR "skeletal musculature" OR "skeleton muscle" OR "trunk muscle" OR "Sarcopenia" OR "presarcopenia"	226,391
#3	TS="Subcutaneous Fat" OR "fat, subcutaneous" OR "panniculus adiposus" OR "subcutaneous adipose tissue" OR "subcutaneous fat tissue" OR "intra-abdominal fat" OR "abdominal visceral adipose tissue" OR "abdominal visceral fat" OR "intra-abdominal adipose tissue" OR "intraabdominal adipose tissue" OR "intraabdominal fat" OR "organ adipose tissue" OR "organ fat" OR "visceral abdominal adipose tissue" OR "visceral abdominal fat" OR "visceral adipose tissue" OR "visceral fat" OR "body composition" OR "composition, body"	113,631
#4	#2 OR #3	325,823
#5	#1 AND #4	161

Cochrane searching strategy

Mesh word search

#1	MeSH descriptor: [Muscle, Skeletal] explode all trees	15,568
#2	MeSH descriptor: [Sarcopenia] explode all trees	835
#3	MeSH descriptor: [Adiposity] explode all trees	964
#4	MeSH descriptor: [Subcutaneous Fat] explode all trees	407
#5	MeSH descriptor: [Intra-Abdominal Fat] explode all trees	576
#6	MeSH descriptor: [Body Composition] explode all trees	7120
#7	MeSH descriptor: [Portal Pressure] explode all trees	71
#8	MeSH descriptor: [Hepatic Veins] explode all trees	115
#9	MeSH descriptor: [Hypertension, Portal] explode all trees	1374
#10	("hepatic venous pressure gradient"):ti,ab,kw (Word variations have been searched)	332
#11	("hepatic vein pressure gradient"):ti,ab,kw (Word variations have been searched)	26
#12	#10 or #11	353
#13	#1 or #2 or #3 or #4 or #5 or #6	22,925
#14	#7 or #8 or #9 or #12	1,663
#15	#13 and #14	6

Text word search

#1	(muscles, skeletal):ti,ab,kw OR (skeletal muscles):ti,ab,kw OR (muscle, voluntary):ti,ab,kw OR (muscles, voluntary):ti,ab,kw OR (voluntary muscle):ti,ab,kw (Word variations have been searched)	18,384
#2	(voluntary muscles):ti,ab,kw OR (skeletal muscle):ti,ab,kw OR (soleus muscle):ti,ab,kw OR (muscle, soleus):ti,ab,kw OR (plantaris muscle):ti,ab,kw (Word variations have been searched)	18,848
#3	(muscle, plantaris):ti,ab,kw OR (anterior tibial muscle):ti,ab,kw OR (muscle, anterior tibial):ti,ab,kw OR (tibial muscle, anterior):ti,ab,kw OR (gastrocnemius muscle):ti,ab,kw (Word variations have been searched)	1,894
#4	(muscle, gastrocnemius):ti,ab,kw (Word variations have been searched)	1,597
#5	#1 or #2 or #3 or #4	19,793
#6	(sarcopenias):ti,ab,kw OR (presarcopenia):ti,ab,kw OR (skeletal muscle index):ti,ab,kw OR (SMI):ti,ab,kw OR (muscle atrophy):ti,ab,kw (Word variations have been searched)	8,939
#7	(fats, subcutaneous):ti,ab,kw OR (subcutaneous fats):ti,ab,kw OR (adipose tissue, subcutaneous):ti,ab,kw OR (fat, subcutaneous):ti,ab,kw OR (subcutaneous adipose tissue):ti,ab,kw (Word variations have been searched)	3,239
#8	(fats, intra-abdominal):ti,ab,kw OR (intra abdominal fat):ti,ab,kw OR (intra-abdominal fats):ti,ab,kw OR (fat, intra-abdominal):ti,ab,kw OR (fat, intra abdominal):ti,ab,kw (Word variations have been searched)	1,259
#9	(intra-abdominal adipose tissue):ti,ab,kw OR (adipose tissue, intra-abdominal):ti,ab,kw OR (intra abdominal adipose tissue):ti,ab,kw OR (retroperitoneal fat):ti,ab,kw OR (fat, retroperitoneal):ti,ab,kw (Word variations have been searched)	594
#10	(fats, retroperitoneal):ti,ab,kw OR (retroperitoneal fats):ti,ab,kw OR (retroperitoneal adipose tissue):ti,ab,kw OR (adipose tissue, retroperitoneal):ti,ab,kw OR (visceral fat):ti,ab,kw (Word variations have been searched)	3,087
#11	(fat, visceral):ti,ab,kw OR (fats, visceral):ti,ab,kw OR (visceral fats):ti,ab,kw OR (abdominal visceral fat):ti,ab,kw OR (abdominal visceral fats):ti,ab,kw (Word variations have been searched)	3,066
#12	(fat, abdominal visceral):ti,ab,kw OR (fats, abdominal visceral):ti,ab,kw OR (visceral adipose tissue):ti,ab,kw OR (adipose tissue, visceral):ti,ab,kw (Word variations have been searched)	2,301
#13	#8 or #9 or #10 or #11 or #12	3,486
#14	(body compositions):ti,ab,kw OR (composition, body):ti,ab,kw OR (compositions, body):ti,ab,kw (Word variations have been searched)	23,051
#15	(pressure, portal):ti,ab,kw OR (portal venous pressure):ti,ab,kw OR (pressure, portal venous):ti,ab,kw OR (venous pressure, portal):ti,ab,kw (Word variations have been searched)	1,133
#16	(hepatic vein):ti,ab,kw OR (vein, hepatic):ti,ab,kw OR (veins, hepatic):ti,ab,kw (Word variations have been searched)	1,743
#17	(portal hypertension):ti,ab,kw OR (portal hypertensions):ti,ab,kw OR (cruveilhier-baumgarten syndrome):ti,ab,kw OR (cruveilhier baumgarten syndrome):ti,ab,kw OR (syndrome, cruveilhier-baumgarten):ti,ab,kw (Word variations have been searched)	1,815
#18	(cruveilhier-baumgarten disease):ti,ab,kw OR (cruveilhier baumgarten disease):ti,ab,kw OR (disease, cruveilhier-baumgarten):ti,ab,kw (Word variations have been searched)	0
#19	#17 or #18	1,815
#20	(Hepatic venous pressure gradient):ti,ab,kw OR (hepatic vein pressure gradient):ti,ab,kw OR (HVPG):ti,ab,kw (Word variations have been searched)	497
#21	#5 or #6 or #7 or #13 or #14	47,332
#22	#15 or #16 or #19 or #20	3,731
#23	#21 and #22	86
#23 includes two Cochrane reviews and 84 trials		

Online Resource 1.

Quality assessment based on QUADAS-2							
Study	Risk of bias				Applicability concerns		
	P	I	R	FT	P	I	R
Jeong, J. Y.(2018)	?	✓	✓	✓	?	✓	✓
Paternostro, R.(2021)	✓	✓	?	✓	✓	✓	?
Maruyama, H. (2017)	?	✓	✓	✓	?	✓	✓
Kim, T. Y. (2014)	✓	✗	?	✓	✗	✗	?
Kang, S. H. (2018)	✓	✓	✓	✓	✓	✓	✓
Matsui, T. (2022)	?	✓	✓	?	?	✓	✓
Cho, Y. S.(2021)	?	✓	✓	✓	?	✓	✓
Rodrigues, S. G.(2019)	✓	✓	✓	✓	✓	✓	✓
Xin Zeng(2023)	✓	✓	✓	✓	✓	✓	✓

Note: P = Patient Selection; I = Index Test; R = Reference Standard; FT = Flow and Timing.

✓ indicates low risk; ✗ indicates high risk; ? indicates unclear risk.

Detailed description of included studies

Study	Domain	Item	Description of decision
Jeong, J. Y.(2018)	Risk of bias	P	A consecutive or random sample was not described, but with a clear period
		I	
		R	
		FT	
Paternostro, R.(2021)	Applicability concerns	P	A consecutive or random sample was not described, but with a clear period
		I	
		R	
Paternostro, R.(2021)	Risk of bias	P	
		I	
		R	The value of TPMT for sarcopenia definition compared with SMI was uncertain
		FT	
Paternostro, R.(2021)	Applicability concerns	P	
		I	
		R	The value of TPMT for sarcopenia definition compared with SMI was uncertain
Maruyama, H. (2017)	Risk of bias	P	Of 98 patients, one with paraumbilical vein was excluded due to shunt-related increase of portal venous flow(pr oportion less than 20%)
		I	
		R	
		FT	
Maruyama, H. (2017)	Applicability concerns	P	Thirteen patients with HCC at early stage were included, the impact of early HCC on muscle loss is uncertain
		I	
		R	
Kim, T. Y. (2014)	Risk of bias	P	
		I	The threshold was derived from mortality with maximum

		log-rank statistic instead of a pre-specified value
	R	The value of PMTH for sarcopenia definition compared with SMI is uncertain
	FT	
Applicability concerns	P	All included patients were non-critically-ill patients with decompensated cirrhosis
	I	The threshold was derived from mortality with maximum log-rank statistic instead of a pre-specified value
	R	The value of PMTH for sarcopenia definition compared with SMI is uncertain
Risk of bias	P	
	I	
	R	
Kang, S. H. (2018)	FT	
Applicability concerns	P	
	I	
	R	
Risk of bias	P	A consecutive or random sample was not described, but with a clear period
	I	
	R	
Matsui, T. (2022)	FT	The interval was not described; liver fibrosis or cirrhosis is a chronic condition.
Applicability concerns	P	A consecutive or random sample was not described, but with a clear period
	I	
	R	
Cho, Y. S.(2021)	P	A consecutive or random sample was not described, but with a clear period
	I	
	R	
	FT	

		P	A consecutive or random sample was not described, but with a clear period
	Applicability concerns	I	
		R	
		P	
	Risk of bias	I	
		R	
Rodrigues, S. G.(2019)		FT	
	Applicability concerns	P	
		I	
		R	
		P	
	Risk of bias	I	
		R	
Xin Zeng(2023)		FT	
	Applicability concerns	P	
		I	
		R	

Note: hepatocellular carcinoma: HCC



Experimental study of a canine model for a newly designed adjustable prefenestration aortic stent graft

Lei Zhang^{1,2*}
 Chang Shu^{1,2,3*}
 Yuchen Qiu⁴
 Zeliang Fu⁴
 Pengcheng Guo^{1,2}
 Xin Li^{1,2}

¹Central South University, The Second Xiangya Hospital, Vascular Center, Department of Vascular Surgery, Changsha, China

²Central South University, The Institute of Vascular Diseases, Changsha, China

³State Key Laboratory of Cardiovascular Diseases, Center of Vascular Surgery, Fuwai Hospital, National Center for Cardiovascular Diseases, Chinese Academy of Medical Science and Peking Union Medical College, Beijing, China

⁴APT Medical, Shenzhen, China

*Joint first authors

Corresponding author: Xin Li

E-mail: lixin1981@csu.edu.cn

Received 30 August 2023; revision requested 30 September 2023; accepted 15 December 2023.



Epub: 31.01.2024

Publication date: 06.11.2024

DOI: 10.4274/dir.2023.232440

PURPOSE

When performing thoracic aortic endovascular repair (TEVAR) on lesions of the aortic arch, physician-modified fenestration or *in situ* fenestration is often used to maintain patent branches. We designed a new adjustable prefenestration aortic stent graft that can both isolate pathologies in the aortic arch and obtain patent branches simultaneously. In this study, we use this new type of stent to perform fenestrated TEVAR in a canine's aorta. This study aims to evaluate the safety and feasibility of the new device, which may provide preliminary data for potential human application.

METHODS

Eight Labrador Retriever canines underwent fenestrated TEVAR using the new stent device. Digital subtract angiography (DSA) was performed before and after fenestrated TEVAR to evaluate the safety and feasibility of the procedure. For the device deployment, at the "large curvature" side in the endograft, there is a rectangular prefenestration area (2 × 5 cm) without the polytetrafluoroethylene membrane, and at both longer side edges of the fenestration, there are two slide rails. A moveable membrane that covers the same area as the prefenestration area is initially set at the prefenestration position. A stay line is connected from the distal site of the moveable membrane that controls it to the distal position along the slide rail, which releases the fenestration. After the positioning of the prefenestration is determined, the outer sheath of the delivery system is released, and the stay line at the end of the delivery system is pulled outside the body. The animals were divided into a 1-month group (n = 4) and a 3-month group (n = 4) after the fenestrated TEVAR. Computed tomography (CT) was performed before euthanasia, and video of the DSA during the procedures and CT angiography (CTA) images were then studied.

RESULTS

The procedure success rate was 100%, but the total survival rate was only 87.5%. There were no aortic-related deaths during follow-up, and during the operation, there were no stent-graft-related accidents. In addition, no stent-graft migrations were observed in the CTA, and all branch arteries were kept patent by the adjustable fenestration. Finally, histological examination and electron microscope results showed no obvious vascular injury or inflammation.

CONCLUSION

Based on the results of this study, we judge the safety and feasibility of the use of the newly designed adjustable prefenestration aortic stent graft in a fenestrated-TEVAR canine model to be acceptable. Our preliminary data may serve as an initial reference for evaluating the potential application of the new stent in humans.

KEYWORDS

Thoracic aortic endovascular repair, fenestrated thoracic aortic endovascular repair, adjustable prefenestration aortic stent graft, canine, aortic arch

Thoracic aortic endovascular repair (TEVAR) is the most successful minimally invasive treatment for aortic pathologies developed in the past 3 decades. Currently, there is also a “hybrid operation” involving TEVAR and extra-anatomic bypass for lesions involving the aortic arch, which is even more minimally invasive and may reduce complication rates compared with open surgery under extracorporeal circulation.^{1,2} At present, the most difficult issue for the use of TEVAR in the aortic arch is simultaneously isolating the pathologies without endoleak and keeping the superior arch branches patent; fenestration in the stent graft is often used to meet both of these objectives.

The fenestration technique falls into two categories, physician-modified graft fenestration (PMGF)^{3,4} and *in situ* fenestration.⁵ The former involves relatively simple manipulation but carries with it the possibility of misfitting the fenestration and branch orifices. The latter method requires a large number of endovascular devices. However, both these techniques share a common shortcoming—the modification of the structure of the endograft may result in physical and dynamic risk. Therefore, TEVAR for proximal aortic arch lesions must be evaluated carefully through further studies with long-term timeframes and specific standardized designs.⁶

Physicians treating aortic arch lesions with an endograft may significantly benefit from an adjustable fenestration device that can adapt to the orifices of the branches. To this end, we designed a method using pre-fenestration in the stent graft and made its position and area adjustable. The new device was fabricated by APT Medical (Xiangxiang,

China, 411400), and we have already tested it in a fluid-dynamic mimic tube system (Figure 1). In this paper, we further examine its safety and feasibility in a canine model based on fenestrated TEVAR.

Methods

This study was approved by the Ethics Committee of the Second Xiangya Hospital (ethics approval number: 2018-S034) and it is also obeyed the laboratory animals practice guidelines of China (YY/T1754.1-2020 pre-clinical animal experiment of medical device). The total number of experimental animals was 8, and their specific type was Labrador Retriever (experimental animal quality certificated number, 370825210100047374, Advanced Medical, Shenzhen, China). There were 3 females and 5 males, and the average weight of the 8 animals was 25.8 ± 3.5 kg.

Device description

The stent graft is composed of a nickel–titanium (NiTi) alloy scaffold and an expanded polytetrafluoroethylene membrane woven to the surface of the scaffold structure. At

the “large curvature” side in the endograft, there is a rectangular prefenestration area (2×5 cm) without the polytetrafluoroethylene membrane, and at both longer side edges of the fenestration, there are two slide rails. A moveable membrane in the same area as that of the prefenestration is initially set at the position of the prefenestration (Figure 1). A stay line is connected from the distal site of the moveable membrane that controls it to the distal position along the slide rail, which releases the fenestration (Figure 1). The stay line is connected to the moveable membrane by a fixed device, and the moveable membrane can be moved backward when the stay line is pulled back. There are also radiopaque markers in the tip head of the delivery system that can show the direction of the fenestration and a radiopaque marker in the middle of the movable membrane that can show the position of the membrane (Figures 1, 2).

The implantation procedure

All the fenestrated-TEVAR procedures using this new stent graft were performed at Advanced Medical’s digital subtraction an-

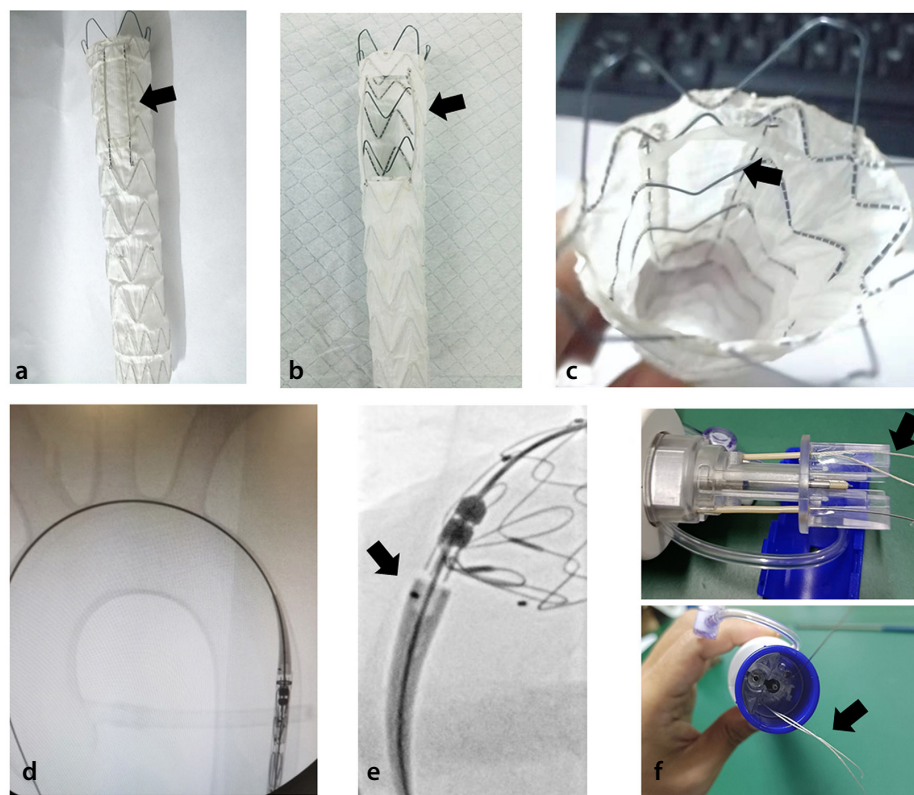


Figure 1. Adjustable prefenestration stent graft. (a) Black arrow shows the prefenestration sealed by a membrane patch. (b) Black arrow shows the fenestration already opened by the membrane patch moving distally. (c) View from the inner angle of the adjustable prefenestration stent graft; black arrow shows the initial situation of the fenestration. (d) X-ray screening of the device by mimicking deployment in a digital subtract angiography operation room. (e) Black arrow shows the radiopaque marker in the tip of the stent graft. (f, g) Black arrows show the stay line at the end of the delivery system that can be loaded in an independent tube.

Main points

- When performing thoracic aortic endovascular repair (TEVAR) on lesions of the aortic arch, fenestration techniques require structural modification of the stent graft.
- We designed a new adjustable prefenestration aortic stent graft that can simultaneously isolate pathologies in the aortic arch and obtain patent branches. In this study, we used this new type of stent to perform fenestrated TEVAR in canine aortas.
- Based on the results of this study, we judge the safety and feasibility of the newly designed adjustable prefenestration aortic stent graft to be acceptable. Our preliminary data may provide a first reference for evaluating the new stent’s potential use in humans.

giography (DSA) theater. The details of the procedures (Figure 2) are as follows. (1) The dogs were placed in a supine position with their extremities fixed. General anesthesia with intubation was then administered, the fur was removed from the groin area, and the exposed skin was sterilized. (2) An incision was then made to the femoral artery on one side using an arterial tourniquet control. After this, the femoral artery was punctured and a 5-French sheath was inserted. (3) The animal was then given 200 IU/kg of heparin, and the 5-French Pigtail catheter (William Cook Europe Aps, Sandet 8 DK-4832 Bjaeverskov, Denmark) was sent to the ascending aorta. Subsequently, DSA was performed to show the aorta and the configuration of its branches. (4) Next, the Lunderquist super stiff guide wire (William Cook Europe) was exchanged through the pigtail catheter, and the sheath was withdrawn. The adjustable prefenestration stent-graft system was then sent to the aortic arch, and the X-ray radiopaque marker in the tip of the head was observed to ensure that the fenestration was in the right position at the aortic "greater curvature" side. (5) The outer sheath of the delivery system was released, and the stay line at the end of the delivery system was pulled outside the body. The radiopaque marker at the movable membrane was used to adjust the position of the fenestration. (6) After the fen-

estration position and release were deemed satisfactory, the rear-release apparatus was unlocked and the entire delivery system was withdrawn. (7) Another DSA was performed to clarify the position of the stent graft/fenestration and the patency of the branches. (8) Finally, the femoral artery was sutured using 6-0 Prolene sutures, and the incision was closed.

All 8 animals were then divided into a 4-week and 12-week follow-up group, at which times computed tomography angiography (CTA) was performed before euthanasia. The specimens of the aortae with the stent grafts were dispatched for pathology and electron microscope assay.

Histological treatment, examination protocol, and electron microscope examination protocol

For the examination of the specimens, we used the following procedures. (1) The tissue was fixed with formalin, dehydrated with gradient alcohol, soaked with polymeric solutions I and II, immersed in an embedding solution, placed under a vacuum to complete plastic embedding, sliced with a precision cutting machine (to a thickness of approximately 200 μm), polished, and, finally, dyed with hematoxylin and eosin (H&E). (2) The tissue samples were then fixed with for-

malin, and 5 mm-thick slices were cut from each specimen. These were then dehydrated with gradient alcohol, soaked in paraffin for embedding, and sliced with a Leica 2135 slicer (Leica Biosystems Nussloch GmbH Postfach 1120 D-69222 Nussloch) using the conventional method (5 μm thickness). (3) Next, these sections were scanned with a digital pathology scanner, and the following indicators were determined using image analysis software: lumen area (LA), neointima thickness, and internal elastic membrane area (IEMA). From this, the additional indicators of neointima area (NA) ($\text{NA} = \text{IEMA} - \text{LA}$) and occlusion % ($\text{NA} / \text{IEMA} \times 100\%$) were calculated. (4) Finally, the blood vessels at the implantation site were fixed using glutaraldehyde, and the surface attachments were analyzed through electron microscopy after alcohol gradient dehydration.

Results

The technical success rate of the fenestrated TEVAR was 100%. The procedure time was 54 ± 32 min, with a radiation exposure time of 16 ± 8 min. There were no major bleeding events in any of the procedures, and no cardiovascular or cerebral events occurred during the procedures. Furthermore, no limb ischemia or instant retrograde dissection occurred after the procedures. The stent-graft delivery processes were all successful, and fenestration release obstruction did not occur. The adjustment of the movable membrane was smooth in every case. All the stent-graft delivery systems were withdrawn safely. In both the 4-week and 12-week groups, the fenestration was selected to preserve only one branch artery on the aortic arch in one of the 4 animals. In the rest of the animals, the fenestration was released to keep both branches on the arch.

One animal died of an infection condition that was not aortic related; the total survival rate for follow-up was therefore 87.5%. The CTA results of both groups show that there was no stent-graft migration in any of the remaining 7 animals. In addition, at the proximal and distal sites of the stent graft, we observed no retrograde or distal dissection, and no pseudoaneurysms were found around the stent graft or fenestration. All the branch arteries reserved by the fenestration were patent in the CTA results, with no dissections observed in any of the patent branch arteries (Figure 3). Finally, no thrombosis was observed at the branch arteries or the location of the fenestration. The above information and stent-type information are summarized in Table 1.

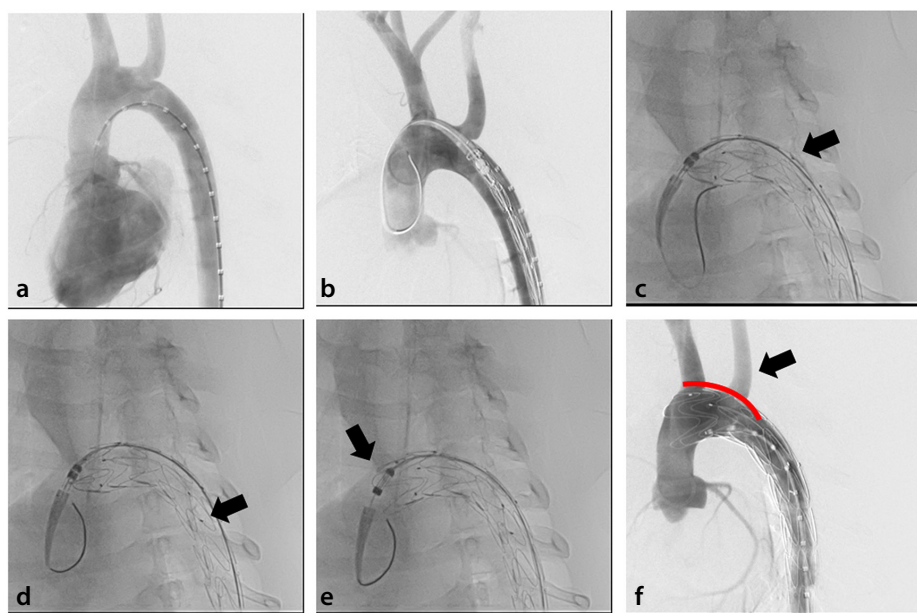


Figure 2. Operation steps performed during canine-fenestrated thoracic aortic endovascular repair (TEVAR) using the adjustable prefenestration stent graft. (a) Digital subtract angiography (DSA) before TEVAR. (b) When the stent graft approaches the aortic arch, DSA is performed again to check the location of the branches. (c) Outer sheath is already pulled distally, and main body of the stent graft is deployed; pulling the membrane patch distally makes it move distally. Black arrow shows the radiopaque marker on the membrane patch at its initial site. (d) Black arrow shows the radiopaque marker on the membrane patch at its final site. (e) Black arrow shows that the fenestration location is satisfactory and that the rear-release lock is unlocked. (f) DSA after the operation was completed; black arrow shows that both branches on the aortic arch remained patent; red curve shows the rough location of the fenestration.

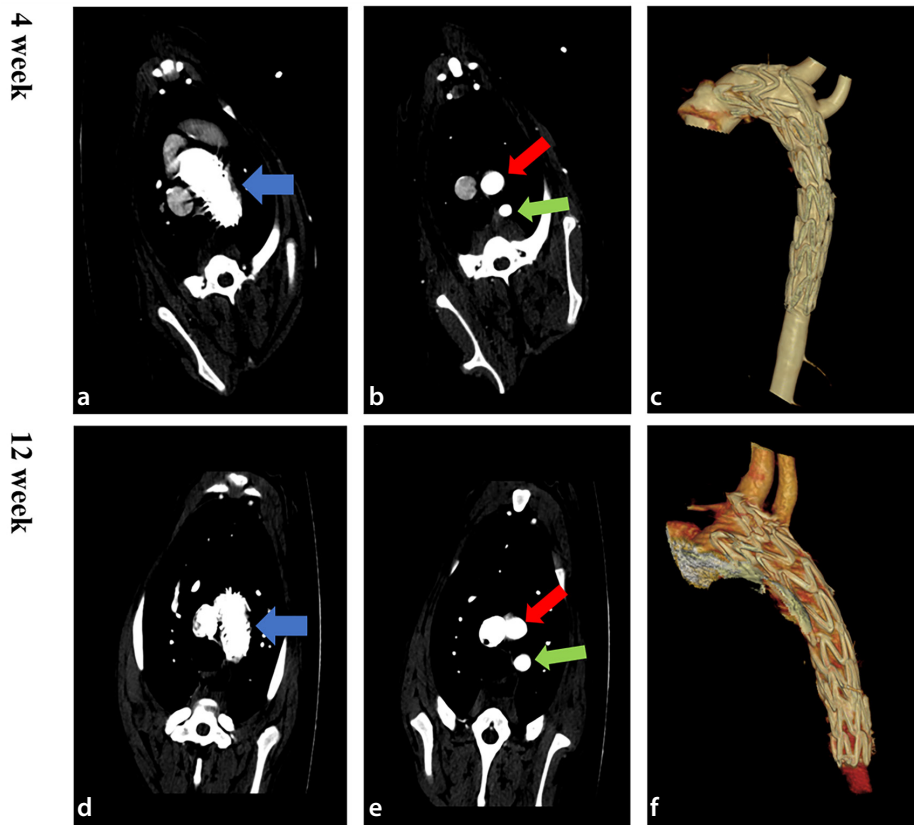


Figure 3. Computed tomography (CT) follow-up results of the canine fenestrated thoracic aortic endovascular repair; (a-c) show the 4-week group's CT follow-up results; blue arrow shows the stent graft in the aortic arch, and red and green arrows show the patent branch arteries; (d-f) show the 12-week group CT follow-up results; blue arrow shows the stent graft in the aortic arch, and red and green arrows show the patent branch arteries.

size and location of the prefenestration are adjustable by moving the membrane distally along the slide rail in the main body of the stent graft. If the proximal site of the membrane is located just distal to the innominate artery orifice, the fenestration release may keep the left subclavian artery patent, and if the proximal site of the membrane is proximal to the site of the innominate artery orifice, the prefenestration release may keep both the innominate artery and left subclavian artery patent.

In humans, the fenestration can be selected to retain 1–3 branch arteries due to the device's proximal membrane edge position. Once the stent-graft delivery and fenestration setup are deemed satisfactory, the stent or stent graft in a branch can be deployed through the same femoral access and further through the fenestration.^{7,8} The advantage of this design is that it preserves the patency of the branch arteries and leaves a minimal area of fenestration, which may decrease endoleak risk.

Introduction of the cable release window laminating system

There is a long window preset on the bracket of the device, and the axial sides of the window are provided with a support frame to ensure that the edge of the window is attached to the wall to avoid leakage at this site. The vertices around the window contain X-ray-proof platinum markers to show the window position, and the outer side of the support frame comes equipped with a guide rail located between the metal bracket and the film covering. The window of the device has a movable film covering sheet along the guide rail axial direction with a width greater than the preset window width. The use of metal support and blood vessel wall compression make the mobile film covering sheet and support film form a relative closure, preventing leakage from the window.

A row of holes is arranged on both sides of the mobile film covering sheet for use on the guide rail. At the proximal end of the removable laminate, there is an X-ray-proof platinum marker to move the proximal end of the laminate, and the distal end of the removable laminate sheet is equipped with a V-shaped frame that is used to adjust the window size of the combined conveying system to avoid laminate damage and serious folding during adjustment. The bottom of the V-shaped frame, which has a movable film covering sheet, is fixed to the adjusting line through the core wire. When pulled back, the

Table 1. General information and operation data of the animals

Group (week)	Animal number	Gender	Weight (kg)	Stent-graft size (proximal diameter × distal diameter × length mm)	Outer sheath diameter (French)	Branch preserved by fenestration
4	C642	Female	24.0	24 × 20 × 140	16	Innominate A.+ LSA
4	C646	Female	27.0	26 × 22 × 140	18	LSA
4	C649	Male	23.0	22 × 18 × 140	16	Innominate A.+ LSA
4	C650	Male	28.0	24 × 20 × 140	17	Innominate A.+ LSA
12	C651	Female	26.0	22 × 18 × 140	16	Innominate A.+ LSA
12	C652	Female	24.8	22 × 18 × 140	16	Innominate A.+ LSA
12	C655*	Female	27.4	22 × 18 × 140	16	LSA
12	C656	Male	32.0	24 × 20 × 140	17	Innominate A.+ LSA

*C655 dog died of systemic infection 5 days after surgery. Innominate A., innominate artery; LSA, left subclavian artery.

The histological results (H&E staining) showed no obvious injuries on the stent-graft segments of the aortae. In most parts of the aorta, there were no obvious inflammation reactions (Figure 4). Electron microscope results also showed that the endothelial cells provided effective coverage of the stent-graft surface in all cases (Figure 5).

Discussion

A new adjustable prefenestration aortic stent-graft device was specially designed for aortic arch pathologies. The design allows the device to avoid partially releasing and changing the structure of the endograft in PMGF. In addition, it avoids the need to use a large number of endovascular devices during the *in situ* fenestration procedure. The

adjusting line causes the mobile film to move back. After adjustment, the core wire can be withdrawn to realize the relief of the bottom of the V-shaped frame and adjustment line. Although this type of pre-opening may not guarantee the prevention of leakage, its use in conjunction with a branch bracket with a leak-prevention device can dramatically reduce the risk of leakage.

Safety evaluation of the new stent graft

In this canine fenestrated-TEVAR procedure study, the survival rate was 87.5%. One animal died on postoperative day 5. However, autopsy results showed that the death was not related to the aortic stent-graft implantation but was the result of a severe infection. In the other 7 animals, the rate of branch arteries' patency retained by fenestration was 100% (Figure 3). The patency of branches (both one and two branches) was also maintained. Our observations of one/two-branch patency by fenestration also demonstrated the safety and flexibility of the stent graft, which is possibly better than the current three-branch endograft designs.⁹⁻¹¹ In reviewing the results of the CTA, we found that the branch arteries were all kept patent. None of the surviving animals suffered cerebral vessel events due to thrombosis at the fenestration location.¹²⁻¹⁴ In addition, the stent graft was able to smoothly cross the very steep canine aortic arch. There were no

aortic rupture events and no access vessel injuries when the delivery systems were withdrawn. Hence, we judge the safety of this new stent graft to be satisfactory.

Feasibility evaluation of the stent graft in fenestrated TEVAR

Here, we summarize our evaluation of the feasibility of our new adjustable prefenestration aortic stent graft. The compliance of the stent graft was good in all 8 cases, despite the steeper nature of a canine's aortic arch curvature compared with a human's. In fact, it is similar to a type III aortic arch in a human.¹⁵ A higher aortic curvature increases the level of difficulty and rate of complications in TEVAR.¹⁶ In this canine study, all the stent-graft proximal sites were located in zone 0. However, all the delivery systems crossed the arch successfully without aortic rupture or other complications. In one case of extremely steep curvature of the aortic arch, the stent graft crossed the arch successfully by partially withdrawing the outer sheath to decrease the friction. This is where the device's X-ray radiopaque marker at the tip of the delivery system came into play. The design aimed to "take the marker out" of the NiTi wire and make it more readily directionally functional. When the marker is viewed as a longitudinal shape, the cephalic direction of the longitudinal axis is the fenestration (Figure 1d, e).

The fenestrations in this study all occurred in the greater curvature of the aorta, and we deemed the reliability of this marker to be satisfactory. The core part of our new stent graft is the movable membrane located and initially overlapped at the prefenestration area. There is also a radiopaque marker at the middle part of the movable membrane. When the stay wire is pulled back at the rear part of the movable membrane, the radiopaque marker indicates where the membrane is and how large the fenestration is (Figure 2c, d). The stay wire, which is the control part of the movable membrane, can be pulled distally at the end site of the delivery system. During the procedures in this study, the stay wire was stable and comfortable during the fenestration-releasing procedure, even in very steep aortic arches. No twining occurred with other parts (Figure 1f, g).

The follow-up data for the 4-week and 12-week groups showed that the branches in all surviving cases remained patent. In addition, no thrombosis was observed in the branch arteries involved in fenestration. To lower the risk of misfitting the fenestration and branch orifices, we designed a relatively large prefenestration area. The area of fenestration could be controlled and adjusted more agilely by physicians based on their specific needs. In addition, our stent graft can potentially be used in repairing proximal arch lesions, as the proximal end can land in the ascending aorta.¹⁷⁻¹⁹

In the presence of anatomical branch artery variations, the adjustable position and area of fenestration provide a definite advantage over other methods.^{20,21} Furthermore, we judge both histological safety and overall healing to be satisfactory based on our H&E staining and electron microscope results. Microvascular injury and minor inflammation reactions were not found in the stent graft. Electron microscope results showed that the endothelial cell cover was also satisfactory (Figure 5).

When designing this device, our primary concern was to create an "off-the-shelf" stent graft that could be used for fenestration without the need to modify the endograft or use multiple steps to puncture the membrane. Accordingly, the use of our device could be indicated for most pathologies in the aortic arch.⁴ However, we still have several ideas for improving the design.

First, we aim to construct more apparatuses to help prevent endoleak around the prefenestration area. Endoleak is the first complication that should be prevented in

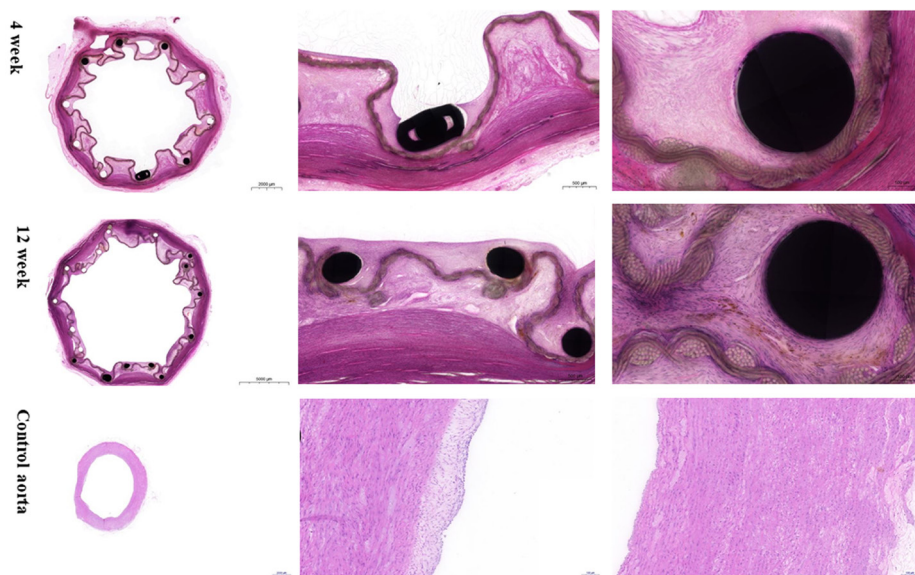


Figure 4. Histological examination (hematoxylin and eosin staining) after stent-graft implantation. Four-week group: there was no vascular injury, and endothelialization of the stent and covered membrane and thrombus organization of the vascular and covered space was observed, as was the proliferation of fibroblasts, scattered infiltration of inflammatory cells, a small number of necrotic cells, and attachment of foreign giant cells on the covered surface. Twelve-week group: slight vascular injury, vascular wall media compression, and intimal hyperplasia were observed, as well as a small amount of inflammatory cell infiltration and hemosiderin powder deposition; blank control group: intima was slightly thickened, and there was no vascular injury, degeneration, or necrosis.

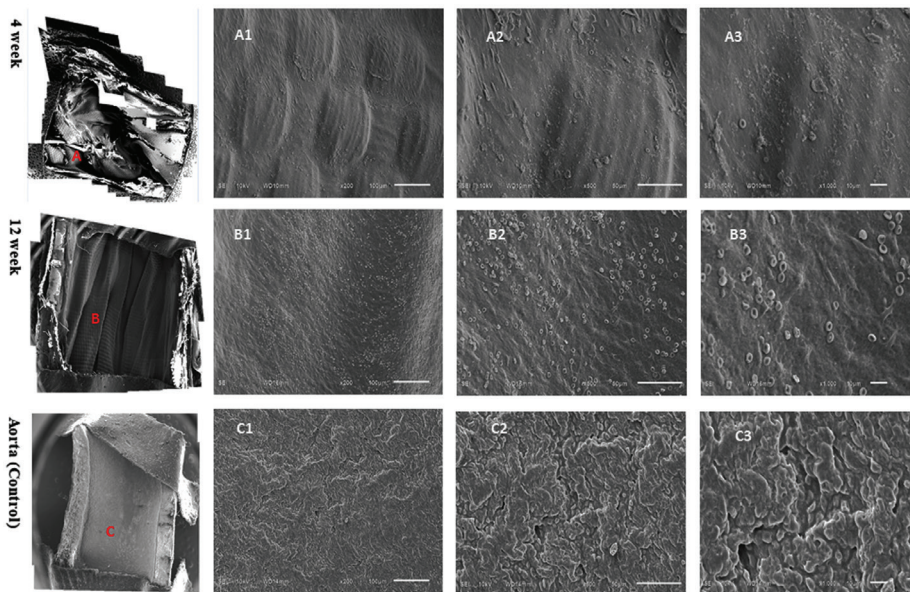


Figure 5. Electron microscope results of 2 groups of canines after stent-graft implantation and a control aorta. All locations in the stent graft or the aorta (red "A, B, C") have been highly magnified at three different powers. Four-week group: stent surface was partially covered by tissue, with a small number of endothelial and red blood cells attached. Twelve-week group: stent surface was completely covered with endothelial cells and a small number of red blood cells. Blank control group: mature endothelial cells can be seen on the surface of blood vessels.

TEVAR, especially under conditions using the chimney or fenestration techniques. In the very early design phase, we did not design extra endoleak prevention apparatuses for our device, since a special gutter-free branch artery stent-graft device already exists,^{22,23} and we believe that our fenestration procedure, combined with the new gutter-free branch artery stent graft, can lower endoleak risk. However, if we design more endoleak preventive devices around the edge of the fenestration, the device could be made even more effective at preventing endoleak when combined with a gutter-free branch stent graft. Second, this study only tested the safety and feasibility of the new device in healthy animals and not in pathologic ones.^{24,25} Third, there are differences in the anatomical structure of the human and canine aortic arch. Although our new adjustable prefenestration aortic stent graft, used in fenestrated TEVAR to preserve canine branch arteries, achieved satisfactory results, its application to a human aortic arch requires further study. In addition, the follow-up period of this experimental study was short, and the stability of this new adjustable prefenestration aortic stent graft cannot be satisfactorily explained. As such, this study has limitations in terms of demonstrating the effectiveness, safety, and feasibility of our new device for repairing dissection or aneurysm. This remains a topic for future investigation.

In conclusion, we found our new adjustable prefenestration aortic stent graft, used in fenestrated TEVAR to preserve canine branch arteries in the aortic arch, to be satisfactory in terms of both safety and feasibility. During the procedures in this study, the adjustment and manipulation of the position and area of the fenestration were smooth. Furthermore, the results for the stability of the stent graft and the patency of the branch arteries on the aortic arch were also satisfactory. These preliminary data derived from a canine model may serve as a reference for the use of our fenestrated-TEVAR device in humans.

Conflict of interest disclosure

The authors declared no conflicts of interest.

Funding

This research is supported by the Natural Science Foundation of Hunan Province (2020JJ2054).

References

1. Lombardi JV, Hughes GC, Appoo JJ, et al. Society for Vascular Surgery (SVS) and Society of Thoracic Surgeons (STS) reporting standards for type B aortic dissections. *J Vasc Surg.* 2020;71(3):723-747. [\[CrossRef\]](#)
2. National Society of Vascular Surgery. Chinese Expert Consensus on Hybrid Technique on Treating Thoracic Aortic Pathologies Involving

the Aortic Arch. *Chinese Circulation Journal.* 2020;35(2):124-130. [\[CrossRef\]](#)

3. Li X, Shu C, Li QM, et al. Self-radiopaque markers guiding physician-modified fenestration (S-fenestration) in aortic arch endovascular repair. *Front Cardiovasc Med.* 2021;8:713301. [\[CrossRef\]](#)
4. Li X, Li Q, Zhang W, et al. Early experience and technical aspects of physician-modified fenestration in thoracic endovascular aortic repair for aortic arch pathologies. *J Int Med Res.* 2020;48(2):300060519870903. [\[CrossRef\]](#)
5. Shu C, Fan B, Luo M, et al. Endovascular treatment for aortic arch pathologies: chimney, on-the-table fenestration, and *in-situ* fenestration techniques. *J Thorac Dis.* 2020;12(4):1437-1448. [\[CrossRef\]](#)
6. Wang C, von Segesser LK, Berdajs D, Ferrari E. Endovascular treatment of the dissected proximal aortic arch: a systematic review. *Interact Cardiovasc Thorac Surg.* 2021;33(5):746-754. [\[CrossRef\]](#)
7. Li X. Chinese Patent: An adjustable prefenestration aortic stent-graft and its deployment system (Patent#: ZL2017 1 0941546.0; Authorization of publication#: CN 107550601 B) [P]. 2018-01-09. [\[CrossRef\]](#)
8. Shu C, Li X, Li QM, et al. Application of self-radiopaque markers guiding physician-modified fenestration in aortic arch endovascular repair: an international multi-center retrospective analysis of 113 cases. *Chinese General Surg Journal.* 2020;29(12):1426-1434. [\[CrossRef\]](#)
9. Shahverdyan R, Gawenda M, Brunkwall J. Triple-barrel graft as a novel strategy to preserve supra-aortic branches in arch-TEVAR procedures: clinical study and systematic review. *Eur J Vasc Endovasc Surg.* 2013;45(1):28-35. [\[CrossRef\]](#)
10. Soeda T, Yokoi Y, Yuri K, Saito Y, Setozaki S, Harada H. Perfect and least invasive sealing technique on the lesser curvature of the aortic arch: application of a novel stent graft to an aneurysm developing on a postoperative ductus arteriosus. *Ann Thorac Cardiovasc Surg.* 2013;19(2):162-165. [\[CrossRef\]](#)
11. Kim SP, Lee HC, Park TS, et al. Safety and efficacy of a novel, fenestrated aortic arch stent graft with a preloaded catheter for supraaortic arch vessels: an experimental study in Swine. *J Korean Med Sci.* 2015;30(4):426-434. [\[CrossRef\]](#)
12. Yang J, Liu Y, Duan W, et al. A feasibility study of total endovascular aortic arch replacement: from stent-graft design to preclinical testing. *J Thorac Cardiovasc Surg.* 2016;151(4):1203-1212. [\[CrossRef\]](#)
13. Yang F, Qiu J, Fu Z, et al. Safety and feasibility study of a novel stent-graft for thoracic endovascular aortic repair: a Canine Model Experiment. *Braz J Cardiovasc Surg.* 2017;32(5):401-407. [\[CrossRef\]](#)

14. Li M, Shu C, Xiao B, Liu D, Zhang W. Short-term results in canines of novel stent-graft design for chimney technique in TEVAR. *J Interv Med.* 2020;3(3):128-131. [\[CrossRef\]](#)
15. Marrocco-Trischitta MM, Rylski B, Schofer F, et al. Prevalence of type III arch configuration in patients with type B aortic dissection. *Eur J Cardiothorac Surg.* 2019;56(6):1208. [\[CrossRef\]](#)
16. Chassin-Trubert L, Gandet T, Ozdemir BA, Lounes Y, Alric P, Canaud L. Aortic arch anatomy pattern in patients treated using double homemade fenestrated stent-grafts for total endovascular aortic arch repair. *J Endovasc Ther.* 2020;27(5):785-791. [\[CrossRef\]](#)
17. Baikoussis NG, Antonopoulos CN, Papanonstantinou NA, Argiriou M, Geroulakos G. Endovascular stent grafting for ascending aorta diseases. *J Vasc Surg.* 2017;66(5):1587-1601. [\[CrossRef\]](#)
18. Plichta RP, Hughes GC. Thoracic endovascular aortic repair for the ascending aorta: experience and pitfalls. *J Vis Surg.* 2018;4:92. [\[CrossRef\]](#)
19. Shi J, Liu L, Wei X, Ma M. Back-table modified stent-graft for endovascular repair of ascending aorta. *J Endovasc Ther.* 2021;28(6):888-896. [\[CrossRef\]](#)
20. Zhang W, Li X, Cai W, Li M, Qiu J, Shu C. Midterm outcomes of endovascular repair for stanford type B aortic dissection with aberrant right subclavian artery. *J Vasc Interv Radiol.* 2019;30(9):1378-1385. [\[CrossRef\]](#)
21. Zhang W, Li X, Cai W, Li M, Qiu J, Shu C. Midterm outcomes of endovascular repair for stanford type B aortic dissection with aberrant right subclavian artery. *J Vasc Interv Radiol.* 2019;30(9):1378-1385. [\[CrossRef\]](#)
22. Fang K, Shu C, Luo M, et al. First-in-human implantation of gutter-free design chimney stent graft for aortic arch pathology. *Ann Thorac Surg.* 2020;110(2):664-669. [\[CrossRef\]](#)
23. Shu C, Li X, Dardik A, et al. Early results of a novel gutter-free chimney stent-graft system to treat aortic arch dissection: single-center data from a prospective clinical trial. *J Endovasc Ther.* 2021;29(2):258-265. [\[CrossRef\]](#)
24. Tang J, Wang Y, Hang W, Fu W, Jing Z. Controllable and uncontrollable Stanford type B aortic dissection in canine models. *Eur Surg Res.* 2010;44(3-4):179-184. [\[CrossRef\]](#)
25. Wang LX, Wang YQ, Guo DQ, et al. An experimental model of Stanford type B aortic dissection with intravenous epinephrine injection. *Kaohsiung J Med Sci.* 2013;29(4):194-199. [\[CrossRef\]](#)



Pivotal role of the synovioentheseal complex in the imaging of arthritis and rheumatic diseases

Adalet Elçin Yıldız
 Üstün Aydingöz

Hacettepe University Faculty of Medicine,
Department of Radiology, Ankara, Türkiye

ABSTRACT

Imaging plays a key role in the diagnosis and management of rheumatic diseases. Although joints and periarticular tissue are commonly involved in rheumatic diseases, entheses further away from joints, such as in the Achilles tendon or plantar fascia insertion onto the calcaneus, as well as skin and subcutaneous tissue, are among other -sometimes overlooked- targets. The link of enthesitis, which describes inflammation at the insertions of ligaments, tendons, or joint capsules, with spondyloarthritis (SpA) was established just before the turn of the century as a characteristic feature based on imaging studies with histopathological correspondence. To highlight the association between enthesitis and synovitis in SpA, the anatomical unit of the “synovioentheseal complex” (SEC) and the concepts of “functional enthesitis” and “articular enthesitis,” apart from the better known “insertional enthesitis,” were introduced to encompass other inflammatory lesions associated with SpA. Studies from the last two decades revealed the involvement of the SEC in rheumatic and non-rheumatic disorders with different pathogeneses. Although such involvement is sometimes distinctive, it does not necessarily point to a specific diagnosis at other times. Nevertheless, the potential of SEC inflammation in the differentiation of SpA from other forms of arthritis remains important. The purpose of this review was to provide essential information concerning the involvement of the SEC in the diagnosis of rheumatic diseases and arthritis, focusing on imaging characteristics.

KEYWORDS

Arthritis, enthesitis, synovioentheseal complex, magnetic resonance imaging, ultrasonography

Rheumatic diseases, including arthritis, are common and disabling health problems.¹ In the last few decades, the widespread use of disease-specific medications that carry the promise of treating arthritis at earlier phases, before deformities develop, has bolstered the importance of reaching a correct diagnosis.² Imaging-based diagnosis in arthritis relies mainly on the distribution across the body of inflammatory soft tissue and bone lesions and structural bone changes.² Algorithms using an imaging-based diagnosis of arthritis that historically relied on radiographs, which mostly show chronic lesions at joints and bones, usually prioritize proximal or distal and axial or appendicular skeletal distribution.³ However, there are many challenging instances in daily practice whereby such distribution-based generalizations simply do not work. The additional information that cross-sectional imaging provides is crucial yet sometimes confusing with distribution-based algorithms or in the case of subtle findings. Therefore, it is imperative for radiologists to know where to look and what to search for on cross-sectional imaging to both identify the presence of pre-radiographic findings of arthritis and attempt to classify the disease. In other words, factoring the characteristic involvement of some specific microanatomic sites, such as “the enthesitis organ,” which we explain below, may take precedence over the more generalized, distribution-based algorithmic approach to diagnosis, especially when cases that do not conform to the existing algorithms are encountered.

The term “enthesopathy,” which describes inflammation at the insertions of ligaments, tendons, joint capsules, or fasciae to bone, was first used in 1966.⁴ Although the link between enthesitis and spondyloarthritis (SpA) has been mentioned thereafter in several studies, it

Corresponding author: Adalet Elçin Yıldız

E-mail: aelcindr@gmail.com

Received 04 March 2024; revision requested 12 April 2024; accepted 20 May 2024.



Epub: 10.06.2024

Publication date: 06.11.2024

DOI: 10.4274/dir.2024.242740

You may cite this article as: Yıldız AE, Aydingöz Ü. Pivotal role of the synovioentheseal complex in the imaging of arthritis and rheumatic diseases. *Diagn Interv Radiol.* 2024;30(6):409-418.

was just over two decades ago that enthesitis was highlighted as a characteristic feature of SpA in the light of magnetic resonance imaging (MRI).^{5,6} Based on high-resolution (HR) MRI and histological studies, micro-anatomical detailed analyses of entheses culminated in the concept of the “entheses organ”. The latter not only involves a group of related tissues at the insertional sites across the bones but also encompasses the fibrocartilaginous periosteal or tendinous/ligamentous lining that facilitates the gliding of tendons/ligaments during motion.^{7,8} In 2007, to better delineate the association between enthesitis and synovitis in SpA, McGonagle et al.⁹ introduced the concept of an anatomical unit dubbed the “synovioenthesal complex” (SEC). According to this concept, the normal fibrocartilage related to an entheses is critically dependent on the immediately adjacent synovium.⁹ Currently, based on studies from the last two decades, it has been established that the SEC is involved in various ways in several rheumatic and non-rheumatic disorders with different pathogeneses, somewhat limiting its value as a discriminating factor favoring rheumatic versus non-rheumatic diseases.¹⁰⁻¹⁷ Nevertheless, the potential of SEC inflammation in the differentiation of SpA from other forms of arthritis remains important, given the differences in the treatment of SpA versus other forms of inflammatory arthritis. The purpose of this review is to provide essential information on SEC involvement in the diagnosis of rheumatic diseases and arthritis, focusing on imaging characteristics.

The anatomical rationale behind the term “synovioenthesal complex”

Enthesis, which means “insertion” in ancient Greek, refers to the locations where tendons, ligaments, fascia, or articular capsules attach to a bone. There are two types of entheses: fibrous and fibrocartilaginous. Fibrous entheses attach tendons of large muscle bodies directly to a broad surface of diaphysis and metaphyses of long bones, where the bone cortex is thick.^{6,12} Fibrocartilaginous entheses, which are the main target of inflammatory lesions in SpA, comprise the majority of entheses in the body. Classic fibrocartilaginous entheses are located often in the vicinity of synovial joints, have a unique composition that allows joint movement, and attach tendons to epiphyseal and apophyseal long bone ends, where the bone cortex is thin.^{6,12} In addition to classic fibrocartilaginous entheses, the concepts of “functional” and “articular” fibrocartilaginous entheses related to inflammatory lesions of SpA have been introduced.¹⁸

Fibrocartilaginous entheses, which, in their classical form, serve as a functional unit in the dissipation of mechanical stress at the soft tissue-bone interfaces, are made up of the following subunits: distal tendon, ligament, or fascia; sesamoid and enthesal fibrocartilage of the tendon; fat pads; bursae; synovium; periosteal fibrocartilage; and the bone. This overall arrangement of contiguous structures is also known as the “entheses organ”. The most common fibrocartilaginous entheses that are targeted by SpA are the calcaneal insertions of the Achilles ten-

don and plantar fascia, and patellar, lateral humeral epicondylar, and greater trochanteric insertions of the quadriceps, common extensor, and hip abductor tendons, respectively (Figures 1 and 2).^{19,20}

The term “functional entheses” is coined to define the fibrocartilage interface between two musculoskeletal infrastructural parts that absorb friction-related stress during activity.² In other words, fibrocartilaginous entheses exist not only at the tendon attachment sites but are also found in friction interfaces of tendons versus bones, such as the extensor digitorum tendon and central slip of the extensor tendon crossing over the metacarpal head and the proximal interphalangeal joint, respectively, or the peroneus longus tendon wrapping around the peroneal trochlea of the calcaneus and cuboid (the latter is referred to as the “cuboid pulley”) (Figure 3). Other sites of friction interface are pulleys on the volar surfaces of fingers and toes versus the tendon sheaths that they wrap around, whereby finger pulleys show fibrocartilaginous characteristics at their inner gliding layer (Figure 4).^{18,21-23}

The “articular” form of fibrocartilaginous entheses is found in synovial joints that are lined by fibrocartilage as well as hyaline cartilage, such as the sacroiliac joints (SIJs), symphysis pubis, acromioclavicular, temporomandibular, and manubriosternal joints.^{18,24-26} Fibrocartilage/hyaline cartilage proportions in some of these joints change during skeletal maturation.^{18,24-26} The articular surface at the iliac side of the SIJ consists of hyaline and fibrous cartilage, whereas the

Main points

- As a major target site of involvement in many forms of rheumatic diseases, the synovioenthesal complex (SEC) needs to be a primary focus on imaging-based assessment of arthritis.
- Although the gross anatomic distribution has long been a primary consideration in the radiography-based differential diagnosis of arthritis, the ascertainment of SEC involvement may be a better approach in target-site prioritization on high-resolution (HR) cross-sectional imaging.
- Enthesal bone marrow edema (suggesting SEC involvement) is more common in spondyloarthritis patients compared with rheumatoid arthritis and osteoarthritis patients.
- Focused or HR magnetic resonance imaging that incorporates new technological advances is the best imaging tool for depicting the entire SEC (i.e., osseous as well as soft tissue components).

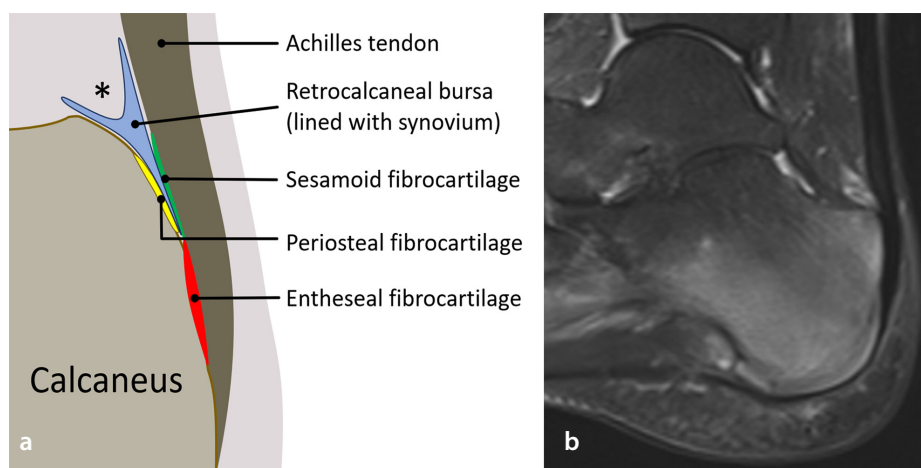


Figure 1. Synovioenthesal complex in a classic fibrocartilaginous entheses in the ankle. (a) Schematic illustration of a midsagittal ankle section through the Achilles tendon shows the synovioenthesal complex including subunits of the enthesal organ: distal tendon, sesamoid (green), and enthesal (red) fibrocartilages of the tendon, periosteal fibrocartilage (yellow) of the calcaneus, retrocalcaneal bursa lined with synovium (blue), and the surrounding fat pad (asterisk). (b) Sagittal fat-saturated T2W magnetic resonance image shows Achilles tendon enthesitis as well as insertional plantar fasciitis, which also is a type of enthesitis, in a 16-year-old girl with enthesitis-related arthritis. Note retrocalcaneal bursitis and extensive bone marrow edema related to enthesitis.

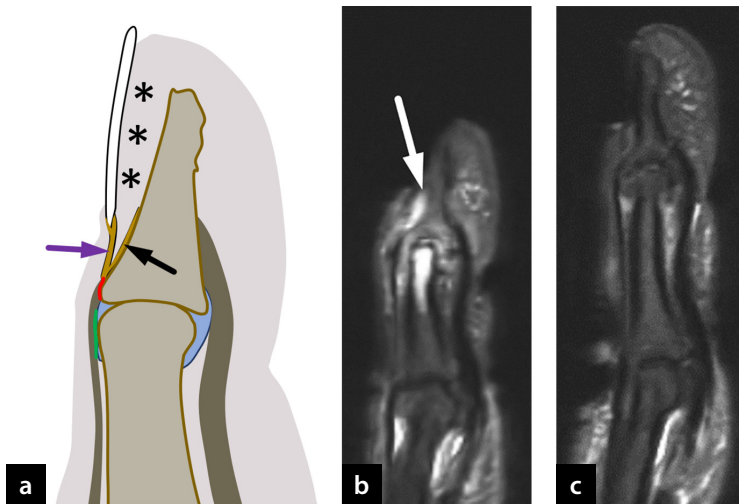


Figure 2. Synovioentheseal complex in the classic fibrocartilaginous enthesis of extensor tendon with its nail root extensions. (a) Schematic illustration of a midsagittal distal finger section shows sesamoid fibrocartilage (green) and enthesal fibrocartilage (red) of the extensor tendon with its extensions to the nail root (superficial lamina, purple arrow) and the dorsal distal phalangeal periosteum (deep lamina, black arrow). Asterisks denote the nail bed. (b, c) Sagittal fat-saturated T2W magnetic resonance images of the second (b) and third (c) fingers in a 58-year-old woman with psoriatic arthritis reveal extensor tendon enthesitis of the second finger characterized with peritendinous, nail root, and bed inflammation (b, arrow), extensive periarticular osteitis of the middle and distal phalanges and synovitis of the second distal interphalangeal joint in addition to uniform joint space narrowing and mild periarticular bone proliferation. Extensor tendon enthesis, nail root, and bed of the third finger (c) are normal.

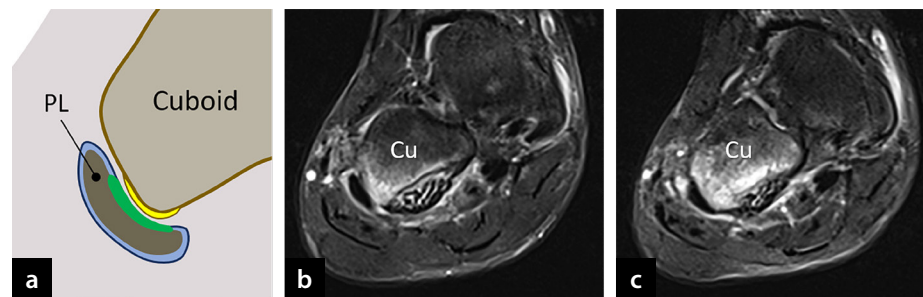


Figure 3. Synovioentheseal complex in a functional enthesis at a tendon–bone friction site. (a) Schematic illustration of a midfoot coronal section shows the peroneus longus tendon (PL) enveloped in its synovial tendon sheath. The sesamoid fibrocartilage (green) at the peroneus longus tendon facing the cuboid and the corresponding periosteal fibrocartilage (yellow) at this site constitute a functional enthesis. (b, c) Consecutive coronal fat-saturated T1W post-contrast magnetic resonance images through midfoot show functional enthesitis at the cuboid pulley in a 16-year-old girl with enthesitis-related arthritis. Cu, cuboid.

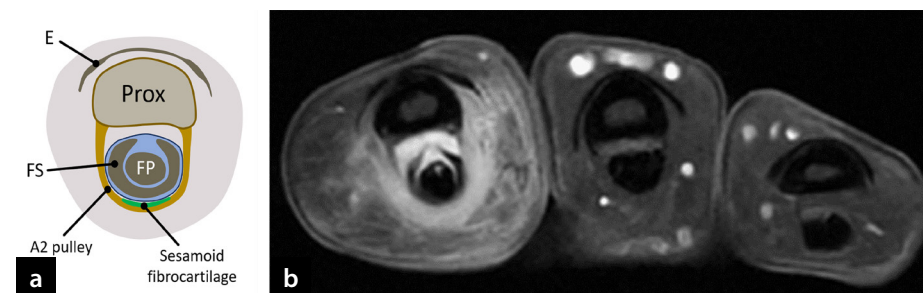
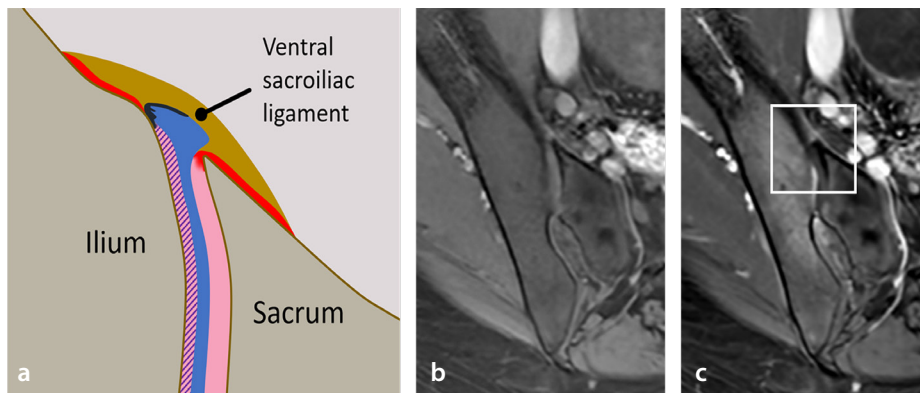


Figure 4. Synovioentheseal complex in a functional enthesis at the finger pulley-flexor tendon gliding site. (a) Schematic illustration of a transverse section through the mid-level of a proximal phalanx shows the extensor mechanism (E), proximal phalanx (Prox), superficial (FS), and deep (FP) flexor tendons, which are enveloped in a synovial sheath (blue). Phalangeal insertions of pulleys are classic entheses. The sesamoid fibrocartilage at the A2 pulley (green) facing the flexor tendon group (which is a friction site) is a functional enthesis. (b) Transverse fat-saturated T1W post-contrast magnetic resonance image shows functional enthesitis of A2 pulley with accompanying subcutaneous inflammation, dactylitis, in a 34-year-old woman with psoriatic arthritis.

sacral side joint surface is covered exclusively with hyaline cartilage (Figure 5). Articular hyaline and fibrous cartilage blend with the strong fibrous tissue of surrounding ligaments through a transitional zone of fibrocartilage (i.e., fibrocartilaginous enthesis). On the iliac side of the SIJs, the articular hyaline and fibrous cartilage are thinner compared with the pure hyaline cartilage found on the sacral side. At the iliac side, the abundance of fibrocartilaginous components, which are considered to be attacked first in SpA, as well as the relative thinness of the articular cartilage, results in a tendency for erosions in sacroiliitis to occur earlier (and more prevalently) on the iliac (rather than the sacral) side of the joint (Figure 5); progression to the sacral side usually occurs later. Interestingly, but not surprisingly, diskovertebral joints are also considered “articular (fibrocartilaginous) entheses,” since disks contain fibrocartilage and are juxtaposed to the hyaline end-plate cartilage of the vertebral bodies (without any synovium involved). It is not coincidental that inflammatory lesions of SpAs tend to involve diskovertebral junctions as well as vertebral corners (classic entheses).¹⁸ A summary of fibrocartilaginous enthesis subtypes and examples of SEC sites across the body are shown in Table 1.

In healthy conditions, the synovial subunit of an enthesis organ lubricates and nourishes the avascular fibrocartilage and provides immunity to enthesis, just as the neighboring bone marrow does when needed. Cytokine-based pathophysiological pathways that drive the disease processes involving the SEC are a prime area of arthritis research.^{27,28} However, these are beyond the scope of this review. Any pathological process affecting the enthesis organ, including inflammation, metabolic disorders, trauma, or degeneration, is called “enthesopathy” and may manifest as adjacent synovitis and tenosynovitis or bursitis (Figure 6). However, the microanatomical location of the epicenter of inflammation within a single joint, either the synovium or the enthesal organ, may be different in the early phase of the disease, particularly in cases of inflammatory arthritis. In the later phases, both types of these closely located inflamed structures seem to be affected. This pathophysiological fact, which is grounded in anatomy, underscores the crucial importance of using HR MRI to detect the epicenter of inflammation in early phases.^{2,13,29}



Imaging approach to the synovioentheseal complex

Radiographs are generally the first-line imaging modality used to assess patients suspected of having arthritis. However, when it comes to enthesitis, radiographs may only reveal late signs of enthesopathy, such as the presence of new bone formation (enthesophytes and syndesmophytes), erosions, and sclerosis (e.g., “shiny corner” lesions of vertebrae). In certain sites, such as the Achilles or patellar tendon insertions, which are surrounded with fat tissue, subtle enthesitis-related soft tissue edema and increased thickness of the tendon may be detectable, especially if a comparative radiograph of the corresponding normal side is available. In terms of differential diagnosis of arthritis, radiographs still maintain their diagnostic yield in structural (i.e., chronic) lesions.³⁰

Ultrasonography (US) is particularly valuable for small and peripheral joints, with its widespread availability, lack of ionizing radiation, and HR probes. B-mode and Doppler US (color and power) both depict the morphological features and vascularity of the enthesis and may aid in the diagnosis and treatment response evaluation. According to the Outcome Measures in Rheumatology (OMERACT) US Working Group, US features of enthesitis were grouped into lesions as either active inflammatory (hypoechoogenicity, increased thickness with morphologic abnormalities and Doppler activity of the enthesis) or structural (insertional bone erosions, intratendinous calcifications, and enthesophytes).³¹ Ultrasound is disadvantageous for large and deep joints and the axial skeleton, where MRI is the preferred modality.

Table 1. Synovioentheseal complex sites across the body		
Site	Characteristic	Examples*
Classic fibrocartilaginous enthesitis	Tendon, ligament, fascia, or joint capsule attachments to bones	Achilles tendon (Figure 1) Plantar fascia-calcaneus insertion Supraspinatus tendon Extensor tendon's nail root extension (Figure 2) Peroneus brevis tendon-5 th metatarsal insertion Collateral ligament-phalanx insertions
Functional enthesitis	At friction interfaces where tendons, pulleys, or retinacula wrap around another structure	Cuboid pulley (Figure 3) Extensor tendon-metacarpal head interface Finger pulleys (Figure 4)
Articular enthesitis	In synovial joints with a fibrocartilage-as well as hyaline cartilage-lining	Sacroiliac joint (Figure 5) Temporomandibular joint Acromioclavicular joint Sternoclavicular joint

*Please refer to the figures mentioned in parentheses for sample cases.

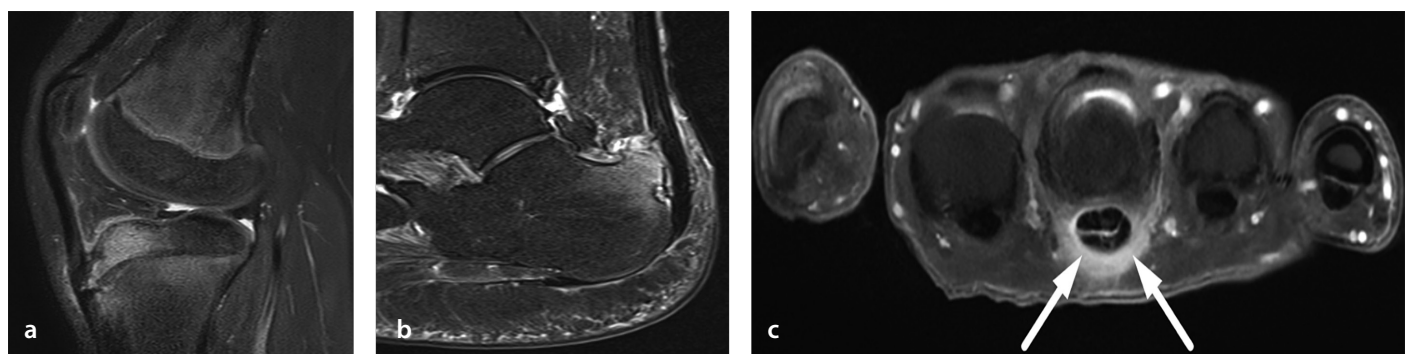


Figure 6. Synovioentheseal complex inflammation in chronic overuse, degenerative, and traumatic injuries. (a) Sagittal fat-saturated proton density-weighted magnetic resonance image (MRI) of a 12-year-old boy with Osgood-Schlatter disease, which is an overuse injury, reveals distal patellar tendon enthesopathy characterized by intra- and peritendinous hyperintensity, subcortical bone marrow edema at the entheseal insertion, and deep infrapatellar bursitis. (b) Sagittal fat-saturated T2W MRI of a 54-year-old woman with Haglund syndrome shows Achilles tendon enthesopathy characterized by intra- and peritendinous hyperintensity, subcortical bone marrow edema, and erosion at the entheseal insertion, and retrocalcaneal bursitis with Haglund deformity of the calcaneus. (c) Transverse fat-saturated T1W post-contrast MR image of a 44-year-old man with a 1-month history of pain following an episode of lifting luggage with a single finger shows traumatic A1 pulley enthesopathy (arrows) with mild flexor tenosynovitis.

MRI, with its potential to visualize the entire enthesis organ (including its subcortical medullary bone component), is the best imaging modality for enthesitis involving both the axial and peripheral skeleton. An MRI examination to assess inflammatory and structural lesions at entheses should include at least short tau inversion recovery, T2-weighted fat-saturated images, or T1-weighted fat-saturated images with and without gadolinium enhancement.³² According to the OMERACT Heel Enthesitis MRI Scoring System, MRI features of enthesitis were grouped into lesions as either active inflammatory (intratendinous and/or peritendinous hyperintensity, subcortical bone marrow edema at the enthesial insertion, retrocalcaneal bursitis, and tendon thickening) or structural (insertional bone erosions and enthesophytes).³² Advancements in hardware and software over the past few decades have enabled HR MRI of small joints, which, in turn, has enhanced understanding of the pathogenesis of psoriatic arthritis (PsA) by providing insights into its microanatomical aspects. HR MRI also enabled the visualization of different types of enthesitis and discrimination of inflammatory arthritis.^{2,8,33-36} The term “HR MRI” does not imply employing a specific set of parameters for imaging small joints and body parts. Rather, it describes an attempt to reduce slice thickness and fields of view (by using the most appropriate surface coils and up-to-date software) to such a degree that the signal-to-noise ratio of images and acquisition times remain within an acceptable limit while ensuring patient comfort and compliance.

Since SIJs are an articular enthesis, as explained above, sacroiliitis is a type of enthesitis that manifests itself on imaging as contrast enhancement at the joint capsule and within the articular fibrocartilage (Figure 5). Inflammation may extend continuously from the joint to the pericapsular tendon and ligament attachments.²⁵ For both active inflammatory and chronic structural lesions of sacroiliitis, MRI is indispensable. Osteitis, which is a cardinal finding of the Assessment of SpondyloArthritis International Society classification criteria for axial SpA,³⁷ represents an extension of inflammation of articular fibrocartilage to the subcortical bone marrow of the SIJ.²⁵ Chronic sacroiliitis is characterized by subcortical marrow fat metaplasia, erosions, subchondral sclerosis, transarticular bone bridges, and bone buds.³⁷

The developmental process involving SIJs has a bearing on the imaging assessment of

SpA in children. The sacrum is formed by the fusion of numerous primary and secondary ossification centers throughout early childhood and adolescence. Predominantly on the sacral side, the metaphyseal-equivalent high signal intensity is typically symmetrical and results from ossifying epiphyseal cartilage and the underlying newly formed subchondral bone, which may be misinterpreted as osteitis. Distinctly in children, the ossifying subchondral bone plate shows partial absence of the cortical black line and frequently appears irregular and blurred at the iliac side of the S1 level, mimicking erosions.³⁸

As with sacroiliitis, the imaging assessment of enthesitis in children can also be challenging due to the pitfalls related to the ongoing development of the immature skeleton.³⁸ In children, enthesial radiographic findings within the bone occur very late in the disease. In particular, enthesophytes are seen less frequently in children than in adults.³⁹ In evaluating enthesitis in growing children, physiological cortical irregularities at the bone-cartilage interface and the presence of normal intra-/peritendinous vascularity detected by power Doppler US (PD US) pose challenges that are not typically encountered in adults.⁴⁰ Nevertheless, a standardized US definition of enthesitis in children is not available, and observers have to resort to a combined assessment of grayscale and PD US findings while considering these physiological findings.⁴¹

Depending on the involved anatomical structure, enthesitis in the axial skeleton is grouped as inflammatory lesions of either the vertebral body or the remainder of a vertebra. Anterior or posterior vertebral corner inflammatory lesion, vertebral endplate inflammatory lesion (which is called “aseptic spondylodiskitis”), and thoracic lateral inflammatory lesion (which is at the costovertebral joint) involve the vertebral bodies. Other inflammatory lesions involve the facet and costotransverse joints or spinal ligaments (ligamentum flavum, interspinous, and supraspinous ligaments). All those inflammatory lesions show edema/contrast enhancement of bones and/or adjacent ligaments and/or synovium. In chronic phases of SpA, structural lesions occur, including erosions, focal fat metaplasia and sclerosis of vertebral corners, bone spurs/syndesmophytes at the attachment sites of annulus fibrosus, and ankylosis of vertebrae with bridging syndesmophytes and/or bony fusion across the intervertebral disks or facet and costovertebral joints.⁴²

Whole-body MRI, which came of age in the last decade in terms of the extent of practical applications, presents the potential advantage of detecting multiple sites of enthesial involvement in a single imaging session.⁴³

Synovioentheseal complex involvement in different forms of arthritis and rheumatic diseases

This section describes the current knowledge of SEC involvement in a wide spectrum of rheumatic diseases. The entities covered here encompass all conditions whereby SEC involvement has so far been described in the literature.

Spondyloarthritis with a highlight on psoriatic arthritis

SpA refers to a group of rheumatic diseases primarily affecting the spine and peripheral joints. PsA is one of the main forms of SpA that affects the skin [psoriasis (PsO)] as well as the joints. The established primary lesion in PsA is enthesitis, reported in 30%–50% of patients with PsA.³⁰ In contradistinction to other forms of SpA, PsA tends to involve in particular the small joints of the hands and feet, resembling the joint involvement seen in different forms of arthritis, such as rheumatoid arthritis (RA) and osteoarthritis (OA).^{2,12,34,44} Although numerous studies utilizing HR MRI and US have identified the SEC as the epicenter of inflammatory lesions in PsA, conflicting results have also emerged suggesting that SEC inflammation may not be specifically linked to PsA.^{8,29,33,35,36,44-48}

PsA tends to involve distal interphalangeal (DIP) joints where OA is common, and both of these arthritis forms may present with bone proliferation and inflammation, causing diagnostic challenges.⁴⁴ Although inflammatory changes of ligament, tendon, enthesis, and adjacent bone are common both in PsA and OA, HR MRI studies have shown that they are much less prominent in OA than in PsA.⁹ In a detailed microanatomical analysis of inflammatory lesions with HR MRI and histology, the epicenter of inflammation in DIP joints is at the extensor tendon enthesis including the nail root, as a part of the enthesis organ, in PsA rather than patients with OA (Figure 2).³³ Nail bed (as well as nail root) involvement with active inflammation has been shown in patients with PsA but without PsO.^{34,49} The corollary here is that the nail bed, as well as the nail root, may also be considered part of the DIP extensor tendon enthesial organ, which is a SEC. A re-

cent study comparing PsA with PsO and OA by utilizing US, MRI, and radiography found no imaging variable as a positive predictor for PsA.⁴⁴ Nevertheless, the major limitation of that study was patient selection bias, because a considerable number of patients with PsA and PsO had been receiving disease-modifying anti-rheumatic drugs, and this may have caused subdued inflammatory imaging findings.⁴⁴

Another characteristic feature of PsA is dactylitis (or “sausage” digits), which is described in approximately 30%–40% of patients with PsA.^{2,30} Studies performed with HR MRI and US have demonstrated that dactylitis is a combination of multiple “digital polyenthesitis,” featuring “classic” enthesitis at the collateral ligament and extensor tendons, and “functional” enthesitis at other sites. Functional enthesitis in this context comprises inflammation of the extensor tendons (and/or central slips of extensor tendons) where they cross over bones, abnormal enhancement of volar and plantar plates, microenthesopathy of flexor tendon pulleys/flexor sheaths, and edema/inflammation of the surrounding soft tissue.^{35,36,45} Interestingly, although synovitis is the epicenter of inflammation in patients with RA with generalized involvement of hand joints, enthesitis

may also be involved. This is because synovitis may spread to involve entheses of collateral ligaments or pulleys, particularly in small joints where anatomic structures are very close (Figure 7).³⁶ In challenging cases, determining the dominant inflammatory lesion pattern in conjunction with clinical characteristics and diagnostic laboratory tests can help make a decision. Another important differential diagnosis of digital enthesitis is traumatic or overuse injury of tendons or ligaments, whereby history of trauma, localized findings (e.g., isolated pulley enthesitis) without arthritis, and the presence of characteristic bone deformity (e.g., Haglund syndrome) are helpful clues (Figure 6).

Extensive bone marrow edema at the phalangeal or metacarpal diaphyses (away from entheses or subchondral bone) favors PsA over other forms of arthritis (Figure 2).² Moreover, hand or feet bone marrow edema in RA and OA tends to be more confined to the capsular attachments and subchondral areas, respectively.^{19,50} In large joints, bone marrow edema can be more easily demarcated as enthesal or perienthesal, allowing more sensitive evaluation. Enthesal bone marrow edema (suggesting SEC involvement) is more common in patients with SpA compared with patients with RA or OA. In

contradistinction to SpA, both synovitis and perienthesal bone erosions are more prevalent in RA.⁴⁶ Although a study has reported conflicting results in this regard,⁴⁸ specification of enthesal and perienthesal locations was lacking, and the sample size was relatively smaller.

Erosions, calcifications, and new bone formation are late-stage findings of enthesitis, and the latter is a key distinguishing feature seen in PsA but not in RA. New bone formation in PsA can be in the form of an enthesophyte or of periosteal fluffy appearance. The combination of bone erosion and proliferation at an enthesis gives the characteristic appearance of “mouse ears” on the distal surface of the interphalangeal joint, with frequent involvement of the DIP joints.²

In early phases, although asymmetry of sacroiliitis and/or cervical predilection of spinal enthesal inflammatory lesions favor axial PsA involvement, generally there is no additional distinctive feature pointing to a subtype of SpA. However, in late phases, structural lesions show distinguishing characteristics allowing the differential diagnosis of axial PsA and ankylosing spondylitis (AS). Axial PsA presents less with sacroiliitis (which is usually asymmetrical) and more with chunky syndesmophytes, which are predominant at the cervical spine, whereas syndesmophytes in AS are marginal, symmetrical, and well-delimited.⁵¹

Juvenile idiopathic arthritis

Enthesitis and sacroiliitis are diagnostic features of juvenile-onset spondyloarthropathies (JSpAs), which make up approximately 20% of all juvenile idiopathic arthritis (JIA). According to the International League of Associations for Rheumatology, JSpAs are classified as enthesitis-related arthritis (ERA) and juvenile PsA. On the other hand, according to the European Spondyloarthropathy Study Group, JSpAs are a separate group of diseases, divided into entities as in adult patients. In the initial stage of the disease, most JSpA cases are classified as undifferentiated—the so-called “seronegative enthesopathy and arthritis syndrome.” Differentiated forms comprise four entities: juvenile AS, PsA, reactive arthritis, and arthritis associated with inflammatory bowel disease (IBD).^{39,52}

In the early course of the disease, children typically first present with enthesitis and lower extremity peripheral monoarthritis before developing sacroiliitis or spondylitis.⁵³ The commonly involved entheses are located at the lower extremities, including the

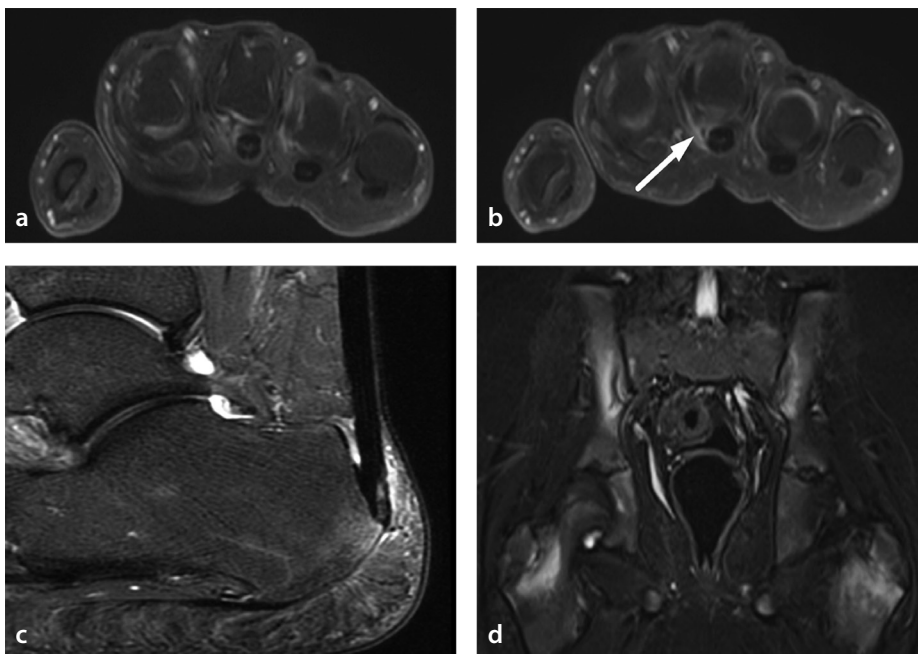


Figure 7. Synovioenthesal complex inflammation in rheumatic diseases other than spondyloarthritis. (a, b) Transverse fat-saturated T1W post-contrast magnetic resonance images (MRI) of a 58-year-old woman with seronegative rheumatoid arthritis show mild second through fourth metacarpophalangeal joint synovitis along with A1 pulley enthesitis of the third finger (b, arrow). (c) Sagittal fat-saturated T2W MR image of a 54-year-old woman with Sjögren syndrome shows Achilles tendon enthesitis characterized by intra- and peritendinous hyperintensity, subcortical bone marrow edema at the enthesal insertion, and retrocalcaneal bursitis. (d) Coronal short tau inversion recovery MR image of a 12-year-old boy with chronic non-bacterial osteomyelitis shows bilateral active on chronic sacroiliitis prominent on iliac sides with characteristic periphyseal osteitis at proximal femurs.

knee, hip, and big toe. Moreover, the tarsal joints and feet exhibit a higher frequency of involvement (Figure 3).^{39,52} In patients with ERA, the prevalence of sacroiliitis was reported to be in approximately 75% of patients with pelvic enthesitis. In keeping with these results, it is recommended to add true axial water-sensitive fat-saturated images to the SIJ MRI protocol with a larger field of view to depict the entire pelvis, including the hips, to assess various enthesal sites at the pelvis.⁵⁴ Subclinical enthesitis, which may be present in ERA as well as with sacroiliitis associated with familial Mediterranean fever (FMF), can predict disease flare-ups.⁵⁵

Although rare, bursitis can be the sole imaging finding in JIA.⁵⁶ The presence of sesamoid fibrocartilage at the Achilles tendon-retrocalcaneal bursa interface is already well known (Figure 1).⁶ Bursitis without accompanying overt classic enthesitis, which may be encountered elsewhere in patients with ERA, warrants studies searching for other sesamoid fibrocartilage–bursa interfaces. Bursitis may represent the involvement of the SEC, along with chronic irritation emanating from adjacent tendons gliding over bones (i.e., functional enthesitis).

Rheumatoid arthritis

As the most common form of autoimmune inflammatory arthritis, RA primarily affects the synovium. Although the joint synovium and periarticular bone are the most significant initial targets in RA, the synovium-lined tendon sheaths, bursae, and entheses are also affected.⁵⁷ Awareness of the SEC involvement patterns (enthesal vs perienthesal) based on the location of bone edema and erosions may help differentiate RA from other inflammatory arthritis.⁴⁶ However, in small joints, the discrimination of such enthesal lesions may be difficult due to the close anatomic alignment of involved structures. Seronegative (for rheumatoid factor and/or anti-cyclic citrullinated peptide) and/or human leukocyte antigen B27 (HLA-B27)-positive patients with RA are the most challenging cases in the early phase of the disease. However, it was shown that HLA-B27-positive patients with RA do not have more pronounced enthesitis than patients lacking this HLA allele.⁵⁸

In studies comparing enthesal abnormalities of PsA and patients with RA with healthy controls, utilizing either US or HR MRI, significantly more enthesal abnormalities in RA were found compared with healthy controls,^{29,36,47} regardless of the comparison

of results between PsA and RA (although PsA was shown to have more enthesal abnormalities than RA).^{36,45} It is likely that RA primarily affects synovial tissue and subsequently involves adjacent structures, such as entheses (Figure 7).

Retrocalcaneal bursitis can occur before or together with Achilles tendon enthesitis in the early phase of RA.¹³ This supports the concept proposed by McGonagle et al.⁵⁹ that inflammation of the SEC in RA arises from the synovial tissue. Moreover, the interesting recent finding of the presence of isolated Achilles tendon enthesitis without retrocalcaneal bursitis in a subgroup of patients who have already been diagnosed with, and are being treated for, RA,¹³ suggests several possibilities. First, enthesitis may be more resistant to RA treatment compared with bursitis. Second, enthesitis may be partially attributed to degenerative changes resulting from damage and deformities caused by RA synovitis. Last, such enthesitis in patients with RA may primarily indicate a reparative process rather than ongoing inflammation.¹³ All these observations underline the importance of increased awareness of the SEC on imaging-based detection of involved structures in RA.

Osteoarthritis

OA leads to inflammation and degeneration of various components within the joint, encompassing not only cartilage, cortical bone, and bone marrow but also the joint capsule and ligaments.⁶⁰ Studies from the last two decades have shown that enthesitis of ligaments and tendons seems to contribute to early OA as a trigger of further inflammatory changes.^{11,61} On the other hand, a recent study challenged the hypothesis that enthesitis is a precursor to OA by revealing a more frequent osseous involvement of the perienthesal (instead of the actual enthesal) regions in patients with OA (as well as those with RA), in contradistinction to the exclusive involvement of enthesal regions (in other words, the SEC) in patients with SpA.⁴⁶ Once again, the SEC is at the forefront of investigations into such distinctions.

Diffuse idiopathic skeletal hyperostosis

Diffuse idiopathic skeletal hyperostosis (DISH) is an ossifying enthesopathy characterized by excessive new bone formation in the axial and peripheral skeleton. In the axial skeleton, DISH usually affects the thoracic spine, whereas in the peripheral skeleton, enthesal sites (mainly in the pelvis) are tar-

geted. The condition is regarded as mechanical or degenerative in nature, although local inflammation may also play a role in its development. DISH may be asymptomatic or may manifest as back and cervical pain, dysphagia, pain at peripheral enthesal sites, or limitation of motion of the spine, often mimicking SpA. Although strict radiographic criteria by Resnick and Niwayama⁶² have long been used in diagnosing DISH, longitudinal studies have highlighted the need for establishing new criteria to identify it earlier.⁶³ Kuperus et al.⁶³ have recently developed and validated criteria for early-phase DISH utilizing computed tomography (CT).

Despite overlapping imaging features in DISH and SpA, new bone formation and enthesophytes in the spine and the appendicular skeleton are generally thicker and more prominent in DISH. In addition, DISH-related osteophytes in the spine are primarily located on the right and are more horizontal, whereas in SpA they are vertically oriented with no side predilection. At peripheral forms of enthesitis, enthesophytes in DISH are also prominent and show a whiskering pattern, without accompanying erosions and sclerosis. SIJ ankylosis of DISH reveals anterior and/or posterior bridging osteophytes without erosions and sclerosis, different from intraarticular ankylosis and erosions of SpA.⁶⁴

Crystal-induced arthritis

The accumulation of calcium-based crystals in the entheses is arguably the most common underlying factor in systemic enthesopathy¹² and can be easily identified through radiography and/or US. Nevertheless, there is a paucity of research on this subject in recent years. On the other hand, enthesitis related to gout (a monosodium urate-based crystal arthropathy) has been reported.⁶⁵ Crystal depositions in gout are found not only in and around joints but also in tendons and entheses, which can be detected by dual-energy CT and US. A recent study utilizing US showed that approximately half of gout patients have enthesal abnormality at their lower extremities, whereby the patellar insertion of the quadriceps tendon was the most common site.⁶⁵ Moreover, sacroiliitis as a feature of gout has also been reported in the form of erosions with multilobulated bases (and an absence of subchondral sclerosis).⁶⁶

Familial Mediterranean fever

FMF is the most common autoinflammatory disease that can be associated with SpA,

PsO, vasculitis, Behçet's disease (BD), JIA, and IBD. In addition to episodes of peritonitis, pleuritis, or acute synovitis, a significant number of patients with FMF are found to exhibit enthesitis and sacroiliitis, which are also characteristic imaging findings of SpA.^{16,67} Pelvic and lower extremity entheses, particularly the Achilles tendon, are the most commonly reported sites.^{67,68} In a recent study, enthesitis was found to be a sign of a more severe FMF phenotype and was associated with other musculoskeletal manifestations that resemble SpA.⁶⁷

Systemic lupus erythematosus

The musculoskeletal system is frequently affected in systemic lupus erythematosus (SLE), whereby enthesitis has also been reported as a manifestation, in addition to arthralgia, arthritis, tenosynovitis, tendon rupture, tendonosis, osteonecrosis, subcortical cysts, osteomyelitis, septic arthritis, and myositis.⁶⁹ The distal insertion of the patellar tendon, which features a SEC, is the most frequently affected site of enthesitis in SLE. In comparison with patients with PsA, enthesitis in SLE is rarely associated with US findings of structural damage.⁷⁰

Systemic sclerosis

Systemic sclerosis (SSc) is a chronic autoimmune disease with a complex pathogenesis characterized by fibrosis and inflammation of the skin and multiple internal organs.⁷¹ Ultrasound studies suggest that synovitis is one of the most common findings in SSc, affecting almost half of all patients. In a recent study using US and featuring healthy controls, it was found that 38% of SSc patients exhibited enthesitis of the lateral epicondylar common extensor tendon. Skin thickening and sarcopenia due to myositis and myopathy may serve as risk factors that alter the distribution of mechanical forces on the underlying entheses and the SEC, thereby contributing to the development of enthesitis.⁷¹

Sjögren syndrome

Sjögren syndrome (SS) is a chronic autoimmune disease marked by lymphocytic infiltration of the exocrine glands. Diffuse pain is a common feature in SS, and entheses zones are one of the leading causes of pain in the musculoskeletal system. A US study has shown that the plantar fascia, Achilles tendon, and distal patellar tendon are the most common sites of enthesitis in patients with SS (Figure 7).⁷²

Behçet disease

BD is a type of vasculitis with six different phenotypes. A study utilizing US has shown that the arthritis/articular involvement-predominant phenotype features more enthesitis compared with other phenotypes of BD without arthritis (as well as to patients with RA and healthy controls).¹⁰ A recent observational multicenter study found that almost one-third of the juvenile patients with BD who tested negative for HLA-B27 had sacroiliitis revealed on MRI.¹⁷ Although the presence of enthesitis and sacroiliitis in BD suggests an association with SpA, there is no conclusive evidence as yet to include BD in the SpA disease complex.

Synovitis, acne, pustulosis, hyperostosis, and osteitis syndrome and chronic non-bacterial osteomyelitis

Synovitis, acne, pustulosis, hyperostosis, and osteitis (SAPHO) syndrome and chronic non-bacterial osteomyelitis (CNO) are autoinflammatory diseases. Whereas CNO is characterized by remitting and relapsing bone lesions throughout the body, SAPHO syndrome presents with both skin and osteoarticular lesions.^{73,74} CNO predominantly occurs in children/adolescents and SAPHO syndrome in adults. The anterior chest wall bones and joints are the most frequent sites for SAPHO lesions, whereas CNO tends to involve predominantly pelvis and lower extremity long bones, characterized by osteitis of metaphyses and epiphyses (or their equivalents), sometimes with frank involvement of the physes that may cause lifelong deformities.^{73,74} In the chronic phase of SAPHO, lesions eventually ossify and cause ankylosis.

In SAPHO syndrome, in addition to subclinical enthesopathy detected with US, axial involvement resembles psoriatic SpA and starts with vertebral corner lesions, such as enthesitis of SpA. In time, corner lesions progress to the adjacent vertebral endplate and/or the anterior cortex of the vertebral body, often accompanied by thickening of the prevertebral soft tissue that may ossify and cause voluminous paravertebral ossification.^{73,75} Sacroiliitis may also be seen, usually unilaterally.

Vertebral lesions of CNO may present as inflammatory corner lesions, such as enthesitis, and/or may involve the entire endplate or body, which may eventually collapse. Unlike SAPHO, paravertebral ossification is not expected. Sacroiliitis is another important imaging feature of CNO that was reported in up to 72% of children in a recent

cohort (Figure 7).⁷⁴ CNO lesions with peripheral enthesitis should raise suspicion of an association with other rheumatic/inflammatory conditions, such as PsA or ERA.⁷⁴

Both in the acute and chronic phases of SAPHO, patterns of chest and vertebral lesions suggest SEC inflammation; however, it is not clear which component of the entheses organ is primarily involved. Since osteitis is the primary lesion of SAPHO or CNO, secondary involvement of joints and surrounding capsular and ligamentous structures appears more reasonable.

In conclusion, the SEC is a pivotal site in the imaging-based assessment of arthritis and other rheumatic diseases. It should be a prime site of attention in the radiologists' search pattern when performing and interpreting modern imaging techniques. With its capability to show the entheses organ exquisitely—and in its entirety, including the bone marrow—HR MRI is the most versatile tool for depicting the SEC. Despite their limitations in various aspects, radiography, US and CT are nevertheless also helpful for this purpose, as long as the SEC, with its involvement in rheumatic diseases, is given due consideration. Radiologists need to be familiar with the anatomic properties of the SEC at different locales across the body and its involvement in different conditions, both rheumatic and non-rheumatic.

Conflict of interest disclosure

The authors declared no conflicts of interest.

References

- Centers for Disease Control and Prevention. Disability and Health Related Conditions. Accessed February 28, 2024. [\[Crossref\]](#)
- Shiraishi M, Fukuda T, Igarashi T, Tokashiki T, Kayama R, Ojiri H. Differentiating rheumatoid and psoriatic arthritis of the hand: multimodality imaging characteristics. *Radiographics*. 2020;40(5):1339-1354 [\[Crossref\]](#)
- Jacobson JA, Girish G, Jiang Y, Sabb BJ. Radiographic evaluation of arthritis: degenerative joint disease and variations. *Radiology*. 2008;248(3):737-747. [\[Crossref\]](#)
- Niepel GA, Kostka D, Kopecký S, Manca S. Enthesopathy. *Acta Rheumatologica et Balneologica Pisticiana*. 1966;1:1-64. [\[Crossref\]](#)
- McGonagle D, Gibbon W, O'Connor P, Green M, Pease C, Emery P. Characteristic magnetic resonance imaging enthesal changes of knee synovitis in spondylarthropathy. *Arthritis Rheum*. 1998;41(4):694-700. [\[Crossref\]](#)
- Braun J, Khan MA, Sieper J. Enthesitis and ankylosis in spondyloarthropathy: what is the

- target of the immune response? *Ann Rheum Dis.* 2000;59(12):985-994. [\[Crossref\]](#)
7. Benjamin M, Moriggl B, Brenner E, Emery P, McGonagle D, Redman S. The “enthesis organ” concept: why enthesopathies may not present as focal insertional disorders. *Arthritis Rheum.* 2004;50(10):3306-3313. [\[Crossref\]](#)
 8. Tan AL, Grainger AJ, Tanner SF, Emery P, McGonagle D. A high-resolution magnetic resonance imaging study of distal interphalangeal joint arthropathy in psoriatic arthritis and osteoarthritis: are they the same?. *Arthritis Rheum.* 2006;54(4):1328-1333. [\[Crossref\]](#)
 9. McGonagle D, Lories RJ, Tan AL, Benjamin M. The concept of a “synovio-enthesal complex” and its implications for understanding joint inflammation and damage in psoriatic arthritis and beyond. *Arthritis Rheum.* 2007;56(8):2482-2491. [\[Crossref\]](#)
 10. Hatemi G, Fresko I, Tascilar K, Yazici H. Increased enthesopathy among Behçet’s syndrome patients with acne and arthritis: an ultrasonography study. *Arthritis Rheum.* 2008;58(5):1539-1545. [\[Crossref\]](#)
 11. Binks DA, Bergin D, Freemont AJ, et al. Potential role of the posterior cruciate ligament synovio-enthesal complex in joint effusion in early osteoarthritis: a magnetic resonance imaging and histological evaluation of cadaveric tissue and data from the Osteoarthritis Initiative. *Osteoarthritis Cartilage.* 2014;22(9):1310-1317. [\[Crossref\]](#)
 12. Slobodin G, Rimar D, Boulman N, et al. Enteseal involvement in systemic disorders. *Clin Rheumatol.* 2015;34(12):2001-2010. [\[Crossref\]](#)
 13. Suzuki T, Hidaka Y, Seri Y. Retrocalcaneal bursitis precedes or accompanies achilles tendon enthesitis in the early phase of rheumatoid arthritis. *Clin Med Insights Arthritis Musculoskelet Disord.* 2018;11:1179544118781094. [\[Crossref\]](#)
 14. Chang MY, Hong SH, Yoo HJ, Choi JY, Chae HD, Moon SJ. MRI of Cuboid Pulley Lesion. *AJR Am J Roentgenol.* 2018;211(4):867-871. [\[Crossref\]](#)
 15. Himuro H, Kurata S, Nagata S, et al. Imaging features in patients with SAPHO/CRMO: a pictorial review. *Jpn J Radiol.* 2020;38(7):622-629. [\[Crossref\]](#)
 16. Acer Kasman S, Duruöz MT. Spondyloarthritis in familial Mediterranean fever: a cohort study. *Rheumatol Int.* 2022;42(10):1729-1739. [\[Crossref\]](#)
 17. Gaggiano C, Maselli A, Sfikakis PP, et al. Musculoskeletal manifestations in children with Behçet’s syndrome: data from the AIDA Network Behçet’s syndrome registry. *Intern Emerg Med.* 2023;18(3):743-754. [\[Crossref\]](#)
 18. Benjamin M, McGonagle D. The anatomical basis for disease localisation in seronegative spondyloarthropathy at entheses and related sites. *J Anat.* 2001;199(Pt 5):503-526. [\[Crossref\]](#)
 19. Mathew AJ, Østergaard M. Magnetic resonance imaging of enthesitis in spondyloarthritis, including psoriatic arthritis—status and recent advances. *Front Med (Lausanne).* 2020;7:296. [\[Crossref\]](#)
 20. Seven S, Pedersen SJ, Østergaard M, et al. Peripheral enthesitis detected by ultrasonography in patients with axial spondyloarthritis—anatomical distribution, morphology, and response to tumor necrosis factor-inhibitor therapy. *Front Med (Lausanne).* 2020;7:341. [\[Crossref\]](#)
 21. Sampson SP, Badalamente MA, Hurst LC, Seidman J. Pathobiology of the human A1 pulley in trigger finger. *J Hand Surg Am.* 1991;16(4):714-721. [\[Crossref\]](#)
 22. Benjamin M, Ralphs JR. Fibrocartilage in tendons and ligaments—an adaptation to compressive load. *J Anat.* 1998;193(Pt 4):481-494. [\[Crossref\]](#)
 23. McGonagle D, Marzo-Ortega H, Benjamin M, Emery P. Report on the second international enthesitis workshop. *Arthritis Rheum.* 2003;48(4):896-905. [\[Crossref\]](#)
 24. Egund N, Jurik AG. Anatomy and histology of the sacroiliac joints. *Semin Musculoskelet Radiol.* 2014;18(3):332-339. [\[Crossref\]](#)
 25. Hermann KG, Bollow M. Magnetic resonance imaging of sacroiliitis in patients with spondyloarthritis: correlation with anatomy and histology. *Rofo.* 2014;186(3):230-237. [\[Crossref\]](#)
 26. Flores DV, Goes PK, Gómez CM, Umpire DF, Pathria MN. Imaging of the acromioclavicular joint: anatomy, function, pathologic features, and treatment. *Radiographics.* 2020;40(5):1355-1382. [\[Crossref\]](#)
 27. Schett G, Lories RJ, D’Agostino MA, et al. Enthesitis: from pathophysiology to treatment. *Nat Rev Rheumatol.* 2017;13(12):731-741. [\[Crossref\]](#)
 28. Schett G, Rahman P, Ritchlin C, McInnes IB, Elewaut D, Scher JU. Psoriatic arthritis from a mechanistic perspective. *Nat Rev Rheumatol.* 2022;18(6):311-325. [\[Crossref\]](#)
 29. Ebstein E, Coustet B, Masson-Behar V, et al. Enthesopathy in rheumatoid arthritis and spondyloarthritis: an ultrasound study. *Joint Bone Spine.* 2018;85(5):577-581. [\[Crossref\]](#)
 30. Watad A, Eshed I, McGonagle D. Lessons learned from imaging on enthesitis in psoriatic arthritis. *Isr Med Assoc J.* 2017;19(11):708-711. [\[Crossref\]](#)
 31. Balint PV, Terslev L, Aegerter P, et al. Reliability of a consensus-based ultrasound definition and scoring for enthesitis in spondyloarthritis and psoriatic arthritis: an OMERACT US initiative. *Ann Rheum Dis.* 2018;77(12):1730-1735. [\[Crossref\]](#)
 32. Mathew AJ, Krabbe S, Eshed I, et al. Atlas of the OMERACT Heel Enthesitis MRI Scoring System (HEMRIS). *RMD Open.* 2020;6(1):e001150. [\[Crossref\]](#)
 33. Tan AL, Benjamin M, Toumi H, et al. The relationship between the extensor tendon entheses and the nail in distal interphalangeal joint disease in psoriatic arthritis—a high-resolution MRI and histological study. *Rheumatology (Oxford).* 2007;46(2):253-256. [\[Crossref\]](#)
 34. Tan AL, McGonagle D. Psoriatic arthritis: correlation between imaging and pathology. *Joint Bone Spine.* 2010;77(3):206-211. [\[Crossref\]](#)
 35. Tan AL, Fukuba E, Halliday NA, Tanner SF, Emery P, McGonagle D. High-resolution MRI assessment of dactylitis in psoriatic arthritis shows flexor tendon pulley and sheath-related enthesitis. *Ann Rheum Dis.* 2015;74(1):185-189. [\[Crossref\]](#)
 36. Abrar DB, Schleich C, Nebelung S, et al. High-resolution MRI of flexor tendon pulleys using a 16-channel hand coil: disease detection and differentiation of psoriatic and rheumatoid arthritis. *Arthritis Res Ther.* 2020;22(1):40. [\[Crossref\]](#)
 37. Maksymowych WP, Lambert RG, Østergaard M, et al. MRI lesions in the sacroiliac joints of patients with spondyloarthritis: an update of definitions and validation by the ASAS MRI working group. *Ann Rheum Dis.* 2019;78(11):1550-1558. [\[Crossref\]](#)
 38. Herregods N, Anisau A, Schietecatte E, et al. MRI in pediatric sacroiliitis, what radiologists should know. *Pediatr Radiol.* 2023;53(8):1576-1586. [\[Crossref\]](#)
 39. Sudoł-Szopińska I, Eshed I, Jans L, Herregods N, Teh J, Vojinovic J. Classifications and imaging of juvenile spondyloarthritis. *J Ultrason.* 2018;18(74):224-233. [\[Crossref\]](#)
 40. Chauvin NA, Ho-Fung V, Jaramillo D, Edgar JC, Weiss PF. Ultrasound of the joints and entheses in healthy children. *Pediatr Radiol.* 2015;45(9):1344-1354. [\[Crossref\]](#)
 41. Roth J, Stinson SE, Chan J, Barrowman N, Di Geso L. Differential pattern of Doppler signals at lower-extremity entheses of healthy children. *Pediatr Radiol.* 2019;49(10):1335-1343. [\[Crossref\]](#)
 42. Baraliakos X, Østergaard M, Lambert RG, et al. MRI lesions of the spine in patients with axial spondyloarthritis: an update of lesion definitions and validation by the ASAS MRI working group. *Ann Rheum Dis.* 2022;81(9):1243-1251. [\[Crossref\]](#)
 43. Althoff CE, Sieper J, Song IH, et al. Active inflammation and structural change in early active axial spondyloarthritis as detected by whole-body MRI. *Ann Rheum Dis.* 2013;72(6):967-973. [\[Crossref\]](#)
 44. Guldberg-Møller J, Mogensen M, Ellegaard K, et al. Multimodal imaging of the distal interphalangeal-joint synovio-enthesal complex in psoriatic arthritis (MIDAS): a cross-sectional study on the diagnostic accuracy of different imaging modalities comparing psoriatic arthritis to psoriasis and

- osteoarthritis. *RMD Open*. 2022;8(1):e002109. [\[Crossref\]](#)
45. Zabotti A, Salvin S, Quartuccio L, De Vita S. Differentiation between early rheumatoid and early psoriatic arthritis by the ultrasonographic study of the synovio-entheseal complex of the small joints of the hands. *Clin Exp Rheumatol*. 2016;34(3):459-465. [\[Crossref\]](#)
 46. Li B, Guo Z, Qu J, Zhan Y, Shen Z, Lei X. The value of different involvement patterns of the knee "synovio-entheseal complex" in the differential diagnosis of spondyloarthritis, rheumatoid arthritis, and osteoarthritis: an MRI-based study. *Eur Radiol*. 2023;33(5):3178-3187. [\[Crossref\]](#)
 47. Genc H, Cakit BD, Tuncbilek I, Erdem HR. Ultrasonographic evaluation of tendons and enthesal sites in rheumatoid arthritis: comparison with ankylosing spondylitis and healthy subjects. *Clin Rheumatol*. 2005;24(3):272-277. [\[Crossref\]](#)
 48. Paramarta JE, van der Leij C, Gofita I, et al. Peripheral joint inflammation in early onset spondyloarthritis is not specifically related to enthesitis. *Ann Rheum Dis*. 2014;73(4):735-740. [\[Crossref\]](#)
 49. Ruscitti P, Esposito M, Gianneramo C, et al. Nail and enthesitis assessment in patients with psoriatic disease by high frequency ultrasonography: findings from a single-centre cross-sectional study. *Radiol Med*. 2022;127(12):1400-1406. [\[Crossref\]](#)
 50. Narváez J, Narváez JA, de Albert M, Gómez-Vaquero C, Nolla JM. Can magnetic resonance imaging of the hand and wrist differentiate between rheumatoid arthritis and psoriatic arthritis in the early stages of the disease? *Semin Arthritis Rheum*. 2012;42(3):234-245. [\[Crossref\]](#)
 51. Lopez-Medina C, Ziade N. Axial Disease in psoriatic arthritis: how can we Define it, and does it have an Impact on Treatment? *Mediterr J Rheumatol*. 2022;33(Suppl 1):142-149. [\[Crossref\]](#)
 52. Sudol-Szopińska I, Gietka P, Znajdek M, et al. Imaging of juvenile spondyloarthritis. Part I: Classifications and radiographs. *J Ultrason*. 2017;17(70):167-175. [\[Crossref\]](#)
 53. Hemke R, Herregods N, Jaremko JL, et al. Imaging assessment of children presenting with suspected or known juvenile idiopathic arthritis: ESSR-ESPR points to consider. *Eur Radiol*. 2020;30(10):5237-5249. [\[Crossref\]](#)
 54. Herregods N, Maksymowych WP, Jans L, et al. Atlas of MRI findings of sacroiliitis in pediatric sacroiliac joints to accompany the updated preliminary OMERACT pediatric JAMRIS (Juvenile idiopathic arthritis MRI score) scoring system: Part I: active lesions. *Semin Arthritis Rheum*. 2021;51(5):1089-1098. [\[Crossref\]](#)
 55. Sener S, Atalay E, Yildiz AE, et al. Subclinical enthesitis in enthesitis-related arthritis and sacroiliitis associated with familial Mediterranean fever. *Mod Rheumatol*. 2024;34(3):607-613. [\[Crossref\]](#)
 56. Alqanatish JT, Petty RE, Houghton KM, et al. Infrapatellar bursitis in children with juvenile idiopathic arthritis: a case series. *Clin Rheumatol*. 2011;30(2):263-267. [\[Crossref\]](#)
 57. Suh JY, Park SY, Koh SH, Lee IJ, Lee K. Unusual, but important, peri- and extra-articular manifestations of rheumatoid arthritis: a pictorial essay. *Ultrasonography*. 2021;40(4):602-616. [\[Crossref\]](#)
 58. Mera-Varela A, Ferreiro-Iglesias A, Perez-Pampin E, Porto-Silva M, Gómez-Reino JJ, Gonzalez A. Ultrasonographic assessment of enthesitis in HLA-B27 positive patients with rheumatoid arthritis, a matched case-only study. *PLoS One*. 2013;8(3):e58616. [\[Crossref\]](#)
 59. McGonagle D, Gibbon W, Emery P. Classification of inflammatory arthritis by enthesitis. *Lancet*. 1998;352(9134):1137-1140. [\[Crossref\]](#)
 60. Schulze-Tanzil G. Intraarticular ligament degeneration is interrelated with cartilage and bone destruction in osteoarthritis. *Cells*. 2019;8(9):990. [\[Crossref\]](#)
 61. Tan AL, Toumi H, Benjamin M, et al. Combined high-resolution magnetic resonance imaging and histological examination to explore the role of ligaments and tendons in the phenotypic expression of early hand osteoarthritis. *Ann Rheum Dis*. 2006;65(10):1267-1272. [\[Crossref\]](#)
 62. Resnick D, Niwayama G. Radiographic and pathologic features of spinal involvement in diffuse idiopathic skeletal hyperostosis (DISH). *Radiology*. 1976;119(3):559-568. [\[Crossref\]](#)
 63. Kuperus JS, Oudkerk SF, Foppen W, et al. Criteria for Early-phase diffuse idiopathic skeletal hyperostosis: development and validation. *Radiology*. 2019;291(2):420-426. [\[Crossref\]](#)
 64. Eshed I. Imaging Characteristics of diffuse idiopathic skeletal hyperostosis: more than just spinal bony bridges. *Diagnostics (Basel)*. 2023;13(3):563. [\[Crossref\]](#)
 65. Xu G, Lin J, Liang J, et al. Enthesal involvement of the lower extremities in gout: an ultrasonographic descriptive observational study. *Clin Rheumatol*. 2021;40(11):4649-4657. [\[Crossref\]](#)
 66. Panwar J, Sandhya P, Kandagaddala M, Nair A, Jeyaseelan V, Danda D. Utility of CT imaging in differentiating sacroiliitis associated with spondyloarthritis from gouty sacroiliitis: a retrospective study. *Clin Rheumatol*. 2018;37(3):779-788. [\[Crossref\]](#)
 67. Sen N, Yilmaz M, Mercan R, et al. Enthesitis may be one of the signs of severe disease in familial Mediterranean fever. *Clin Rheumatol*. 2021;40(4):1479-1485. [\[Crossref\]](#)
 68. Tufan A, Mercan R, Tezcan ME, et al. Enthesopathy in patients with familial Mediterranean fever: increased prevalence in M694 V variant. *Rheumatol Int*. 2013;33(8):1933-1937. [\[Crossref\]](#)
 69. Di Matteo A, Smerilli G, Cipolletta E, et al. Imaging of joint and soft tissue involvement in systemic lupus erythematosus. *Curr Rheumatol Rep*. 2021;23(9):73. Published 2021 Jul 16. [\[Crossref\]](#)
 70. Di Matteo A, Filippucci E, Cipolletta E, et al. Enthesal involvement in patients with systemic lupus erythematosus: an ultrasound study. *Rheumatology (Oxford)*. 2018;57(10):1822-1829. [\[Crossref\]](#)
 71. Terenzi R, Karalilova R, Lepri G, et al. Enthesopathy and involvement of synovio-entheseal complex in systemic sclerosis: an ultrasound pilot study. *Rheumatology (Oxford)*. 2020;59(3):580-585. [\[Crossref\]](#)
 72. Sag S, Sag MS, Tekeoglu I, Kamanlı A, Nas K. Presence of enthesopathy in patients with primary Sjogren's syndrome: ultrasonographic study of a local cohort. *J Med Ultrason (2001)*. 2018;45(1):121-127. [\[Crossref\]](#)
 73. Jurik AG, Klicman RF, Simoni P, Robinson P, Teh J. SAPHO and CRMO: the value of imaging. *Semin Musculoskelet Radiol*. 2018;22(2):207-224. [\[Crossref\]](#)
 74. Aydingöz Ü, Yildiz AE, Ayaz E, Batu ED, Özen S. Preferential involvement of the pelvis and hips along with active sacroiliitis in chronic nonbacterial osteomyelitis: MRI of 97 patients from a single tertiary referral center. *Eur Radiol*. 2024. [\[Crossref\]](#)
 75. Queiro R, Alonso S, Alperi M, et al. Enthesal ultrasound abnormalities in patients with SAPHO syndrome. *Clin Rheumatol*. 2012;31(6):913-919. [\[Crossref\]](#)



Imaging findings of primary lung tumors in children

H. Nursun Özcan¹
 Fırat Atak²
 Berna Oğuz¹
 Tezer Kutluk³
 Mithat Haliloğlu¹

¹Hacettepe University Faculty of Medicine,
Department of Radiology, Division of Pediatric
Radiology, Ankara, Türkiye

²Hacettepe University Faculty of Medicine,
Department of Radiology, Ankara, Türkiye

³Hacettepe University Faculty of Medicine,
Department of Pediatrics, Division of Pediatric
Oncology, Ankara, Türkiye

PURPOSE

Pediatric lung tumors are primarily discussed in the surgical literature. However, limited research has been reported on their imaging findings, and only a few tumor types have been documented. Therefore, the aim of this article is to describe the imaging features of primary lung tumors in children.

METHODS

The archives of the pediatric radiology unit were reviewed for primary lung tumors documented between 2007 and 2023. In total, 24 patients (9 girls and 15 boys; aged 5 months to 16 years) were included in the study. Their demographic characteristics, clinical presentation, and histopathologic results were obtained. All imaging studies were reviewed by two radiologists for various findings (e.g., lymphadenopathy, atelectasis, pleural effusion, calcification, multiplicity, pneumothorax, axial and lobar location, laterality, tumor margin, mediastinal shift, contrast enhancement pattern, signal intensity on T1- and T2-weighted images, and diffusion pattern), and a final decision was made by consensus. The mean tumor size was compared between the benign and malignant groups using a t-test.

RESULTS

There were 15 (62.5%) benign tumors, as follows: inflammatory myofibroblastic tumor (IMT; n = 10, 41%), hemangioma (n = 2, 8%), pneumocytoma (n = 2, 8%), and mature cystic teratoma (n = 1, 4%). Moreover, there were 9 (37.5%) malignant tumors, as follows: pleuropulmonary blastoma (PPB; n = 6, 25%), adenocarcinoma (n = 2, 8%), and lymphoepithelioma-like carcinoma (LELC) (n = 1, 4%). The most frequently reported symptoms were cough, fever, dyspnea, chest pain, and recurrent infection; six patients reported no clinical symptoms. Fifteen tumors (62%) were located in the right lung. The mean tumor diameter at the time of diagnosis was 6.4 ± 3 cm (benign group: 6.7 ± 3.4 cm; malignant group: 6 ± 2.3 cm, $P > 0.050$). Calcification was present in 80% of the patients with IMT. At the time of diagnosis, two (8.3%) patients were found to have metastasis: one was diagnosed with adenocarcinoma and the other with LELC. Tumors were located peripherally in 18 (75%) patients.

CONCLUSION

The symptoms associated with lung masses are non-specific. There is no correlation between tumor size and malignancy. The most common tumors observed in this study were IMT and PPB, respectively. IMT is highly associated with calcification.

CLINICAL SIGNIFICANCE

Primary lung tumors are rarely seen in children, and they have different histopathological types. Calcification might be an important radiological clue for the diagnosis of IMT, which is the most common lung tumor in children.

KEYWORDS

Children, lung, cancer, CT, MRI, inflammatory myofibroblastic tumor

Corresponding author: H. Nursun Özcan

E-mail: drhnozcan@yahoo.com

Received 13 February 2024; revision requested 13 March 2024; last revision received 21 April 2024; accepted 21 May 2024.



Epub: 10.06.2024

Publication date: 06.11.2024

DOI: 10.4274/dir.2024.242714

Primary lung tumors are uncommon in children, have a different histologic spectrum than adult lung tumors, and change with age.¹⁻³ Metastases and congenital lung masses constitute a substantial proportion of lung neoplasms in children. The incidence of primary, metastatic, and congenital/inflammatory lesions is reported to be 1:5:60.⁴ The most prevalent metastatic tumors in the lungs are Wilms tumor and osteosarcoma.⁵ Primary lung masses may be located in the tracheobronchial tree or parenchyma. Furthermore, parenchymal involvement may occur secondarily via local invasion of mediastinal or chest wall masses.

Patients typically present with non-specific and indistinct clinical symptoms. Delayed diagnosis is common due to the lack of specific symptoms and diverse imaging findings at presentation. The mortality rate for primary benign lung neoplasms in children is low (8.7%), and that for primary malignant tumors is approximately 30% overall.⁶ It is paramount that radiologists have a comprehensive understanding of the histopathological spectrum of primary lung masses, enabling them to identify relevant imaging findings, make accurate differential diagnoses, and provide appropriate guidance, particularly considering the relatively low survival rates and often unremarkable clinical presentation.

Research on pediatric lung tumors is primarily found in surgical literature.^{2,7} However, few studies have been conducted on the imaging findings of primary lung tumors in the pediatric population, and only a few tumor types have been reported.^{1,8} The purpose of this paper is to report on our experience with primary lung tumors in children. We have reviewed our cases over the past 16 years and provided a detailed overview of their imaging findings with computed tomography (CT) and magnetic resonance imaging (MRI).

Methods

The archive of the pediatric radiology unit was retrospectively reviewed for lung tumors documented between 2007 and 2023. The inclusion criteria were an available CT and/or MRI scan and pathologic diagnosis of a lung tumor. Tumors of metastatic and tracheobronchial origin were excluded. The search yielded 25 patients, 1 of whom did not have imaging studies available. Therefore, only the remaining 24 patients (9 girls and 15 boys; aged between 5 months and 16 years, median age: 7.5 years) were included in the study (Figure 1). The demographic features, imaging findings, and pathological results were documented. Informed consent was waived due to the retrospective nature of the data analysis. Approval was obtained from the Hacettepe University Non-Interventional Ethics Committee for this retrospective study (decision no: SBA 23/377; date: 30.11.2023).

Chest X-rays were evaluated for several potential findings, including the presence of pleural effusion, pneumothorax, focal abnormal opacity, and asymmetric density (radiolucency or radiopacity) of the hemithorax. No pleural effusion or pneumothorax was detected among the patients with available chest X-rays. Chest CTs and MRIs were assessed for the following characteristics: anatomic location of the tumor, tumor size, margins (smooth or lobulated), tumor pattern (cystic, solid, or mixed), contrast enhancement pattern (homogeneous or heterogeneous), presence of calcification, atelectasis, pleural effusion, pneumothorax, mediastinal shift, lymphadenopathy, local invasion, and metastasis at the time of diagnosis. A cystic component was considered present if septation or a fluid–fluid level

was visible in any region within the mass, irrespective of the imaging study. Note that when an MRI scan is performed, regions with typical fluid intensity are classified as cystic. Furthermore, if post-gadolinium series were available, they were checked for contrast enhancement in these areas. In patients with only CT scans available, areas without marked contrast enhancement and densitometric measurements less than 20 HU were considered cystic. Contrast enhancement was determined by comparing the density of the solid component of the lesion with the muscle density in single-phase studies. It was considered positive if the densitometric value of the solid part was equal to or greater than the muscle density. In cases where at least a two-phase pre- and post-contrast image was obtained or two separate acquisitions were performed at different time points with and without contrast (if the acquisition parameters were the same), a change in tissue density greater than 20 HU was considered positive for contrast enhancement. The tumor size was determined via measuring the two greatest axial dimensions. In group analyses, the largest axial diameter was used. Pleural effusion or pneumothorax was considered positive if seen only on the ipsilateral side with the mass. Mediastinal lymph nodes were considered pathologic if the axial short axis diameter was larger than 7 mm.⁹ Radiologic detection of local invasion can be challenging. Thus, in patients who underwent surgery, we checked whether local invasion was confirmed by the pathological findings. In cases where no pathology report was available, we used predefined imaging criteria for local invasion and deemed all suspicious cases as negative. For central tumors, local invasion was considered positive

Main points

- Primary lung tumors in children are rare. Patients generally present with non-specific symptoms, and imaging features are highly variable.
- The majority of inflammatory myofibroblastic tumors are observed as well-defined, peripheral, and calcified masses.
- Persistent consolidation and atelectasis should alert the radiologist to neoplastic conditions.

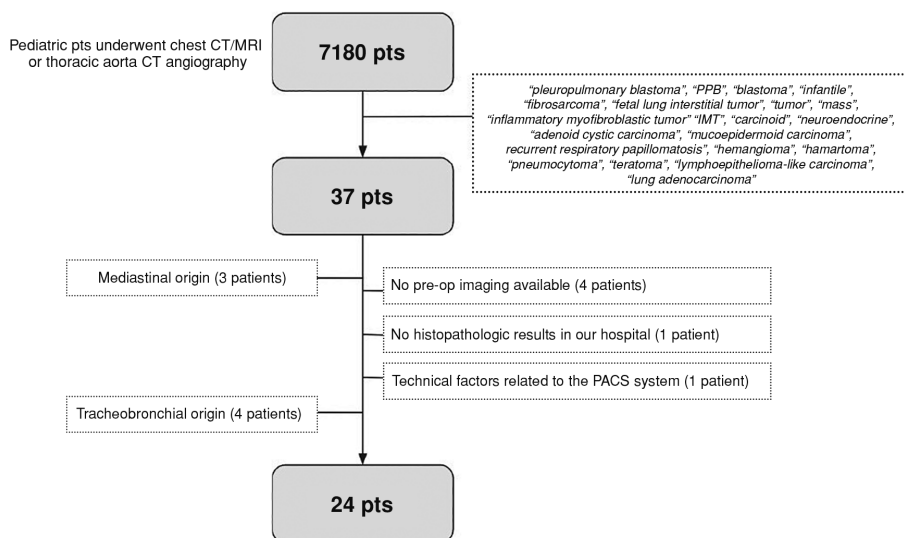


Figure 1. Flowchart of our study.

if, for example, there was an endobronchial nodular lesion, soft tissue density in the mediastinum showing continuity with the main lesion, intracardiac soft tissue lesion, or the presence of at least 180 degrees of surrounding hilar structures. In peripheral lesions, local invasion was considered positive if there was pleural thickening or nodularity, osseous destruction, and/or chest wall muscle involvement. If two radiologists could not reliably determine the presence of invasion, it was reported as negative. If the mass was located within the inner one-third of the concentric imaginary lines drawn from the hilum, it was considered central.¹⁰ If the mass was within the borders of any two parts, the site that contained the majority of the tumor was reported as the tumor location.

Statistical analysis

The data were presented as the mean \pm standard deviation or median (25th–75th percentile), as appropriate. Categorical variables were reported as the frequency (percentage). The normality assumption of the numerical variables was assessed with the Shapiro–Wilk goodness-of-fit test. Differences between groups were analyzed using the independent t-test, Mann–Whitney U test, or chi-squared (χ^2) test. The statistical significance was set as $P < 0.050$.

Results

The patient demographics and clinical characteristics are summarized in Table 1. The chest X-ray and CT findings for the benign and malignant subgroups and the different histopathologic entities are presented in Tables 2 and 3. In total, 15 (62.5%) patients had benign neoplasms, comprising inflammatory myofibroblastic tumor (IMT; $n = 10$, 41.7%), hemangioma ($n = 2$, 8.3%), pneumocytoma ($n = 2$, 8.3%), and mature cystic teratoma ($n = 1$, 4.2%). The remaining 9 (37.5%) patients had malignant tumors, including pleuropulmonary blastoma (PPB; $n = 6$, 25%), adenocarcinoma ($n = 2$, 8.3%), and lymphoepithelioma-like carcinoma (LELC; $n = 1$, 4.2%). The most common presenting symptoms were cough ($n = 12$, 50%), fever ($n = 7$, 29.2%), dyspnea ($n = 5$, 20.8%), and chest pain ($n = 5$, 20.8%). There was no statistically significant difference in the demographics and clinical symptoms between the malignant and benign groups, except for regarding chest pain ($P = 0.03$; Table 4).

In total, 19 (79.2%) patients had available chest radiographs, 22 (91.7%) underwent CT scans, 2 (8.3%) underwent MRI scans, and 4

(16.7%) underwent both CT and MRI scans. Three (13.6%) CT examinations were performed without contrast material at other hospitals. The mass was found incidentally in six (25%) patients. Fifteen (62%) tumors were in the right lung and nine (37%) in the left lung. The frequencies of the involved lobes were as follows: right upper ($n = 6$, 25%), right lower ($n = 6$, 25%), left lower ($n = 5$, 20%), left upper ($n = 4$, 16%), and right middle ($n = 3$, 12%). The mean tumor size at the time of diagnosis was 6.4 ± 3 cm (6.7 ± 3.4 cm in the benign group and 6 ± 2.3 cm in

the malignant group). The analysis revealed that there were no statistically significant differences in terms of tumor size between the malignant and benign groups ($P = 0.48$). Additionally, there was no statistically significant difference in the X-ray and CT findings between malignant and benign diseases, except for a higher prevalence of calcification in the benign tumors ($P = 0.01$).

Calcifications were present in eight patients with IMT (80%), one patient with PPB (16.6%), and one patient with mature cys-

Table 1. Demographics and clinical findings according to the benign and malignant subgroups

	Benign (n = 15)	Malign (n = 9)	Total (n = 24)	P
Demographics				
Age (y) (Median, 25p – 75p)	8 (11 months – 12)	4 (2.5 – 12)	7.5 (2 – 12)	0.92
Sex (F:M)	6:9	3:6	9:15	0.74
Clinical findings, n (%)				
Incidentally detected	4 (26.7%)	2 (22.2%)	6 (25%)	0.81
Cough	7 (46.7%)	5 (55.6%)	12 (50%)	0.67
Fever	4 (26.7%)	3 (33.3%)	7 (29.2%)	0.73
Recurrent infections	1 (6.7%)	0	1 (4.2%)	0.43
Neck swelling	0	1 (11.1%)	1 (4.2%)	0.19
Dyspnea	4 (26.7%)	1 (11.1%)	5 (20.8%)	0.36
Chest pain	1 (6.7%)	4 (44.4%)	5 (20.8%)	0.03
Dysphagia	1 (6.7%)	0	1 (4.2%)	0.43

Numbers in brackets are column percentages. F, female; M, male.

Table 2. Comparison of imaging features between the benign and malignant lesions

Imaging features	Benign (n = 15)	Malign (n = 9)	Total (n = 24)	P
X-ray*				
Abnormal opacity	9 (81.8%)	5 (62.5%)	14 (73.7%)	0.83
Asymmetrical lung opacity	1 ^a (9.1%)	0	1 (5.3%)	0.70
CT				
Size (cm) (mean \pm SD)	6.7 \pm 3.4	6 \pm 2.3	6.4 \pm 3	0.48
Multiplicity	2 (13.3%)	1 (11.1%)	3 (12.5%)	0.87
Lobulated margin	9 (60%)	6 (66.6%)	15 (62.5%)	0.74
Contrast enhancement^b				
Heterogeneous	5 (45.4%)	6 (75%)	11 (57.9%)	0.87
Homogeneous	6 (54.5%)	1 (12.5%)	7 (36.8%)	
Calcification	9 (60%)	1 (11.1%)	10 (41.7%)	0.01
Atelectasis	8 (53.3%)	7 (77.8%)	15 (62.5%)	0.23
Pleural effusion	8 (53.3%)	3 (33.3%)	11 (45.8%)	0.34
Local invasion	7 (46.6%)	3 (33.3%)	10 (41.7%)	0.52
Lymphadenopathy	4 (26.7%)	2 (22.2%)	6 (25%)	0.81
Metastasis	0	2 (22.2%)	2 (8.3%)	0.06

Numbers in brackets are column percentages. *No preoperative radiographs were available for four patients in the benign group and one patient in the malignant group. ^aAn asymmetric radiolucent hemithorax was present on the contralateral side of the mass. ^bTwo patients in the benign group and one patient in the malignant group did not have IV contrast studies. The mature cystic teratoma had a mildly enhancing solid nodule, and one pneumocytoma did not have apparent contrast enhancement. SD, standard deviation.

tic teratoma. The location of the tumor was peripheral in 18 patients (75%) and central in 6 patients (25%). Eleven tumors (57.9%) showed heterogeneous and seven (36.8%) homogeneous contrast enhancement. One (4.8%) pneumocytoma did not show any contrast enhancement, and the mature cystic teratoma presented with only a mildly enhancing solid nodular element. Notably, one adenocarcinoma (4.2%) and one LELC (4.2%) were found to be metastatic at the time of diagnosis.

Inflammatory myofibroblastic tumor

Ten children (four girls and six boys; mean age: 8.1 years) were diagnosed with IMT. Eight (8/10) tumors had calcification (Figure 2). The CT scans of two patients were performed without intravenous contrast. Five (62.5%) tumors showed heterogeneous enhancement, while three showed homogeneous enhancement. Eight (80%) tumors were located peripherally, and seven (70%) were located at the lower zones. Six (60%) tumors had lobulated borders, while four (40%) had fine borders. Seven (70%) patients had pleural effusion, six (60%) had atelectasis, and four (40%) had lymphadenopathies. Moreover, seven patients (70%) had local invasion findings, with two showing pulmonary artery and vein invasion, two esophageal invasion, two pericardial invasion, and one left atrial invasion. No metastasis was detected. On MRI, both tumors were heterogeneous on T2- and T1-weighted images,

hyperintense on T2-weighted images, and isointense/hyperintense on T1-weighted images. Both tumors showed heterogeneous contrast enhancement and diffusion restriction on MRI. Four of these tumors were previously reported.⁵

Hemangioma

Two (8.3%) children (a nine-month-old girl and a five-month-old boy) had hemangiomas. The CT scans revealed that both tumors were located peripherally, with lobulated margins and homogeneous contrast enhancement. The patient with giant hemangioma also demonstrated mediastinal shift. Due to the risk of bleeding, biopsy was not performed on either patient. Both patients were diagnosed as having hemangioma according to their radiologic findings, and they showed dramatic involution after propranolol treatment (Figure 3).

Pneumocytoma

Two (8.3%) children (a 13-year-old girl and a 15-year-old boy) had pneumocytoma. Both patients had single tumors. The tumors had different imaging features in the contrast-enhanced series, with one showing no apparent contrast enhancement and the other having homogeneous enhancement (Figure 4). One (50%) tumor was central. The two tumors had different margin characteristics: one was lobulated, and the other was smooth. The two CTs were unremarkable in terms of the other investigated parameters.

However, ground-glass opacities resembling a "halo sign" were observed to surround one of the tumors. MRI was undertaken for only one patient and showed that the tumor was isointense to the paraspinal muscles on T1-weighted images and hyperintense on T2-weighted images. No restricted diffusion signal was observed on the diffusion-weighted imaging series.

Mature cystic teratoma

An 11-year-old boy was diagnosed with a mature cystic teratoma. The tumor had a maximum diameter of 15 cm and smooth margins and was located peripherally. It had a fluid density and calcification. Atelectasis and pleural effusion were also noted. A 1-cm mildly enhancing hyperdense nodule was detected within the tumor (Figure 5).

Pleuropulmonary blastoma

Six (25%) children (two girls and four boys; mean age: 3.3 years) were diagnosed with PPB. There were three (50%) type 2 tumors, two (33.3%) type 3 tumors, and one (16.7%) type 1 tumor. Calcification was found in only one (16.7%) patient. Five (100%) tumors (excluding a patient imaging performed without intravenous contrast) exhibited heterogeneous contrast enhancement. Four (66.6%) tumors had irregular margins. All six patients had atelectasis, three (50%) had pleural effusion, and one (16.7%) had pneumothorax. The MRI showed two (33.3%) tumors with solid and

Table 3. The imaging features of different histopathological entities

	IMT	PPB	Adenocarcinoma	Hemangioma	Pneumocytoma	MCT	LELC	Total
N of cases	10 (41.6%)	6 (25%)	2 (8.3%)	2 (8.3%)	2 (8.3%)	1 (4.2%)	1 (4.2%)	24
Age (y) (median, 25p – 75p)	8.5 (6 – 12)	3 (2 – 4)	9, 15*	5 mo, 9 mo*	13, 15*	11 mo*	16	7.5 (2 – 12)
L:R	4:6	3:3	0:2	1:1	1:1	0:1	0:1	9:15
Peripheral location	8 (80%)	6 (100%)	0	2 (100%)	1 (50%)	1 (100%)	0	18 (75%)
Greatest axial diameter (cm) (Median, 25p – 75p)	7.9 (5.5 – 10)	7.75 (6.8 – 9.2)	4, 4.4 ^a	4, 8.2 ^a	2.3, 2.4 ^a	15	2.8	7.25 (4.25 – 9.6)
Calcification	8 (80%)	1 (16.7%)	0	0	0	1 (100%)	0	10 (41.6%)
Atelectasis	6 (60%)	6 (100%)	1 (50%)	1 (50%)	0	1	0	15 (62.5%)
Heterogeneous enhancement	5 (62.5%) ^β	5 (100%) ^β	1 (50%)	0 ^β	0 ^β	NE	NA	11 (57.9%)
Lobulated margin	6 (60%)	4 (66.6%)	2 (100%)	2 (100%)	1 (50%)	0	0	15 (62.5%)
Pleural effusion	7 (70%)	3 (50%)	0	0	0	1 (100%)	0	11 (45.8%)
Lymphadenopathy	4 (40%)	0	1 (50%)	0	0	0	1 (100%)	6 (25%)
Local invasion	7 (70%)	2 (33.3%)	1 (50%)	0	0	0	0	10 (41.6%)
Metastasis	0	0	1 (50%)	0	0	0	1 (100%)	1 (4.2%)

Numbers in brackets are column percentages. *Patients' ages are given separately. ^aTumor sizes are given separately. ^βTwo patients with IMT and one with PPB did not undergo preoperative CT or MRI with intravenous contrast. Homogeneous contrast enhancement was observed in two patients with hemangioma and one patient with pneumocytoma. IMT, inflammatory myofibroblastic tumor; PPB, pleuropulmonary blastoma; CT, computed tomography; MRI, magnetic resonance imaging; MCT, mature cystic teratoma; LELC, lymphoepithelioma-like carcinoma; NE, no enhancement; NA, not available; mo, months; L:R: left lung:right lung.

Table 4. A comprehensive presentation of individual tumor characteristics

Patient	Diagnosis	Age (yo)	Sex	Initial symptoms	Imaging studies	Location	Size (cm)	Contours	Contrast enhancement pattern	Calcification	Atelectasis	Peripheral	Pleural effusion	LAP	Local invasion	Metastasis
1	IMT	15	M	Cough, dyspnea, chest pain	CT	LLL	5.5x3.7	Lobulated	Heterogenous	+	+	-	+	-	+	-
2	IMT	8	M	Fever, cough, dyspnea	CT	RLL	11x8	Smooth	Homogeneous	+	+	+	+	+	+	-
3	IMT	9	M	Incidental	CT	RML	10x8	Lobulated	NA	+	-	+	+	+	+	-
4	IMT	12	M	Fever, cough	CT	RLL	7x6	Smooth	Heterogenous	+	+	+	+	-	-	-
5	IMT	2	F	Fever, recurring infection	CT	RUL	7.7x6.6	Lobulated	NA	+	+	+	-	-	+	-
6	IMT	12	F	Dysphagia	CT, MRI	LLL	10x6.5	Lobulated	Heterogenous	+	+	+	+	-	+	-
7	IMT	6	M	Incidental	MRI	LUL	6.6x8.1	Lobulated	Heterogenous	-	+	-	+	-	-	-
8	IMT	9 mo	F	Incidental	CT	LUL	4.1x3.6	Smooth	Homogenous	-	-	+	+	+	+	-
9	IMT	7	M	Cough	CT	RLL	5x4	Lobulated	Heterogenous	+	-	+	-	+	+	-
10	IMT	10	F	Cough	CT	RLL	10x8	Smooth	Homogenous	+	-	+	-	-	-	-
11	PPB	9	M	Cough, dyspnea, chest pain	CT	RLL	8x7.3	Smooth	Heterogenous	-	+	+	-	-	-	-
12	PPB	2	M	Incidental	CT	LUL	5x4.5	Lobulated	NA	-	+	+	-	-	-	-
13	PPB	4	M	Cough, fever, chest pain	CT, MRI	RML	6.3x7.5	Lobulated	Heterogenous	-	+	+	+	-	+	-
14	PPB	3	F	Cough, fever, chest pain	CT	RUL	6.8x6	Lobulated	Heterogenous	+	+	+	+	-	+	-
15	PPB	21 mo	F	Fever	MRI	LLL	10x8	Lobulated	Heterogenous	-	+	+	-	-	-	-
16	PPB	3	M	Chest pain	CT	LLL	9.2x8.7	Smooth	Heterogenous	-	+	+	+	-	-	-
17	Adenocarcinoma	15	F	Cough, neck swelling	CT	RML	4.4x3.8	Lobulated	Homogenous	-	+	-	-	+	+	+
18	Adenocarcinoma	9	M	Cough	CT, MRI	RUL	4x3.8	Lobulated	Heterogenous	-	-	-	-	-	-	-
19	Hemangioma	9 mo	F	Dyspnea	CT	LLL	8.2x7.5	Lobulated	Homogenous	-	+	+	-	-	-	-
20	Hemangioma	5 mo	M	Fever	CT	RUL	4x3	Lobulated	Homogenous	-	-	+	-	-	-	-
21	Pneumocytoma	15	M	Incidental	CT, MRI	RUL	2.3x1.7	Lobulated	Homogenous	-	-	+	-	-	-	-
22	Pneumocytoma	13	F	Cough	CT	LUL	2.4x2.3	Smooth	Absent	-	-	-	-	-	-	-
23	Mature cystic teratoma	11 mo	M	Cough, dyspnea	CT	RLL	15x15	Smooth	Absent	+	+	+	+	-	-	-
24	LELC	16	M	Incidental	CT	RUL	2.8x2.5	Smooth	NA	-	-	-	-	+	-	+

IMT, inflammatory myofibroblastic tumor; PPB, pleuropulmonary blastoma; MEC, mucocoeplithelioma-like carcinoma; LELC, lymphoepithelioma-like carcinoma; yo, years old; mo, months old; RUL, right upper lobe; RML, right middle lobe; RLL, right lower lobe; LUL, left upper lobe; LLL, left lower lobe; NA, not applicable; CT, computed tomography; MRI, magnetic resonance imaging; M, male; F, female; LAP, lymphadenopathy.

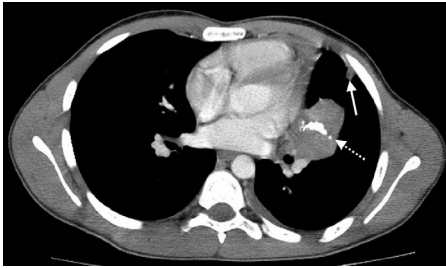


Figure 2. A 15-year-old boy with inflammatory myofibroblastic tumor. The axial contrast-enhanced computed tomography image shows a lobulated mass with heterogeneous enhancement and calcifications (dashed arrow) in the left upper lobe. Note the subpleural atelectasis (arrow).



Figure 3. (a, b) A nine-month-old girl with hemangioma. (a) The axial contrast-enhanced computed tomography (CT) image shows large, homogenous contrast-enhanced tumor in the left lower lobe (arrows). (b) Following one year of propranolol treatment, a contrast-enhanced chest CT showed a significant decrease in the overall tumor size (arrows).

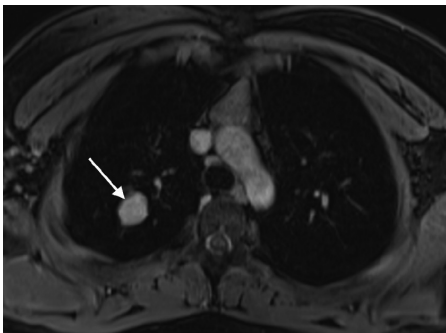


Figure 4. A 15-year-old girl with pneumocytoma. The axial contrast-enhanced T1-weighted image demonstrates a homogeneously enhancing mass lesion (arrow).

cystic parts. The cystic parts were hyperintense on both T2- and T1-weighted images, indicating the presence of hemorrhage. The solid parts were heterogeneous due to cystic/necrotic areas and had lobulated margins. Both tumors had marked enhancement and diffusion restriction in the solid components (Figure 6). One type 2 tumor had local invasion into the mediastinum, and one type 3 tumor had right pulmonary vein thrombosis extending to the left atrium at the time of diagnosis. One patient with type 3 PPB developed brain metastasis during follow-up.

Adenocarcinoma

Two (8.3%) children (a 15-year-old girl and a 9-year-old boy) were diagnosed with adenocarcinoma. Both patients underwent CT, and one patient had both CT and MRI exams. One patient presented with bilateral and multifocal lesions along with interlobular septal thickening compatible with lymphatic spread. There were also visceral and lymph node metastases. The other patient

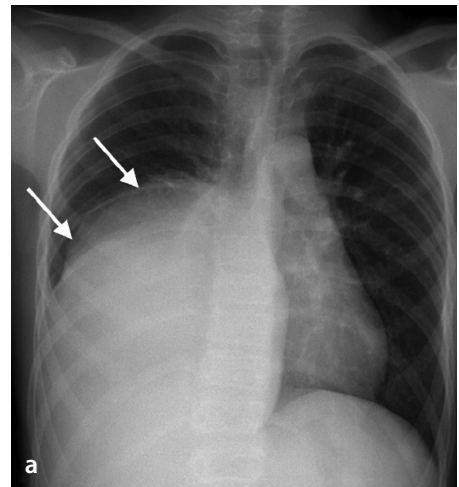


Figure 5. (a, b) An 11-month-old boy with mature cystic teratoma. (a) The chest X-ray shows large opacity in the lower zone of the right lung. (b) The axial chest computed tomography image demonstrates a large cystic mass with calcification (black arrow) and a nodular solid component (not shown).

had a central solitary tumor without atelectasis, lymphadenopathy, or local invasion. Neither tumor showed calcification. The tumor was hyperintense on T2-weighted images, isointense/hypointense on T1-weighted images, and had restricted diffusion signal (Figure 7).

Lymphoepithelioma-like carcinoma

A 16-year-old boy was diagnosed with LELC after a mass-like opacity was incidentally found on a chest X-ray in the right upper zone. The tumor measured 2.8 cm and was centrally located, with smooth margins and no calcification on CT. There was also mediastinal and ipsilateral hilar lymphadenopathy. It was not possible to comment on contrast enhancement due to the lack of pre-contrast

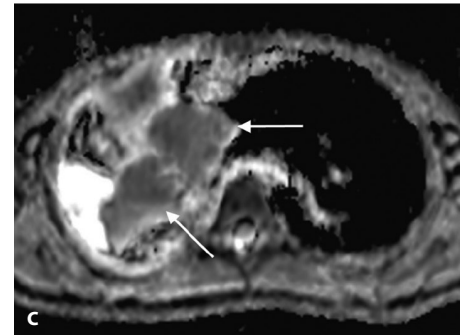
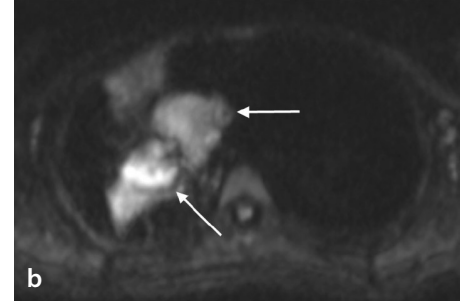
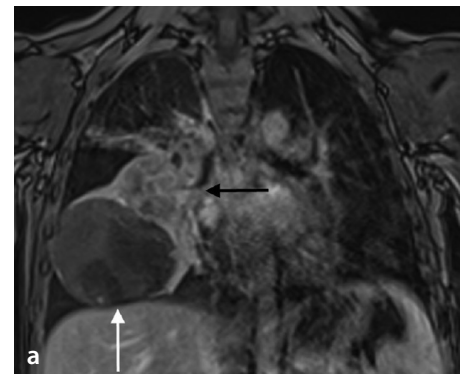


Figure 6. (a-c) A four-year-old boy with type 2 pleuropulmonary blastoma. (a) The coronal post-contrast magnetic resonance image shows a large and heterogeneous tumor with a lobulated margin consisting of solid (black arrow) and cystic (white arrow) parts. (b) The diffusion-weighted image ($b = 800 \text{ s/mm}^2$) and (c) apparent diffusion coefficient map show the diffusion restriction of the solid components of the tumor (arrows).

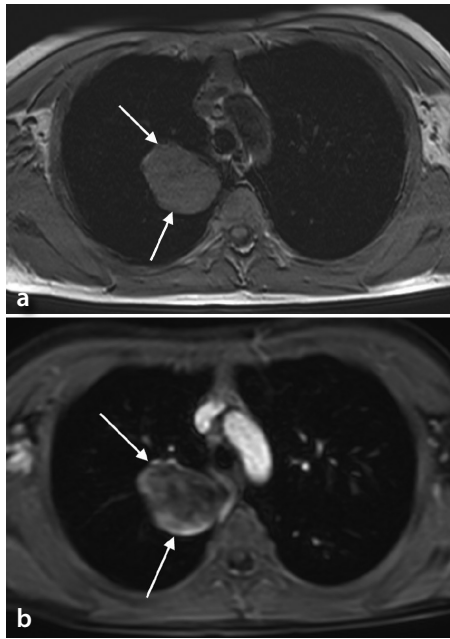


Figure 7. (a, b) A nine-year-old boy diagnosed with lung adenocarcinoma. (a) The axial T1-weighted image shows a well-circumscribed and isointense tumor in the right upper lobe (arrow). (b) Note the heterogeneous enhancement on the T1-weighted post-contrast image (arrow).

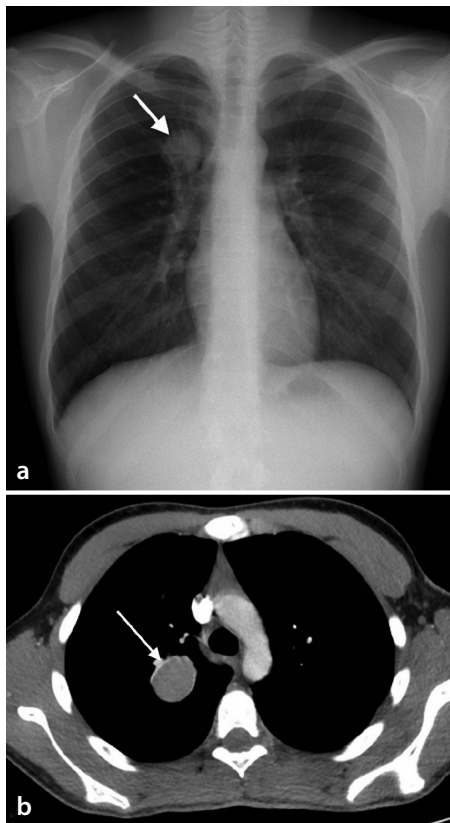


Figure 8. (a, b) A 16-year-old boy with lymphoepithelioma-like carcinoma. (a) The chest X-ray taken prior to the orthopedic surgery shows a nodule with smooth contours (arrow). (b) The axial contrast-enhanced chest computed tomography scan shows a uniform mass lesion (arrow).

images. There was neither pleural effusion nor atelectasis (Figure 8).

Discussion

This study yielded two major findings. First, pediatric patients with lung tumors generally have non-specific and indistinct clinical presentations, which can lead to misdiagnosis. Second, the most common lung tumors in children are benign, specifically dominated by IMT.

Previously known as inflammatory pseudotumor, plasma cell granuloma, or inflammatory fibrosarcoma, IMT is a rare mesenchymal tumor that may occur throughout the body, where the lung is the most affected organ.¹¹ The World Health Organization's fifth edition of *Thoracic Tumors* classifies IMT as having "borderline or uncertain behavior," possibly due to its potential for local invasion, tumor recurrence, and metastasis, despite previously being considered a benign entity.^{12,13} Similar to the literature, in our series, the most common primary lung tumor was IMT.² However, in some patient cohorts, the most commonly reported tumor is carcinoid.^{2,14} Among our patients, the most common presenting symptoms were cough and fever. IMT was predominantly located in the lower lung zones, consistent with the available literature.^{12,15} Our study identified three major imaging findings suggestive of IMT, including calcification, peripheral location, and lobulated margins. In our series, calcification was present in four-fifths of the patients, whereas the literature reports varying rates (15%–77.8%) depending on the patient demographics and anatomic origins involved.^{16,17} The inclusion of only parenchymal IMTs in our study may have contributed to this difference.¹⁷ Additionally, calcification is reported to be more common in pediatric cases.^{15,17} Atelectasis, pleural effusion, and local invasion were relatively common in our series, while lymphadenopathy was rare, which is consistent with the literature.¹⁵

Hemangioma, pneumocytoma, and mature cystic teratoma were the other benign tumors found in our patients. Pulmonary hemangioma is a rare tumor that typically presents as a solitary, well-defined lesion in the early neonatal period. Co-occurrence with other sites, such as the skin or liver, may be observed.¹⁸ According to the classification system developed by the International Society for the Study of Vascular Anomalies, hemangiomas are categorized as either infantile or congenital based on the age of presentation and the presence of endothelial cell glucose

transporter 1 (GLUT-1).¹⁹ Infantile hemangiomas tend to grow after birth and are GLUT-1 positive. Dynamic CT and MRI studies may help to differentiate hemangiomas from other pulmonary tumors. Hemangiomas typically show early, peripheral and strong enhancement with sharply defined borders, and do not cause a mass effect.²⁰ Other presentations, such as multifocal masses, lesions with cystic spaces, and endobronchial lesions, may be seen.¹ Additionally, pulmonary artery or vein enlargement may be present due to increased supply.¹ Pneumocytoma (previously known as pulmonary sclerosing hemangioma) is a rare benign neoplasm of the lung and is frequently seen as a well-defined intraparenchymal nodular mass (often peripherally). Although size variability has been reported, most pneumocytomas are <3.5 cm in largest diameter,²¹ which is compatible with our results. Although mediastinal teratomas are far from rare, primary pulmonary teratomas are extremely uncommon. Pulmonary teratomas present as encapsulated masses with a thin wall containing liquid tissue, fat, calcifications, or any such combination. In our single patient, the tumor was cystic with a mildly enhancing mural nodule and had calcified components.

PPB is the most common malignant primary lung tumor in the pediatric age group. Most patients are younger than six years old. Likewise, in our series, all patients except one (a nine-year-old boy) were under six years of age at the time of diagnosis.¹ PPB has three histopathological subtypes: type 1 is purely cystic (mean age: 10 months), type 2 is cystic and solid (mean age: 34 months), and type 3 is purely solid (mean age: 44 months).¹ Of note, the age at initial diagnosis is known to correlate with the subtype. In our series, there were three patients with type 2, two patients with type 3, and one patient with type 1. PPB has an association with *DICER1* gene mutations, and approximately 65%–70% of children with PPB display heterogeneous mutations.²² Other tumors associated with *DICER1* mutations include cystic nephroma, pineoblastoma, pituitary blastoma, differentiated thyroid cancer, ovarian sex cord-stromal tumor, and embryonal rhabdomyosarcoma.^{23–25} In the current study, due to the fact that these mutations have only been evaluated in very recent literature, our patients unfortunately did not undergo pertinent analyses. While most PPB cases are reported in the right hemithorax, in our series, three patients had left-sided lesions. At CT and MRI, type 1 tumors might appear as single or multicystic lesions. Type 2 tumors have air- or fluid-filled cavities with possible air-fluid levels along with solid internal nodules. Type

3 tumors are solid lesions. Pleural effusion and pneumothorax are frequently associated findings in PPB. In our series, three patients had pleural effusion, and only one had pneumothorax. One of our type 3 patients had right pulmonary vein thrombosis extending to the left atrium at the time of diagnosis, which is a rare but significant complication of PPB.

Adenocarcinoma is the most common subtype of non-small-cell lung cancer and is extremely rare in children and adolescents. Primary lung adenocarcinoma of children has the poorest prognosis, with a high prevalence of distant metastases.²⁶ Imaging findings are associated with histopathological classification and vary from a focal ground-glass nodule to a solid nodule or a mass.²⁶ They may present as mass-like consolidations and mimic pneumonia.

LELC is a large-cell carcinoma with prominent lymphocyte infiltration and is mostly seen in the nasopharynx. Similar to nasopharyngeal tumor, primary pulmonary LELC has a documented strong relationship with Epstein-Barr virus infection in Asian populations.²⁷ It usually presents with solitary pulmonary nodule or mass. However, primary pulmonary LELC in the pediatric population is extremely rare. During his preoperative workup for an orthopedic surgery, our patient was diagnosed with a chest X-ray incidentally. A subsequent chest CT was performed to confirm the presumptive diagnosis of a benign lesion, such as a bronchogenic cyst. Thus, it is important to note that small size or smooth appearance of a lesion does not exclude a malignant tumor.

Our study had some limitations. First, due to the retrospective design, the imaging studies were heterogeneous. Second, we reviewed only the radiology archives of our institute and could therefore enroll a relatively small sample.

In conclusion, primary lung tumors are rarely seen in children, and they have different histopathological types. Patients generally have non-specific and indistinct clinical presentations, possibly delaying the initial diagnosis. It is noteworthy that calcification might be an important radiological clue for the diagnosis of IMT. Moreover, PPB is the most common malignant lung tumor in the pediatric age group and displays a wide range of imaging findings. Persistent consolidation and atelectasis should necessarily alert the radiologist regarding malignancy. Lastly, small size or smooth contouring of a lesion does not rule out a malignant tumor.

Conflict of interest disclosure

The authors declared no conflicts of interest.

References

- Lichtenberger JP 3rd, Biko DM, Carter BW, Pavo MA, Huppmann AR, Chung EM. Primary lung tumors in children: Radiologic-pathologic correlation. *Radiographics*. 2018;38(7):2151-2172. [\[Crossref\]](#)
- Yu DC, Grabowski MJ, Kozakewich HP, et al. Primary lung tumors in children and adolescents: a 90-year experience. *J Pediatr Surg*. 2010;45(6):1090-1095. [\[Crossref\]](#)
- Giuseppucci C, Reusmann A, Giubergia V, et al. Primary lung tumors in children: 24 years of experience at a referral center. *Pediatr Surg Int*. 2016;32(5):451-457. [\[Crossref\]](#)
- Cohen MC, Kaschula ROC. Primary pulmonary tumors in childhood: a review of 31 years' experience and the literature. *Pediatr Pulmonol*. 1992;14(4):222-232. [\[Crossref\]](#)
- Eggl KD, Newman B. Nodules, masses, and pseudomasses in the pediatric lung. *Radiol Clin North Am*. 1993;31(3):651-666. [\[Crossref\]](#)
- Hancock BJ, Di Lorenzo M, Youssef S, Yazbeck S, Marcotte JE, Collin PP. Childhood primary pulmonary neoplasms. *J Pediatr Surg*. 1993;28(9):1133-1136. [\[Crossref\]](#)
- Rojas Y, Shi YX, Zhang W, et al. Primary malignant pulmonary tumors in children: a review of the national cancer data base. *J Pediatr Surg*. 2015;50(6):1004-1008. [\[Crossref\]](#)
- Amini B, Huang SY, Tsai J, Benveniste MF, Robledo HH, Lee EY. Primary lung and large airway neoplasms in children: current imaging evaluation with multidetector computed tomography. *Radiol Clin North Am*. 2013;51(4):637-657. [\[Crossref\]](#)
- Alves GR, Marchiori E, Irion KL, et al. Mediastinal lymph nodes and pulmonary nodules in children: MDCT findings in a cohort of healthy subjects. *American Journal of Roentgenology*. 2015;204(1):35-37. [\[Crossref\]](#)
- Casal RF, Vial MR, Miller R, et al. What exactly is a centrally located lung tumor? Results of an online survey. *Ann Am Thorac Soc*. 2017;14(1):118-123. [\[Crossref\]](#)
- Oguz B, Ozcan HN, Omay B, Ozgen B, Haliloglu M. Imaging of childhood inflammatory myofibroblastic tumor. *Pediatr Radiol*. 2015;45(11):1672-1681. [\[Crossref\]](#)
- Narla LD, Newman B, Spottswood SS, Narla S, Kolli R. Inflammatory pseudotumor. *Radiographics*. 2003;23(3):719-729. [\[Crossref\]](#)
- WHO Classification of Tumours Editorial Board, ed. Thoracic Tumours. In: WHO Classification of Tumours. Vol 5. 5th ed. ; 2021:288-290. [\[Crossref\]](#)
- Shao W, Liu J, Li B, et al. Primary lung cancer in children and adolescents: analysis of a surveillance, epidemiology, and end results

database. *Front Oncol*. 2023;13:1053248. [\[Crossref\]](#)

- Agrons GA, Rosado-de-Christenson ML, Kirejczyk WM, Conran RM, Stocker JT. Pulmonary inflammatory pseudotumor: Radiologic features. *Radiology*. 1998;206(2):511-518. [\[Crossref\]](#)
- Kim TS, Han J, Kim GY, Lee KS, Kim H, Kim J. Pulmonary inflammatory pseudotumor (inflammatory myofibroblastic tumor): CT features with pathologic correlation. *J Comput Assist Tomogr*. 2005;29(5):633-639. [\[Crossref\]](#)
- Irodi A, Chacko BR, Prajapati A, et al. Inflammatory myofibroblastic tumours of the thorax: radiologic and clinicopathological correlation. *Indian J Radiol Imaging*. 2020;30(3):266-272. [\[Crossref\]](#)
- Wheeler A, Kozakewich HP, Shashi K, Eng W. Pulmonary infantile hemangioma: clinical and histopathological review of eight cases. *Blood*. 2021;138(Suppl 1):4209-4209. [\[Crossref\]](#)
- International Society for the Study of Vascular Anomalies. ISSVA Classification of Vascular Anomalies. issva.org/classification. [\[Crossref\]](#)
- Pandya R, Tummala V. Giant infantile pulmonary hemangioma. *Pediatr Radiol*. 2010;40(Suppl 1):63-67. [\[Crossref\]](#)
- Shin SY, Kim MY, Oh SY, et al. Pulmonary sclerosing pneumocytoma of the lung: CT characteristics in a large series of a tertiary referral center. *Medicine (Baltimore)*. 2015;94(4):e498. [\[Crossref\]](#)
- Dehner LP, Messinger YH, Schultz KAP, et al. Pleuropulmonary blastoma: evolution of an entity as an entry into a familial tumor predisposition syndrome. *Pediatr Dev Pathol*. 2015;18(6):504-511. [\[Crossref\]](#)
- Bueno MT, Martínez-Ríos C, la Puente Gregorio A, et al. Pediatric imaging in DICER1 syndrome. *Pediatr Radiol*. 2017;47(10):1292-1301. [\[Crossref\]](#)
- van Engelen K, Villani A, Wasserman JD, et al. DICER1 syndrome: approach to testing and management at a large pediatric tertiary care center. *Pediatr Blood Cancer*. 2018;65(1). [\[Crossref\]](#)
- Sabapathy DG, Paul Guillerman R, Orth RC, et al. Radiographic screening of infants and young children with genetic predisposition for rare malignancies: DICER1 mutations and pleuropulmonary blastoma. *AJR Am J Roentgenol*. 2015;204(4):475-482. [\[Crossref\]](#)
- Kayton ML, He M, Zakowski MF, et al. Primary lung adenocarcinomas in children and adolescents treated for pediatric malignancies. *J Thorac Oncol*. 2010;5(11):1764-1771. [\[Crossref\]](#)
- Hoxworth JM, Hanks DK, Araoz PA, et al. Lymphoepithelioma-like carcinoma of the lung: radiologic features of an uncommon primary pulmonary neoplasm. *AJR Am J Roentgenol*. 2006;186(5):1294-1299. [\[Crossref\]](#)